Thin Film Growth and Characterization of the Transition Metal Oxides Magnetite and Layered Perovskite Iridates

Dissertation zur Erlangung des
naturwissenschaftlichen Doktorgrades der
Julius-Maximilians-Universität Würzburg

vorgelegt von
Ozan Seyitali Kirilmaz
aus Würzburg

Würzburg 2018

Eingereicht am: 30.05.2018

bei der Fakultät für Physik und Astronomie

1. Gutachter: Prof. Dr. Ralph Claessen

2. Gutachter: Prof. Dr. Atsushi Yamasaki

3. Gutachter:

der Dissertation.

Vorsitzende(r):

1. Prüfer: Prof. Dr. Ralph Claessen

2. Prüfer: Prof. Dr. Atsushi Yamasaki

3. Prüfer: Prof. Dr. Giorgio Sangiovanni

im Promotionskolloquium.

Tag des Promotionskolloquiums: 29.03.2019

Doktorurkunde ausgehändigt am:

DEDICATION

To My Father and Mother
Selman and Kamile Kırılmaz

This thesis is dedicated to my wonderful parents
who have raised me up to be the person I am today.
Thank you for all the unconditional love, guidance,
and support that you have always given me!

Abstract

This thesis describes the growth and characterization of both the all-oxide heterostructure Fe_3O_4/ZnO and the spin-orbit coupling driven layered perovskite iridates.

As for Fe_3O_4/ZnO, the 100% spin-polarized Fe_3O_4 is a promising spin electrode candidate for spintronic devices. However, the single crystalline ZnO substrates exhibit different polar surface termination which, together with substrate preparation method, can drastically affect the physical properties of Fe_3O_4/ZnO heterostructures. In this thesis two different methods of substrate preparation were investigated: a previously used *in situ* method involving sputtering and annealing treatments and a recent *ex situ* method containing only the annealing procedure. For the latter, the annealing treatment was performed in dry and humid O_2 gas flow for the O- and Zn-terminated substrates, respectively, to produce atomically flat surfaces as verified by atomic force microscopy (AFM). With these methods, four different ZnO substrates were fabricated and used further for Fe_3O_4 film growth. Fe_3O_4 films of 20 nm thickness were successfully grown by reactive molecular beam epitaxy. AFM measurements reveal a higher film surface roughness for the samples with *in situ* prepared substrates. Moreover, X-ray photoelectron spectroscopy (XPS) measurements indicate significant Zn substitution within the Fe_3O_4 film for these samples, whereas the samples with *ex situ* prepared substrates show stoichiometric Fe_3O_4 films. X-ray diffraction measurements confirm the observations from XPS, revealing additional peaks due to Zn substitution in Fe_3O_4 films grown on *in situ* prepared ZnO substrates. Conductivity, as well as magnetometry, measurements show the presence of Zn-doped ferrites in films grown on *in situ* prepared substrates. Such unintentionally intercalated Zn-doped ferrites dramatically change the electrical and magnetic properties of the films and, therefore, are not preferred in a high-quality heterostructure.

X-ray reflectivity (XRR) measurements show for the film grown on *ex situ* prepared Zn-terminated substrate a variation of film density close to the interface which is also confirmed by transmission electron microscopy (TEM). Using polarized neutron reflectometry, magnetic depth profiles of the films grown on *ex situ* prepared substrates clearly indicate Fe_3O_4 layers with reduced magnetization at the interfaces. This result is consistent with earlier observations made by resonant magnetic X-ray reflectometry (RMXR), but in contrast to the findings from XRR and TEM of this thesis. A detailed TEM study of all four samples shows that the sample with *ex situ* prepared O-terminated substrate has the sharpest interface, whereas those with *ex situ* prepared Zn-terminated as well as *in situ* prepared substrates indicate rougher interfaces. STEM-EELS composition profiles of the samples reveal the Zn substitution in the films with *in situ* prepared substrates and therefore confirm the presence of Zn-doped ferrites. Moreover, a change of the Fe oxidation state of the first Fe layer at the interface which was observed in previous studies done by RMXR, was not verified for the samples with *in situ* prepared substrates thus leaving the question of a possible presence of the magnetically dead layer

open.
Furthermore, density functional theory calculations were performed to determine the termination dependent layer sequences which are ...-Zn-O-(interface)-[Fe(octa)-O-Fe(tetra)-Fe(octa)-Fe(tetra)-O]-[...]-... and ...-O-Zn-(interface)-[O-Fe(octa)-O-Fe(tetra)-Fe(octa)-Fe(tetra)]-[...]-... for the samples with O- and Zn-terminated substrates, respectively. Spin density calculations show that in case of O-termination the topmost substrate layers imitate the spin polarization of film layers close to the interface. Here, the first O layer is affected much stronger than the first Zn layer. Due to the strong decrease of this effect toward deeper substrate layers, the substrate surface is supposed to be sensitive to the contiguous spin polarization of the film. Thus, the topmost O layer of the O-terminated substrate could play the most essential role for effective spin injection into ZnO.

The $5d$ transition metal oxides Ba_2IrO_4 (BIO) and Sr_2IrO_4 (SIO) are associated with the Ruddlesden-Popper iridate series with phase type "214" (RP–214), and due to the strong spin-orbit coupling belong to the class of Mott insulators. Moreover, they show many similarities of the isostructural high T_c-cuprate superconductors, e.g. crystal structure, magnetism and electronic band structure. Therefore, it is of great interest to activate a potential superconducting phase in (RP–214) iridates. However, only a small number of publications on PLD grown (RP–214) iridates in the literature exists. Furthermore, published data of soft X-ray angle resolved photoemission spectroscopy (SX-ARPES) experiments mainly originate from measurements which were performed on single crystals or MBE grown films of SIO and BIO. In this thesis La-doped SIO films ($La_{0.2}Sr_{1.8}IrO_4$, further referred as LSIO) were used to pursue a potential superconducting phase.
A set of characterization methods was used to analyze the quality of the PLD grown BIO, SIO and LSIO films. AFM measurements demonstrate that thick PLD grown (RP–214) iridate films have rougher surfaces, indicating a transition from a 2D layer-by-layer growth (which is demonstrated by RHEED oscillations) to a 3D island-like growth mode. In addition, chemical depth profiling XPS measurements indicate an increase of the O and Ir relative concentrations in the topmost film layers. Constant energy k-space maps and energy distribution curves (EDCs) measured by SX-ARPES show for every grown film only weak energy band dispersions, which are in strong contrast to the results obtained on the MBE grown films and single crystals from the literature. In this thesis, a subsequent TEM study reveals missing SrO layers within the grown films which occur mainly in the topmost layers, confirming the results and suggestions from XPS and SX-ARPES data: the PLD grown films have defects and, therefore, incoherently scatter photoelectrons. Nevertheless, the LSIO film shows small additional spectral weight between the highsymmetry M points close to the Fermi level which can be attributed to quasiparticle states which, in turn, indicates the formation of a Fermi-arc. However, neither conductivity measurements nor valence band analysis via XPS confirm an activation of a superconducting phase or presence of spectral weight of quasiparticle states at the Fermi level in this LSIO film.

It is possible that these discovered difficulties in growth are responsible for the low number of SX-ARPES publications on PLD grown (RP–214) iridate films. For further investigations of (RP–214) iridate films by SX-ARPES, their PLD growth recipes have to be improved to create high quality single crystalline films without imperfections.

Zusammenfassung

Diese Arbeit beschäftigt sich mit dem Wachstum und der Charakterisierung der oxidischen Heterostruktur Fe_3O_4/ZnO sowie der durch Spin-Bahn-Kopplung angetriebenen, aus Perowskitlagen geschichteten Iridate.

In Bezug auf Fe_3O_4/ZnO, ist das zu 100% spinpolarisierte Magnetit ein vielversprechender Kandidat, um als Spinelektrode in Spintronikbauteilen eingesetzt zu werden. Die einkristallinen ZnO Substrate besitzen auf deren Oberflächen jedoch unterschiedlich polare Terminierungen, welche, zusammen mit dem verwendeten Verfahren für die Substratpräparation, die physikalischen Eigenschaften von Fe_3O_4/ZnO Heterostrukturen drastisch beeinflussen können. In dieser Arbeit wurden zwei unterschiedliche Verfahren für die Substratpräparation untersucht: zum einen ein bereits früher verwendetes *in situ* Verfahren, das eine Sputter- und Temperbehandlung beinhaltet, zum anderen ein neues *ex situ* Verfahren, das ausschließlich aus einer Temperbehandlung besteht. Im letzteren Fall wurde für O- und Zn-terminierte Substrate die Temperbehandlung entsprechend in trockener und feuchter O_2 Atmosphäre durchgeführt, um atomar glatte Oberflächen zu erzielen. Dies wurde mithilfe der Rasterkraftmikroskopie (AFM) verifiziert. Mit diesen Verfahren wurden vier verschiedene ZnO Substrate hergestellt und anschließend für das Fe_3O_4 Filmwachstum verwendet. 20 nm dicke Fe_3O_4 Filme wurden mithilfe der reaktiven Molekularstrahlepitaxie erfolgreich gewachsen. AFM Messungen zeigen, dass die Proben mit *in situ* präparierten Substraten eine höhere Rauigkeit der Filmoberfläche besitzen. Des Weiteren zeigen Messungen mit Röntgenphotoelektronenspektroskopie (XPS) für diese Proben eine signifikante Zn-Substitution innerhalb des Fe_3O_4 Films, wohingegen Proben mit *ex situ* präparierten Substraten stöchiometrisch gewachsene Filme vorweisen. Messungen mit Röntgenbeugung bestätigen die Beobachtungen aus XPS, indem sie zusätzliche Peaks aufdecken, welche aufgrund der Zn-Substitution in den Fe_3O_4 Filmen mit *in situ* präparierten Substraten entstehen. Sowohl Leitfähigkeits- als auch Magnetometriemessungen zeigen, dass Zn-dotierte Ferrite in den Filmen mit *in situ* präparierten Substraten vorhanden sind. Solche unabsichtlich eingelagerten Zn-dotierten Ferrite ändern die elektrischen und magnetischen Eigenschaften der Filme grundlegend und sind aus diesem Grund für die gewünschte Qualität der Heterostruktur schädlich.

Für die Filme mit Zn-terminierten *ex situ* präparierten Substraten zeigen XRR Messungen eine Veränderung der Dichte des Films in Grenzschichtnähe an, die auch mithilfe der Transmissionselektronenmikroskopie (TEM) bestätigt wird. Unter Verwendung der polarisierten Neutronenreflektometrie zeigen die magnetischen Tiefenprofile der Filme mit *ex situ* präparierten Substraten eindeutig Fe_3O_4 Lagen mit reduzierter Magnetisierung an der Grenzschicht an. Dieses Resultat ist vereinbar mit früheren Beobachtungen aus der resonanten magnetischen Röntgenreflektometrie (RMXR), das jedoch im Gegensatz zu den Ergebnissen aus XRR und TEM aus dieser Arbeit steht. Eine detaillierte TEM Studie über alle vier Proben demonstriert, dass die Probe mit O-terminiertem

ex situ präpariertem Substrat die schärfste Grenzschicht aufweist, während jene mit *in situ* präparierten sowie Zn-terminierten *ex situ* präparierten Substraten rauere Grenzschichten anzeigen. STEM-EELS Kompositionsprofile der Proben lassen die Zn-Substitution in den Filmen mit *in situ* präparierten Substraten erkennen und bestätigen somit die Präsenz von Zn-dotierten Ferriten. Außerdem wurde eine Änderung des Oxidationszustandes von Fe in den ersten Fe Lagen an der Grenzschicht, das in früheren Studien mithilfe RMXR beobachtet wurde, bei den Proben mit *in situ* präparierten Substraten nicht bestätigt. Dadurch bleibt die Frage nach der möglichen Präsenz einer magnetisch toten Schicht offen.
Weiterhin wurden mithilfe der Dichtefunktionaltheorie Rechnungen durchgeführt, um die terminierungsabhängige Lagenabfolge zu bestimmen, welche ...-Zn-O-(interface)-[Fe(octa)-O-Fe(tetra)-Fe(octa)-Fe(tetra)-O]-[...]-... und ...-O-Zn-(interface)-[O-Fe(octa)-O-Fe(tetra)-Fe(octa)-Fe(tetra)]-[...]-... entsprechend für die Proben mit O- und Zn-terminierten Substraten sind. Rechnungen zur Spindichte zeigen, dass im Fall von O-Terminierung die obersten Substratlagen die Spinpolarisation der Filmlagen nahe an der Grenzschicht nachahmen. Hierbei ist die erste O Lage viel stärker beeinflusst als die erste Zn Lage. Aufgrund der starken Abnahme dieses Effekts Richtung tiefere Substratlagen wird die Substratoberfläche als besonders sensitiv auf die angrenzende Spinpolarisation des Films angenommen. Damit könnte die oberste O Lage des O-terminierten Substrates den entscheidensten Faktor für effektive Spininjektion ins ZnO spielen.

Die $5d$ Übergangsmetalloxide Ba_2IrO_4 (BIO) und Sr_2IrO_4 (SIO) hängen mit der Ruddlesden-Popper Iridatserie mit Phasentyp "214" (RP–214) zusammen und gehören aufgrund der starken Spin-Bahn-Kopplung zu der Klasse der Mott Isolatoren. Zudem haben sie viele Gemeinsamkeiten mit den isostrukturellen Kuprat-Hochtemperatursupraleitern, wie zum Beispiel Kristallstruktur, Magnetismus und elektronische Bandstruktur. Daher ist es von großem Interesse eine potentiell supraleitende Phase in (RP–214) Iridaten zu aktivieren. In der Literatur existiert jedoch nur eine kleine Anzahl an Veröffentlichungen über gepulste Laserdeposition (PLD) gewachsene (RP–214) Iridate. Außerdem stammen veröffentlichte Daten von Experimenten mit winkelaufgelöster Photoelektronenspektroskopie mit weicher Röntgenstrahlung (SX-ARPES) hauptsächlich von Messungen, welche an Einkristallen oder MBE gewachsenen Filmen aus SIO und BIO durchgeführt wurden. In dieser Arbeit wurden La-dotierte SIO Filme ($La_{0.2}Sr_{1.8}IrO_4$, im Weiteren bezeichnet als LSIO) verwendet, um eine potentiell supraleitende Phase anzustreben.
Ein Satz von Charakterisierungsmethoden wurde verwendet, um die Qualität der PLD gewachsenen BIO, SIO und LSIO Filme zu untersuchen. AFM Messungen demonstrieren, dass dicke PLD gewachsene (RP–214) Iridatfilme rauere Oberflächen aufweisen, welche durch einen Übergang vom 2D Lagenwachstum (der durch RHEED Oszillationen bekräftigt ist) zu einem 3D Inselwachstumsmodus erklärt werden. Zusätzlich zeigen chemische Tiefenprofilmessungen mittels XPS eine Zunahme der relativen Konzentrationen von O und Ir in den obersten Filmlagen. Die mit SX-ARPES erzeugten k-Raum

Abbildungen mit konstanter Energie und Energieverteilungskurven (EDCs) zeigen für jeden gewachsenen Film nur schwache Energiebanddispersionen, die im starken Gegensatz zu den Resultaten aus der Literatur stehen, welche von MBE gewachsenen Filmen und Einkristallen erhalten wurden. Die darauf folgende TEM Studie in dieser Arbeit enthüllte fehlende SrO Lagen innerhalb der gewachsenen Filme, die vor allem in den obersten Lagen auftreten und bestätigte damit die Resultate und Vermutungen aus den XPS und SX-ARPES Daten: die PLD gewachsenen Filme besitzen Defekte und streuen somit die Photoelektronen inkohärent. Dennoch zeigt der LSIO Film kleines zusätzliches spektrales Gewicht zwischen den M Hochsymmetriepunkten nahe der Fermienergie, das einem Quasipartikelzustand zugeordnet werden kann, der wiederum die Ausbildung eines Fermibogens anzeigt. Aber weder Leitfähigkeitsmessungen noch Valenzbandanalysen mittels XPS bestätigen für diesen LSIO Film die Aktivierung einer supraleitenden Phase oder das Vorhandensein von spektralem Gewicht von Quasipartikelzuständen an der Fermienergie.

Es kann sein, dass diese entdeckten Schwierigkeiten im Wachstum für die geringe Anzahl von SX-ARPES Publikationen über PLD gewachsene (RP–214) Iridatfilme verantwortlich sind. Für weitere Untersuchungen von (RP–214) Iridatfilmen mittels SX-ARPES müssen die Rezepte für deren PLD Wachstum verbessert werden, um hochqualitative einkristalline Iridatfilme ohne Fehlstellen zu erzeugen.

Contents

List of Figures

List of Tables

List of Acronyms

AFM	atomic force microscopy
APB	anti-phase boundary
(SX)ARPES	angle resolved photoelectron spectroscopy (soft X-ray regime)
CTS	charge transfer satellite
DFT(+U)	density functional theory (plus Coulomb interaction)
DOS	density of states
EDC	energy distribution curve
EELS	electron energy-loss spectroscopy
ESCA	electron spectroscopy for chemical analysis
FWHM	full width at half maximum
HAADF	high-angle annular dark field
HAXPES	hard X-ray photoelectron spectroscopy
IMFP	inelastic mean free path
LEED	low-energy electron diffraction
LSDA	local spin-density approximation
MBE	molecular beam epitaxy
ML	monolayer
NE	normal emission
PES	photoelectron spectroscopy
PLD	pulsed laser deposition
PNR	polarized neutron reflectometry
PPMS	physical property measurement system
RHEED	reflection high-energy electron diffraction
SEM	scanning electron microscopy
SQUID	superconducting quantum interference device
STEM	scanning transmission electron microscopy
TEM	transmission electron microscopy
uc	unit cell
UHV	ultrahigh vacuum
UPS	ultraviolet photoelectron spectroscopy
VB	valence band
XPS	X-ray photoelectron spectroscopy
XRD	X-ray diffraction
XRR	X-ray reflectivity

1 Introduction

Since the discovery of the spin degree of freedom of subatomic particles such as electrons, a lot of physical properties of various materials found an explanation involving presence of spin. Starting from magnetization and superconductivity to topological states, the knowledge about the presence of the spin is fundamental for the comprehension of the observed effects in certain materials.

The electron spin was postulated in 1925 by S. A. Goudsmit and G. E. Uhlenbeck for the explanation of the fine structure splitting of spectral lines of hydrogen-like atoms and the anomalous Zeeman effect [1, 2]. Along with the electrical charge and mass, the spin degree of freedom is one of the essential properties of the electron. But in contrast to charge and mass, the electron spin is a pure quantum mechanical value which is not visible in classical physics. However, the electron spin associates with a magnetic moment which enables a direct measure of the spin direction (Stern-Gerlach experiment). Indirectly, the electron spin can be derived from the atomic shell model of elements using the Pauli principle. In detail, the spin vector $\vec{s}$ of the electron has the spin quantum number s=1/2. Thus, its z-component can only have two values as $s_z = \pm 1/2\,\hbar$. In addition, the magnetic spin quantum number m_s describes the orientation of its spin with respect to the z-axis as $m_s = s_z/\hbar = \pm 1/2$.

Since a couple of years, two particular effects relating to the electron spin are of huge interest in modern solid state physics research. The first interesting effect is the possibility of spin polarization of charge carriers in the conduction band of some materials. Such materials are mainly ferromagnetic, exhibiting a band structure which is dependent on the spin orientation of their electrons. The energy bands of the spin-up ($m_s = +1/2$) and spin-down ($m_s = -1/2$) charge carriers are shifted to each other due to exchange interactions, resulting in an excess of electrons of one spin orientation at the Fermi level. This disequilibrium generates the magnetization of the ferromagnetic material. Therefore, the current flow in these materials is spin polarized.

The other interesting feature of the electron spin is the possibility for spin-orbit coupling. Note that this is a fully relativistic effect that couples the orbital and the spin angular momentum of an electron. Since this interaction is regulated by the electric field near the atomic nucleus, it is almost self evident that strong spin-orbit coupling takes place in materials consisting of large heavy atoms. Most prominent materials in which spin-orbit coupling exist and which are extensively studied are the $3d$ transition metal oxides high T_c-cuprate superconductors. However, the interaction in $3d$ systems is quite small compared to other competing atomic interactions like crystal field splitting and electronic correlations. In case of $4d$ and $5d$ systems, the spin-orbit coupling becomes significantly strong and comparable to other effects, such as on-site Coulomb interaction U, hopping integral t, Hund's coupling J_H and the crystal field. Thus, a lot of interaction combination possibilities in transition metal oxides and hence, many material specific properties, make this field of research so rich and promising.

In the ideal case, half metals show a maximum spin polarization of 100% which is determined by density functional theory [3]. Here, the majority charge carriers indicate the metallic character, whereas the minority charge carriers are of semiconducting or even insulting nature. Therefore, one band exhibits a band gap while the other band is partially occupied. Such a band structure is typical of Fe_3O_4 which is studied in this thesis. Another advantage of Fe_3O_4 is a high Curie temperature of about 858 K. Below this temperature, the permanent ferrimagnetic magnetization is conserved, revealing Fe_3O_4 as a good candidate for spintronic applications even at room temperature [4]. An important aspect of this new technology is to connect the properties of the spin polarized current with the controllable electronic properties of semiconductors. The creation of hybrid structures of Fe_3O_4 and semiconductors is a first step for the realization of injection of spin polarized currents, where Fe_3O_4 acts as a spin electrode. For efficient spin injection, the substrate material should have a proper crystal structure and a similar resistance to the film to ensure less strained growth and a necessary impedance match at their interface [5]. For this reasons, semiconducting material ZnO seems to be the best choice for hybrid structures with Fe_3O_4.
As it is already shown in other studies, the epitaxial growth of thin Fe_3O_4 layers on ZnO surfaces with (0001) orientation is generally possible [6, 7]. The MBE grown films indicated a highly crystalline quality with physical properties similar to those of bulk Fe_3O_4. However, ZnO has two polar surfaces in the (0001)-direction: the Zn- and O-terminated surface. A differentiation between these two surfaces with regard to the Fe_3O_4 growth and generated interfaces, which may have different physical properties, was not reported in the literature. Furthermore, in these previous studies both types of ZnO substrate surfaces were similarly prepared resulting in unsatisfying substrate surfaces morphology. In this thesis, both the substrate preparation methods of the two different ZnO surfaces as well as the resulting physical properties of interface and film are analyzed.

The interest in $5d$ Ruddlesden-Popper (RP) phased iridate materials became enormous due to the strong spin-orbit coupling which introduces an additional energy scale to such systems comparable to bandwidth and Coulomb interaction. Moreover, many similarities in crystal structure as well as electronic structure of layered perovskite type (RP-214) iridates to the high T_c cuprate superconductors are given. This thesis pursues the objective to create in this iridate system a similar transition into a superconducting phase. In addition, these iridates are Mott insulators which are also an interesting class by itself. In this thesis, the growth of (RP-214) iridate films by means of PLD is described in details, while a superconducting phase was attempted to be realized by bulk n-doping of these films.

This introduction is followed by chapter 2 in which Fe_3O_4/ZnO heterostructures and (RP–214) iridates together with their individual properties are introduced and their individual substances of substrate and film are explained.
Chapter 3 gives first an introduction into growth techniques and various growth modes used in this thesis. This is followed by a detailed description of the used characterization methods: RHEED, LEED, PES, AFM, XRD, XRR, PNR, magnetometry (SQUID), transport (PPMS), TEM and STEM-EELS.
In chapter 4 the experimental results of the Fe_3O_4/ZnO topic are presented and discussed. Here, the important ZnO substrate preparation methods are specified and the interrelated film and interface properties of the various Fe_3O_4/ZnO heterostructures are determined.
Chapter 5 reflects the experimental results of the growth and characterization of (RP–214) films grown on STO substrates. Here, the PLD growth of these iridates is discussed and followed by an analysis of their crystal and electronic structures.
In the last chapter, the experimental results from the chapters 4 and 5 are concluded with shortly given statements and completed with an outlook about future research possibilities.

2 Material systems

In this chapter, an overview about the studied material systems and their substances is given. For each material system a motivation for its fabrication is emphasized, followed by an introduction of its substrate material and a final part which explains the electronic and crystalline structure of the corresponding film material.

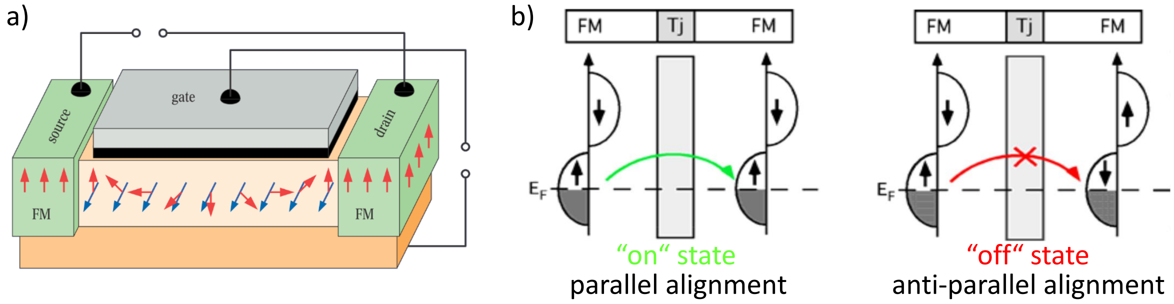

Figure 2.1: *(a) Schematic illustration of a spintransistor based on the idea of S. Datta and B. Das. Adopted from [8]. (b) Sketch of a magnetic tunnel junction. For for parallel alignment of two magnetic electrodes, tunneling of spin–up electrons through the insulating tunnel junction (T_j) can be achieved (left), whereas for anti-parallel alignment a high contact resistance due to unavailable matching states at E_F occurs (right). Adopted from [9].*

2.1 Motivation for Fe_3O_4/ZnO

As the miniaturization of transistor structures in microchips is almost at the limit of technological feasibility, sooner or later the semiconductor industry has to go new paths to increase the efficiency of computer processors. The ultimate goal would be not to only take advantage of the electrical charge but also the spin degrees of freedom. This field of research is known as spintronics which promises much higher switching rates, less power drain as well as higher structure densities [10]. Today, the spin degree of freedom is already utilized by using the giant magnetoresistance (GMR) effect in hard-drives for data storage, e.g. in magnetoresistive random access memory (MRAM). In order to integrate this degree of freedom into microprocessor technology, the Datta–Das spintransistor is the foundation, laying grounds for further development of spintronic devices [11]. Figure 2.1 a) shows such a spintransistor being made of two ferromagnetic electrodes which are connected by a ballistic line channel in a semiconductor which acts as a tunnel junction. One is able to regulate the spin precession of the flowing charge carriers (originating from the source electrode) by applying a gate voltage at the control electrode. This regulation principle is demonstrated in Figure 2.1 b). If the spin direction of the attained charge carriers is equal to the direction of the drain electrode magnetization, the contact resistance becomes small. This results in a stronger electrical current flow than in anti-parallel alignment, representing the "on" state. The necessary condition for such a device is the efficient injection of a spin polarized electron current from the electrodes into the semiconductor. Evidently, the optimum electrode materials should possess 100% spin polarization of the conduction electrons at the Fermi level. This ensures that zero current flows in the "off" state (see Figure 2.1 b)).

What would be the ideal material for 100% spin polarization? First of all it seems to be obvious to use elementary ferromagnetic transition metals as iron, cobalt or nickel. However, these metals exhibit beside their spin polarized d–electrons mainly nonpolarized s–electrons. Furthermore, an effective spin injection is only feasible if the conductances of electrode and semiconductor material match as good as possible [5], making the combination of highly conducting metals with barely conducting semiconductors for this issue unusable. A promising alternative to pure transition metals is the application of nonmetallic materials with high spin polarization of their conduction electrons, e.g. doped semiconductors and half–metals. The advantage of half–metals is their low density of states(DOS) for one spin direction and high DOS for the other spin direction at the Fermi level. Beside Heusler alloys, good candidates for the use as electrode/spin injector in spintronic devices are the transition metal oxides with half–metallic properties as $La_{0.7}Sr_{0.3}MnO$ (LSMO), CrO_2 or magnetite (Fe_3O_4) [12–14]. Both, CrO_2 and Fe_3O_4, can theoretically achieve 100% spin polarization at the Fermi level up to relatively high temperatures(T_Cs are 400 K and 850 K, respectively). However the device performance is not impressively high in both due to a reduced magnetoresistance which can be attributed to surface modifications occurring at their interfaces [9, 13, 14]. Therefore, it is critical to have sophisticated control over the interfaces and to preserve the half–metallic character of the electrode material.

In this thesis Fe_3O_4 will be analyzed as a potential electrode material. It is grown by molecular beam epitaxy (MBE) on a semiconductor substrate. The substrate has to fulfill several requirements for well working spin injection [5], e.g. stability under growth conditions, matching lattice structures, chemically inertness, and similar resistance as the adsorbed film material. Zinc oxide (ZnO) seems to be the most promising substrate candidate for realizing a prospective spin transistor utilizing Fe_3O_4 thin films. Because interface properties play a very crucial role, various substrate preparation techniques as well as the substrate termination types of ZnO were studied. Concerning the used substrate configuration, the dependency of the physical properties of the Fe_3O_4 thin films are identified and pondered in terms of most promising conditions for effective spin injection. Altogether, clear directions for technological relevant substrate/interface combinations will be given. It is demonstrated that the Fe_3O_4/ZnO sample with *ex situ* annealed O-terminated ZnO substrate is the best alternative.

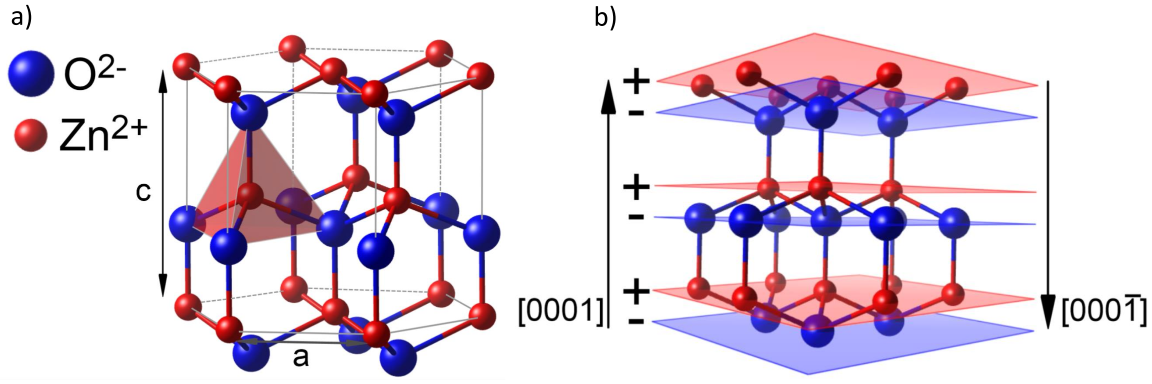

Figure 2.2: *(a) Wurtzite structure of zinc oxide. (b) Polar character of zinc oxide in [0001]-direction based on alternating planes.*

2.2 Substrate material zinc oxide (ZnO)

Zinc oxide as a transparent electrode material is extensively used in the semiconductor industry, e.g. for light-emitting diodes or solar cells. Optimized large surfaces have the potential to serve as an effective gas sensor, where the adsorption of specific gas molecules like H_2 [15] or NO_2 [16] results in a change of the electrical resistance.
The zink oxide substrates used in this work are hydrothermally grown and single crystalline (crystal supplier: CrysTec GmbH). The (0001) or $(000\bar{1})$ surface, oxygen or zinc terminated surface respectively, is chemo-mechanically polished. The surface quality is labeled as "epi-ready" which means that these substrates are in principle applicable for epitaxy. This can, however, be further optimized by purposeful treatments as it will be shown in section 4.1. As standard, 0.5 mm thick substrates with a 5.0x5.0 mm^2 surface area were used. Hydrothermally grown zinc oxide is highly pure and has a charge carrier concentration in the range of 10^{13}–10^{14} cm^{-3}. Analysis via secondary ion mass spectrometry (SIMS) determined the concentrations of impurity atoms (mainly alkali metals, iron and copper) to be merely 10^{17}–10^{18} cm^{-3} [17].
Zinc oxide has a band gap of 3.37 eV [18] and is therefore actually a strong insulator. In order to make the heterostructure employable for spintronic applications, it is necessary to regulate the substrate conductivity by controlled p– or n–doping. Lattice defects, such as oxygen vacancies and interstitials, render as grown zinc oxide intrinsically (lowly) n–doped. Metals from the 3rd main group of the periodic table Al, Ga, In are convenient donor atoms [19]. In contrast, p–doping is much more complicated, since the effects of the acceptor atoms are compensated by other mechanisms. The doping process itself can cause an increased number of the above-mentioned intrinsic donor defects. Therefore, an effective p–doping with acceptor atoms (such as nitrogen or arsenic) presume a perfect lattice without any defects and a very high purity [17].
Another interesting feature, regarding the application for spintronic devices, is the large

spin diffusion length of zinc oxide which was determined to be an impressive number of 10.8 nm at 2 K [20]. This occurs due to the weak spin-orbit coupling in zinc oxide that leads to long spin coherence.

2.2.1 Crystal structure

Zinc oxide crystallizes in the wurtzite structure (space group *P63mc*) which is shown in Figure 2.2. It is composed of two hexagonal close-packed (hcp) planes, each made of zinc or oxygen atoms, which are shifted against each other along the threefold rotationally symmetrical c-axis. Every zinc atom is surrounded by four oxygen atoms forming the corners of a tetrahedra. The lattice parameters are specified with a=3.25 Å and c=5.20 Å. The shift between both hcp–planes amounts to u=0.38$\cdot c$ along the c-axis [18].

Figure 2.2 b) illustrates the zinc oxide structure along the c-axis in [0001]-direction consisting of double layers of alternating zinc and oxygen planes. The bonding length among two double layers is larger than the distance between zinc and oxygen atoms within such a double layer. Thus no inversion center exists regarding to the c-direction in the crystal [18]. This asymmetry is the main reason why both sides of a c-axis cleaved ZnO crystal are not equivalent.

2.2.2 Polar crystal directions

Because of the different electronegativities of zinc and oxygen, the bondings between the substituents are both of covalent type and ionic character. An intrinsic polarization of the crystal lattice arises in [0001]-direction, which is displayed in Figure 2.2 b). If the polarization vector points to the crystal surface, that side is the O-terminated [000$\bar{1}$] surface. The so called Zn-terminated side is with the polarization in the [0001]-direction. These two terminations are expected to differ in physical and chemical properties. For example M. W. Allen *et al.* demonstrated that both polar surfaces exhibit a different accumulation layer at the surface [21], visible by band bending effects at the surfaces. Measurements of the valence band edges via photoemission spectroscopy indicated an approximately 190 meV larger band bending for the Zn-terminated surface, resulting in a higher accumulation of electrons. This difference between both terminations may causes different interfacial electric resistance and therewith different spin injection efficiency. Another discrepancy of the two polar surfaces is their stabilization. Due to the different band bending effects and nonequivalent surface energies two situations are preferred. While in the case of Zn-terminated surfaces a saturation with chemisorbed hydroxyl groups is necessary for stabilization, O-terminated surfaces need only chemisorbed H-atoms. The different chemical situation for both terminated surfaces is shown in Figure 2.3.

During the hydrothermal crystal growth more impurity atoms are embedded on the O-terminated side than on the other side [17]. One reason for this may be various growth

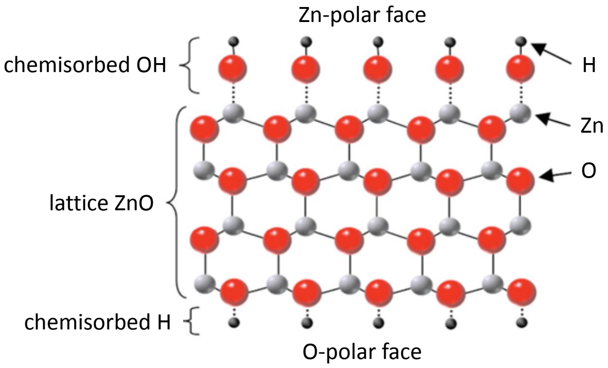

Figure 2.3: *Stabilized (0001)-Zn terminated and* $(000\bar{1})$*-O terminated surface of ZnO. Adopted from [21].*

kinetics of both polar sides. While etching the surfaces in dilute acids, one can see that the O-terminated side is much more affected and forms etch pits faster than the Zn-terminated side. This variation enables an easy method to determine the polarisation direction in a ZnO crystal [22].
In this thesis substrates with both terminations were prepared and utilized for epitaxy. A major objective was to identify whether the termination and preparation has an influence on the magnetite film growth and the overall film quality (regarding stoichiometry, magnetism and interfacial structure). Here, it was essential to invent a preparation process which guaranties surfaces as smooth as possible in order to produce an atomically sharp interface. Photoemission spectroscopy, as discussed in Chapter 4, was then utilized for a confirmation of the termination type and advanced electronic and surface characterization.

2.3 Film material magnetite (Fe_3O_4)

Being a mineral in iron ore, magnetite (Fe_3O_4) is deemed to be the oldest known magnetic material. Its magnetic porperties were realized by humankind already 2500 years ago [23]. Beside being an ore material, Fe_3O_4 is a widespread magnetic mineral in the earth's crust and well known as corrosion product of iron containing materials such as steel. Additionally, Fe_3O_4 functions as a biomineralized magnetic sensor for several biological organisms, e.g. in brains of birds, also as magnetic item in core memories in PCs and magnetic tapes for recording, or as chemical catalyst for conditioning of surfaces. Today, the broad scientific interest on Fe_3O_4 is based on the naturally appearance as a biomarker [24] and especially on the potential application as a spin polarized electrode material.

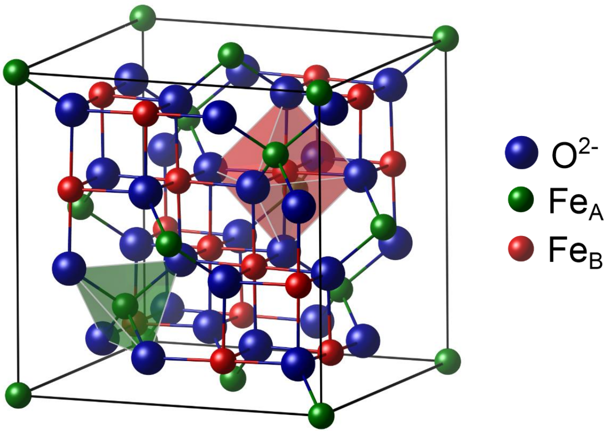

Figure 2.4: *Inverse-spinel unit cell of magnetite with the tetrahedrally (Fe_A) and octahedrally (Fe_B) coordinated iron sublattices.*

2.3.1 Crystal structure and Verwey transition

The transition metal oxide magnetite has an inverse-spinel structure (space group $Fd\bar{3}m$) that is illustrated in Figure 2.4. The unit cell has a lattice parameter of a=8.394 Å [25] and is spanned by a slightly distorted face-centered cubic (fcc) lattice of 32 oxygen anions. According to the chemical structural formula Fe_3O_4 it contains 8 formula units of magnetite in total. The weak lattice distortion gives rise to a more favorable positioning of the anions related to the iron cations [26]. Within this oxygen lattice 64 free lattice sites are tetrahedrally coordinated (A-sublattice), while 32 free lattice sites are localized in octahedra centers (B-sublattice) surrounded by the anions. From all these vacancies only 8 are occupied in the A-sublattice by trivalent iron Fe^{3+} and 16 in the B-sublattice by 8 Fe^{2+} and 8 Fe^{3+} cations. The B-sublattice has therefore a mixed valency, however the Fe^{2+} and Fe^{3+} ions have no defined arrangement inside the B-sublattice sites [27]. This structure is relevant for the high temperature phase of magnetite. For temperatures below ~125 K a characteristic phase transition appears in this mineral. This so-called Verwey transition was observed as a metal-insulator transition in conductivity measurements [28]. At the critical temperature, the resistance increases abruptly by several orders of magnitude during cooling. E. J. W. Verwey assumed the mixed valency of the B-sublattice responsible for his observations. The argumentation is that thermally activated electrons are able to move within the sublattice:

$$Fe^{2+} - e^{-} \longleftrightarrow Fe^{3+} \quad . \tag{2.1}$$

At low temperatures this degree of freedom gets frozen up and electric charges on the sublattice become arranged on fixed lattice sites. Thus the resistance strongly increases. But the Verwey transition is also a transformation of the crystal structure to a monoclinic phase which is connected to an abrupt change in specific heat capacity as well as in ma-

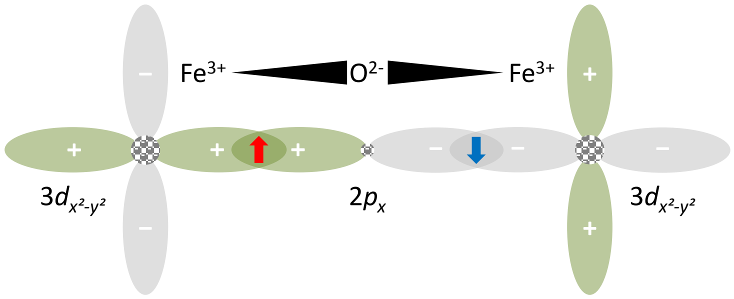

Figure 2.5: *Schematic illustration of the super-exchange interaction among two* $3d_{x^2-y^2}$*-orbitals of* Fe^{3+}*-cations over the fully occupied* $2p_x$*-orbital of the* O^{2-}*-anion. Adapted from [27].*

gnetization. These comprehensive changes in the properties of magnetite can not be acceptably explained with the above model and are still subject of current research. Much more deatiled summaries including extensive discussions are given in [29] and [30]. Since the Verwey transition is also affected by stoichiometric defects and contaminations, it is often used as an indicator of phase-pure magnetite with high crystalline quality. For instance, a stoichiometric deviation of only x=0.012 in $Fe_{3-x}O_4$ results in a second order phase transition and a transition temperature less than 100 K [31]. In comparison, deposited thin films show a similar behavior [32], probably due to the strain effects and crystal defects.

2.3.2 Magnetism

In most magnetic oxides direct exchange interactions among neighboring cations play a negligible role for the magnetic order, since these cations are separated by oxygen ions from each other. Instead of that, indirect coupling mechanisms are dominant which are employed over the fully occupied oxygen $2p$ orbitals. This mechanism is the so-called super-exchange which is illustrated in Figure 2.5 for two trivalent iron atoms. The $3d_{x^2-y^2}$-orbitals of Fe are connected by σ-bondings to the $2p_x$-orbital of O, in which each orbital wave functions with the same phase are overlapped. The bonding electron has a finite probability density in both the $2p_x$-orbital of O and the $3d_{x^2-y^2}$-orbital of Fe. Here the spin orientation remains preserved. By the Pauli exclusion principle and the symmetry of the p_x-orbital, the spin of the binding electron on the left-hand side has to be antiparallel to that on the right-hand side (see Figure 2.5). According to Hund's rule all spins in case of Fe^{3+}-ions have parallel orientation in the half occupied d-orbitals, schematically demonstrated in Figure 2.6. The different symmetry of the p- and d-orbital wave functions gives rise to an antiferromagnetic orientation of Fe to each other.

The strength of the super-exchange interaction depends on the angle and distance among the two involved cations. In case of Fe $^{3+}$-ions it is strongly antiferromagnetic for 180°

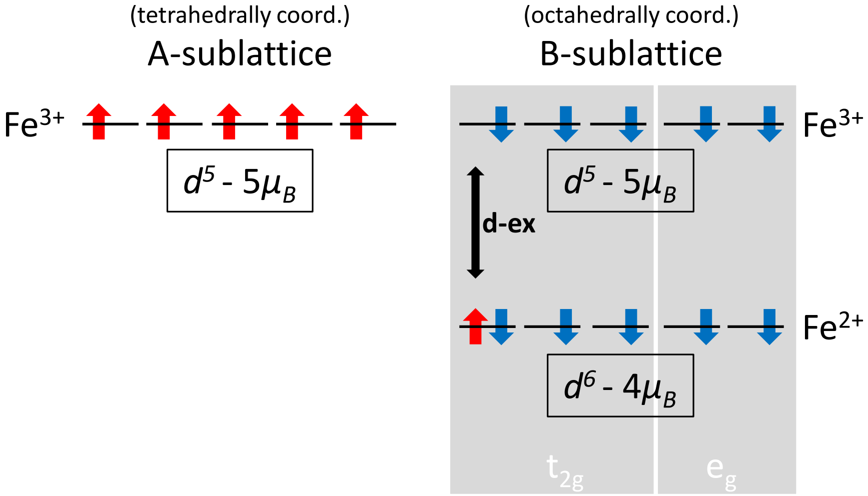

Figure 2.6: *Demonstration of the electronic occupation of the 3d-orbitals within both cation-sublattices in one formula unit* Fe_3O_4*. The double arrow indicates the double-exchange in the octahedrally coordinated sublattice.*

and weak ferromagnetic for 90° [26]. The geometrical configurations which emerge in the first coordination shell of a spinel lattice are presented in Figure 2.7. A strong antiferromagnetic coupling is effected by the inter-lattice exchange in Fe_A-O-Fe_B with an angle of 125° and 154°, while on the contrary intra-lattice super-exchange interactions in Fe_A-O-Fe_A and Fe_B-O-Fe_B due to small angles and larger distances of the ions are much less antiferromagnetic or even slightly ferromagnetic [33].
The exchange in Fe_B-O-Fe_B within the octahedrally coordinated sublattice is superposed by another strong ferromagnetic coupling. This so-called double-exchange was suggested first by C. Zener [34] and is based on the delocalization of one excess electron from each

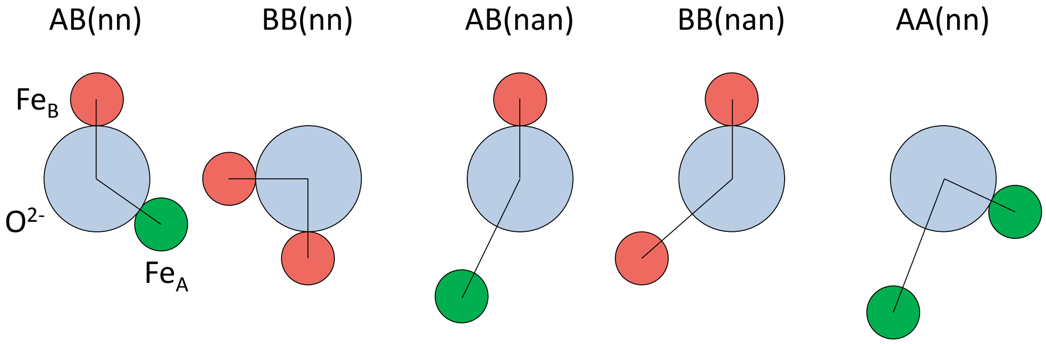

Figure 2.7: *Sketch of possible orientations of the super-exchange interaction in the first coordination shell of a spinel crystal. Adapted from [26] (nomenclature: nn=next neighbor, nan=neighbor after next).*

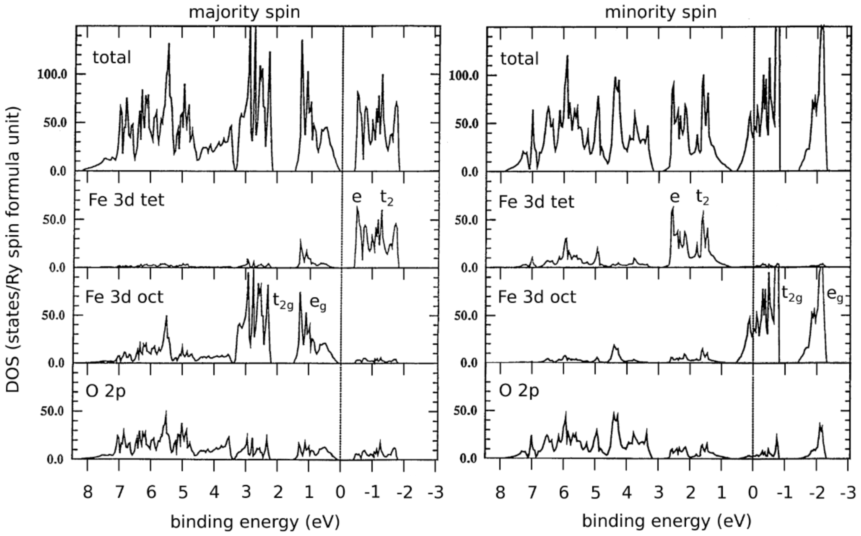

Figure 2.8: *Total (top view) and site-decomposed (underneath) DOS for spin-up (left) and spin-down (right) calculated by means of DFT in LSDA approximation. Adopted from [35].*

of the Fe^{2+}-ions on the B-sublattice. As mentioned before the d-orbitals of the Fe^{3+}-ions are occupied by unpaired electrons of one spin orientation, according to Hund's rule. An exchange or spontaneous transition of the additional electron between two iron atoms is only possible, if all spins of the Fe^{3+}-ions are parallel orientated to each other. Therefore this process comes along with a ferromagnetic coupling. This makes a relevant contribution to the conductivity of magnetite and provides an explanation for the spin polarization of the electrons in the conduction band (see also Figure 2.8).

The spin configuration shown in Figure 2.6 is most favorable in energy, because of the antiferromagnetic coupling of the sublattices over the super-exchange and the ferromagnetic orientation of the spins by the double-exchange inside the B-sublattice. This configuration has a resulting magnetic moment of 4 μ_B/f.u. and was already suggested in 1948 by L. Néel [36] in order to explain the magnetism of ferrites. The antiferromagnetically coupled moments of the trivalent cations accurately balance out each other. In total, the magnetic moments of the unpaired electrons of the Fe^{2+}-ions remain. Although this pure ionic model seems to be an oversimplification, the such obtained value for the saturated magnetization equals the value obtained by X-ray magnetic circular dichroism (XMCD) measurements with only a small deviation of 3.9 μ_B/f.u. [37]. The ferrimagnetic ordering temperature of magnetite is 850 K [38].

2.3.3 Electronic band structure and spin polarization

Another important characteristic of magnetite is its half-metallicity. Especially in terms of spintronic applications this fact is of great interest. Several theoretical calculations indicate 100% spin polarized electrons at the Fermi energy [39, 40]. In contrast, spin re-

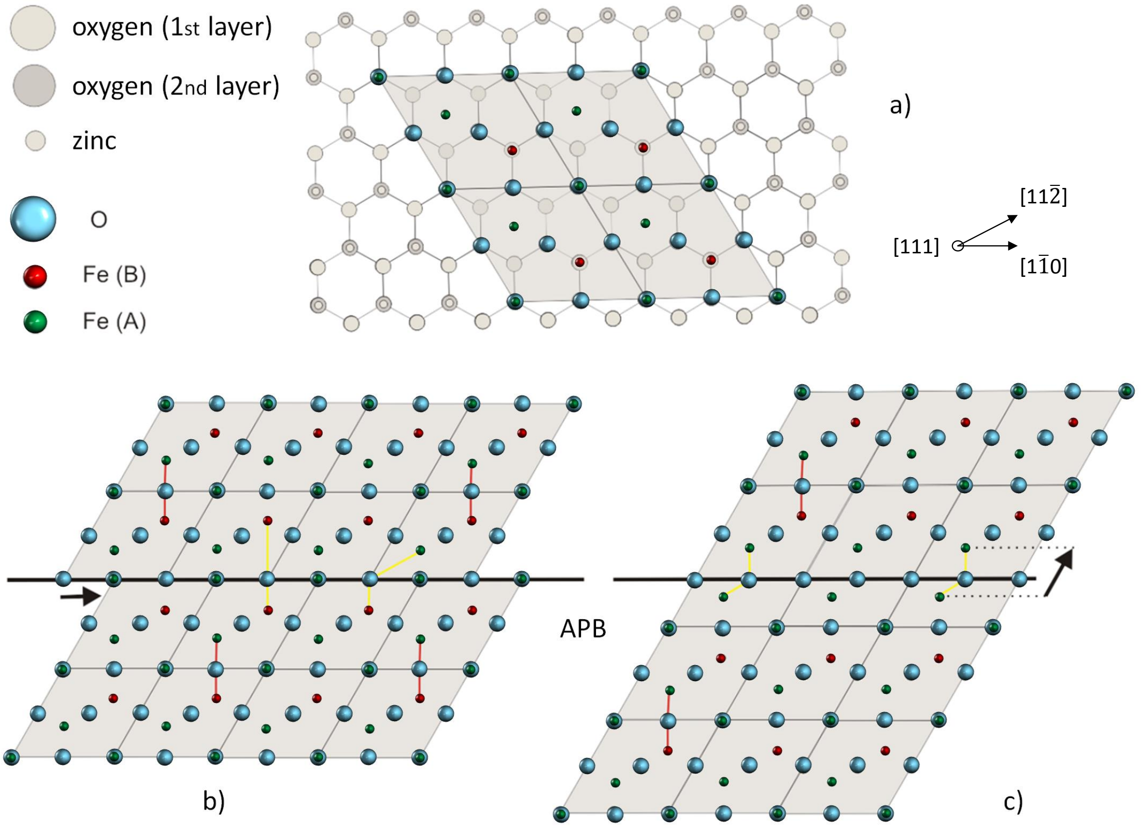

Figure 2.9: *Idealized two-dimensional model for demonstrating the antiphase boundaries of Fe_3O_4(111) on ZnO. APBs are indicated by black lines. Yellow and red lines show various magnetic couplings between neighboring cations. (a) Four unit cells of Fe_3O_4 with one of the two possible terminations of its (111)-surface [41] on the hexagonal structured ZnO. Octahedrally coordinated iron atoms are red, tetrahedrally coordinated iron atoms are labeled in green. Shifted unit cells (b) parallel and (c) perpendicular to an APB plane.*

solved photoemission spectroscopy gives only a value of 80% [42]. There are some reasons why this discrepancy can occur. On the one hand, deviations of the magnetic structure from surface to bulk could play a crucial role, since photoemission spectroscopy is a surface sensitive characterization method. On the other hand, theoretical band structure calculations are often just approximatively valid, because most assume that the crystal is infinitely extended and impacts of boundaries are thereby neglected. In addition, strain effects in films are often not considered. As a counter example, the DFT-calculations of M. Friák *et al.* show the stability of the half-metallic state of magnetite under the influence of various strain effects. A notable result is a half-metal to metal transition that depends on the distance of the octahedrally coordinated iron atoms and can be reduced by strain effects [43].

Figure 2.8 shows the density of states (DOS) obtained by the local spin density approximation (LSDA) [35]. The DOS of each spin orientation is shifted relative to one

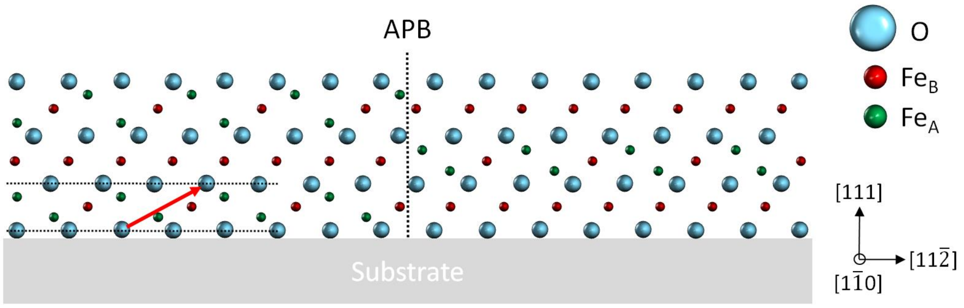

Figure 2.10: *Projection of the Fe_3O_4 lattice with a potential APB in the (1$\bar{1}$0) plane. The red arrow indicates the displacement by a shifting vector of ($\frac{1}{2}$,$\frac{1}{4}$,-$\frac{1}{4}$) inside the iron lattice. The oxygen lattice at the APB persists in phase.*

another due to the magnetic exchange interaction. The spin-up DOS shows a gap at the Fermi energy, whereas the spin-down electrons have a finite DOS there. Based on this metallic behavior of the spin-down electrons, a 100% spin-polarized charge transfer across the B-sublattice is expected. The calculation gives a value for the magnetic moment of about 4 μ_B/f.u. Fe_3O_4 [40].

2.3.4 Antiphase boundaries

Magnetometry measurements reveal that for magnetite thin films this aforementioned value for the saturation magnetization can not be reached even at high magnetic fields. Its magnetization rises asymptotically to a lower saturation value [44]. This observation is attributed to the formation of stacking faults in the iron sublattices in the film. These are the so-called antiphase boundaries (APB).

The growth of magnetite begins with the formation of separated nucleations whose oxygen lattices are oriented toward the substrate (see Figure 2.9 a)). In the spinel structure there are 8 potential arrangements of the iron sublattices with the oxygen lattice fixed. These configurations can be transformed into each other by a simple shift of $\frac{1}{4}$<110> and $\frac{1}{2}$<100> or a linear combination of these vectors. Due to this formation of configuration domains APBs are produced in the film [45], see Figure 2.9 b) and c). There, the oxygen lattice continues periodically and is therefore not a classic crystal boundary.

There are two possibilities for APB types in Fe_3O_4 films, the in-plane and out-of-plane APB. The in-plane formation occurs from inter- and intra-shifted unit cells and the out-of-plane formation arises from variations in the stacking sequence. In Figure 2.9 the in-plane formations of APBs are schematically illustrated. At the APB, Fe_3O_4 unit cells are shifted by a half unit cell in [1$\bar{1}$0]- or [11$\bar{2}$]-direction.

In contrast Figure 2.10 shows the out-of-plane APB. In this case the shifting vector is ($\frac{1}{2}$,$\frac{1}{4}$,-$\frac{1}{4}$). Such a displacement can be realized by omitting a half unit cell in the stacking sequences of two neighboring nucleations.

A detailed study of the potential geometry of APBs, using the example of Fe_3O_4 films grown in the [100]-direction on MgO substrates, is given in [45]. From transmission electron microscopy (TEM) studies, it is known that Fe_3O_4 films contain a larger number of APBs accompanied with decreased distance for the atoms neighboring the interface. An annealing of thick films leads to a decrease of APBs and increase of domain sizes. This observation is in good agreement with the results which were found for Fe_3O_4 films grown in the [111]-direction on α-Al_2O_3 substrates [46]. A similar behavior is expected for Fe_3O_4 films grown on ZnO(0001) substrates, since the growth direction is also in [111].

APBs exhibit different angles and distances for the super-exchange among the cations. The alternated coupling forces in such areas can result in antiferromagnetic order between the crystallites [45]. This type of interaction at APBs was already investigated in magnetotransport measurements [47] and by magnetic scanning force microscopy [48]. Due to the antiferromagnetic coupling, the magnetic moments in films are typically retained. Only high magnetic fields allow for a reorientation towards the external magnetic field. This results in the already mentioned widely extended saturation magnetization in magnetometry measurements. In addition W. Eerenstein *et al.* [49, 50] showed that Fe_3O_4 films grown on MgO with a greater number of APBs have a higher electric resistance. It is supposed that especially in thin films a high density of APBs interrupts considerably the long range order in the crystal and causes a suppression of the Verwey transition and therefore a shift of the phase transition point to lower temperatures.

2.3.5 Other iron oxides

Magnetite represents only a small part of the phase diagram of iron oxides. Depending on the oxidation states of the iron atoms different oxide crystal phases can be generated [51]. The other most important iron oxides have the chemical structural formula Fe_2O_3 and FeO, with iron valencies of 3+ and 2+ respectively. These both materials can be seen also as over oxidized and under oxidized magnetite, since in comparison magnetite has an average mixed iron valency of 2.66+.

The most common crystal structures of Fe_2O_3 are the γ-phase spinel structure (so-called maghemite) and the α-phase corundum structure (so-called hematite). Especially γ-Fe_2O_3 is interesting for the growth of magnetite, because it has a very similar lattice parameter of a=8.336 Å. Its structure is the same as in magnetite, but here all cations are trivalent and 8 iron atoms per three unit cells are vacant in the octahedrally coordinated sublattice. Occupied with a different number of iron atoms, both sublattices still couple antiferromagnetically with each other and cause a saturation moment of 2.5 μ_B/f.u. Fe_2O_3 [12] and an ordering temperature of about 800 K in maghemite [38].

In contrast FeO (so-called wustite) is formed when not enough oxygen is present to form phase pure magnetite during growth. Wustite has a by cation defects stabilized rock-salt structure with a lattice parameter of about 4.30 Å and a chemical structural formula $Fe_{1-x}O$ with $0.05 < x < 0.2$. It is antiferromagnetic below 200 K and paramagnetic at room temperature [38].

2.4 Motivation for (RP–214) iridates

The discovery of high–T_c cuprates in the late eighties [52] sought understanding of the mechanisms for unconventional superconductivity and inspired the research for a material which is superconductive at room temperature. Therefore, such transition metal oxides (TMOs) have been one of the most fascinating material classes in the past few years [53]. While $3d$ and $4d$ TMOs were tremendously investigated in the past decades, yielding many various exotic states and phenomena, $5d$ TMOs have attracted a lot of attention as a candidate for novel Mott insulators. In most TMOs, strong Coulomb interactions along with contributive interactions of charge, spin and orbital degrees of freedom are responsible for their resulting plethora of phenomena. In $3d$ and $4d$ systems, these contributive interactions are in principle separable [54], whereas in $5d$ systems spin and orbital degrees of freedom are strongly entangled. Coulomb interactions (U) for $5d$ electrons (∼1–3 eV) are estimated to be smaller than for $3d$ electrons (∼5–7 eV) due to their more extended $5d$ orbitals, while the spin–orbit coupling (λ_{SOC}) for $5d$ (∼0.1–1 eV) is larger than for $3d$ (∼0.01–0.1 eV) [55].

Recent studies of the $5d$ TMOs revealed a high potential of this material class for electronic applications [56]. Ba_2IrO_4 (BIO) and Sr_2IrO_4 (SIO) are of particular interest. Both belong to the 214 iridate phase of their Ruddlesden–Popper series and, surprisingly, are Mott insulators despite the weak Coulomb interaction in their $5d$ orbitals. The reasons for their unique electronic structure are both the crystal field splitting in the perovskite and the spin–orbit coupling which for iridium atoms with the atomic number Z=77 is very strong by nature. Thus, already a weak Coulomb interaction in the $5d$ orbitals is enough to induce the Mott insulating ground state [57]. While several experiments, in particular by angle resolved photoemission spectroscopy (ARPES), were done on BIO and SIO single crystals [57–60], only a few publications about ARPES measurements of molecular beam epitaxy (MBE) grown thin films of SIO and BIO are available [61–63]. For thin films grown by pulsed laser deposition (PLD), there are even none ARPES measurements done yet. This represents the big difficulties in growth of high quality RP–214 iridates thin films, although there is already a small number of publications in which the bulk quality of PLD grown SIO thin films is stated as sufficiently high [56, 64–66]. Another interest of BIO and SIO lies in their structural and electronic similarity to La_2CuO_4 (LCO), the parent compound of $3d$ high–T_c cuprate superconductors. Theoretical calculations predict that SIO could become superconductive by a certain electron doping level [67–69]. However, recent experiments show that both electron and hole doped SIO single crystals indicate no superconducting phase [70–73]. The reason for this is still under debate and needs more research of the physical nature of doped Mott insulators.

In this thesis, BIO and SIO thin films are grown on $SrTiO_3$ (STO) substrates by PLD and analyzed by a set of characterization methods. Note that one focus was to produce high quality PLD grown thin films of SIO and BIO which are suitable for ARPES measurements. A major achievement is the production of n–doped (La–doped) SIO thin films by PLD, aiming to activate a superconducting phase, and to compare this material to the undoped samples BIO and SIO.

2.5 Substrate material strontium titanate (STO)

Strontium titanate $SrTiO_3$ (STO) is probably one of the most common substrate materials in thin film growth. This is especially due to its lattice constant which nicely matches many other perovskite materials [74]. Moreover, STO is a band insulator with a relatively large indirect band gap of 3.25 eV [75]. Beside today's thin film application, STO was established as diamond simulant in the early fifties owing to its cubic structure and high dispersion [76]. Futhermore, STO is also integrated as a strontium-90 containing material in radioisotope thermoelectric generators (RTG, RITEG) [77, 78].
STO substrates used in this thesis are grown by the Verneuil process, also known as flame fusion, and single crystalline (crystal supplier: CrysTec GmbH). STO grown by the Verneuil process is highly pure, transparent and colorless. Moreover, it has a large dielectric constant of approximately 300 at room temperature and owns a specific resistivity of about 10^9 Ωcm [79].
The here used substrates are chemo-mechanically polished and their quality are labeled as "epi-ready" which means that they are, in principle, applicable for epitaxy. Since these substrates do not have a single termination on their surface which can cause unintentional growth modes at the primary step of the thin film growth process, it is necessary that the substrates undergo a surface termination procedure as it will be shown in section 5.1. As standard, 0.5 mm thick substrates with a 5.0x5.0 mm^2 surface area were used.

2.5.1 Crystal structure and physical properties

Like many other ABO_3 perovskite compounds, $SrTiO_3$ crystallizes in the cubic perovskite structure at room temperature (space group $Pm\bar{3}m$) with a lattice parameter of a=3.905 Å [80]. The unit cell of the cubic perovskite structure in STO is schematically illustrated in Figure 2.11. Here, the heavier and larger Sr^{2+} cations (with respect to the atomic radii) are found in the corners of the unit cell, whereas the lighter and smaller Ti^{4+} cation is located at the body-centered position of the unit cell [81] and surrounded by the O^{2-} anions which are positioned face-centered on all sides creating an octahedron.
For an ABO_3, one can think of the crystal being composed of alternating planes with an AO and a BO_2 composition along the [001] crystal direction. In the case of STO, these planes are respectively made of SrO and TiO_2 compositions which are charge neutral and nonpolar.
Below 105 K, STO undergoes a phase transition from a perfectly cubic to a tetragonal structure (space group $I4/mcm$) in which neighboring TiO_6 octahedra are slightly antiferrodistortively rotated in opposite directions [82, 83].

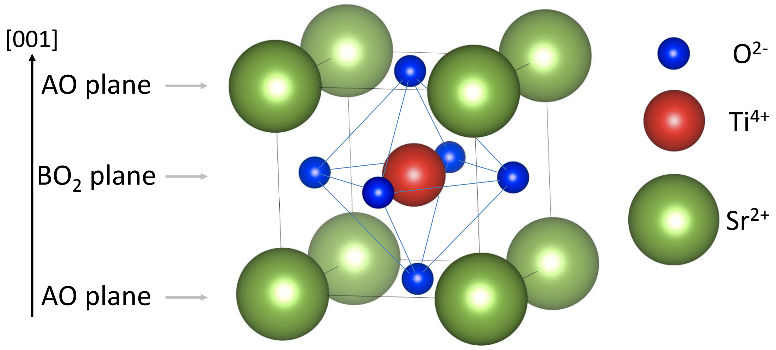

Figure 2.11: *Schematic representation of the $SrTiO_3$ unit cell. While the Sr^{2+} cations are located in the corners of the cubic perovskite unit cell, the Ti^{4+} cation is in its center and surrounded by the octahedrally coordinated O^{2-} anions. In a general perovskite ABO_3, alternating planes with an AO and a BO_2 composition are arranged along the [001] crystal direction.*

STO can be easily doped n-type, even into a metallic state, e.g. by creating oxygen vacancies [84, 85] or by substituting small amounts of Nb for Ti [85]. In addition, doped STO (with high enough charge carrier densities) shows superconductivity with a critical temperature of <300 mK [86–89]. Small concentrations of dopants cause often a grayish color in STO, whereas heavily doped STO crystals are opaque and almost black.

In this thesis, pure undoped STO(001) as well as 0.1–0.5 wt% Nb-doped STO(001) substrates were used for transport and photoemission spectroscopy measurements, respectively.

2.6 Film material (RP–214) iridates

Transition metal oxides (TMOs), in particular $3d$ and $4d$ perovskites, have been the topic of extensive research, since they offer a wide field of intriguing phenomena such as superconductivity, spin–orbital ordering, Mott transition and colossal magnetoresistance [53, 54, 90]. This variety originates from the coupling of various degrees of freedom such as charge, lattice, orbital and spin, thus including on-site Coulomb, electron–phonon, hopping and spin–orbit interactions. However, $5d$ TMOs represent an individual class due to their strong spin–orbit coupling (SOC). As a result, it introduces an additional energy scale to the system that is comparable to the bandwidth and Coulomb correlation, therefore being important for describing the physical properties of $5d$ systems in general.

Ruddlesden–Popper (RP) iridates form a series of compounds which show due to the strong spin–orbit interaction of their large iridium atoms a whole slew of different emergent physics [91]. Especially Sr_2IrO_4 and Ba_2IrO_4 ((RP–214) strontium iridate and (RP–214) barium iridate) which are Mott insulators, are of particular interest, because of their many similarities to the isostructural cuprates.

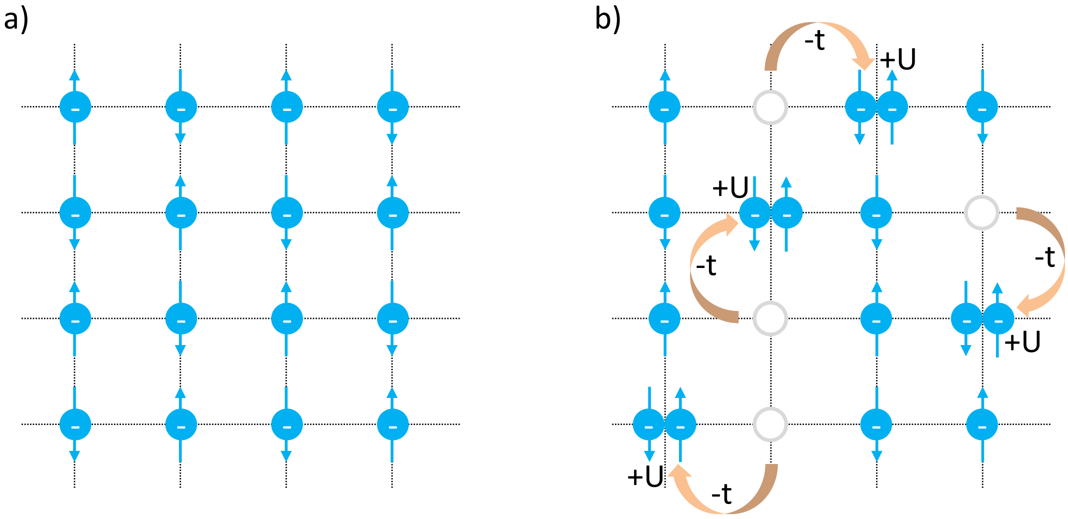

Figure 2.12: *Sketch of the Hubbard model exemplarily pictured on a cubic crystal lattice: (a) Crystal lattice with one electron per lattice site, representing half band filling. (b) Hopping processes of the electrons with transfer integral t and Coulomb repulsion U.*

2.6.1 Mott insulators and Hubbard model

The properties of many materials, especially their insulating state, can be described by rather conventional mechanisms, such as by band theory, Peierls instability and Anderson localization. However, there are still several materials which conventional band theory predicts to show metallicity, but indeed are found to be insulating in experiments. N. F. Mott assumed already in 1937 that the strong electrostatic interaction between the electrons is responsible for this physical behavior [92]. Due to the neglect of the crucial electron–electron interaction and the exclusive consideration of hopping processes of electrons from one lattice site to a neighbor lattice site only, the conventional tight binding model seems to collapse for such materials, e.g. for some TMOs. Such materials, whose insulating behavior is based on electron–electron interaction, are referred to as Mott insulators. In 1963, J. Hubbard [93], M. C. Gutzwiller [94] and J. Kanamori [95] described independently from each other a quantum-mechanical model of this electron correlation. Owing to continuing works by J. Hubbard in this field [96–98] it is nowadays known as the so-called Hubbard model which is illustrated in Figure 2.12 and describes two contrary tendencies of electrons in a partially filled band [99]:

- By delocalization into Bloch states the kinetic energy can be minimized, leading to metallicity. The transfer integral t which is well known from the tight binding approximation, is a measure of this delocalization.
- The Coulomb interaction U between the electrons which favors the localization of one valence electron per one atomic core, resulting in a minimization of the potential energy and thus in an insulating state.

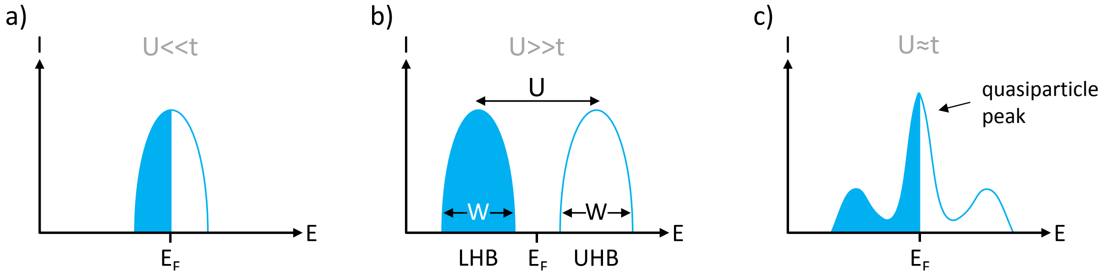

Figure 2.13: *Schematic illustration of the spectral function predicted by the Hubbard model at half band filling for various U/t ratios. (a) For U≪t, representing no correlations, the band structure of a metal is obtained by itinerant electrons, whereas (b) for U≫t the band splits up into a fully occupied lower (LHB) and an empty upper (UHB) Hubbard band. This is the common case of a Mott insulator in which the energy cost for double occupation of lattice sites is too high, resulting in a gap between LHB and UHB. The gap itself has a value of U–W, where W is the bandwidth of the two Hubbard bands. (c) For U≈t, the increasing correlation leads to broadened Hubbard bands with decreased spectral weight and the formation of a narrowed quasiparticle peak at the Fermi level.*

Taking both tendencies into account, the Hamiltonian of the one dimensional Hubbard model can be written as

$$H_{Hubbard} = -t \sum_{\langle i,j\rangle,\sigma} \left(c^{\dagger}_{i,\sigma} c_{j,\sigma} + c^{\dagger}_{j,\sigma} c_{i,\sigma} \right) + U \sum_{i} n_{i,\uparrow} n_{i,\downarrow} \quad , \tag{2.2}$$

where i and j label lattice indices and $\sigma = \uparrow, \downarrow$ denote the spin indices. The summation over $\langle i,j\rangle$ considers only nearest neighbor interactions, while $c_{i,\sigma}$ and $c^{\dagger}_{i,\sigma}$ describe the fermionic annihilation and creation operators of an electron with spin σ at the lattice site i, respectively. The $n_{i,\sigma}$ operator yields the total number of electrons with spin σ found at lattice site i. In the first summand, t indicates the hopping integral which describes the probability (amplitude) of an electron moving to one of its nearest neighbor lattice sites. In the second summand, U denotes the Coulomb repulsion originating by two electrons with opposite spin at the same lattice site. Therefore, if all lattice sites are already occupied by one electron, further electrons can find a place in the lattice only by expense of the Coulomb energy U. Whether a material with an integer band filling is a metal or rather a Mott insulator depends on the contributions from t and U.

For the case of $U \ll t$, representing weak electron correlation, the first summand of Equation 2.3 dominates the Hubbard Hamiltonian, resulting in a tight binding–like Hamiltonian. Considering a material with half filled band, all lattice sites are occupied by one electron because of the small U. If here an electron moves from lattice site to lattice site, it gains the energy t and in return only loses the energy U whereby at delocalization the overall energy gain is much larger than the Coulomb repulsion of the electrons, resulting in a metallic band structure which is shown in Figure 2.13 a).

In contrast, for the case of $U \gg t$, representing strong electron correlation, the second summand of Equation 2.3 dominates the Hubbard Hamiltonian and dissolves the lattice into isolated atoms. It is energetically unfavorable for the electrons to move to another

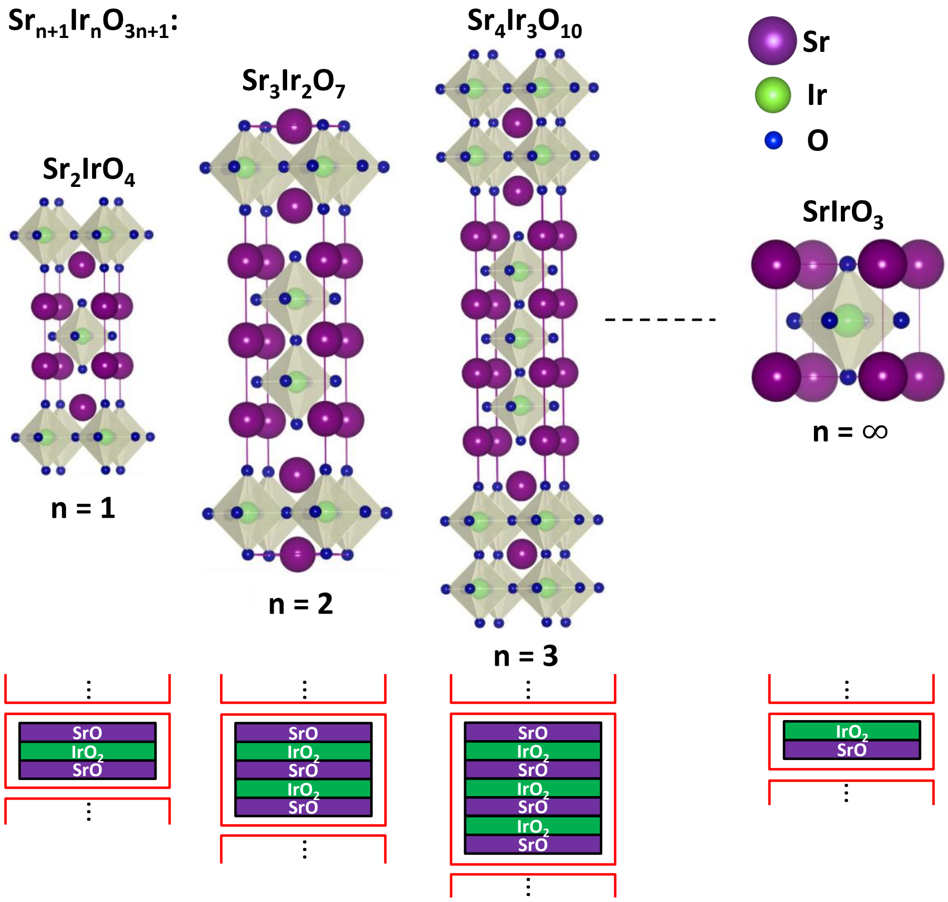

Figure 2.14: *Schematic demonstration of the Ruddlesden–Popper series using the example of* $Sr_{n+1}Ir_nO_{3n+1}$. *Adopted from [91]. Structural changes from* n=1 *to* $n=\infty$ *shown on top, repeating units (marked in red) for each phase shown below.*

lattice site, since a hopping electron loses the energy U and in return only wins the small energy t. Here, the overall energy gain at delocalization of the electrons is not large enough to overcome the Coulomb repulsion. Therefore, the electrons remain localized near the atomic cores. To reach a nearest neighbor lattice site, the electron has to overcome an energy gap which makes this system a Mott insulator with an insulating ground state. In a band structure picture two energetically separated sub–bands form as it is demonstrated in Figure 2.13 b). The energetically lower located band is the so-called lower Hubbard band (LHB) which is composed of the electronic states of single occupied lattice sites, whereas the energetically higher located band is the so-called upper Hubbard band (UHB) which consists of electronic states of double occupied lattice sites. At half band filling the LHB is entirely occupied, while the UHB is completely empty, defining the Mott insulating state. A more accurate derivation to the formation of these bands is given in [96–98]. However, these Hubbard bands are not comparable to any common bands known in solids, since the merely existence of the UHB is directly coupled

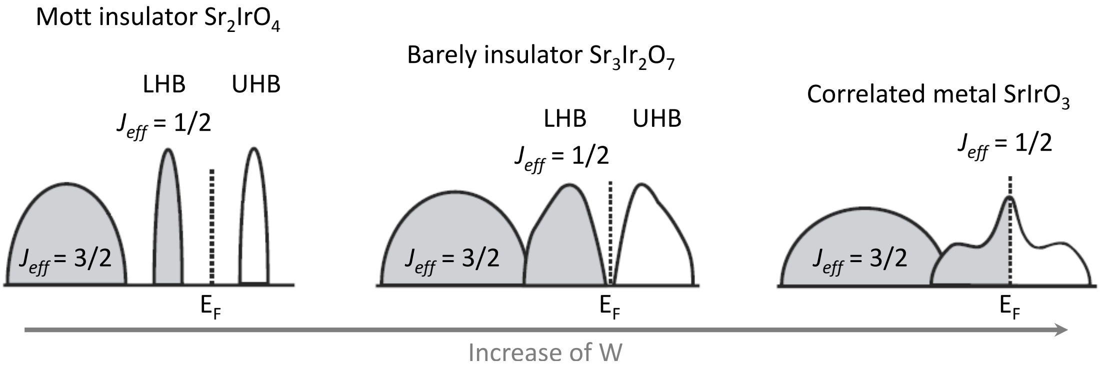

Figure 2.15: *Schematic illustation of the band structure of the 5d $Sr_{n+1}Ir_nO_{3n+1}$ compounds Sr_2IrO_4, $Sr_3Ir_2O_7$ and $SrIrO_3$, which are well described by the effective total angular momentum J_{eff} states as a result of strong spin-orbit coupling. E_F represents the Fermi level and the grey arrow indicates the increase of the the bandwidth W. Adopted from [100].*

to the electron occupation of the LHB.

The question which summand in Equation 2.3 is stronger and thus defines the conductivity properties of a material, is highly interrelated to the band width W. Since t is directly proportional to W ($W \sim 2Zt$, where Z is the atomic coordination number), it can be regarded as measure for the electron hopping between two lattice sites. For the case $U \approx t$, the increasing correlation leads to broadened Hubbard bands and a narrowed quasiparticle peak at the Fermi level which indicates the states of a correlated metal as illustrated in Figure 2.13 c).

Consequently, it is actually possible to induce a metallic phase in a Mott insulator. Such a metal insulator transition (MIT) can be carried out by making use of two different methods. Doping, e.g. by impurity atoms, is one possibility which is also known as filling–controlled MIT (FC–MIT). Another way is to affect directly t, e.g. by applying external forces like strain or pressure, thus manipulating the orbital overlap and changing the correlation strength U/t. This method is called a bandwidth–controlled MIT (BC–MIT).

2.6.2 Ruddlesden–Popper phases of layered iridates

Layered perovskites consist of stacked two dimensional slabs of the ABO_3 layer. Beside the Aurivillius and Dion–Jacobson phases, there is a third class of layered perovskites which is the so-called Ruddlesden–Popper (RP) series. It provides a whole series of perovskite–like materials with equal element types but with gradual decrease of their A/B ratio from 2 to 1. Its general formula is $A_{n+1}B_nO_{3n+1}$ (or rather $AO(ABO_3)_n$) [101, 102], where n is the number of octahedral BO_6 layers in the repeating unit. The series is illustrated in Figure 2.14 using the example of strontium iridates $Sr_{n+1}Ir_nO_{3n+1}$.

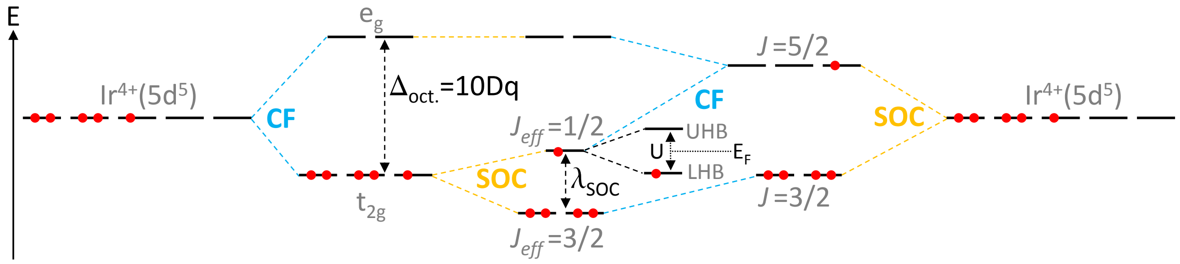

Figure 2.16: *Two equivalent views of the energy split–up of the 5d orbital states due to the crystal field CF with energy $\Delta_{oct.}$ and strong spin–orbit coupling SOC with energy λ_{SOC}. Starting from the left side which depicts the crystalline view, the crystal field splitting occurs first and then spin–orbit coupling generates J_{eff} states with resultant total angular momenta of 3/2 and 1/2. This result can be also reached from the right side which represents the atomic view. Here, the atomic fivefold degeneracy is first split by SOC to total angular momentum quantum numbers J=5/2 and 3/2 and then turned into J_{eff} states by the CF.*

For n=1, only one IrO_2 layer is present in the repeating unit, while for n=2 and n=3 there are two and three of them, respectively. Start and end of an repeating unit are always terminated by SrO layers, while contiguous units are laterally shifted by opposite cation lattice sites. This is not valid in the case of $n=\infty$, since it evolves to the common perovskite formula and structure of ABO_3. As n increases from 1 to ∞, the dimensionality of the material converts from two into three. During this conversion, the bandwidth W increases due to the rise in number of iridium atom neighbors Z from 4 to 5 and 6 in Sr_2IrO_4, $Sr_3Ir_2O_7$ and $SrIrO_3$, respectively.
Moreover, due to the relatively weak on-site Coulomb interaction U between their 5d electrons, these compounds exhibit different electronic behavior compared to the common scenarios in 3d and 4d systems. Their corresponding band structures are illustrated in Figure 2.15, while for increasing n the bandwidth increases. It results that the (RP–214) phase (n=1) of strontium iridate is a Mott insulator, whereas its (RP–327) phase (n=2) and (RP–113) phase ($n=\infty$) form a barely insulator and correlated metal, respectively. In principle, the band structures of these RP iridates can be well described by the effective total angular momentum states whose origin will be discussed next.
However, since only a limited number of RP iridates are stable and available as synthesized single crystals, the growth of single crystalline RP iridate thin films which differ in accurate layer sequences is a big challenge. The related problems, especially in terms of RP iridates grown by pulsed laser deposition will be discussed in Chapter 5.

2.6.3 Spin–orbit coupling (SOC) driven Mott insulators Ba_2IrO_4 and Sr_2IrO_4

While Mott insulators of 3d and 4d TMOs are an important topic in condensed matter physics for quite some time, they were not expected to exist in 5d electron systems. These have comparatively broad bands with weak Coulomb repulsion due to the larger

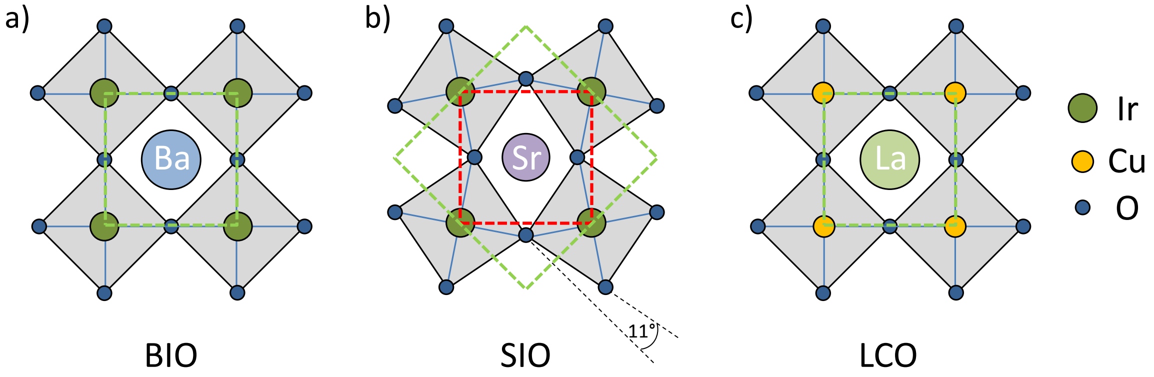

Figure 2.17: *Crystal structures projected on (001): (a) Ba_2IrO_4 with no oxygen octahedral rotations, (b) Sr_2IrO_4 with rotations of the octahedra about the c–axis by 11°, resulting in a larger unit cell by $\sqrt{2} \times \sqrt{2} \times 2$, and (c) similar crystal structure of La_2CuO_4. The green dashed squares indicate the in–plane Brillouin zones and unit cells. The red dashed square in (b) represents the similar pseudo in–plane Brillouin zone and unit cell of Sr_2IrO_4.*

spatial extent of their $5d$ orbitals [100]. Therefore, the requirements for a Mott insulating state are not fulfilled for most of the $5d$ TMOs. They can be correctly described by common band theory as metals. Owing to their unique electronic structures, caused by the combination of spin–orbit coupling (SOC), crystal field (CF) splitting and correlation effects, Ba_2IrO_4 and Sr_2IrO_4 are exceptions to this rule. In their crystalline condition, the iridium cations have the oxidation number [+4] which means that five electrons remain in $5d$ orbitals of the iridium valence shell as it is illustrated in Figure 2.16. These $5d$ orbitals are split by the crystal field (CF) into an energetically higher (twofold, e_g) and lower (threefold, t_{2g}) band, whereas the latter undergoes another energetic split by spin–orbit coupling (SOC). These two generated states can be described very well by an "effective" total angular momentum, resulting in a fully occupied fourfold J_{eff}=3/2 and half filled twofold J_{eff}=1/2 band. The J_{eff}=1/2 states can be expressed as $|J_{eff} = 1/2, m_{J_{eff}} = \pm 1/2\rangle = 1/\sqrt{3}\,(|yz, \pm\sigma\rangle \mp i|zx, \pm\sigma\rangle \mp |xy, \mp\sigma\rangle)$, where $|yz, \pm\sigma\rangle$, $|zx, \pm\sigma\rangle$ and $|xy, \pm\sigma\rangle$ are the t_{2g} states and $\pm\sigma$ corresponds to the spin up or down state [57]. Within this half filled narrow J_{eff}=1/2 band, already a relatively weak Coulomb repulsion is able to open a charge gap between the LHB and UHB, thereby inducing the Mott insulating ground state [100].

Both BIO (space group $I4/mmm$) and SIO (space group $I4_1/acd$) crystallize in the tetragonal K_2NiF_4–perovskite type structure in which the Ir atoms are octahedrally sorrounded by oxygen ligands and located in the center of a imaginary cube with its corners taken by Ba or Sr atoms, respectively. There is a noticeable structural difference between BIO and SIO in their Ir–O–Ir bond angles of 180° and 157°, respectively, resulting in IrO_6 octahedra rotations of approximately 11° about the c–axis [103]. This geometrical disparity is shown in Figure 2.17 a) and b). Due to these rotations, the Brillouin zone and unit cell of SIO is enlarged by $\sqrt{2} \times \sqrt{2} \times 2$. It might be interesting to compare BIO and SIO with their 3d isostructural counterparts La_2CuO_4 (LCO) (see Figure 2.17 c)), a

parent compound to hole–doped high–T_c cuprate superconductors, as well as Sr_2RhO_4, a correlated metal [57, 100, 104–114].
The bulk crystal lattice parameters of BIO are $a = 4.030\,\text{Å}$ and $c = 13.333\,\text{Å}$ [103], whereas for SIO they are $a = 5.4979\,\text{Å}$ and $c = 25.798\,\text{Å}$ [104] while its pseudo–cubic in–plane lattice parameter $a' = 5.4979\,\text{Å}/\sqrt{2} = 3.888\,\text{Å}$. Band gap energies of BIO and SIO were estimated by optical absorption spectroscopy to approximately 110 meV and 150 meV, respectively [115]. Often a magnetic order in the crystal is induced by the insulating Mott state which is also present in BIO and SIO [53]. While SIO is an antiferromagnet with a very small negligible ferromagnetic contribution due to the slightly tilted electron spins and resulting finite Dzyaloshinskii–Moriya (DM) interaction [107], BIO is purely antiferromagetic because of the missing IrO_6 octahedra rotations [60, 116]. The Néel temperatures for BIO and SIO are approximately 230 K and 240 K, respectively [116, 117].

2.6.4 n–doping of Sr_2IrO_4 for activating a superconducting phase

The spin–orbit Mott ground state of (RP–214) iridates can be described by a Kramers doublet of so-called isospin states. Here, the down–spins and up–spins ($\downarrow\uparrow$) strongly couple with the t_{2g} manifold of xy, xz and yz orbitals to create an isospin at each site. Thus, the J_{eff}=1/2 down and up isospins can be written as

$$\begin{aligned} \left|\tilde{\downarrow}\right\rangle &= \sin\theta \left|xy,\downarrow\right\rangle - \cos\theta \left|-(i\left|xz\right\rangle - \left|yz\right\rangle)/\sqrt{2},\uparrow\right\rangle \quad \text{and} \\ \left|\tilde{\uparrow}\right\rangle &= \sin\theta \left|xy,\uparrow\right\rangle - \cos\theta \left|-(i\left|xz\right\rangle + \left|yz\right\rangle)/\sqrt{2},\downarrow\right\rangle \quad , \end{aligned} \tag{2.3}$$

respectively, where θ is given by the tetragonal crystal field splitting [107, 118]. These isospins show that the J_{eff}=1/2 states are notably different to a common $3d$– and $4d$–orbital states of relative TMOs in which the real wave functions are defined by $t_{2g}(xy, yz, \text{and } zx)$ and $e_g(x^2 - y^2, \text{and } 3z^2 - r)$ orbitals. However, the J_{eff}=1/2 state is a much more complicated state owing to hybridization by spin and orbital degrees of freedom. H. Okabe *et al.* explain that if charge carriers are implemented into the J_{eff}=1/2 Mott state, they adopt at the same time the specific feature of the Kramers doublet [118]. In the case of a stable superconducting state and a cubic symmetry ($\sin\theta$=$1/\sqrt{3}$), the pseudospin–singlet Cooper pair of the J_{eff}=1/2 quasiparticles ($a^+_{k\tilde{\uparrow}}$ and $a^+_{-k\tilde{\downarrow}}$) can be written as

$$\begin{aligned} a^+_{k\tilde{\uparrow}} \cdot a^+_{-k\tilde{\downarrow}} &= (c^+_{kxy\uparrow} + c^+_{kyz\downarrow} + ic^+_{kzx\downarrow})/\sqrt{3} \;\times\; (c^+_{-kxy\downarrow} - c^+_{-kyz\uparrow} + ic^+_{-kzx\uparrow})/\sqrt{3} \\ &= 1/3\,(c^+_{kxy\uparrow}c^+_{-kyz\downarrow} - ... + i... + ... - ... + i... + i... - i... - c^+_{kyz\downarrow}c^+_{-kzx\uparrow}) \quad , \end{aligned} \tag{2.4}$$

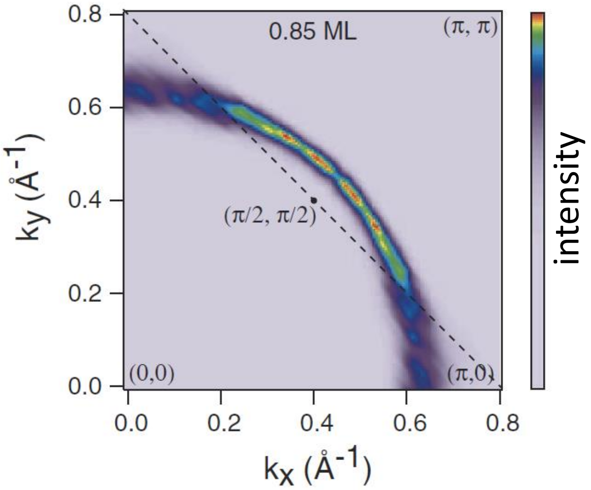

Figure 2.18: *ARPES measurement of a n–doped Sr_2IrO_4 single crystal with 0.85 monolayer potassium coverage at 70 K, clearly indicating the structure of a Fermi arc in a quadrant of the Brillouin zone of the undistorted square lattice. Adopted from [70].*

where a^+ and c^+ are the wave functions for a quasiparticle with an isospin state and for electrons, respectively [118]. Therefore, the Cooper pair of the quasiparticles incorporates the components of interorbital electron pairs with parity mixing for both singlet and triplet pairs [68, 118]. Therefore, a possible superconducting state based on the strong spin–orbit coupled Mott state should turn out to be unique and anisotropic.

As predicted by theory, an unconventional superconducting phase should be possible in the J_{eff}=1/2 (RP–214) iridate Mott insulators by inducing charge carriers [67–69]. However, unfortunately this phase remains unrealized to date, although a lot of investigations are already done in both hole and electron doping experiments of (RP–214) iridates [70–73, 118–126]. Nevertheless, there are some outstanding signs which clearly show that doped (RP–214) iridates could be on the verge to superconductivity.

One of the most promising indications of this situation is the appearance of so-called Fermi arc structures observed in ARPES. While the nature of the pseudogap, which is the region of the phase diagram extending above the superconducting dome, is still a subject of debate, the Fermi arc structures denote an intrinsic signature of this uncommon phase. A Fermi arc, as shown in Figure 2.18, is a region in k–space with spectral weight at zero energy resulting in an ungapped Fermi surface. In the case of a superconducting transition, this gapless region collapses to a point, the so-called "node" which is characteristic of the d–wave superconducting order parameter [127]. Y. K. Kim *et al.* impressively demonstrated that potassium–doped SIO single crystals show Fermi arcs in ARPES measurements by metallizing their surfaces [70]. Unfortunately, they could not observe a collapse of the nodal gap due to charging effects at very low temperatures by reasons of the insulating bulk SIO. Additionally, as in the case of high–T_c cuprates, the Fermi arc structure seems to spread out on the Fermi surface by increasing the potassium concentration on the sample surface as well as the temperature. However, not only

SIO and cuprates but also non–superconducting materials can show Fermi arcs [128], giving rise to more speculations about the general comparison of (RP–214) iridates and cuprates. One should note that the pseudogap in (RP–214) iridates could be originated by other fundamental reasons than in cuprates. One of the challenges in this thesis is to produce bulk doped (RP–214) strontium iridate with pulsed laser deposition combined with a proper target material of the desired stoichiometry. This more elaborated doped material could give more information about the Fermi arc nature and the behavior of the nodal gap.

3 Growth and characterization methods

This chapter deals with various growth techniques that were used in this thesis for crystalline thin film fabrication, followed by an illustration of the diverse growth modes. Finally, all utilized *in situ* and *ex situ* characterization methods are explained in required detail.

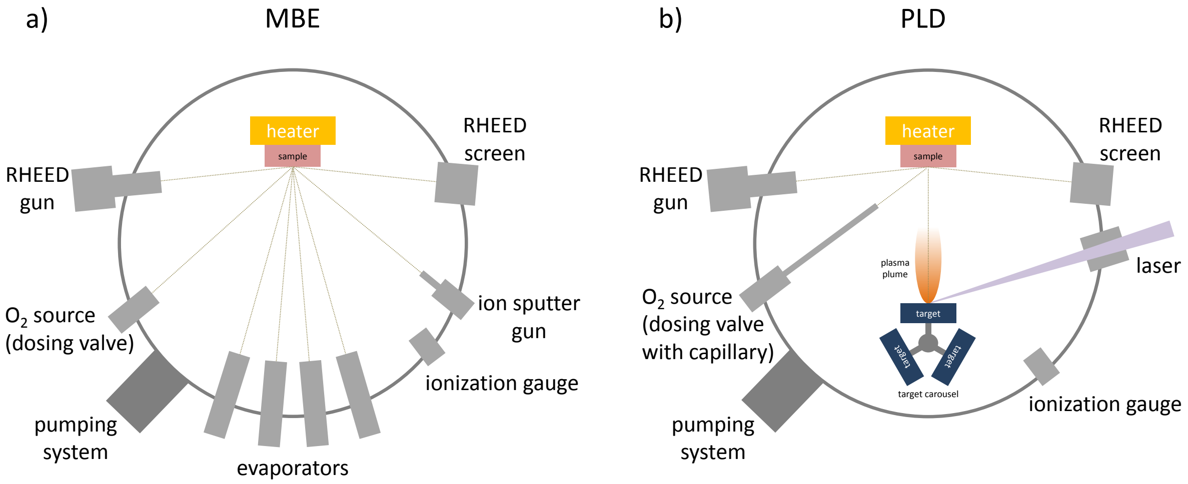

Figure 3.1: *Exemplary setups of (a) molecular beam epitaxy and (b) pulsed laser deposition growth chambers.*

3.1 Molecular beam epitaxy and pulsed laser deposition

Nowadays, many epitaxial growth techniques for thin film deposition are available which are developed and established since almost half a century. In the subgroup of physical vapor deposition (PVD), two of the most important methods are molecular beam epitaxy (MBE) and pulsed laser deposition (PLD). Figure 3.1 schematically shows the corresponding setups exemplarily. Both techniques require at least high vacuum conditions and allow to produce very clean samples with the desired composition. Equipped with a RHEED apparatus (see also subsection 3.2.1) both are perfectly suited to define layered material systems accurately. These two methods have advantages and disadvantages. Depending on the particular deposition material one has to balance these techniques.

In the following, both techniques will be discussed next to each other, focusing on the conceptional and technical description.

3.1.1 Principle of molecular beam epitaxy (MBE)

MBE was invented in the early sixties [129] and is a multifunctional epitaxial production process for thin single crystalline structures which can consist of semiconductors, metals, superconductors or insulators. "Epitaxy" stands here for nothing else than that the grown crystal structure adapts to that one of the substrate. This is possible when the physical properties, in particular lattice parameters and heat transfer coefficients, of both materials differ not too much from each other, at least for the plane vertical to the crystal growth.

Figure 3.1 a) demonstrates a typical MBE chamber with the most important components required for epitaxial growth. The MBE process itself can be explicated into three separated major steps.

The very first step is the creation of molecular beams using evaporators like effusion cells, Knudsen cells, standard electron beam evaporators or cracker cells operating as heaters/smelters of pure solid materials with certain vapor pressures. Therefore such a molecular beam is made up of element specific atomic particles, while its flux is direct proportional to the applied heating power. Since the homogeneity of the beam and stability of the flux current are very sensitive to variations in temperature, it is indispensable to apply a precise power supply and an exact temperature read-out with an accuracy of tenth °C. However, to ensure the uniformity of the film thickness, one has to align the beam direction nearly perpendicular to the substrate surface and the deposition spot as central as possible.

The second step is the transport of the evaporated atomic particles through the beam to the substrate surface. Due to the fact that the energy-rich particles may react with the residual gas molecules one has to guarantee a very low base pressure in the growth chamber (typically about $1 \cdot 10^{-10}$ mbar) to avoid unintentional integration of contaminations. Simultaneously, the use of ultra pure evaporates is essential for the MBE process. Furthermore, reactions of the particles on their way to the substrate and on its surface are sometimes intended, for example with ultra pure oxygen gas molecules for fabricating an oxide as is the case in this thesis. Here, the growth pressure must be kept below 10^{-4} mbar both to prevent the reduction of the mean free path of the molecular beam and the lifetime of all heating filaments caused by oxidation processes.

The final step is the deposition and nucleation of the atomic particles on the substrate surface. In which preferred way this nucleation proceeds, depends a lot on factors pertaining to the substrate conditions and will be discussed in subsection 3.1.3. By simple opening and closing the shutters of the evaporators one can exactly dictate the sequence of atomic layers. Here the big advantage over other deposition techniques is the independence on self-organization of unit cell constructions and lowered intermixing effects of different adatoms. In the case of MBE, the overall tunable parameters for the evaporated material are the background gas type and pressure, the evaporator-to-substrate distance and the speed of growth dictated by the change of applied heating power to the evaporators.

3.1.2 Principle of pulsed laser deposition (PLD)

Pulsed laser deposition is another multifaceted PVD technique for epitaxial thin film growth and was invented and promptly enhanced in the eighties when the first high-temperature superconducting oxides were discovered [52]. Similar as the MBE method, it is a very clean growth technique with much higher deposition rates. A tremendous advantage is that a material with very complex stoichiometry can be grown by using only one crystalline or polycrystalline target material with an equivalent stoichiometry. Figure 3.1 b) shows a typical setup of a PLD growth chamber. The selectable target is mounted on a target carousel while the target surface is parallel to that one of the substrate. This geometry is important, since the material deposition direction is perpendicular to the target surface as well as the deposition spot is strongly areal confined. An eximer laser is installed outside the growth chamber which delivers the laser pulses. The laser beam is energetically adjusted by an attenuator and focussed by an optical lens before it enters a laser window into the chamber (not shown in Figure 3.1 b)). When the laser pulse strikes the target surface, the material gets evaporated by absorption of the laser pulse energy and forms a luminous plasma plume with a very short life-time. This plasma plume transports the particles to the substrate before the deposition process begins. Thus the PLD process can be explicated into three separated major steps, which will be explained in more detail below [130, 131].

The first step is the interaction of the laser pulse with the target material followed by a plasma formation. Since the laser pulse has an energy above the plasma frequency of the target material, it can penetrate through its surface and can get absorbed. Depending on the laser fluency (describing the energy density of the laser spot incident on the target surface) and the absorption coefficient of the material, the absorbed photons heat up the target. Hereupon the target material gets evaporated by reaching its critical vaporization temperature, while the evaporated particles still interact with the laser pulse leading to an extensive ionization and the formation of a plasma. Since the interaction with the laser pulse still continues, the plasma absorbs energy too and results in a three-dimensional isothermal expansion. Due to the fact that the velocity of the particles perpendicular to the target surface is larger than that one parallel to it, the plasma gets formed to a conoidal plasma plume. The plasma plume is composed of energetically various particles as neutral atoms, ions and electrons.

The second step is the propagation of the plasma and a subsequent deposition on the substrate. After the laser pulse, the particles adiabatically propagate towards the substrate and may interact with the background gas, if applied. By selecting the process gas type and regulating the background pressure one can influence a lot of mechanisms. For instance, if the pressure is high enough, the particles can get retarded and scattered causing a dramatically change in stoichiometry of the grown film. In addition, if a reactive process gas like oxygen, nitrogen oxide or ozone is applied, the particles in the plasma plume can react with this, mainly in a oxidation process. To retain the amount of contaminants as low as possible, one has to guarantee a very low base pressure (typically about $5{\cdot}10^{-10}$ mbar) and the application of ultra pure process gases (minimum purity 99.9995%). Typical PLD growth pressures range from $1{\cdot}10^{-7}$ to 0.5 mbar. Therefore, the overall tunable parameters for the ablated material are the laser fluency, the background gas type and pressure, the target-to-substrate distance and the speed of growth dictated by change of the laser pulse repetition rate.

The last step is the nucleation and growth on the substrate. As in MBE the nucleation and growth process depends on a lot of factors pertaining to the substrate conditions and will be discussed next. In the case of PLD growth, a multitude of mechanisms can be expected, since the deposited material contains all elements of the target. There are both, the self-organization for unit cell construction and intermixing effects of different adatoms, happening simultaneously.

3.1.3 Growth modes

For both, MBE and PLD, the substrate conditions are of pivotal importance for the growth. The surface quality, the temperature of the substrate, as well as the lattice misfit between the substrate and the film are crucial.

In cases of rough surfaces with defects, the incident particles are incorporated just in the local positions where they impacted. For epitaxial growth therefore, one uses typically atomically flat substrates to obtain sharp interfaces and a definite number of layers. Such substrates have surfaces with wide smooth terrace structures and steps heights of only one unit cell, where incoming particles can interact versatilely with the substrate. In this case, a lot more processes than a simple embedding can occur. However, atomically flat substrates are not the only requirement for perfect films. Typically, incident particles cannot rearrange on the surface to build up a regularly structured film but the substrate has to be additionally heated up to several hundreds K. If very high substrate temperatures are used, one has to take care of incident volatile constituent parts which may thermally desorb back into the vacuum. Furthermore, the lattice misfit between substrate and film determines the further growth progress after the first few particles are incorporated. Bascially, there are four possible modes of film growth which can occur. These are schematically shown in Figur 3.2. The arrangement of the particles depends on the thermodynamic precondition of the surface, in which the free energies of substrate surface (γ_S), film surface (γ_F) and interface (γ_I) play a decisive role. The growth modes are now briefly clarified [74, 132, 133]:

- The **2D layer-by-layer** growth and is also referred to as Frank-van-der-Merwe and illustrated in Figure 3.2 a). This results in atomically flat film surfaces, thus it is the most favored growth mode. Here, the surface energy of the bare substrate

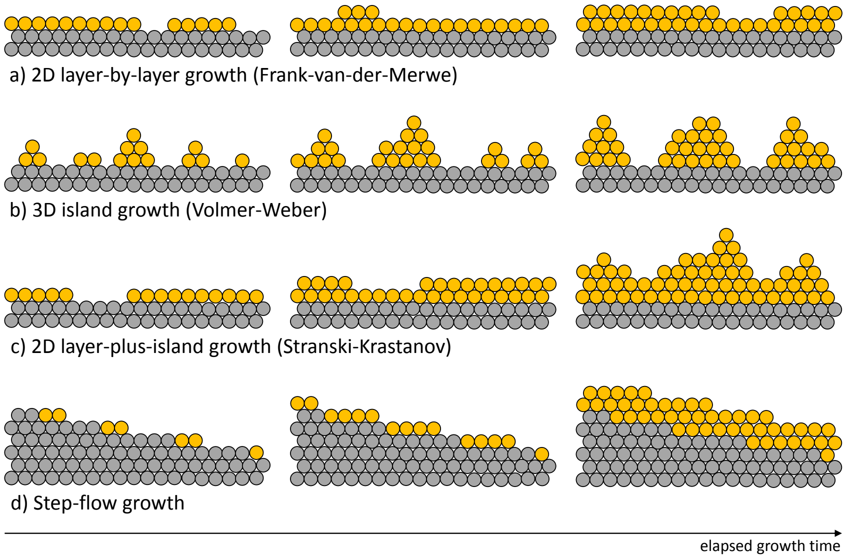

Figure 3.2: *Various growth modes: (a) Frank-van-der-Merwe, (b) Volmer-Weber, (c) Stranski-Krastanov and (d) Step-flow growth.*

(γ_S) is larger than that of a covered one with film material ($\gamma_F+\gamma_I$). This is caused by an energy gain due to the strong binding of film material to the substrate. Therefore, it is energetically more favorable for the system to complete a film layer before the next layer starts to grow. Moreover, the film may grow strained depending on the misfit value. Tolerable misfit values for this growth mode are up to $\pm 2.5\%$.

- In contrast, there is the **3D island** growth, also referred to as Volmer-Weber and shown in Figure 3.2 b). This mode is developed if the energy gain from binding the film material to the substrate is smaller than the gain for the clustering of film material. Since by this reason the substrate surface can not be wetted in the initial growth state, three dimensional islands are built up which can coalesce later on. Generally, the grown film is fully relaxed and exhibits a rather rough surface. As a rule of thumb, the bigger the lattice mismatch value the more probable is the appearance of this growth mode.

- The **2D layer-plus-island** growth, also referred to as Stranski-Krastanov and illustrated in Figure 3.2 c). This is a hybrid growth mode involving the two former modes. The film grows first two dimensional layer-by-layer and then changes its growth character after only few layers to a three dimensional island growth. This is due to the increase of strain energy caused by the lattice mismatch between film and substrate. This kind of growth mode often happens if the lattice mismatch is not suitable enough for pure layer-by-layer growth and not such as large as to allow for island growth.

- The **step-flow** growth, shown in Figure 3.2 d), is another growth mode which can occur on graded substrates. In this case, the particles can only nucleate at step edges without any formation of islands. Here it seems as if the step edges move across the surface while creating new layers on the substrate. Since during growth the roughness and number of step edges are kept constant, the layer growth is not observable by RHEED monitoring (see also subsection 3.2.1).

3.2 *In situ* characterization

The *in situ* sample characterization consists of high as well as low energy electron diffraction, and photoelectron spectroscopy. Their techniques and thus obtained knowledge about the sample status are discussed in the following.

3.2.1 Reflection high energy electron diffraction (RHEED)

During crystal growth, it is essential to monitor the growth quality continuously. This can be achieved by using reflection high energy electron diffration (RHEED). In Figure 3.3 the basic principle of RHEED is illustrated. Here, electrons are accelerated from an electron gun to energies of about 5–30 keV. The focused electron beam strikes the sample surface under an almoust grazing angle (typically $\alpha_i < 3°$) whereby a high surface sensitity is ensured. Afterwards, the electrons are reflected and interfere with each other depending on the crystal symmetry of the sample surface. The result is a diffration pattern on the fluorescent screen. Since the electrons exhibit high energies and the electron source plus fluorescent screen are spatially seperated from the sample position, growth characterization by RHEED is feasible even at high pressures up to 10^{-1} mbar [134]. The diffraction of electrons is a specific phenomenon due to the wave character of particles. The de Broglie wavelength λ of an electron wave is given by

$$\lambda = \frac{h}{\sqrt{2m_e E}} \tag{3.1}$$

where h is the Planck constant, m_e and E the mass and kinetic energy of an electron, respectively. A RHEED spot appears on the fluorescent screen if the difference between the incident $\vec{k_0}$ and deflected $\vec{k}$ momentum vectors corresponds to a reciprocal lattice vector $\vec{G}_{hkl}$:

$$\vec{G}_{hkl} = \vec{k} - \vec{k_0}. \tag{3.2}$$

This is the so-called Laue condition. Due to the high surface sensitivity of this method, diffraction only happens at the outmost layers of the crystal which one can regard as a two dimensional lattice with a δ–shaped elongation in its third dimension. The reciprocal lattice corresponds to the three dimensional Fourier transform of the real space lattice. Hence, the reciprocal lattice is a formation of parallel one dimensional rods in the recipro-

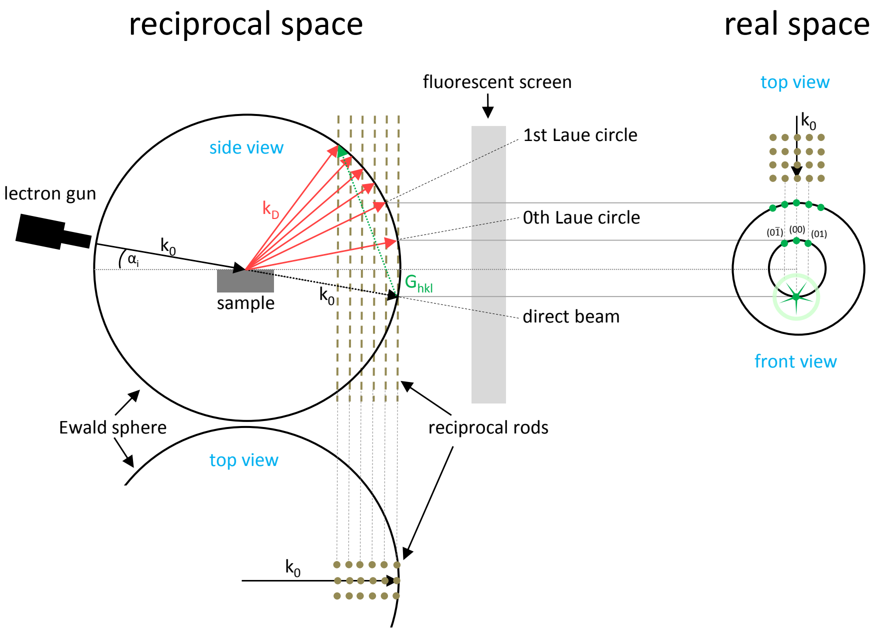

Figure 3.3: *Sketch of RHEED geometry of a simple cubic lattice in real and reciprocal spaces. The side view (left) shows the formation of RHEED spots developed from cuts of the reciprocal rods by the Ewald sphere in the reciprocal space (Ewald construction). The resulting real space RHEED pattern on the fluorescent screen is demonstrated in the front view (right). The RHEED spots are located on the Laue circles originated by the circular cuts of the Ewald sphere.*

cal space, because the Fourier transformed δ-function is a constant. In this case the Laue condition can be written as

$$\vec{G}_{hk} = \vec{k_D} - \vec{k_0}. \tag{3.3}$$

In terms of mainly elastic scattering processes ($|\vec{k_0}| = |\vec{k_D}| = k$) one can depict the Laue condition by the Ewald construction. Figure 3.3 illustrates such a construction for a simple cubic lattice. In the reciprocal space, the radius of the Ewald sphere is given by the wave vector of the incident electrons, while its center is shifted by $\vec{k_0}$ from a reciprocal lattice point. All cuts of the reciprocal rods by the Ewald sphere cause RHEED spots which are visible by the projection onto a fluorescent screen in real space. The RHEED spots are located on the invisible Laue circles which derive from the typical cuts by the Ewald sphere. Strictly speaking, such a real space RHEED pattern is not only composed by elastic scattering. Inelastically scattered electrons are responsible for both a homogeneous diffuse background and the so-called Kikuchi lines in RHEED patterns. Kikuchi lines are principally generated by diffusely scattered electrons by phonons and plasmons of the crystal lattice before those are elastically scattered complying the Laue condition. These scattering processes are strongly dependent on the crystal quality. Therefore distinct Kikuchi lines indicate qualitatively well-defined crystal surfaces and

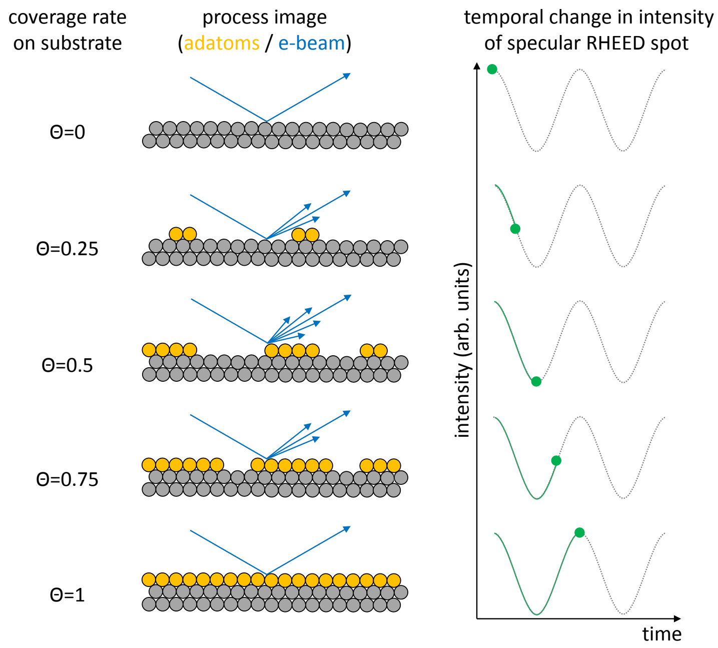

Figure 3.4: *RHEED oscillations (right) depending on the coverage rate of adatoms on the sample surface (left). The middle view shows respective images of the coverage with the corresponding reflection of the electrons.*

well ordered bulk lattices, since this lines can be widely broadened by many surface configurations as step edges, contaminations, defects and roughness too. But not only Kikuchi lines are affected by these surface configurations. A RHEED spot itself directly correlates with the width of the reciprocal rod depending on the number of coherent scattering centers. Every further surface configuration reduces this number and consequently the reciprocal rod width and real space spot sharpness too. Furthermore, three dimensional islands on the surface with a lateral elongation smaller than the inelastic mean free path of the electrons can generate additional spots due to transmission diffraction [134].

But RHEED patterns are not the only useful information one can get from this technique. Especially, if a material grows two dimensionally layer-by-layer on a substrate, a definite number of monolayers can be grown by monitoring the growth process in real time. The growth of monolayers by RHEED is demonstrated in Figure 3.4. Before starting the growth, the coverage with adatoms on a flat and smooth substrate surface is zero whereas the reflected electron beam is maximum in intensity resulting in a bright specular reflected spot. For RHEED oscillations the intensity of this specular reflected spot is recorded during growth. After starting the growth, more and more material are deposited on the substrate surface while the specular reflected spot drops in intensity due to diffusely scattered electrons on island edges. When half of the sample is covered with adatoms, the surface has its maximum roughness while the intensity of the specular reflected spot is minimum. With even more deposition the islands merge and decrease

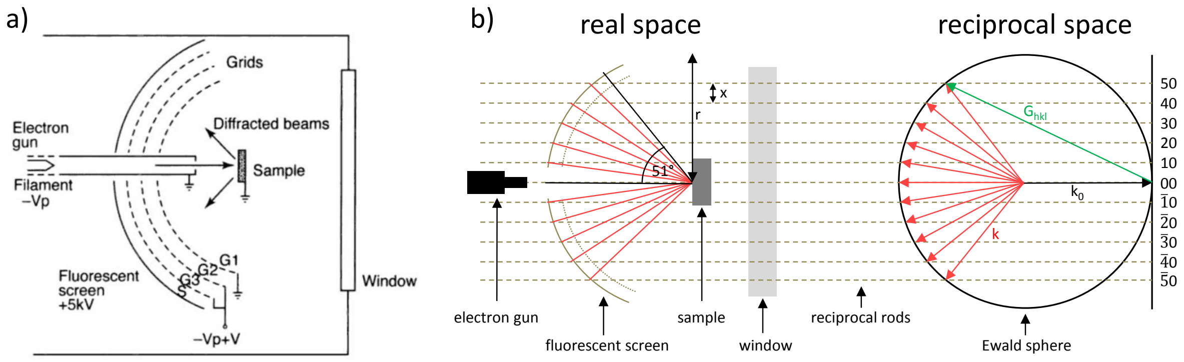

Figure 3.5: *(a) Experimental setup of a LEED system. Adopted from [135]. (b) Sketch of LEED geometry in real and reciprocal space.*

the number of sources for diffuse scattering causing an upturn in intensity of the specular reflected spot. If a layer is formed completely closed, the specular reflected spot reaches again a maximum in intensity, before the next oscillation begins. With this one is able to grow a definite number of monolayers with the feasibility to stop the growth in the moment when a layer is properly finished.

On the other hand, RHEED oscillations are not always and for every material system meaningful. The correct geometry of the RHEED system and direction to the sample surface is essential, since a misalignment can cause a reduced amplitude in the oscillations and therefore a difficult determination of its periodic time. The observation of distinct RHEED oscillations indicate a well ordered growth, but is not a guarantor for the desired material system, for instance in Ruddlesden-Popper phase materials. Moreover, a thick two dimensional layer-by-layer grown system can form in the late growth process additional islands (Stranski-Krastanov growth) affecting the oscillation amplitude over time.

3.2.2 Low energy electron diffraction (LEED)

Another useful diffraction technique is utilized in low energy electron diffraction (LEED) measurements. Figure 3.5 a) shows a typical LEED setup. Electrons emitted by an electron gun pass through an aperture in the middle of the fluorescent screen and impinge perpendicular on the sample surface. One part of the electrons are elastically back scattered at angles >90° and create a diffraction pattern on the fluorescent screen.

Since the kinetic energies of the electrons range typically from 30–250 eV and therefore the de Broglie wavelength $\lambda = \frac{h}{\sqrt{2 m_e E}}$ is of the order of or smaller than the interatomic distances, LEED is a very surface sensitive characterization method. Such low kinetic energies require ultra high vacuum conditions. One should keep in mind that low contamination amounts on the sample surface can already prevent most diffractions. Insulating properties of the samples are also critical, since charging effects by reasons of non-discharged incoming electrons impede the diffraction. Furthermore the LEED operation is not feasible while sample growth, because the measurment setup has to be close in front of the sample surface. According to C. A. Lucas in [136] the coherence length of the electrons is typically about 50–100 Å (depending on the kinetic energy) and therefore smaller than for RHEED. Structures bigger than the coherence length do not influence the diffraction pattern, whereby consequently the large-scale morphology of a surface can not be reliably evaluated with LEED.

In comparison to RHEED the big advantage of LEED is demonstrated in Figure 3.5 b). Due to the lower electron energies much more rods of the reciprocal lattice are cut by the smaller originated Ewald sphere within the angular field of the fluorescent screen. Here both lateral directions of the reciprocal lattice are displayed simultaneously and under the same geometrical conditions onto the screen. With this, LEED is a quite simple technique to determine the symmetry and lattice parameters of the reciprocal and real space lattice.

The diffraction in LEED obeys mostly the Laue condition that describes the elastic scattering of the electrons. Due to the strong surface sensitivity of LEED the three dimensional Laue diffraction condition from equation (3.2)

$$\vec{G}_{hkl} = \vec{k} - \vec{k_0}$$

has to be replaced by its two dimensional correspondents (similar as in the RHEED model). Hence the incoming and outgoing electrons with the momentum vectors $\vec{k_0}$ and $\vec{k}$ and the three dimensional reciprocal lattice vector $\vec{G}_{hkl}$ become respectively $\vec{k_0^{\parallel}}$, $\vec{k^{\parallel}}$ and $\vec{G}_{hk}$. Then the Laue diffraction condition is as follows:

$$\vec{G}_{hk} = \vec{k^{\parallel}} - \vec{k_0^{\parallel}}. \tag{3.4}$$

With the specific LEED geometry shown in Figure 3.5 b) one can get a relation between the LEED spot distance x, the fluorescent screen radius r and the reciprocal space vectors as

$$\frac{|\vec{G}_{hk}|}{|\vec{k_0}|} = \frac{x}{\frac{r}{sin\,51°}}. \tag{3.5}$$

The reciprocal basis vectors $\vec{a^*}$ and $\vec{b^*}$ can be calculated as

$$\vec{a^*} = 2\pi \cdot \frac{\vec{b} \times \vec{n}}{|\vec{a} \times \vec{b}|}, \qquad \vec{b^*} = 2\pi \cdot \frac{\vec{n} \times \vec{a}}{|\vec{a} \times \vec{b}|} \tag{3.6}$$

where $\vec{n}$ is the normal vector (with $|\vec{n}|$=1) to the sample surface and $\vec{a}$ and $\vec{b}$ represent the basis vectors in real space [137]. Vice versa one can determine now the length of the real space basis vectors by

$$|\vec{a}| = \frac{2\pi}{|\vec{a^*}| \cdot sin\angle(\vec{a}, \vec{b})}, \qquad |\vec{b}| = \frac{2\pi}{|\vec{b^*}| \cdot sin\angle(\vec{a}, \vec{b})}. \tag{3.7}$$

When inserting the energy dispersion relation of the electrons by $|\vec{k_0}| = \sqrt{\frac{2m_eE}{\hbar^2}}$ one can rearrange the equations above and determine the real space lattice parameters as

$$|\vec{a}| = \frac{\frac{r}{sin\,51°}}{x} \cdot \frac{2\pi}{\sqrt{\frac{2m_eE}{\hbar^2}} \cdot sin\angle(\vec{a},\vec{b})} \tag{3.8}$$

and $|\vec{b}|$ (analog calculation) by using the occurred LEED spots along the horizontal and vertical direction, respectively. The angle between both basis vectors $\vec{a}$ and $\vec{b}$ depends on the crystal symmetry of the sample. For instance the angle is 60° for a hexagonal lattice structure.

Beside the lattice parameters LEED can provide some other information. On the one hand the sharpness of the occurred LEED spots give evidence about the perfection of the crystal surface. On the other hand additional spots between the actual from the crystal symmetry expected LEED spots give some clues about potential surface reconstructions.

3.2.3 Photoelectron spectroscopy (PES)

From its invention in the mid fifties by K. Siegbahn [138, 139] and subsequent advancements, photoelectron spectroscopy (PES, also known as photoemission spectroscoy) became one of the most powerful tools to probe the electronic structure of complex solids, their surfaces and interfaces, molecules or atoms [140–142]. PES enables quantitative investigations of both, stoichiometry and chemical environment of the elements (ESCA: electron spectroscopy for chemical analysis) [143]. Depending on the applied photon energy, one distinguishes between ultraviolet photoemission spectroscopy (UPS: $E_{ph} \lesssim$ 100 eV), soft X-ray photoemission spectroscopy (XPS: 100 eV $\lesssim E_{ph} \lesssim$ 1500 eV) and hard X-ray photoemission spectroscopy (HAXPES: $E_{ph} \gtrsim$ 1500 eV). Furthermore, one is able to observe directly the energy-momentum relation $E(\mathbf{k})$, representing the band structure of a crystalline solid by means of angle resolved photoemission spectroscopy (ARPES). Here, the dispersing valence band electrons can offer valuable access to the Fermi surface of an electronic system. However, PES is a very surface sensitive characterization method due to the energy dependent inelastic mean free path (IMFP) of photoelectrons, providing information depths in the range of several Å up to a few nm.

Fundamentals

PES is based on the photoelectric effect which, beside the Compton effect and pair production, is one of the interactions of electromagnetic radiation with matter. The photoelectric effect, describing the excitation of an electron from a bound state in the solid into a free state in the vacuum by absorbing an irradiated photon, was already discovered in 1887 by H. Hertz [144]. However, at that time only the variation of charge

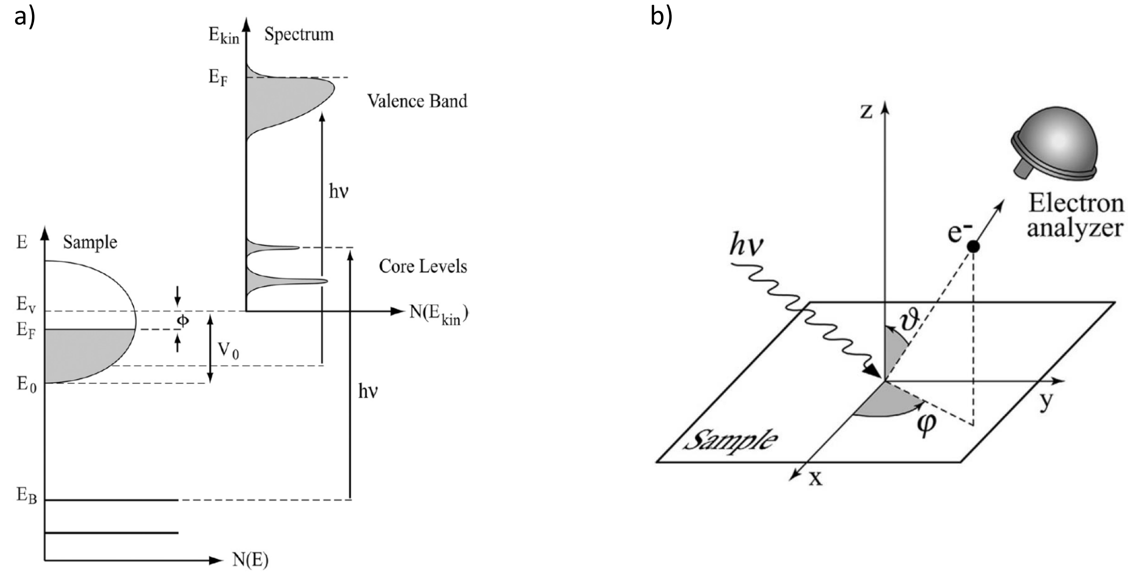

Figure 3.6: *Fundamentals of the photoemission process: (a) Common illustration of the photoemission process in the single-particle picture at fixed photon energy* $h\nu$*, adopted from [140]. The real energetics of the solid are shown on the left, while the resulting photoemission spectrum after excitation is represented on the right. Here, the work function* ϕ *is defined as the difference between the Fermi energy* E_F *and the vacuum level* E_V*. In the spectrum, all structures are broadened due to the limited lifetime and energy resolution. The valence band (VB) follows the Fermi distribution at* E_F*. (b) Geometry of the experimental ARPES setup, adopted from [145]. The incoming photon with* $h\nu$ *impinges onto sample and the emitted photoelectron is detected by a hemispherical electron analyzer under certain azimuth (*φ*) and polar (*ϑ*) angles.*

of an electrode under incidence of monochromatic light was referred by him. In 1905 A. Einstein with his innovative "light quanta hypothesis" delivered a precise explanation for this effect [146]. He introduced the interaction of light with matter by a quantum mechanical description and postulated the fundamental relation between the photon energy of the incident light ($h\nu$) and the kinetic energy (E_{kin}) of the emitted electron, the so-called photoelectron. The binding energy of the electron in the solid E_B can be determined by the Einstein equation that follows from the energy conservation:

$$E_{kin} = h\nu - |E_B| - \phi, \tag{3.9}$$

where ϕ is the energy difference between the Fermi energy E_F and the vacuum level E_V, depicting the work function (typically in the range of 3–5 eV). To be precise, note that although the "Fermi level" E_F is actually only valid for the chemical potential $\mu(T)$ at T=0, it will be used continuously for finite temperatures, being a common practice in photoemission experiments. By dint of Equation 3.9 and application of monochromated light, it is possible to identify the elemental composition of the material from the element specific binding energies of their corresponding core-shell electrons, representing the standard procedure of an ESCA experiment. Figure 3.6 a) shows schematically the photoemission process, containing the energetic situation in a solid in the ground state as well as the resulting photoemission spectrum. In the solid, the core levels occur as δ-peaks and are fixed at defined energies E_B. In contrast, in the photoemission spectrum, they are broadened by a Lorentzian shape due to the finite lifetime of the core photo-holes and additionally affected by another broadening, resulting from the Gaussian resolution of the analyzer. Altogether, the final core level peak shape in a spectrum is described by a Voigt profile that is created by a convolution of a Gaussian and a Lorentzian function. A Voigt profile frequently satisfies the description of the line shapes of peaks in a spectrum. But metals, in which screening effects due to interactions of the photo-hole with electrons of the conduction band can arise and thus form an asymmetric line shape towards higher binding energies, are an exception. In this case, the Doniach-Sunjic function is a suitable descriptions of such peak shapes [147]. For an exact treatment of idiosyncratic peak shapes of investigated samples with even higher complexity much more complex and sophisticated theories would be needed [140]. In the single particle picture the valence band (VB) spectrum near E_F represents basically the density of states (DOS), aside from matrix element effects and the above mentioned spectral broadenings. On the other hand, the measured VB, ending with a Fermi distribution, has no certain peak shape, even though both lifetime and resolution broadenings are existent, since PES is restricted to occupied states only.

Taking advantage of momentum conservation, one is also able to gain the electronic dispersion $E(\boldsymbol{k})$ of VB electrons by means of ARPES. The vacuum momentum $\boldsymbol{P} = \hbar\boldsymbol{K}$ of a photoelectron parallel and perpendicular to the sample is

$$
\begin{aligned}
\hbar\boldsymbol{K}_{\parallel} &= \sqrt{2mE_{kin}}\sin\vartheta \quad \text{, with} && (3.10)\\
\boldsymbol{K}_x &= \frac{1}{\hbar}\sqrt{2mE_{kin}}\sin\vartheta\cos\varphi, && (3.11)\\
\boldsymbol{K}_y &= \frac{1}{\hbar}\sqrt{2mE_{kin}}\sin\vartheta\sin\varphi\,. && (3.12)\\
\hbar\boldsymbol{K}_{\perp} &= \sqrt{2mE_{kin}}\cos\vartheta \qquad \text{, as} && (3.13)\\
\boldsymbol{K}_z &= \frac{1}{\hbar}\sqrt{2mE_{kin}}\cos\vartheta \qquad , && (3.14)
\end{aligned}
$$

where ϑ indicates the emission angle between the sample surface normal and the direction under which the emitted photoelectrons are detected typically with a hemispherical analyzer. The measuring geometry is illustrated in Figure 3.6 b). Furthermore m is the electron mass, $\boldsymbol{K}_{\parallel}$ and $\boldsymbol{K}_{\perp}$ are parallel and perpendicular momenta, $\boldsymbol{K}_x$, $\boldsymbol{K}_y$ and $\boldsymbol{K}_z$ are their relevant components, respectively. The momentum transfer from the irradiated photon to the electron is negligible for excitation energies $\leq$100 eV, whereby one can put the electron excitation on a level with a vertical transition in the reduced zone scheme with $\boldsymbol{k}_f - \boldsymbol{k}_i = 0$, where f and i denote the final and initial state, respectively. However, in the repeated zone scheme the momenta can differ strictly by an integer multiple of the reciprocal lattice vector, namely as $\boldsymbol{G} = \boldsymbol{k}_f - \boldsymbol{k}_i$. To define the relationship between the momenta of an electron in the vacuum $\boldsymbol{K}$ and in the solid $\boldsymbol{p} = \hbar\boldsymbol{k}$, one can split the one-step photoemission process into three independent and destinct single steps, described in the so-called three-step model [140]:

(1st step) photoexcitation of the electron from a bound initial state to an unbound final state within the solid (creation of a photoelectron),

(2nd step) transport of the excited photoelectron through the matter to the surface of the sample,

(3rd step) transition of the photoelectron from the solid into the vacuum.

Regarding the 3rd step, one should keep in mind that although in the normal direction translational invariance is annulled, the momentum parallel to the sample surface ($\boldsymbol{k}_\parallel$) is conserved, leading to

$$\hbar\boldsymbol{k}_\parallel = \hbar\boldsymbol{K}_\parallel = \sqrt{2mE_{kin}}\sin\vartheta, \tag{3.15}$$

whereas the momentum perpendicular to the sample surface is not conserved. This fact makes ARPES a well-suited technique for investigations of one- or two-dimensional systems, since in such systems changes of $\boldsymbol{k}_\perp$ can be neglected. Nevertheless, one can determine $\boldsymbol{k}_\perp$ by further assumptions. The dispersion of the electron's unbound final state can be described with a free-electron model [145]:

$$E_f(\boldsymbol{k}) = \frac{\hbar^2\boldsymbol{k}^2}{2m} - |E_0| = \frac{\hbar^2(\boldsymbol{k}_\perp^2 + \boldsymbol{k}_\parallel^2)}{2m} - |E_0|, \tag{3.16}$$

where E_0 indicates the valence band minimum. For the momentum perpendicular to the sample surface one is now able to formulate

$$\hbar\boldsymbol{k}_\perp = \sqrt{2m(E_{kin}\cos^2\vartheta + V_0)}, \tag{3.17}$$

where V_0 is the inner potential of the sample that can be well estimated experimentally if a light source with tunable photon energy is available. Since $\boldsymbol{k}_\perp$ is not of relevance for the studies presented in this thesis, it rather will not be discussed in much more detail.

Theoretical description

The one-step model describes photoemission as one coherent quantum mechanical process (namely as "photon in, electron out"). In contrast, the above mentioned three-step model interpretates it in a much more precise way, thus being of particular importance to understand the whole photoemission process in detail. The following descriptions are substantially based on the explanatory notes by A. Damascelli in Ref.[145].

One should keep in mind that a common simplification, the so-called "sudden approximation", will be used continuously in the next theoretical interpretations. It assumes that by excitation an electron is instantaneously removed from the solid and the effective potential of the system changes discontinuously at that moment, such that the remaining N–1 particle system is not able to interact with the created photoelectron. In general, one starts with the Fermi's Golden rule [140, 141, 145] which depicts the transition rate ω between two states and is deduced from first-order perturbation theory:

$$\omega_{f,i}(h\nu) = \frac{2\pi}{\hbar} \left|\langle \Psi_f^N | H_{int} | \Psi_i^N \rangle\right|^2 \delta(E_f^N - E_i^N - h\nu) \quad , \tag{3.18}$$

where $E_i^N = E_i^{N-1} - E_B^{\boldsymbol{k}}$ and $E_f^N = E_f^{N-1} + E_{kin}$ are the energies of the N particle initial and final states Ψ_i^N and Ψ_f^N, respectively, with i=0 being the ground state. $E_B^{\boldsymbol{k}}$ is the (negative) binding energy of an electron with crystal momentum $\boldsymbol{k}$, $E_{kin} = \hbar^2\boldsymbol{k}^2/2m$ its final state free electron kinetic energy and $\langle \Psi_f^N | H_{int} | \Psi_i^N \rangle$ is the N particle transition matrix element. The included perturbation operator H_{int} represents the interaction of the electrons with an electromagnetic field $\boldsymbol{A}(\boldsymbol{r}, \mathrm{t})$ that yields with the electronic momentum operator $\boldsymbol{p}$ the following expression:

$$H_{int} = \frac{e}{2mc}(\boldsymbol{A} \cdot \boldsymbol{p} + \boldsymbol{p} \cdot \boldsymbol{A}) \approx \frac{e}{mc}\boldsymbol{A} \cdot \boldsymbol{p} \quad , \tag{3.19}$$

One should take into account that due to sufficiently low photon densities of excitation sources the terms quadratic in $\boldsymbol{A}(\boldsymbol{r}, \mathrm{t})$ are negligible. In addition, the dipole approximation $\nabla\cdot\mathbf{A} = 0$, i.e. representing the Coulomb gauging, can usually be neglected too [141]. It is fulfilled as long as the spatial variations of the light wave is comparatively large in terms of the atomic scale. Furthermore, note that the sudden approximation allows a factorization of the wave functions of initial and final state into the wave function of the photoelectron $\varphi^{\mathbf{k}}$ and the remaining N–1 particle system which can be written in second quantization as

$$\Psi_f^N = A\varphi_f^{\boldsymbol{k}}\Psi_f^{N-1} = Ac_{\boldsymbol{k}}^{\dagger}\Psi_f^{N-1} \quad , \quad \Psi_i^{N-1} = A\varphi_i^{\boldsymbol{k}}\Psi_i^N = Ac_{\boldsymbol{k}}\Psi_i^N \quad , \tag{3.20}$$

where A is an antisymmetric operator taking into consideration for Pauli's exclusion principle, $c_{\boldsymbol{k}}^{\dagger}$ and $c_{\boldsymbol{k}}$ are fermionic operators which create and annihilate an electron, respectively. In addition, the final state wave function of the N–1 particle system is an excited state which is not an eigenstate of the N–1 particle system. Thus, the transition matrix element from Equation 3.18 can be formulated as

$$\langle \Psi_f^N | H_{int} | \Psi_i^N \rangle = \langle \varphi_f^{\boldsymbol{k}} | H_{int} | \varphi_i^{\boldsymbol{k}} \rangle \; \langle \Psi_f^{N-1} | \Psi_i^{N-1} \rangle \quad , \tag{3.21}$$

where $\langle \varphi_f^{\boldsymbol{k}} | H_{int} | \varphi_i^{\boldsymbol{k}} \rangle$ is the one electron transition matrix element and $\langle \Psi_f^{N-1} | \Psi_i^{N-1} \rangle$ is the N–1 electron overlap integral. With this notation, one can write the interaction Hamiltonian as

$$H_{int} = \sum_{f,i} \langle \varphi_f^{\boldsymbol{k}} | H_{int} | \varphi_i^{\boldsymbol{k}} \rangle \; c_{\boldsymbol{k}}^{\dagger} c_{\boldsymbol{k}} = \sum_{f,i} M_{f,i}^{\boldsymbol{k}} \; c_{\boldsymbol{k}}^{\dagger} c_{\boldsymbol{k}} \quad . \tag{3.22}$$

When putting this factorization into Equation 3.18 and supposing T=0 (initial state = ground state), one can get by the sum of $\omega_{f,i}$ over all possible states the total photoemission intensity

$$I(\boldsymbol{k}, E_{kin}) = \sum_{f,i} \omega_{f,i} \propto \sum_{f,i} |M_{f,i}^{\boldsymbol{k}}|^2 \sum_m |c_{m,i}|^2 \; \delta(E_{kin} + E_m^{N-1} - E_i^N - h\nu) \quad , \tag{3.23}$$

where $|c_{m,i}|^2 = |\langle \Psi_m^{N-1} | \Psi_i^{N-1} \rangle|^2$ is the probability that the N–1 particle system results in an excited state m after an electron is removed from the state i. It is appropriate to introduce the energy $\varepsilon = h\nu - E_{kin}$. With this, one can rewrite Equation 3.23 to

$$\begin{aligned} I(\boldsymbol{k}, E_{kin}) &= \frac{2\pi}{\hbar} \sum_{f,i} |M_{f,i}^{\boldsymbol{k}}|^2 \sum_m |\langle \Psi_m^{N-1} | c_i | \Psi_i^N \rangle|^2 \; \delta(\varepsilon + E_m^{N-1} - E_i^N) \\ &= \frac{2\pi}{\hbar} \sum_{f,i} |M_{f,i}^{\boldsymbol{k}}|^2 \; A^{<}(\boldsymbol{k}, \varepsilon) \quad , \end{aligned} \tag{3.24}$$

where $A^{<}(\boldsymbol{k},\ \varepsilon)$ is the one-particle removal spectral function which acts as a central quantity in the description of electron emission (and absorption) spectra. It can be written as

$$\begin{aligned} A^{<}(\boldsymbol{k}, \varepsilon) &= \sum_m |\langle \Psi_m^{N-1} | c_i | \Psi_i^N \rangle|^2 \; \delta(\varepsilon + E_m^{N-1} - E_i^N) \\ &= -\frac{1}{\pi} \; \mathrm{Im}\, G(\boldsymbol{k}, \varepsilon) \; f(\varepsilon, T) \quad , \end{aligned} \tag{3.25}$$

where $f(\varepsilon, T)$ is the Fermi-Dirac distribution function, whereas the spectral function is defined by the imaginary part of the one-particle Green's function $G(\boldsymbol{k}, \varepsilon)$ which is given by

$$G(\boldsymbol{k}, \varepsilon) = \frac{1}{\varepsilon - E(\boldsymbol{k}) - \Sigma(\boldsymbol{k}, \varepsilon)} \quad , \tag{3.26}$$

where $E(\boldsymbol{k})$ is the electron band dispersion and $\Sigma(\boldsymbol{k}, \varepsilon)$ is the complex self energy. The Green's function contains all contributions from many-body processes in photoemission, e.g. electron-electron or electron-phonon interactions. While the real part of the Green's function describes a renormalization of the energy dispersion, its imaginary part specifies

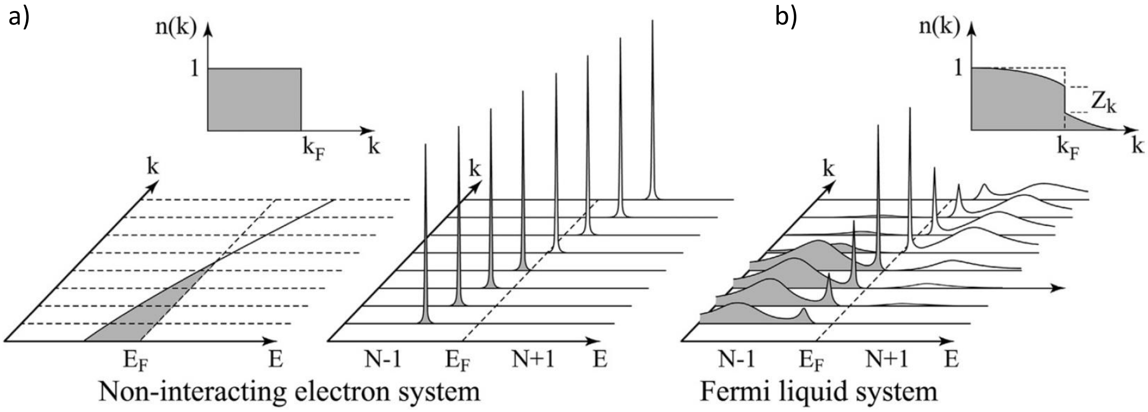

Figure 3.7: *Spectral functions: (a) A non-interacting electron system with a single energy band dispersing across the Fermi level. (b) An interacting Fermi liquid system with a coherent quasiparticle peak near the Fermi level and a broad incoherent spectral part at higher binding energies. In both cases the inset shows the corresponding ground state (T = 0 K) momentum distribution function n($\boldsymbol{k}$). Adopted from [145].*

the finite lifetime of excitations. One is able to gain both terms directly from an ARPES experiment from the momentum distribution curves (=spectra at constant energy).
A Fermi liquid (FL) will be now exemplarily used to show these relations and to introduce so-called quasiparticles which can be an important indication of such a system. Figure 3.7 illustrates the momentum-resolved electron removal and also electron addition spectra for a non-interacting and interacting electron system. In Figure 3.7 a) the case of a non-interacting electron system is shown. Here, one can see how the self energy disappears, resulting in a Green's function with a single pole, since the eigenfunction is a single Slater determinant, while removing or adding an electron with momentum $\boldsymbol{k}$ to the system produces a single eigenstate. Due to the single pole, the spectral function is given by a single δ-peak structure at an energy $E_{\boldsymbol{k}}$ with a certain dispersion, crossing the Fermi energy at $\boldsymbol{k}_F$. This leads to a sudden drop of the momentum distribution $N(\boldsymbol{k})$ at $\boldsymbol{k}_F$ (see Figure 3.7 a) inset). On the contrary, when interactions are switched on in a FL system and electrons have to be considered as so-called quasiparticles, this drop diminishes to a certain discontinuity with a characteristic trend caused by the quasiparticle weight $0 < Z_{\boldsymbol{k}} < 1$ (see Figure 3.7 b) inset). Related to the complex self energy $\Sigma_{\boldsymbol{k}}(\varepsilon) = \mathrm{Re}\Sigma_{\boldsymbol{k}}(\varepsilon) + i\mathrm{Im}\Sigma_{\boldsymbol{k}}(\varepsilon)$, this weight can be written as

$$Z_{\boldsymbol{k}} = \left(1 - \frac{\partial \mathrm{Re}\Sigma}{\partial \varepsilon}|_{E_{\boldsymbol{k},\mathrm{FL}}}\right)^{-1} \quad , \tag{3.27}$$

where $E_{\boldsymbol{k}} = Z_{\boldsymbol{k}} E_{\boldsymbol{k}}$, representing the renormalized energy. Since several electron-electron and electron-hole correlations appear due to the adding and removal of particles, the electrons can be regarded as being dressed by excited states, leading to an renormalization of the band energy to $E_{\boldsymbol{k},\mathrm{FL}}$ owing to the real part of $\Sigma_{\boldsymbol{k}}(\varepsilon)$ connected, amplified band mass m^* of the quasiparticle. Thus, the intrinsic lifetime $\Gamma_{\boldsymbol{k}} = Z_{\boldsymbol{k}}|\mathrm{Im}\Sigma|$, being linked to the imaginary part, becomes finite. Figure 3.7 b) shows the resulting photoemission spectrum. While for the non-interacting electron system the excited states are indicated by poles of the Green's function, the spectral function of the interacting FL system splits into a coherent and incoherent part. The coherent part is formed by a peak, the so-called quasiparticle peak. It is located at lower binding energies which becomes continuously sharper and gains more and more spectral weight towards $\boldsymbol{k}_F$ (characteristic for a FL system). In comparison, the incoherent part is a broad hump at higher binding energies, representing the dressed electrons by electron-hole pairs. Altogether, the sum rules for the spectral function can be written as

$$\int_{-\infty}^{+\infty} A(\boldsymbol{k},\varepsilon)\ \mathrm{d}\varepsilon = \int_{-\infty}^{+\infty} A_{coh.}(\boldsymbol{k},\varepsilon)\ \mathrm{d}\varepsilon + \int_{-\infty}^{+\infty} A_{incoh.}(\boldsymbol{k},\varepsilon)\ \mathrm{d}\varepsilon = 1 \quad , \tag{3.28}$$

$$\int_{-\infty}^{+\infty} A_{coh.}(\boldsymbol{k},\varepsilon)\ \mathrm{d}\varepsilon = Z_{\boldsymbol{k}} \quad , \tag{3.29}$$

$$\int_{-\infty}^{+\infty} A_{incoh.}(\boldsymbol{k},\varepsilon)\ \mathrm{d}\varepsilon = 1 - Z_{\boldsymbol{k}} \quad . \tag{3.30}$$

Since in ARPES experiments only the electron-removal part of $A(\boldsymbol{k},\ \varepsilon)$ is measured, the correct weight is given by using the Fermi-Dirac distribution function:

$$\int_{-\infty}^{+\infty} A(\boldsymbol{k},\varepsilon)\ f(\varepsilon,T)\ \mathrm{d}\varepsilon = n(\boldsymbol{k}) \quad . \tag{3.31}$$

Important aspects of quantitative PES analysis

In order to evaluate the obtained PES data correctly, one has to pay attention to a few quantitative aspects to avoid big or fundamental errors in their interpretation. One of the most essential aspects of PES is its inherent surface sensitivity which is a result of the strong interaction of the photoelectrons (mainly with other electrons) on their way to the sample surface. These processes are dominated by plasmon excitations due to the typical energy range of the photoelectrons and are (in a first approximation) only dependent on the valence electron density of the material which has approximately the same order for all solids. Thus, the inelastic mean free path (IMFP) of electrons, representing the distance electrons are able to travel through the solid before experiencing an inelastic collision, to a maximum extent which is independent on the solid type. S. Tanuma et al. studied the IMFP of electrons in several material classes and specified a prognostic equation, named as "TPP-2M" [148]:

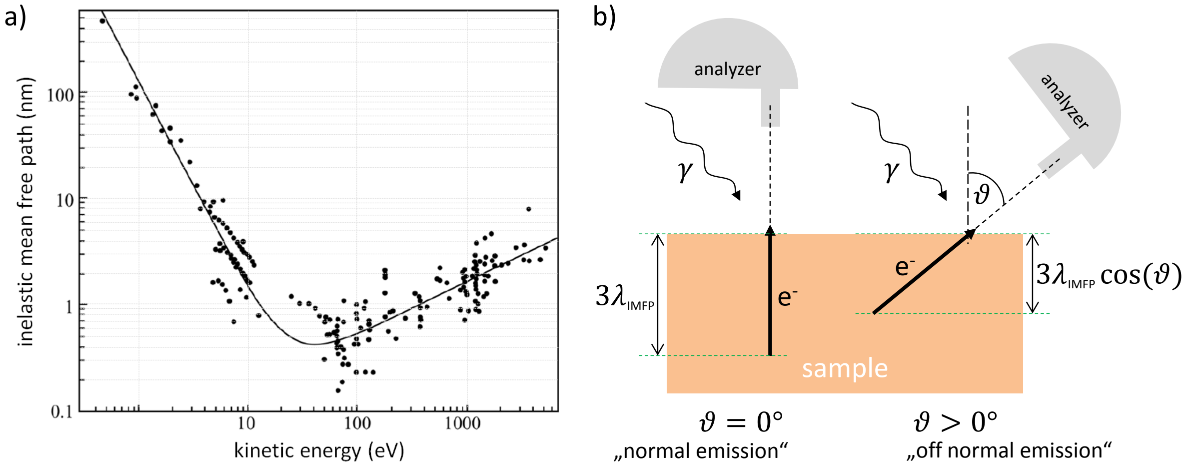

Figure 3.8: *(a) 'Universal curve': Electron inelastic mean free path plotted versus the kinetic energy of excited electrons in solids [149]. (b) Principle of depth profiling via PES: The effective IMFP of photoelectrons and consequently the information depth can be changed by variation of the emission angle* ϑ.

$$\lambda_{\mathrm{IMFP}} = \frac{E}{E_p^2\left\{\beta \cdot \ln(\gamma E) - (C/E) + (D/E^2)\right\}} \quad , \tag{3.32}$$

where E and E_p are the kinetic energy of the electron and the plasmon energy, respectively. The other parameters β, γ, C and D are material specific and consequently related to density, atomic or molecular weight, number of valence electrons per atom or molecule, and band-gap energy. Figure 3.8 a) shows the resulting kinetic energy dependent IMFP of electrons for several solid types. If logarithmic scales are used (as it is the case here), one can recognize a universal behavior of the IMFP of electrons by the course of the plotted data, depicted by the so-called "universal curve" (see solid black curve) [149]. Note that this curve is just a representative fit and can be located slightly different depending on the analyzed material. It has a local minimum at kinetic energies about 50 eV, while it shows an almost $\sqrt{E}$- and $E^{-1/2}$-dependence to higher and lower energies, respectively. However, within kinetic energies ranging from 1 eV to several keV, the energy dependent IMFP of electrons changes only in the order of a few Å up to several nm, accounting for the detection of electrons from only near surface regions. Assuming that electrons from a certain depth z are exponentially damped by scattering processes, the measured intensity of the photoemission signal is then given by

$$I(z) \propto \exp\left(-\frac{z}{\lambda_{\mathrm{eff}}}\right) \quad \text{, with} \quad \lambda_{\mathrm{eff}} = \lambda_{\mathrm{IMFP}}\cos(\vartheta) \quad , \tag{3.33}$$

where the z-direction is perpendicular to the sample surface. λ_{eff} is the effective mean free path of an electron which is emitted under a particular detection angle ϑ, including its longer penetration way. This situation is also illustrated in Figure 3.8 b). The maximum obtainable information depth z in a photoemission process is defined as

$$z = 3\lambda_{\text{eff}} = 3\lambda_{\text{IMFP}}\cos(\vartheta) \quad . \tag{3.34}$$

Here, about 95% of all emitted photoelectrons stem from a sample region between its surface and a depth of $3\lambda_{\text{eff}}$:

$$\frac{\int_0^z e^{-x/\lambda_{\text{eff}}}\ dx}{\int_0^\infty e^{-x/\lambda_{\text{eff}}}\ dx} = 0.95 \quad . \tag{3.35}$$

It becomes obvious that generally there are two options to vary the information depth, either one utilizes various excitation energies or changes the emission angle between sample surface normal and the orientation of the analyzer. These two techniques, also known as depth profiling, are of extreme importance, since one is able to determine the variation of a sample stoichiometry along its depth. A practical fact which should be noticed in measurements of photoemission spectra is the increasing background signal with decreasing kinetic energy (equal to increasing binding energy). This occurs because one part of the inelastically scattered electrons still reaches the analyzer and gets additionally counted in a spectrum.

This small discrepancy of background spectral weight must be corrected, especially if one wants to obtain quantitative informations from peak intensities in a photoemission spectrum. A common method for this purpose, which is also used for PES analysis in this thesis, was developed by D. A. Shirley [150]. It is based on the assumption that the background intensity at a certain energy E is proportional to the total number of all photoelectrons at higher energies $E^* > E$. With this, one is able to determine the background spectrum which is reflected by a convolution of a constant loss function with the corresponding intrinsic core level spectrum. Accordingly, the experimentally measured intensity of a core level spectrum $I^m(E)$ is a combination of an intrinsic core level spectrum $I(E)$ and the unknown background intensity $I^n(E)$ which is however definable by an iterative procedure:

$$I^{(n+1)}(E) = I^m(E) - I^n(\varepsilon)\,\frac{\sum_{E^*>E} I^m(E^*)}{\sum_{E^*>\varepsilon} I^m(E^*)} \quad , \tag{3.36}$$

where the measured spectrum $I^m(E)$ is appropriated for the starting point, whereas ε defines the limit of the background correction on the lower kinetic energy side. Generally, a few iteration steps ($n \leq 10$) are enough to produce an adequately converged spectrum. Once the background of the photoemission core level spectra is subtracted, one can simply identify the stoichiometry of the investigated sample, since their intensities, i.e., the corresponding areas below the spectrum line, are directly proportional to the relative element concentrations within the analyzed sample volume. In the case of a homogeneous sample volume, the intensity *I(E)* of the measured core level at a certain kinetic energy can be written as [151]:

$$I(E) = \sigma(h\nu)\ N\ F(h\nu)\ L(\gamma)\ \lambda_{\mathrm{IMFP}}(E)\ D(E)\ T(E)\ \cos\vartheta \quad , \tag{3.37}$$

where N is the atomic concentration of the relative element species, $F(h\nu)$ the photon flux, ϑ the emission angle of the photoelectron, and $D(E)$ and $T(E)$ are the detector efficiency and transmission function of the analyzer, respectively. Furthermore, $\sigma(h\nu)$ is the excitation energy dependent photoionization cross section of the electron and $L(\gamma)$ the asymmetry function related to the symmetry of its excited atomic orbital while γ is the angle between analyzer and incident light. Cross section- and asymmetry function-values are tabulated in the publications of J. J. Yeh and I. Lindau [152] or M. B. Trzhaskovskaya *et al.* [153]. Due to the fact that the electron analyzer is continuously operated in the constant energy mode, being a byword for measurements with fixed pass energy, the detector efficiency is independent of the photoelectron kinetic energy. Moreover, the transmission function of the utilized electron analysator EA125 by Omicron Nanotechnology was determined by P. Ruffieux *et al.* as $T(E) = E^x$ [154], where x has an approximate value of –1.

Since the detector efficiency can not be estimated and the photon flux is unknown, one does not have the ability to calculate absolute atomic concentrations of the elements A and B, but can calculate the relative atomic concentrations from background corrected photoemission intensities using the following relation:

$$R_{A/B} = \frac{N_A}{N_B} = \frac{I_A\ \sigma_B(h\nu)\ L(\gamma_B)\ \lambda_{\mathrm{IMFP}}(E_B)\ T(E_B)}{I_B\ \sigma_A(h\nu)\ L(\gamma_A)\ \lambda_{\mathrm{IMFP}}(E_A)\ T(E_A)} \quad . \tag{3.38}$$

Note that one should always keep in mind that the largest error bars in N_A/N_B stem from the errors of $\sigma(h\nu)$ and $L(\gamma)$, as their calculated values originate only from isolated atoms without any bonding properties which are actually essential parts in a solid. Therefore, the error bars are quite large and estimated to be up to 20%.

If available, one can also check precisely the ratio of element types in a sample by comparison of its measured spectra with those from well defined reference compounds.

3.3 *ex situ* characterization

Beside surface sensitive *in situ* characterization, there is the need for *ex situ* characterization in order to obtain a complete physical picture about the sample. For this, samples generally need to be removed from the ultra high vacuum (UHV). It can not be ruled out that this results in unintentional reactions with the sample. According to that, measurements must be rethought sometimes to avoid misinterpretations.

For instance, in terms of conductivity measurements, the sample surface is directly bond *ex situ* by Al wires. Here, the results can be falsified due to unintentional reactions of the surface with adsorbates or contaminations which cause a different resistance value

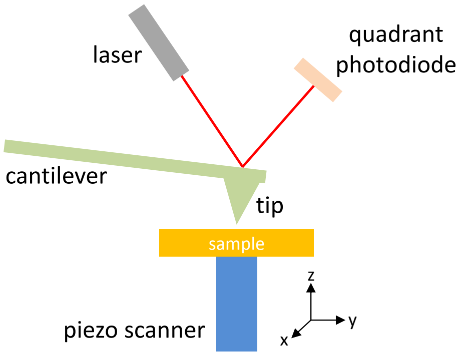

Figure 3.9: *Experimental setup of an atomic force microscope. Adopted from [155]. The interaction between tip and sample surface is measured by the cantilever deflection using the reflection of a laser beam. The scanning of sample surfaces are managed by piezo actuators.*

and accordingly high Schottky-barriers between contact electrode and film volume. Furthermore, some characterization methods can only be done *ex situ*, because they are not installed or just too complex to be used for *in situ* analysis. In the following, all *ex situ* characterization methods which are used in this thesis will be presented and discussed in detail.

3.3.1 Atomic force microscopy (AFM)

In order to characterize the sample surfaces *ex situ*, atomic force microscopy (AFM) was used as a complementary technique to the *in situ* utilized electron diffraction methods. It allows a direct mapping of the local real space topography of a sample by scanning its surface with a cantilever. A pyramidial tip located at the end of the cantilever is approached to the sample surface with only a few nanometers interspace. The situation is sketched in Figure 3.9. Here the tip interacts with the sample surface resulting in forces which cause a deflection of the cantilever. The deflection is registered by reflection of a focused laser beam on the backside of the cantilever. The reflection angle of the laser as a function of the deflection is detected by a spatially resolved photodetector. In turn, the deflection as a function of the lateral position of the tip gives information about the interspace between tip and sample surface, e.g. the surface topography. The measured force type depends on both the operating mode of the AFM and the applied tip. In this thesis all AFM measurements were done only in the non contact mode in which the distance between tip and sample surface is about 10-50 nm. In such distances, long-range forces like magnetic and electrostatic dipol interactions as well as attractive Van-der-Waals forces are dominant. Especially the last interaction type is here of vital importance, since nonmagnetic semiconducting silicon tips are used. In the case of two atoms with distance z the potential of the Van-der-Waals forces is given by the London term of the Lennard-Jones potential [136]:

$$V_{attr} = -\frac{C}{z^6} \tag{3.39}$$

The topography measurement itself was done in the so-called dynamic mode [156]. Here the cantilever is excited to a forced oscillation in z-direction as a damped harmonic oscillator near at its resonance frequency ω_0. While approaching to the sample surface the resonance of the cantilever is slightly mistuned by the force gradient $\frac{dF_z(\vec{r})}{dz}$ of the Van-der-Waals interaction:

$$\omega = \sqrt{\frac{k'}{m}} = \omega_0\sqrt{1 - \frac{1}{k}\frac{dF_z(\vec{r})}{dz}} \tag{3.40}$$

where k and m are the spring constant and mass of the cantilever that fix the intrinsic resonance frequency. By excitation of the oscillation at the resonance frequency a phase shift of about 90° consists between the exciting and resulting oscillation. The modulation of the resonance frequency by the force gradient leads also to a variation of this phase shift which is detected by the laser reflection. While lateral scanning of the sample surface a feedback loop regulates the z-position of the cantilever such that the phase shift preserves. This corresponds to a constant distance between tip and sample surface. From the plot of feedback loop signal against respective x-y-position one can directly get the height profile of the sample.
In AFM, the vertical resolution in height is defined by the high force sensitivity ($< 10^{-9}$ N) of the dynamic mode and therefore is of atomic scale. In contrast, the lateral resolution is much weaker since here the limiting factor is the radius of the tip [156]. Therefore, the maximum horizontal resolution is about two orders of magnitude lower than the vertical one, typically about 5–10 nm.

Additional to the surface sensitive measurements, several volume sensitive measurements techniques were used to characterize the samples in their structure, chemical composition and electrical or magnetic behavior which are described next.

3.3.2 X-ray diffraction (XRD) and X-ray reflectivity (XRR)

In addition to the surface sensitive LEED technique, the samples were analyzed by X-ray diffraction (XRD) [157]. Due to the long mean free path and wavelengths which are comparable to the interatomic distances in a crystal lattice, X-ray photons are predestined for diffraction of the whole sample, including substrate and film material. A copper anode acts as a X-ray source providing monochromated K_α radiation with a wavelength of $\lambda_{Cu} = 1.54$ Å. The diffraction condition is the same as in the case of LEED (see also subsection 3.2.2), except it is a three dimensional configuration, and will not be discussed here in more detail. Figure 3.10 a) shows a typical XRD setup performing a θ–2θ scan for locating the diffraction spots which are numbered by means of Miller indices (hkl) of the corresponding lattice planes. In such a scan, the sample is irradia-

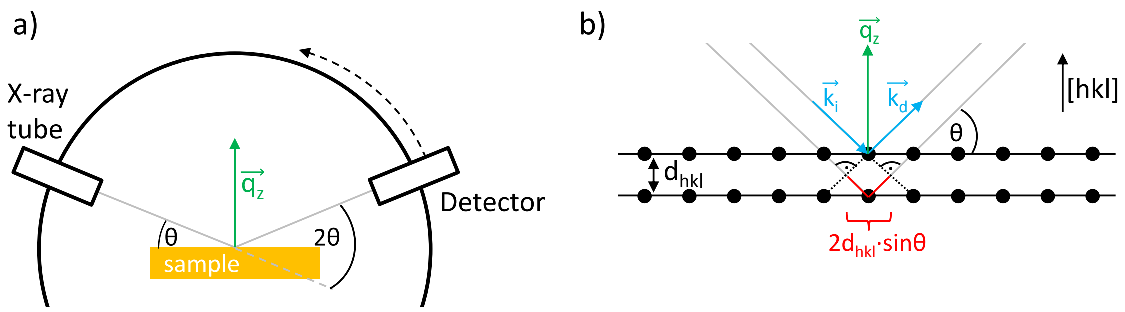

Figure 3.10: *Principle of X-ray diffraction: (a) Experimental setup of a X-ray diffractometer performing a θ–2θ scan. (b) The Bragg condition for constructive interference, schematically illustrated on a periodic crystal. $\vec{p_z}$ indicates the momentum transfer of the X-ray photon perpendicular to the sample surface.*

ted by X-ray photons and successively rotated by the angle θ. Since the angle of diffracted photons is kept equal to that of the incident ones, the detector has to be repositioned at every step. Figure 3.10 b) shows the Bragg condition for constructive interference in a periodic crystal. Here the sequence of identical atomic layers diffract the X-ray photons and provides perfectly sharp peaks by fulfilling the Bragg condition for constructive interference as

$$n\lambda = 2d_{hkl}\sin\theta, \tag{3.41}$$

where n is a natural number, λ the wavelength of the X-ray photons, d_{hkl} the distance between the atomic layers and θ the angle of incident and diffracted photons. With this, one can identify, for instance, the phase of a grown film and determine the quality and lattice parameter of that crystal. Worth mentioning, this scan is always done with respect to the out-of-plane normal vector of the sample surface corresponding to the growth direction of the film. To determine the correct lattice parameters, one should therefore pay attention to that sample direction. The more oscillating peaks on both sides of a main Bragg peak occur, the better the film quality can be considered. This is since the number of such peaks and their shapes depend directly on the film thickness and crystal defect density. These side peaks are the so-called Laue fringes and are useful aspects to examine the film quality. The intensity distribution of these fringes is described by the Laue function

$$I \propto \frac{\sin^2(N\vec{q}\cdot\vec{a}/2)}{\sin^2(\vec{q}\cdot\vec{a}/2)}, \tag{3.42}$$

where N is the number of lattice planes, $\vec{q}$ the reciprocal diffraction vector and $\vec{a}$ the translation vector of the lattice. Since the number of Laue fringes and the decrease of their distance to each other are proportional to N, one can easily estimate the thickness of the grown film.

Another well established scan that is closely related to a θ–2θ scan is the rocking curve scan. Commonly this scan is done after a θ–2θ scan, whereby the angle θ and the detector position 2θ is hold fixed at a certain Bragg peak diffraction angle. To obtain a rocking curve one has to operate the scan with changing the orientation of the sample by angle steps of $\Delta\omega$ around its equilibrium position. Therefore the rocking curve is defined as a ω scan at a fixed 2θ angle. With this, one is able to determine the mosaicity implicating the average extent of variously oriented crystalline domains in an imperfect crystal. To verify its degree, one determines the full width at half maximum (FWHM) of the rocking curve peak that gives an important information about the crystalline quality of a sample. As a rule of thumb, for high quality thin films a FWHM value of 0.05° should not be exceeded. For comparison, in single crystalline substrates this value is about one magnitude smaller. Therefore, one should aspire to a FWHM value as small as possible with regards to that of the rocking curve of the substrate to ensure best crystal quality.

Another method to study the crystal structure is X-ray reflectivity (XRR) which is operated in a grazing incidence geometry [157]. In XRR experiments one measures also in a θ–2θ geometry the intensity of the specular beam reflection, where θ is typically in the range of about 0°–4°. Starting with an angle of 0° of the incident X-ray photons, one observes total reflection since the refraction index of X-ray photons in solids is generally smaller than 1. By increasing the incidence angle a critical point for transmission is attained. For bilayer materials, as mostly analyzed in this thesis, shrinking intensity modulations after that critical angle are generated by interference effects of the reflected photon waves from the interface and surface of the sample. Since these paths of the waves are different in the material, minima and maxima are consequently created in intensity. These peaks are the so-called Kiessig fringes. As in XRD, one can use the distance between two Kiessig fringes to estimate the film thickness by using the Bragg diffraction condition described in equation 3.41. Usually in XRR spectra, the intensity is plotted versus momentum transfer q_z instead of diffraction angle θ. In this case the film thickness is then:

$$d_{film} = 2\pi/\Delta q_z, \tag{3.43}$$

where Δq_z indicate the distance between the maxima of the intensity modulation. As a standard tool, it is common to fit the measured data by employing a model accounting for the roughness of interface and surface as well as the film thickness. The incorporated transmission and reflection coefficients can be calculated from the refraction indices of each material which can be obtained from standardized databases. Therefore XRR is not only powerful to determine the film thickness but also to trace back roughnesses of interface and surface.

XRR is furthermore a complementary method to polarized neutron reflectometry although X-ray photons can not interact with the magnetization due to their missing magnetic moment. Therefore, XRR provides an opportunity to measure the chemical depth profile of a sample. The reflection formalism is equivalent to that of the nonmagnetic neutron reflectometry, discribed in subsection 3.3.3, whereas the underlying scattering processes for photons are different. Dominating in XRR is the so-called Thomson scattering, consisting mainly of nonresonant elastic scattering processes of photons off the electrons in the material. In contrast to neutron scattering, this interaction can not be supposed as punctual since the wavelength of the photons are in the same range as the dimension of the electron cloud. Thus, the forward directed atomic form factor $f_i(0)$ of the involved atoms, declaring the electron distribution inside the atomic shell, is introduced into the refraction index n [158]:

$$n = 1 - \delta + i\beta = 1 - \frac{\lambda^2}{2\pi} r_e \sum_i n_i f_i(0), \tag{3.44}$$

where λ is the X-ray photon wave length, n_i the particle number density of a atom sort i in the material, r_e the conventional electron radius, δ and β the dispersion decrement and absorption coefficient, respectively. Generally $f_i(0)$ is a complex variable as $f(0) = f_1 + if_2$, while the imaginary part f_2 is easily determined by X-ray absorption experiments. Then, using the Kramers-Kronig relation

$$f_1 = Z^* + \frac{2}{\pi} \int_0^\infty \frac{\varepsilon f_2(\varepsilon)}{E^2 - \varepsilon^2} d\varepsilon, \tag{3.45}$$

where Z^* is the atomic number including a relativistic correction, one is able to calculate f_1 for photons with an energy E. The real part f_1 is an analog measurand as the coherent nuclear scattering length of neutrons and adopts the value Z^* for high photon energies [158]. Therefore, the scattering length and the corresponding contrast ratio in the measured signal are proportional to the atomic number. With this, XRR is especially sensitive to heavy atoms sorts.

3.3.3 Polarized neutron reflectometry (PNR)

Instead of X-ray photons, one can use neutrons in reflectometry experiments to study the stoichiometric homogeneity, roughness, film thickness as well as chemical interdiffusion at buried sample interfaces. In the case of magnetite heterostructures, reflectometry measurements with neutrons are exceptionally useful for a magnetic depth profiling, since neutrons exhibit a magnetic moment which can interact with the sample magnetization. The theoretical and experimental basics of polarized neutron reflectometry (PNR) are dicussed below and mainly based on the publications [159] and [160]. The PNR measurements were done at the spallation source (ISIS) of the Rutherford-Appleton laboratory in the UK. All important values of the used neutrons are listed in Table 3.1.

In order to become familiar with PNR measurements, one has first to get knowledge about the nonmagnetic interactions and reflectivities of neutrons with matter. Due to

Table 3.1: *Fundamental values of neutrons [159].* μ_N *is the nuclear magneton* $e\hbar/2m_{proton}$. *Neutrons with the specified de Broglie wavelength and energy values were used at the beamline "Crisp":*

neutron mass m_n	$1.675 \cdot 10^{-27}$ kg
spin	± 1/2
magnetic moment μ_n	$-1.91\ \mu_N$
charge	0
wave length (@"Crisp")	0.5 Å – 13.0 Å
energy (@"Crisp")	0.5 meV – 320 meV

their neutral charge, neutrons do not interact via Coulomb forces with the atomic electron shell but rather via scattering processes by direct interactions with the atomic nuclei, dominated by the strong nuclear force. Since their wavelengths (a few Å) are much larger than the diameter of a typical atomic nucleus, the interaction can be described as a scattering process of a matter wave (de Broglie wave) by a punctual scattering center. Such interaction can be described by the so-called Fermi pseudo-potential which is given for an atomic nucleus at position $\vec{r}$ by

$$V(\vec{r}) = \frac{2\pi\hbar}{m_n} b\delta(\vec{r}), \tag{3.46}$$

where b is the nuclear scattering length of the nucleus. The out-going scattering amplitude of the neutron wave is isotropic in space, e.g., it is described by a spherical wave:

$$A_{sc} = -A_i b \frac{e^{-ikr}}{r}, \tag{3.47}$$

where A_i is the amplitude of the incident neutron radiation field. Therefore, b is a measure for the scattering strength of an atomic nucleus and can be written as [161]

$$b = b_{Nc} + \{I(I+1)\}^{1/2} b_{Ni} \hat{\sigma} \cdot \hat{I}. \tag{3.48}$$

The nuclear scattering length b consists of two contributions, the coherent (b_{Nc}) and incoherent scattering length (b_{Ni}). $\hat{\sigma} \cdot \hat{I}$ describes the interaction of the nuclear spin $\hat{I}$ with the spin of the neutron which is represented by the Pauli matrix $\hat{\sigma}$. Since the incoherent part leads to an isotropic background signal in reflectometry measurements, mainly resulting in a marginal influence on the signal to noise ratio, it is enough to measure the coherent scattering length in PNR experiments ($b = b_{Nc}$).

If a neutron is reflected on a real crystal under small angles without fulfilling the diffraction condition, it sees an average scattering potential of

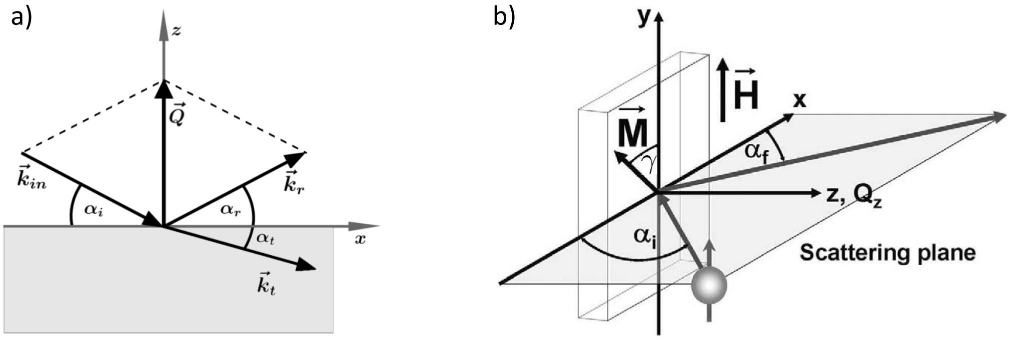

Figure 3.11: *(a) Schematic illustration of the reflection geometry. (b) Geometry in the case of PNR [162]. Here, the neutrons are collinear to the y-axis and polarized to the external applied magnetic field* $\vec{H}$*, while* γ *is the angle between the projection of the sample magnetization* $\vec{M}$ *and the external field.*

$$V = \frac{2\pi\hbar}{m_n}\frac{1}{V_0}\sum_j b_j = \frac{2\pi\hbar}{m_n}\rho b, \tag{3.49}$$

where V_0 is the unit volume and ρ describes the density of formula units of a material, while b is the sum of scattering lengths of all atomic nuclei j existing in such a formula unit. The product ρb is also referred to as scattering length density (SLD). In Table A.1 (see Appendix A) ρ and b for the relevant materials are tabulated. Note that the scattering length is a complex variable in which the imaginary part describes the absorption of neutrons by the atomic nuclei. Since it is for the relevant materials more than two orders of magnitude smaller than the real part and the absorption lengths are quite large (μm), it can be neglected for investigations of thin films [163].
Figure 3.11 a) shows the geometry of a common specular reflection experiment. Generally, the incident angle α_i is in the range of a few degrees and equal to the specular reflection angle α_r, while the momentum transfer vector $\vec{Q}$ is parallel to the sample surface normal and can be written as

$$|\vec{Q}| = Q_z = 2k\sin(\alpha), \tag{3.50}$$

where $k = |k_i n| = |k_r| = 2\pi/\lambda$ and λ are the absolute value of the wave vector and the de Broglie wave length of the neutrons, respectively. The specular reflection on an isotropic material can be described by the Schrödinger equation as scattering of a particle by a potential step in z-direction with the height of the Fermi pseudo-potential (see equation 3.46):

$$\left\{-\frac{\hbar^2}{2m}\Delta + V(z) - E\right\}\Psi(\vec{r}) = 0. \tag{3.51}$$

When inserting $k_t^2 = \frac{2m}{\hbar^2}(E - V)$ in equation 3.51, one can formulate:

$$-\frac{d^2\Psi(\vec{r})}{dr^2} - k_t^2\Psi(\vec{r}) = 0. \tag{3.52}$$

This describes a homogeneous electromagnetic wave equation. As in optics, one can define a refraction index n_n for neutrons:

$$n^2 = \frac{k_t^2}{k_0^2} = 1 - \frac{V}{E} = 1 - \frac{\lambda^2}{\pi}\rho b, \quad \text{with} \quad k_0^2 = \frac{2mE}{\hbar^2}. \tag{3.53}$$

Since the interaction and thus the product ρb of neutrons in this energy range with matter is small [163], one determines n as follows:

$$n \approx 1 - \frac{\lambda^2}{\pi}\rho b. \tag{3.54}$$

When solving the Schrödinger equation with the assumption of continuity of the wave function Ψ and its derivation $\Delta\Psi$, one gets a set of reflection and transmission coefficients (r and t) for the interface between two materials with the refraction indices n_j and n_{j+1}:

$$r = \frac{n_j \sin(\alpha_i) - n_{j+1}\sin(\alpha_t)}{n_j \sin(\alpha_i) + n_{j+1}\sin(\alpha_t)}, \qquad t = \frac{2n_j \sin(\alpha_i)}{n_j \sin(\alpha_i) + n_{j+1}\sin(\alpha_t)}. \tag{3.55}$$

The reflectivity which is the ratio of incident and reflected intensities, is defined as

$$R = |r|^2 = \left|\frac{n_j \sin(\alpha_i) - n_{j+1}\sin(\alpha_t)}{n_j \sin(\alpha_i) + n_{j+1}\sin(\alpha_t)}\right|^2. \tag{3.56}$$

The refraction index for most materials is smaller than 1 for neutrons as well as for X-ray photons. This generates a critical angle α_c (accordingly, a critical momentum transfer Q_c), while total reflection occurs only for smaller values. This critical point can be derived from the law of Snellius $\cos(\alpha_i) = n_1 \cos(\alpha_t)$:

$$R = |r|^2 = \left|\frac{Q_z - \sqrt{Q_z^2 - Q_c^2}}{Q_z + \sqrt{Q_z^2 + Q_c^2}}\right|^2. \tag{3.57}$$

Let us yet consider multiple reflections within the film. These will cause a phase shift on each reflection of $k_t \sin(\alpha_t) d$, where d is the thickness d of a single film. The phase shifted waves interfere with each other and result in an angle dependent oscillating reflectivity with decreasing intensity at higher Q_z values. The film thickness can be easily calculated by the reciprocal distance between two maxima δQ_z as follows:

$$d = \frac{2\pi}{\delta Q_z}. \tag{3.58}$$

Fundamentally, PNR utilizes the magnetic moment μ of a magnetic material which is given by its operator

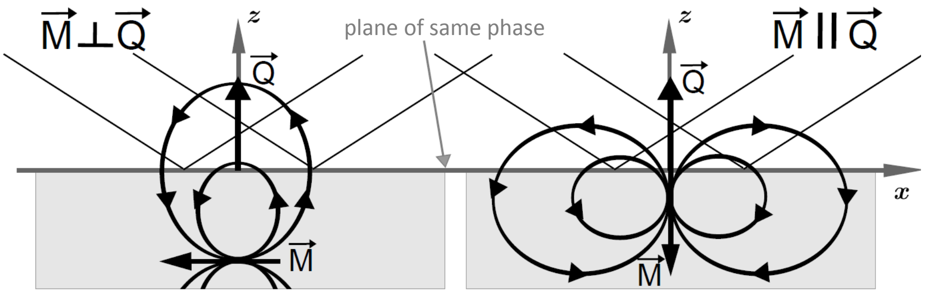

Figure 3.12: *Schematic illustration of the dipole field at specular reflection. If the magnetization is in the direction of the scattering vector, the dipole field components in the plane of same phase of the neutrons cancel each other out on average (see on the right-hand side). Thus, the magnetization in this direction has no effect on the reflection [164].*

$$\hat{\mu} = \mu_n \hat{\sigma}, \tag{3.59}$$

where $\hat{\sigma}$ is the Pauli spin-operator [159]. The interaction between the magnetic moment with a magnetic flux density $\vec{B}$ leads to the scattering potential of the magnetic dipole interaction. Its operator is defined as follows:

$$\hat{V}_m = -(\hat{\mu} \cdot \vec{B}). \tag{3.60}$$

The geometry of a PNR experiment is shown in Figure 3.11 b). The spin orientation of the incident neutrons, representing their polarization, is collinear to the external applied magnetic field $\vec{H}$ in y-direction. By the discontinuity of the potential which is in PNR the sum of the magnetic and Fermi pseudo-potentials, the neutrons are reflected by the sample and subsequently detected. The magnetic flux density inside a sample with the magnetization $\vec{M}$ is specified as

$$\vec{B} = \mu_0(\vec{H} + \vec{M}). \tag{3.61}$$

Since the external field $\vec{H}$ is equal in both, the sample and the region in front of it, it does not contribute to the reflection contrast. For that reason it can be neglected in the interaction potential of equation 3.60.

In general, the sample magnetization $\vec{M}$ is not fully aligned in the external field direction due to anisotropy effects. Components parallel to the sample surface normal and hence to the direction of the scattering vector Q_z have no influence on the neutron reflection. This is pointed out in Figure 3.12 by means of geometrical consideration of the dipole interaction. In case of parallel orientation (see right-hand side) of scattering vector Q_z and magnetization $\vec{M}$ direction, the dipole field components in the plane of same phase of the neutrons cancel each other out due to its symmetry. In contrast, if $\vec{M}$ is perpendicular to Q_z, the dipole field effectively contributes to the scattering potential [164]. Therefore, in PNR it is sufficient to consider only the projection of the magnetization onto the sample surface. This projection embed an angle γ with the neutron polarization axis as shown in Figure 3.11 b). The perpendicular component $M_x = |\vec{M}| \cos\gamma$ leads to a finite probability of a spin-flip which represents a rotation of the neutron spin (spin-up $\xleftrightarrow{\text{spin-flip}}$ spin-down). By inspection of such processes, one can get informations about the lateral direction dependence of the magnetization. Since magnetite samples have no distinct magnetically preferred direction within the film plane [165], the M_x magnetization component as well as the spin-flip signal are assumed to be irrelevant. Therefore, only the magnetization in direction of the external field $M_y = |M|$ effectively contributes to the magnetic dipole potential V_m which can be expressed as the eigenvalues of the interaction operator in equation 3.60:

$$V_m = \pm(\mu_n \cdot M). \tag{3.62}$$

Consequently one gets the overall potential V of the neutrons in the film (including the Fermi pseudo-potential):

$$V_m = \frac{2\pi\hbar}{m_n}\rho b \pm (\mu_n \cdot M) = \frac{2\pi\hbar}{m_n}\rho(b \pm b_m), \tag{3.63}$$

where b_m is defined as the magnetic scattering length which is directly proportional to the field direction aligned average magnetic moment μ of the film material:

$$\mu = \frac{\mu_n m_n}{2\pi\hbar} b_m, \tag{3.64}$$

The elementary magnetic scattering lengths of ferromagnetic transition metals are in the same range as the nuclear scattering lengths. For the resulting reflectivity, both magnetic and chemical contrasts in the depth profile contribute similarly intense. Because of the two possible collinear neutron polarization directions which are directed to the external field, one gets two different refraction indices:

$$n \approx 1 - \frac{\lambda^2}{\pi} N(b \pm b_m), \tag{3.65}$$

and consequently two critical angles:

$$Q_c = 2k\sin(\alpha_c) = \sqrt{16\pi N(b \pm b_m)}. \tag{3.66}$$

Therefore, a grown film acts like a birefringent crystal and provides two reflectivity curves owing to the two different refraction indices. The difference between these two curves is proportional to the film magnetization. The measured signal with neutron spin orientation being antiparallel to the external magnetic field is denoted as R^{++} or "spin-up" signal and that of the contrary spin orientation as R^{--} or "spin-down" signal. To analyze the sample magnetization, one uses the spin asymmetry SA which is the normalized difference of the two above-mentioned signals, representing the pure magnetic signal:

$$SA = \frac{I_{R^{++}} - I_{R^{--}}}{I_{R^{++}} + I_{R^{--}}}. \tag{3.67}$$

A collective work on all important aspects of neutron scattering on magnetic materials and especially on the necessary experimantal procedure of PNR measurements are given in [166].

3.3.4 Magnetometry (SQUID)

A very effective and sensitive technique to investigate the magnetic properties of a sample is magnetometry with a superconducting quantum interference device (SQUID). Moreover it is one of the very few instruments that one can use to characterize the overall magnetic moment of a sample in absolute units over a wide range of temperature and applied magnetic field. A SQUID magnetometer is made of a combination of superconducting materials and special junctions, the so-called Josephson junctions [167], to enable the detection of magnetic fields as small as 10^{-15} T. This corresponds to a resolution of 10^{-11} times the earth's magnetic field.

The functionality of a SQUID that is briefly presented in the following, is mainly based on the references [168] and [169]. A much more detailed description of this technique with many explanations and discussions is given in [170–172], whereas introductions to superconductivity and magnetic materials can be found in [173, 174].

A DC SQUID is a relatively simple constructed instrument, consisting of two Josephson junctions that are combined with each other to form a closed superconducting ring as shown in Figure 3.13 a). Such ring can only contain quantized magnetic fluxes that are n-times the magnetic flux quantum $\Phi = \frac{h}{2e} = 2.07 \cdot 10^{-15}$ Wb. Therefore, the latter represents the sensitivity limit of SQUID. By this hyperfine quantization one can use the SQUID as an extremely sensitive detector of the magnetic field variations, or technically speaking as a magnetic flux-to-voltage converter. By biasing the superconducting ring, the Cooper pairs are able to tunnel through the Josephson junctions, while the flow changes correspondingly if a magnetic field is applied. In detail, the phase difference $\Delta\varphi$ across each of the Josephson junctions gets varied and influences therefore the critical SQUID current. When increasing or decreasing the magnetic field gradually, the critical current oscillates, while a maximum or minimum arises if the flux through the ring is an integral or half-integral number of Φ, respectively. The applied flux can exhibit any value, unlike the flux comprised in a closed superconducting ring being an integral number. In experiments, rather the voltage than the current across the SQUID is measured, since it also oscillates by a gradual variation in magnetic field as it is shown in Figure 3.13 b). Due to these quantum interference effects one can use this as a digital magnetometer, where every "digit" describes one Φ. Hence, the SQUID is basically a flux-to-voltage converter that allows to transform a very small variation in magnetic flux into a voltage.

SQUID magnetometry is commonly used in a commercial magnetic property measure-

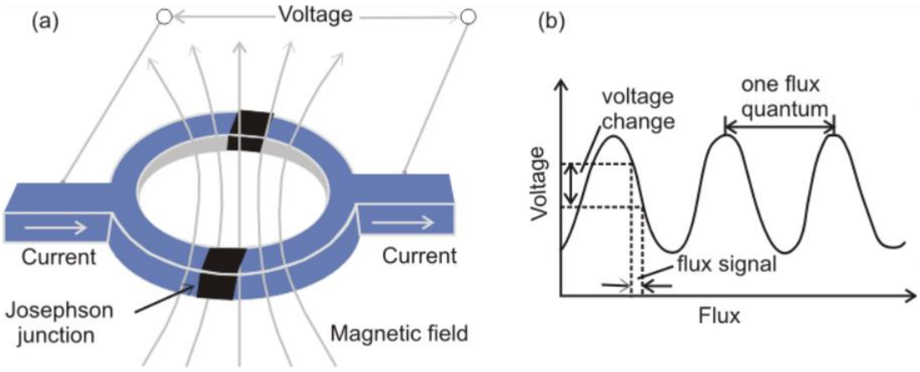

Figure 3.13: *DC SQUID: (a) Schematic construction of two Josephson junctions forming a superconducting ring. (b) Output voltage as a function of applied flux. A very small flux signal leads to a corresponding measurable voltage swing across the SQUID, adopted from [168].*

ment system (MPMS)[175]. Here, the sample is positioned in the center of a superconducting solenoid providing magnetic fields up to several T. To manage temperature dependent measurements in the range of 2 to 300 K, the sample space is filled up with helium at low pressure. The specified sensitivity of most MPMS is about 10^{-8} emu or 10^{-11} J/T which is equal to the saturation magnetization of a very small quantity of six billionth (6/1 000 000 000) mm^3 of iron or 10^{12} Bohr magnetons. To achieve the magnetic signal of a sample, one has to utilize a superconducting pick-up coil with 4 loops and a SQUID antenna. This superconducting circuit transfers the magnetic flux from the sample to a device that serves as a magnetic flux-to-voltage converter which is located away from the sample in the liquid helium. For read-out, the measured voltage must be additionally amplified by electronics. In operation, the sample is shifted up and down and creates an alternating magnetic flux in the pick-up coil leading to an alternating output voltage of the SQUID device. By adjusting the frequency of the read-out to that of the sample shifting (RSO, reciprocating sample oscillation), the SQUID system can reach the preeminent sensitivity as mentioned above.

3.3.5 Conductivity measurements (PPMS)

In order to investigate the electronic behavior of the thin film samples, one can measure their temperature dependent conductance via a commercial physical property measurement system (PPMS). Here, a 4-point probe is used to minimize the amount of errors caused by finite contact resistances. To implement this, electrical contacts are applied using a wire bonding technique where a thin aluminum wire is approached and welded by an ultrasonic pulse to the sample surface. By maintaining the van–der–Pauw geometry, which is illustrated in Figure 3.14, one is able to determine the specific resistivity of thin films too [176, 177]. Several conditions have to be fulfilled:

- The sample must be homogeneous and does not have any isolated holes.

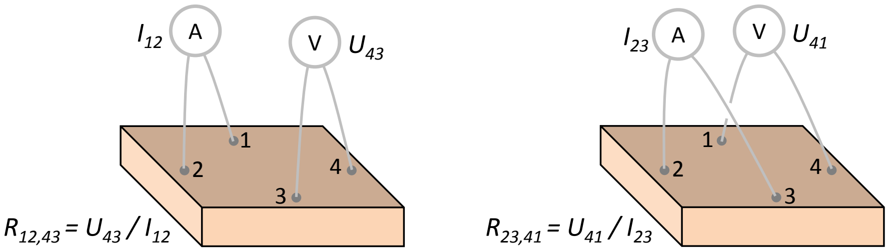

Figure 3.14: *Typical conductivity measurement performed in the van–der–Pauw geometry.*

- The film has to be flat and exhibits a constant thickness.
- The contacts must be fixed at the edges of the sample.
- The size of the contacts has to be negligibly small compared to the sample surface.

For a 4-point measurement, a current I_{12} is passed between the contacts 1 and 2, while the applied voltage between the contacts 3 and 4 is measured. Another measurement (independent of the previous one) is done for a current flow between contact 2 and 3, and an applied voltage at the contacts 4 and 1. Consequently the measured resistivities for these configurations are:

$$R_{12,34} = \frac{U_{34}}{I_{12}}, \qquad R_{23,41} = \frac{U_{41}}{I_{23}}. \tag{3.68}$$

By assumption of a squarish arrangement of the contacts on a homogeneous sample, the van–der–Pauw equation yields

$$e^{-(\frac{d\pi}{\rho}R_{12,34})} + e^{-(\frac{d\pi}{\rho}R_{23,41})} = 1, \tag{3.69}$$

where ρ and d are the specific resistance and the thickness of the film, respectively. But even though in the strict sense the contacts are not perfectly symmetrically and the contacts are not perfect, equation 3.69 is still a decent approximation to determine the specific sheet resistance. Since both resistivities are almost equal ($R_{12,34}{\approx}R_{23,41}{=}R$), the specific sheet resistance can be solved from the van–der–Pauw equation as

$$\rho_s = \frac{\rho}{d} = \frac{\pi}{ln2}R \approx 4.532R. \tag{3.70}$$

By measuring the temperature dependence of this specific sheet resistance $\rho_s(T)$, a lot of information about the sample can be gained, for instance if it is of insulating or metallic nature.

3.3.6 Transmission electron microscopy (TEM) and electron energy loss spectroscopy in scanning transmission electron microscopy (STEM-EELS)

The bulk sensitive transmission electron microscopy (TEM) is a widely used versatile characterization method that is able to image the crystal structure with the highest spatial and energy resolutions. Actually, TEM is very similar to a common optical microscope, except that one uses electrons instead of photons and glass lenses are replaced by electromagnetic ones. Additionally, TEM must be operated in vacuum to prevent scattering of the electrons with gas molecules. A typical setup of a TEM is illustrated in Figure 3.15 c). A thermal field emission gun generates electrons that are subsequently accelerated by high voltages of up to 300 keV onto the sample. Since these electrons have rather small IMFPs, the sample must be extremely thin (typically below 100 nm) to be electron transparent. But due to their small de Broglie wavelength, the limitation in resolution as defined by E. K. Abbe [178] is raised to the sub-nm region making TEM a powerful tool for investigations. In the standard TEM mode, shown in Figure 3.15 a) left, a thin sample is illuminated incoherently by almost parallel electron beams. After transmission through the sample, the electrons are projected by an objective lens (OL) through an OL aperture onto a florescence screen or camera for observation of the generated image. In such image most of the contrast details are produced by Bragg diffraction effects. By varying the exact position of the OL aperture, one is able to utilize either the unscattered electrons (bright field region, BF) or the diffracted electron beam (dark field region, DF) to create the final image. An adjuvant method for quantitative analysis is the reconstruction of the phase and amplitude of the exit wave functions by using a focus series. But even though it makes possible to get rid of imaging aberrations, there is still the issue of limited chemical sensitivity.

In comparison to this mode, scanning transmission electron microscopy (STEM) is a special enhancement concerning the potential for outstanding analysis. In principle a STEM is a TEM, except its electron source and detector are interchanged and therefore the run of the electron beam through the lenses and apertures is inverted. This is illustrated in a simplified view in Figure 3.15 a) right. Moreover a STEM is operated in a very similar way as a scanning electron microscope (SEM). Here, the generated electron beam from the source passes through the condenser lens (CL) aperture, that limits the convergence angle α, and gets highly focused by the aberration suffering objective lens onto the sample. This ultra-fine beam (only about 1 Å in diameter), representing an electron probe, is a demagnified image of the source and illuminates the sample coherently and can be used for scanning the sample. Transmitted electrons can be collected to create many different transmission patterns by various detectors that operate in a specific scattering angle range that are located behind the sample in the diffraction plane as shown in Figure 3.15 b). Basically, there are three crucial detector areas to create a STEM micrograph.

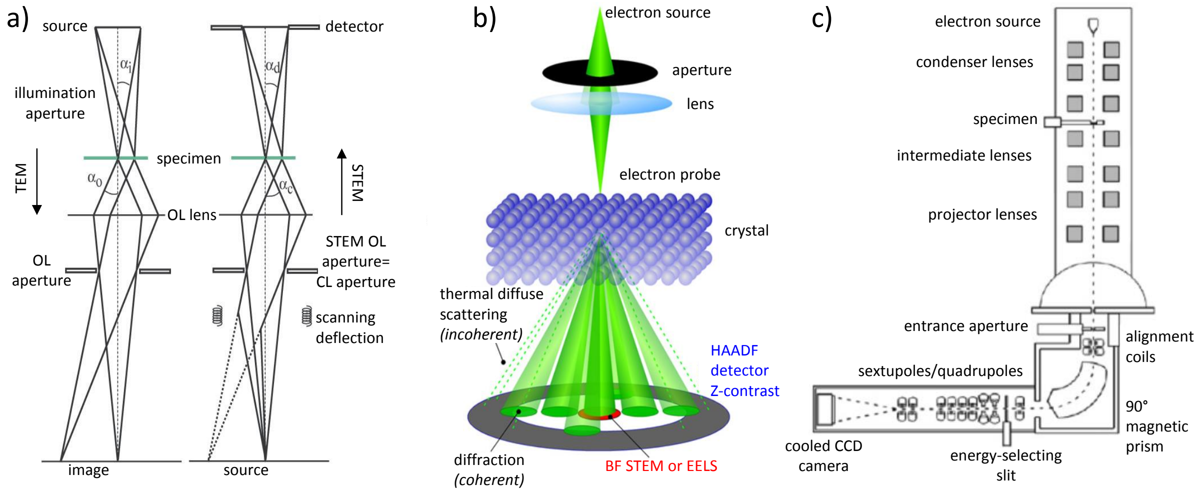

Figure 3.15: *Tansmission electron microscopy: (a) Schematic illustration of the courses of electron beams in TEM- (left) and STEM-mode (right) [179]. (b) Interaction of the focused electron beam with a thin sample resulting in detectable signals [180]. (c) A typical STEM setup with a post-column filter (EEL spectrometer, GIF), consisting of one 90° magnetic sector mounted as an attachment below the microscope camera chamber [181].*

The so-called BF detector works mainly in the central diffraction plane area where the detection angle $\alpha_d \leq \alpha$ and collects the intensity of the forward scattered beam, including un-scattered, elastically and in-elastically scattered electrons. In a BF image weak and strong scatterers are displayed bright or dark, respectively. Such an image can also indicate some phase contrast, however its interpretation is not trivial.

In contrast, the so-called annular dark field (ADF) detector operates between angles of $\alpha \leq \alpha_d \leq 3\alpha$ and collects the intensity of low-order diffracted beams including elastically and inelastically scattered electrons, while weak and strong scatterers are displayed dark or bright in an ADF image, respectively. But as in BF images, the phase contrast is often ambiguous.

The most important detector in STEM is probably the so-called high-angle annular dark-field (HAADF) detector that is designed to collect the intensity of high-order diffracted beams including mainly elastically scattered electrons and thermal diffuse scattering and works at $\alpha_d \geq 3\alpha$. Since the detection area is wide, the signal is usually incoherent, while weak and strong scatterers are displayed dark or very bright in a HAADF image, respectively. The phase contrast in such an image is actually easy to interpret, since due to the large scattering angles, the scattering amplitudes become proportional to the protons number Z of the corresponding atoms. This phase contrast, also known as the STEM Z-contrast, roughly scales with Z^2 and has the potential of excellent imaging type with information about the atomic element distribution in the sample.

Another great advantage of STEM is the availability of electron energy loss spectroscopy (EELS) signals from the BF detection area (see also Figure 3.15 b)) that one can obtain simultaneously with an atomically resolved HAADF image. Here, the primary electrons of the beam which interact with the shell electrons of the atoms, loose a specific amount of energy due to momentum transfer. In turn, this energy loss is element specific and depends on the electron excitation and its resulting energy difference. Therefore characteristic core loss edges, corresponding to inner shell excitations into the first available unoccupied states, show element specific features. Indeed EELS is similar to X-ray absorption spectroscopy (XAS), but except that it is able to provide spatial resolution in the atomic scale with the aid of STEM. By that combination of structure and chemistry, it is possible to analyze interfaces and defects in highest resolution. An EEL spectrometer is commonly a GATAN image filter (GIF) that is connected below the STEM camera chamber as demonstrated in Figure 3.15 c). The inelastically scattered electrons can be resolved into their EEL spectrum using a 90° electromagnetic prism, the so-called omega energy filter. The fine structure of the spectrum indicates not only chemical bonding but also chemical composition in the nanometer regime while the number of maximums as well as their distances to each other allows the determination of the oxidation state (= valency) of the atoms.

Of course, beside the transmitted electrons, there are a several more signals that are generated by the interaction of the electron beam with a specimen, such as Auger electrons, secondary and back-scattered electrons, characteristic X-rays and photons. Since these additional signals are not investigated in this thesis they are not discussed here.

Complete overviews and detailed explanations regarding TEM techniques and all resulting detectable signals can be found in [182–185].

4 Fe_3O_4 thin films on terminated ZnO substrates

This chapter describes various surface preparation methods of ZnO substrates and the growth of Fe_3O_4 thin films on these substrates by means of molecular beam epitaxy (MBE). It will be demonstrated which substrate preparation method is the most favorable one for producing well defined ZnO surfaces for further epitaxial thin film growth procedures. Special attention will be given to differentiation of the two types of ZnO substrate terminations, since both could be crucial for different interface properties in the Fe_3O_4/ZnO heterostructure system. It will be followed by the description of the physical properties of Fe_3O_4 thin films on ZnO substrates in order to figure out which combination of substrate preparation and termination is the most promising for constructing a potential spin injection heterostructure. Here, particular attention will be payed on the interface properties of the resultant Fe_3O_4/ZnO sample configurations regarding sharpness, differences in iron valencies and starting structure sequences at the interface which might be directly affected by the substrate surface quality and termination type.

4.1 Preparation of polar ZnO substrates

Accurately defined and smooth substrate surface is one of the most important requirements for the successful growth of thin films with thicknesses of only a few nanometers. Since one of the objectives of this thesis is to analyze possible differences in quality of the Fe_3O_4/ZnO heterostructures which could originate from the termination type of the used ZnO substrates, first of all equivalent preparation methods for achieving smooth surfaces of both polarities were strived. Here, mechanisms for the stabilization of the polar surfaces indicate a huge influence on the preparation process, because the intrinsic polarity of the ZnO crystal which is caused by the alternating positively and negatively charged zinc (Zn) and oxygen (O) layers, respectively, leads with increasing crystal thickness to a diverging electrostatic potential along the [0001] direction. Since this scenario represents an energetically unstable configuration, the potential has to be compensated by a rearrangement of charges that can basically occur as a reduction of positive or negative charges on the Zn or O polar surface, respectively, compared to the planes in bulk ZnO [186]. Mostly three different mechanisms are suggested in the literature for this. Beside the mainly theoretically argued possibility of a direct charge transfer between both surfaces [187, 188], the formation of imperfections in stoichiometry at the surfaces, e.g. by reconstructions and superlattices, are often mentioned. For instance, scanning tunnel microscopy (STM) experiments could verify that the stabilization of a non-contaminated Zn terminated surface is accompanied by the formation of triangular islands with sizes of about a few nm whose edges are completed with O atoms instead of Zn atoms [189, 190]. Another way to stabilize the surfaces is to a change the charge state via the adsorption of, e.g., H^+, CO or CO_2 [191]. Especially the latter mechanism plays a basic role in the below introduced ZnO substrate preparation methods.

Commercially available ZnO substrates are often labeled as "epi-ready" which means that these substrates are generally suitable for epitaxial film growth. However, such substrates after being cleaned by a triple organic solvent clean (TOSC) in an ultrasonic bath (first 15 min. with acetone, then next 15min. with isopropanol and finally another 15 min. with ethanol) show many less-than-1-nm-deep defects like scratches or bumps which are caused by the chemomechanical polish from the crystal supplier (not explicitly presented). Additionally, several impurities (some as big as a few nm) can be found on the substrate surfaces, indicating presence of dirt or most likely particles of the substrate itself. This suggests that the surfaces of both O-terminated and Zn-terminated "epi-ready" substrates are relatively rough and need some accurate additional surface preparation methods for a distinct improvement.

Basically there are three (combinable) substrate preparation methods. Beside a pure *ex situ* annealing treatment, a chemical etching treatment [192, 193] as well as a combination of *in situ* ion beam sputtering and subsequent annealing process [6] are popular methods. In this thesis a closer look at the first and the third surface preparation methods will be presented.

As a start, the procedure of the combined preparation method will be explained in detail. Note that this method was used in the extensive study of Fe_3O_4/ZnO samples in M. C. Paul's dissertation [6]. However here, a detailed characterization of the resulting surface morphology of the ZnO substrates was not performed, leaving their surface quality insufficiently determined and information about the interface properties of Fe_3O_4/ZnO heterostructures still dubious. A clarification of this will give the current thesis. The "epi-ready" ZnO substrate, independent of its surface termination type, was first cleaned by TOSC and afterwards loaded into the UHV chamber and resistively heated/degased at 750°C for 15 min. in pure O_2 (minimum purity 99.9995%) of a partial pressure of $5{\cdot}10^{-6}$ mbar to remove potential adsorbates and weakly bonded impurities from its surface. After this, the substrate was sputtered in a partial pressure of $3{\cdot}10^{-6}$ mbar of pure Ar (minimum purity 99.9995%) by Ar–ions at accelerating voltage of 1 keV and ion current of 50 μA at room temperature for 30 min., causing a milling of the topmost substrate layers including potentially remained surface impurities. However, after this step the substrate surface became much more rough. An undesired surface damage and possibly formed imperfections in stoichiometry caused by preferential sputtering can be recovered by a post–annealing treatment. Therefore, the substrate was additionally heated at 700°C for 50 min. in pure O_2 of a partial pressure of $5{\cdot}10^{-6}$ mbar. This recipe, representing the preparation type "S", for *in situ* sputtered and post–annealed ZnO substrates, is listed in Table 4.1 b), thus O- and Zn-terminated ZnO substrates

Table 4.1: *Preparation methods for polar ZnO substrates: (a) ex situ annealing treatment and (b) in situ sputtering and post–annealing treatment, labeled as preparation type ”A” and ”S”, respectively.*

a) *ex situ* annealing treatment: preparation type ”A”	
O-terminated surface	Zn-terminated surface
TOSC	
8 h in dry O_2 atmosphere at 1000°C	2 h in humid O_2 atmosphere at 980°C

b) *in situ* sputtering & post–annealing treatment: preparation type ”S”	
O-terminated surface	Zn-terminated surface
TOSC	
15 min. degas in $5{\cdot}10^{-6}$ mbar pure O_2 at 750°C	
30 min. Ar–ion sputtering (1 keV, $I_{ion} = 50\ \mu A$) in $3{\cdot}10^{-6}$ mbar pure Ar at RT	
50 min. surface recovery in $5{\cdot}10^{-6}$ mbar pure O_2 at 700°C	

prepared with this recipe will be marked from now on with ”SO” and ”SZn”, respectively.

In constrast, for the *ex situ* annealing preparation method both ZnO substrate terminations must be separately considered, since distinct differences between them arise. At first the preparation of the O-terminated substrate will be pointed out as already similarly documented in the dissertation of A. Müller [7] and in other publications [194, 195]. Here, the substrate was first cleaned by TOSC and afterwards heated in a crystal furnace at 1000°C for 8 hours under dry oxygen gas atmosphere (purity about 99.5%) that exhibited a flow of 1.1 liters/min.

In the case of Zn-terminated substrates reproducibly smooth surfaces could not be obtained by annealing treatments in dry oxygen gas atmosphere. This was also identified by S. Graubner *et al.*, who found more disordered and less well-defined stepped surfaces as compared to O-terminated substrates [194]. Density functional theory (DFT) calculations [190] and etching experiments with NaOH leach [196] showed that the Zn-terminated surface can be stabilized by chemo-adsorbed hydroxyl groups (OH^-). This is illustrated in a simplified picture in Figure 2.3 (see subsection 2.2.2) using its atomic configuration. Here, the OH^- groups saturate free bondings of the Zn atoms on the substrate surface and compensate their positive charge to a great extent. In contrast, on the other crystal side (O-terminated surface), OH^- groups can be formed in a H rich atmosphere by protonation of O atoms on the surface thus balancing the polar potential. Based on this model, an *ex situ* annealing treatment in humid, thus hydroxyl containing, O_2 gas atmosphere was applied on Zn-terminated ZnO substrates. To produce enough humidity, the O_2 gas (minimum purity 99.9995%) was directed through a gas-washing bottle with warm (∼50–60°C) distilled H_2O before flowing into the crystal furnace. The substrate was first cleaned by TOSC and afterwards heated at 980°C for 2 hours. After

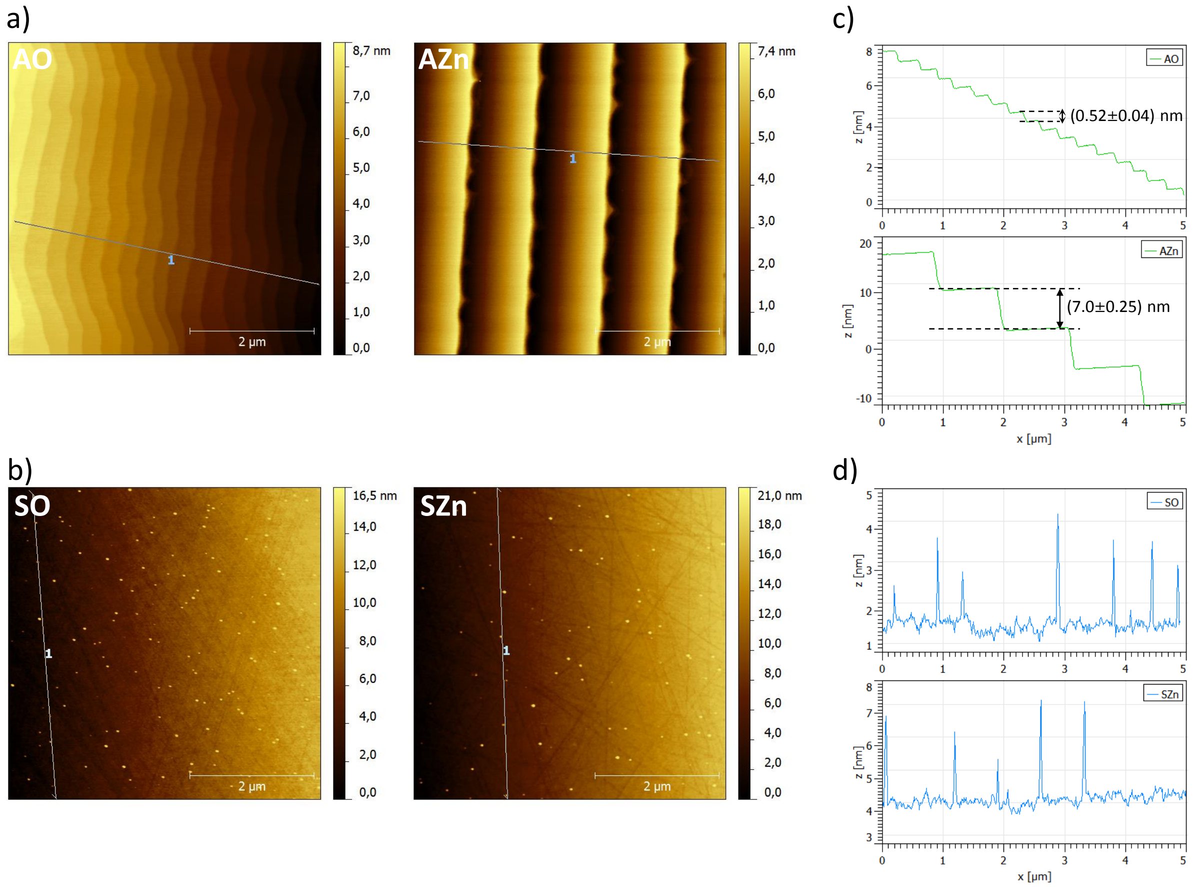

Figure 4.1: *AFM pictures (5x5 μm^2) of (a) ex situ annealed (AO, AZn) and (b) in situ sputtered and annealed (SO, SZn) ZnO substrates and the corresponding height profiles (c) and (d), respectively.*

switching off, the water was also cooled down to room temperature to avoid condensation in the crystal furnace.
These both recipes, representing the preparation type "A", for *ex situ* annealed ZnO substrates, are listed in Table 4.1 a), O- and Zn-terminated ZnO substrates prepared with preparation type "A" are marked from now on with "AO" and "AZn", respectively.

4.1.1 Surface morphology and structure

The surface quality of the prepared ZnO substrates will be now studied by AFM, RHEED and LEED. Figure 4.1 a) demonstrates the surface morphology of the *ex situ* annealed O-terminated (AO) and Zn-terminated (AZn) substrates measured with AFM. AO exhibits a long range ordered surface structure with homogeneously smooth and approx. 300-nm-wide terraces, resulting from the crystal miscut of <0.3°. Step height of (0.52±0.05) nm (shown in Figure 4.1 c)) is similar to the unit cell height of ZnO in [0001]-direction. In contrast, while AZn shows also a long range ordered surface structure with homogeneously smooth terraces, the terrace width and the step height are found to be about

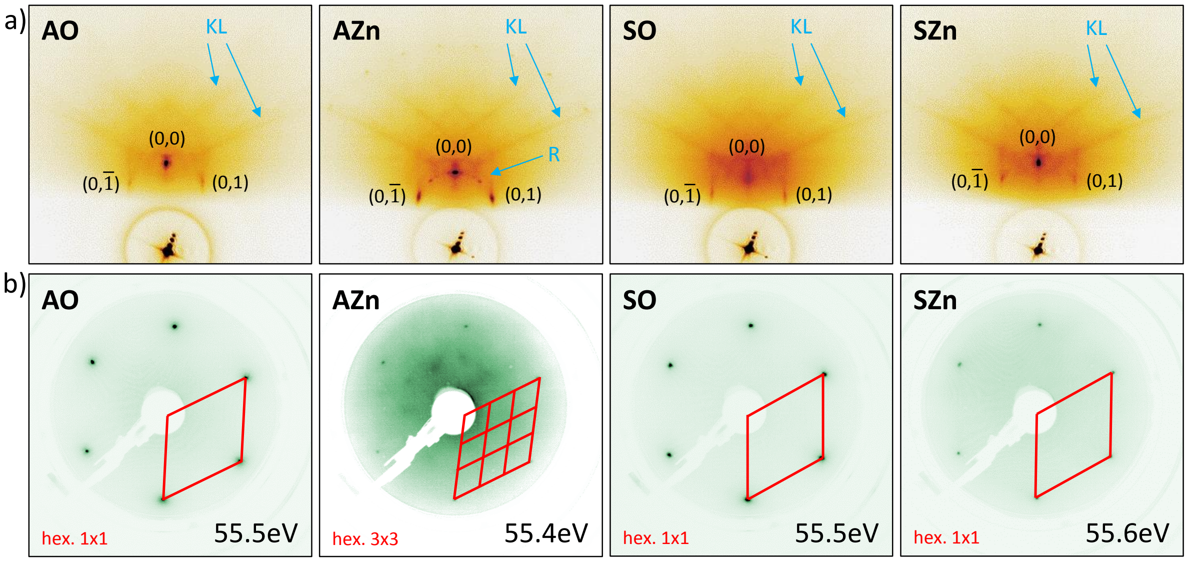

Figure 4.2: *(a) RHEED patterns in [$\bar{1}$10]-direction of ex situ annealed (AO, AZn) and in situ sputtered and annealed (SO, SZn) ZnO substrates. Kikuchi lines and surface reconstructions are indicated by "KL" and "R", respectively. (b) The corresponding LEED patterns, displaying the respective surface structures.*

1 μm and (7.0±0.25) nm, respectively. The latter is most probably caused by multiple step bunching. The terrace surface roughnesses of AO and AZn are only (0.05±0.01) nm and (0.5±0.1) nm, respectively, which evidence atomically flat surfaces.

Figure 4.1 b) demonstrates the surface morphology of the *in situ* sputtered and annealed O-terminated (SO) and Zn-terminated (SZn) substrates. Both SO and SZn show still many scratches as in the initial "epi-ready" state with no ordered terrace structure. Furthermore, some particles cover them indicating possible diffusion and accumulation of Zn atoms. The corresponding height profiles in Figure 4.1 d) reveal particles with 1–3 nm size and a surface roughness of about (0.3±0.1) nm in both cases. All four surface roughness values of the differently prepared ZnO substrates are listed in Table 4.2 for comparison. Indeed, additive sputtering and annealing cycles delete the surface scratches and particles, but also result in a high number of up to ∼1.5 nm deep holes in the surface and much higher roughness that can not be healed up even by a longer post–annealing treatment.

The RHEED patterns of AO, AZn, SO and SZn at room temperature are presented in Figure 4.2 a). All four substrates exhibit sharp Kikuchi lines, indicating well-defined crystal surfaces, as well as three sharp 0-order Laue spots. However, these Laue spots seem to be sharpest for AO and AZn, while they are slightly blurred for SO and SZn. Moreover, the background-to-Laue spot signal ratio is minimal for AO, medium for AZn and high for SO and SZn, signifying a graded surface quality. Interestingly, several additional spots occur between the main spots on the 0-order Laue circle of the AZn sample. These spots represent an additional reconstruction of the surface structure

Table 4.2: *Determined surface roughnesses $\sigma_{substrate}$ (by AFM) and lattice constants $a_{ZnO(0001}$ (by LEED) of ex situ annealed (AO, AZn) and in situ sputtered and annealed (SO, SZn) ZnO substrates.*

ZnO type	AO	AZn	SO	SZn
$\sigma_{substrate}$	(0.06±0.02) Å	(0.5±0.1) Å	(0.3±0.1) Å	(0.3±0.1) Å
$a_{ZnO(0001)}$	(3.25±0.11) Å	(3.27±0.13) Å	(3.26±0.12) Å	(3.26±0.12) Å

which could be generated by the absorption of OH^- groups on the Zn-terminated surface as a result of the prior humid oxygen annealing treatment.
For the following characterizations by LEED and XPS, only AO and AZn have to be degased in pure O_2 of a partial pressure of $3{\cdot}10^{-6}$ mbar at 800°C for a few sec. and additionally annealed 1 hour at 400°C, as this is the same procedure before the Fe_3O_4 growth. SO and SZn are already degased after their last preparation step (see Table 4.1 b)). The corresponding LEED patterns at E_e of 55.5 eV, are shown in Figur 4.2 b). The AO, SO and SZn substrates have the hexagonal 1x1 surface structure typical of ZnO. Only AZn is an exception, because it shows a surface reconstruction by a hexagonal 3x3 superstructure which is observable for E_e from 50 to 120 eV. Above 120 eV, this superstructure is not visible in LEED anymore and is replaced by a unreconstructed 1x1 surface structure. M. Valtiner *et al.* showed that similarly prepared Zn-terminated substrates have a hexagonal ($\sqrt{3}$x$\sqrt{3}$)R30 surface superstructure [193]. They argued that this is caused by adsorbed OH^- groups as well as O atoms and confirmed their results by DFT, however, the 3x3 superstructure was not mentioned. This difference could be due to the slightly different preparation methods. The absence of surface reconstructions on other three substrates could be a hint to the different potential mechanisms that are able to compensate the polarity of the crystal. The lattice constants determined by LEED are in good agreement with the literature value for bulk ZnO and listed in Table 4.2.

4.1.2 Surface inspection via XPS and termination identification by valence band analysis

A characterization by XPS can give a lot of information about existing adsorbates or other impurities on the prepared ZnO substrate surfaces. Note that the substrates were directly transferred after the LEED measurements into the PES chamber to retain their conditions. Figure 4.3 presents the XPS overview spectra of all four ZnO substrate types, measured at a surface sensitive 50°off normal emission (NE) angle using a monochromated Al K_α irradiation ($h\nu$=1486.6 eV). They show equivalently the characteristic photoemission peaks of ZnO, whereas the carbon C 1s peak is missing in all spectra indicating very clean substrate surfaces. Additionally, segregation of impurity atoms such as alkali metals, which are always present in small amounts in hydrothermally wound ZnO, can not be found on the studied surfaces in contrast to M. C. Paul [6]. This can

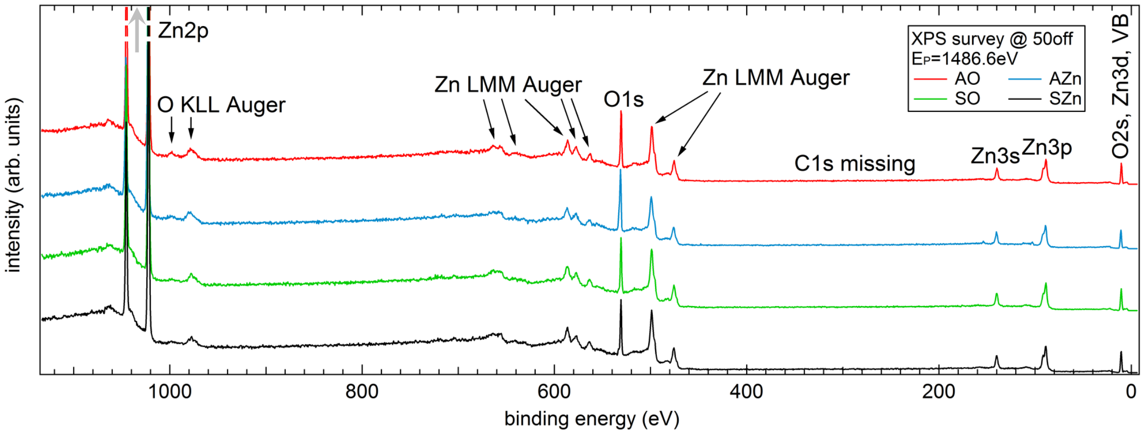

Figure 4.3: *XPS overview spectra of ex situ annealed (AO, AZn) and in situ sputtered and annealed (SO, SZn) ZnO substrates measured at 50°off NE. The characteristic photoemission peaks of ZnO are plotted, while the missing C 1s peak in all four spectra indicates clean surfaces without contamination.*

be a result of slightly different substrate preparation methods or different crystal purities from the diverse crystal suppliers.

Regarding the stabilization mechanisms of the differently terminated surfaces, an oxygen O 1s core level analysis can give information about present adsorbates like the above mentioned OH^- groups. In Figure 4.4 a) and b), the insets show a comparison between the substrates AO and AZn as well as between SO and SZn, measured at a rather bulk sensitive NE and at surface sensitive 50°off NE angles. All O 1s core level spectra are normalized to same spectral weight, while the peak positions are in good agreement with the literature value of 530.8 eV [21].

AO has almost symmetrical line shapes and identical trends for both emission angles. There are only small differences like minor increase of spectral weight at higher and lower binding energies due to a slightly broader peak shape at grazing emission angle. Comperable observations were done by C. Woell, who attributed it to a chemical shift in binding energy of the surface oxygen in ZnO by formation of OH^- groups due to protonation [191]. Note that adsorbed hydrogen extensively desorbes from the ZnO surface at about 300°C, which results in a 1x3 reconstruction at a clean O-terminated surface [196]. However, it is argued that the surface has a high chemical affinity for adsorption of H and H_2O which results in 1x1 surface reconstruction already after a few minutes in UHV conditions due to re-adsorption of H. Because process gases have always remaining H_2 and H_2O impurities and therefore a significant amount of such adsorbates, the stabilization of the 1x1 surface structure most likely occurs after every heating/degas process.

In contrast, AZn shows a clear asymmetrical shoulder located at higher binding energy of about 532.3 eV, while its spectral weight increases for the surface sensitive measurement (Figure 4.4 a)). This definitely indicates a local effect at the surface which can be assigned again to adsorbed OH^- groups. Other adsorbate types like H_2O and carbon

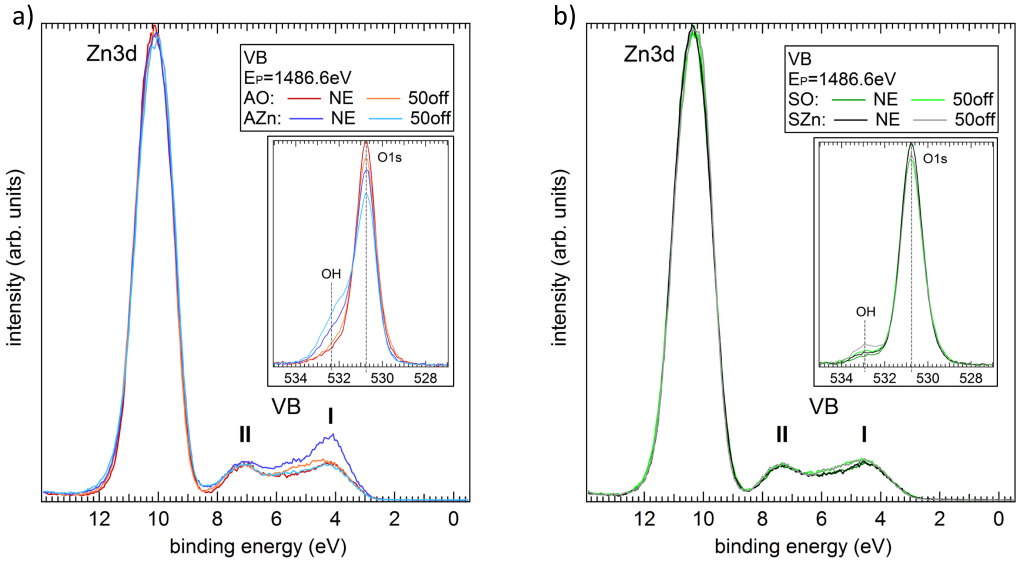

Figure 4.4: *XPS valence band (VB) spectra and O 1s core level spectra (see insets) of (a) ex situ annealed (AO, AZn) and (b) in situ sputtered and annealed (SO, SZn) ZnO substrates. Information about the polarity of a ZnO crystal can be obtained by means of the peak structure I.*

oxides (CO, CO_2) can be neglected due to the high degasing temperature and missing C 1s core level peak in XPS. Due to the annealing treatment with humid oxygen, the number of these adsorbates is much larger than in the case of AO. Moreover, not all of them can be solved by an additional *in situ* heating/degasing procedure, most probably owing to chemisorption with strong bonds to the surface. The remaining OH^- groups could be responsible for the observed 3x3 surface reconstruction in AZn (see Figure 4.2 b)). The chemical shift of the OH^- shoulder from the main O 1s peak of about 1.4 eV is in good agreement with the value of 1.2 eV determined by L. Zhang *et al.* [197].

Interestingly, SO and SZn show very different O 1s core level peak shapes, compared to AO and AZn. Both exhibit a shoulder at higher binding energy, whose spectral weight increases slightly at higher emission angle. The binding energy of the shoulder is about 533.0 eV. Such difference in the OH- binding energy values could be due to a small change of the substrate surface stoichiometry, possibly caused by the sputtering process, resulting in a different environment for the adsorbates. Note that sputtering always preferentially removes lighter atoms, e.g. O atoms more than Zn atoms in ZnO. The additional *in situ* heating process after sputtering, which was used to recover the topmost ZnO layers, seems to be uncompleted especially in terms of a stoichiometry balance. This situation can induce a small shift of the peak position of the O 1s shoulder to higher binding energy.

Beside the differences in chemical affinity for adsorbates as well as in the corresponding substrate preparation methods, it becomes apparent that the valence band (VB) spectra of both terminations significantly vary too. Figure 4.4 a) and b) demonstrates the VBs of AO, AZn and SO, SZn, respectively, measured at more bulk sensitive NE and at surface sensitive 50°off NE angle. The Zn 3d core levels of all four substrates are located at about 10.3 eV and are in good agreement with the results of R. T. Girard *et al.* [198]. All VB spectra from approx. 3 eV to 8 eV were normalized to the same spectral weight of the Zn 3d core level peaks. Here, the VB consists of two characteristic peak structures marked as peak **I** and peak **II**. While peak **II** is located at about 7.0 eV and mostly referred to hybridized Zn 4s, Zn 3d and O 2p states, peak **I** is fixed at about 4.2 eV and usually related to O 2p orbitals [199].

For the *ex situ* annealed AZn substrate, peak **I** has much more spectral weight at NE than at the surface sensitive 50°off NE angle, thus excluding adsorbates as possible reasons for this observation. This discrepancy is also documented in literature [21, 200]. For AO this behavior is hardly visible, while there is an additional slight increase of spectral weight between peak **I** and **II**. X-ray photoelectron diffraction (XPD) as a possible origin of this "inter-peak" was excluded experimentally in [200] and similar effect was found in other wurtzite structures [21]. This suggests that an intrinsic behavior of the polar crystal direction play the major role. Therefore, PES can be used to identify the termination of well defined *ex situ* annealed ZnO substrates.

Surprisingly, the *in situ* sputtered and annealed substrates SO and SZn do not show this difference between each other. However, both indicate an increase of the "inter-peak" spectral weight for the surface sensitive measurement. As in the case of their O 1s core level spectra, their VBs seem to behave very similar. It could be that the sputtering process not only destructs the substrate surface morphology but also equals somehow their polarity differences or, more likely, reconstructs the Zn-terminated to a pseudo–O-terminated surface. However, to determine a correct mechanism for such a transformation, a lot more detailed studies would be necessary. Consequently, this possible scenario will not be further discussed.

4.2 Fe_3O_4 thin film growth procedure

The growth of Fe_3O_4 thin films was performed in a MBE chamber of the UHV analysis system (equipment of the oxide lab at the chair EP4 in Würzburg), holding a base pressure of about $2{\cdot}10^{-10}$ mbar. As mentioned in subsection 4.1.1, the ZnO substrates need first to be degased before the actual growth process. To recall, AO and AZn are degased in pure O_2 of a partial pressure of $3{\cdot}10^{-6}$ mbar at 800°C for a few sec. and additionally annealed 1 hour at 400°C, whereas for SO and SZn only the temperature needs to be reduced from 700°C to 400°C after their last preparation step. The corresponding RHEED patterns just before growth are shown in Figure B.1 (see Appendix B.1).

Fe_3O_4 thin films with thicknesses of about 20nm were grown at 400°C by reactive deposition of ultra pure iron in an O_2 background atmosphere, while the iron was generated by evaporation of an iron rod (2 mm diameter, minimum purity of 99.99%) by an electron beam evaporator which is installed perpendicular to the substrate surface in a distance of approx. 25 cm. The Fe_3O_4 growth rate for an iron flux of (45±1) nA was calibrated

Table 4.3: *Growth parameters for homogeneous stoichiometry of the 20nm thick Fe_3O_4 films.*

used ZnO type	AO or AZn	SO or SZn
growth temperature	400°C	
iron flux	(45±1) nA	(45±1) nA
O_2 partial pressure first 8 min.	$3.5 \cdot 10^{-6}$ mbar	$5.0 \cdot 10^{-6}$ mbar
O_2 partial pressure next 40 min.	$2.2 \cdot 10^{-6}$ mbar	$3.6 \cdot 10^{-6}$ mbar
O_2 partial pressure last 1 min.	$7.0 \cdot 10^{-7}$ mbar	$6.0 \cdot 10^{-7}$ mbar
cool down to RT in	vacuum	

by XRR to 0.43 nm/min. During growth, the O_2 partial pressure was adjusted to get an optimum stoichiometry through the whole film. Especially at the initial growth process, a slightly higher O_2 partial pressure is necessary to prevent an incipient growth of FeO which has a better lattice match to ZnO than Fe_3O_4 [165]. Moreover, it is crucial to finish the growth process with a lower O_2 partial pressure to avoid the formation of Fe_2O_3 by over-oxidation at the film surface. Therefore, it is obvious that directly after the iron flux is turned off the Fe_3O_4 thin film has to cool down to room temperature in oxygen-free vacuum. All important parameters for the Fe_3O_4 thin film growth on the differently prepared and terminated ZnO substrates are listed in Table 4.3. Interestingly, the determined values of the O_2 partial pressure are a bit higher for the case of *in situ* sputtered and annealed ZnO substrates. Again, this can be a result of uncompleted recovery of the ZnO substrate surface stoichiometry, yielding to oxygen deficiency in the topmost ZnO layers. Such layers can act like O_2 extractors which cause a lack of oxygen in the first Fe_3O_4 layers forming mainly FeO. This can be compensated by a slightly higher O_2 partial pressure during growth. Depending on the ZnO substrate type used, the Fe_3O_4/ZnO heterostuctures are described from now on by an added "F" to the ZnO substrate notation as FAO, FAZn, FSO and FSZn.

4.3 Characterization of Fe_3O_4/ZnO heterostuctures

In the following, the MBE grown Fe_3O_4 thin films on the various ZnO substrates will be analyzed by a set of *in situ* and *ex situ* charakterization methods. However, the differentiation between the ZnO substrate termination types and preparation methods was not done in former studies, e.g. in [6, 7]. In contrast, in this thesis the influence of both factors on the physical properties of Fe_3O_4 thin films are investigated and particular attention is given to the resulting interface properties of the four different Fe_3O_4/ZnO heterostructures. First of all, the Fe_3O_4 film surfaces are analyzed by AFM, RHEED, LEED and XPS. Additionally, the bulk properties of the films are explored by XRD and XRR, while transport measurements are performed to determine their electrical behavior. Moreover, SQUID and PNR experiments are performed to characterize their

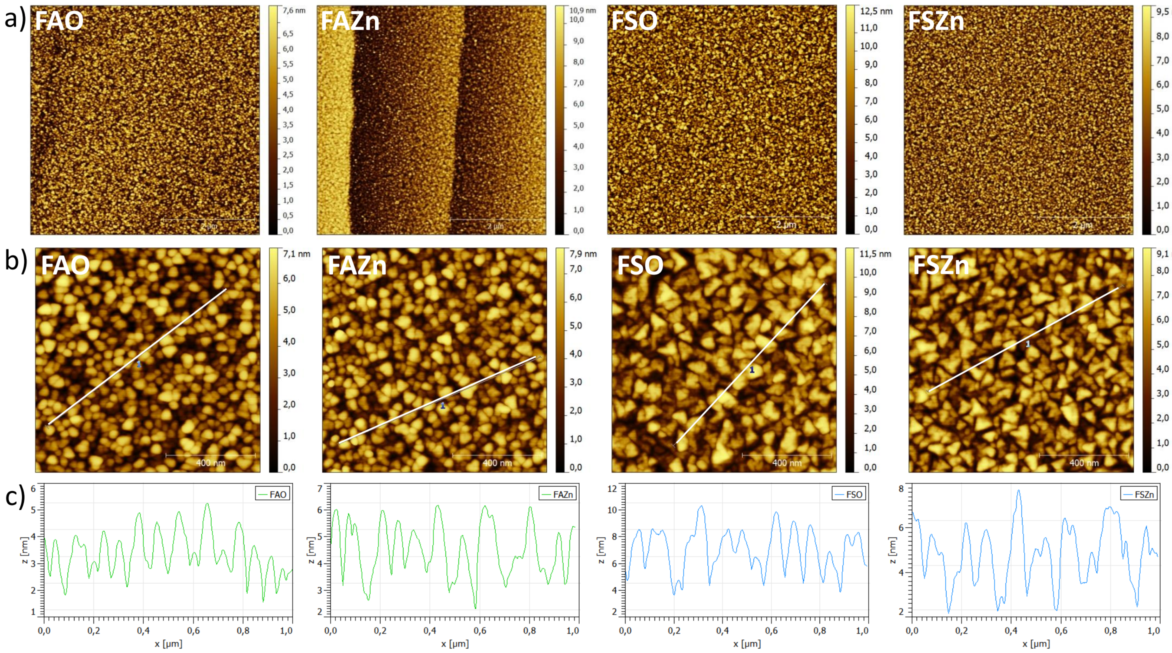

Figure 4.5: *(a) 5x5 μm^2 and (b) 1x1 μm^2 AFM pictures of 20 nm Fe_3O_4 films grown on ex situ annealed (FAO, FAZn) and in situ sputtered and annealed (FSO, FSZn) ZnO substrates with (c) the corresponding height profiles.*

magnetic properties. Finally, a TEM study is done to determine the microstructure of the Fe_3O_4/ZnO heterostructures in detail, especially in the interface region. A DFT study completes this chapter, identifying the most favorable interface structures for both terminations and confirming some of the TEM results.

4.3.1 Surface morphology and structure

During the growth of Fe_3O_4 films no RHEED oscillations on the (0,0) Laue peak of ZnO were observed. However, one large maximum showed up at the beginning and was followed by a slow decrease of the main spot intensity. This single maximum appeared after approx. 4 min., indicating possibly a wetting layer of 2 unit cells Fe_3O_4 on ZnO. Moreover, within these 4 min. the initial RHEED spots became smeared over to vertical thin stripes, signifying an increase of the surface roughness due to the deposited material. But no additional RHEED spots appeared here and the RHEED pattern became not completely diffuse, being a result of a quasi-epitaxial or rather approximatively pseudomorphous growth of the Fe_3O_4 lattice with the lattice constant of ZnO. The film grows in (111) direction on the ZnO substrate. Note that Fe_3O_4 with $a_{Fe_3O_4(111)}$=5.94 Å has about a two times bigger lattice constant than the ZnO surface $a_{ZnO(0001)}$=3.25 Å [25]. Therefore, the first Fe_3O_4 layers experience strong strain effects. During the further growth process (about 6 min. after start), additional smeared stripes appeared between the former spots. These inter-stripes correlate with the doubling of the sample surface

Table 4.4: *Determined surface roughnesses (by AFM) and lattice constants (by LEED) of the 20 nm thick Fe_3O_4 films with respect to the used ZnO substrate type.*

Fe_3O_4 film on ZnO type	FAO	FAZn	FSO	FSZn
roughness$_{AFM}$	(0.9±0.1) nm	(1.1±0.1) nm	(2.0±0.1) nm	(2.1±0.1) nm
$a_{Fe_3O_4(111)}$	(5.93±0.21) Å	(6.13±0.28) Å	(6.05±0.24) Å	(6.07±0.25) Å

lattice constant. With increasing deposition, all stripes converted into defined spots arranged in rows which can be explained by the relaxation from the former compressively strained to the bulk Fe_3O_4 lattice. The strong distortion of the first deposited unit cells causes a significant energy gain of the Fe_3O_4 lattice. At a critical film thickness a relaxation is energetically more favorable [137]. The RHEED spots arranged in rows are also a sign of transmission diffraction of electrons in three-dimensional surface structures, which indicates the characteristic island growth. The lattice constant of the Fe_3O_4 film is not exactly equal to the doubled lattice constant of ZnO. As a result, a relatively big lattice mismatch of

$$\frac{a_{Fe_3O_4(111)} - 2a_{ZnO(0001)}}{2a_{ZnO(0001)}} = -8.62\% \tag{4.1}$$

arises that activates the transition to island growth. Altogether, the formation of a pseudomorphous wetting layer with the following island growth implies a Stranski-Krastanov growth mode for Fe_3O_4/ZnO heterostructures (see also subsection 3.1.3).

Figure 4.5 a) shows 5x5 μm^2 AFM pictures of the 20 nm thick films grown on the differently prepared and terminated ZnO substrates. All four films have a homogeneous distribution of island accumulation over their entire surfaces. Due to the non-stepped surface of the used substrates for FSO and FSZn, there are no structures that show through the Fe_3O_4 film. Even FAO which has a substrate with steps of about 0.52 nm indicates no additional surface pattern, which is most likely caused by the relatively large film thickness and the much higher film surface roughness. Only FAZn still reflects the terrace structure of its substrate with step heights of several nm. A significant difference is found in the grain size of the agglomerated islands. Figure 4.5 b) demonstrates enlarged 1x1 μm^2 AFM pictures of the corresponding films. While FAO and FAZn exhibit almost only oval grain structures, FSO and FSZn have mostly just triangular grains. This could be induced by the various substrate preparation methods, even more than by different substrate surface reconstructions. The atomically flat substrate surfaces of AO and AZn could be responsible for a well defined Fe_3O_4 wetting layer in the initial growth process and makes the formation of such oval island favorable. In contrast, the surfaces of SO and SZn which are relatively destructed by the sputtering process, could prevent this and favor the development of triangular islands. Regarding their wetting layers, an analysis of very thin Fe_3O_4 films (1–2 nm) may give more information about the preferred island formation. The height profiles of the sample surfaces are given in

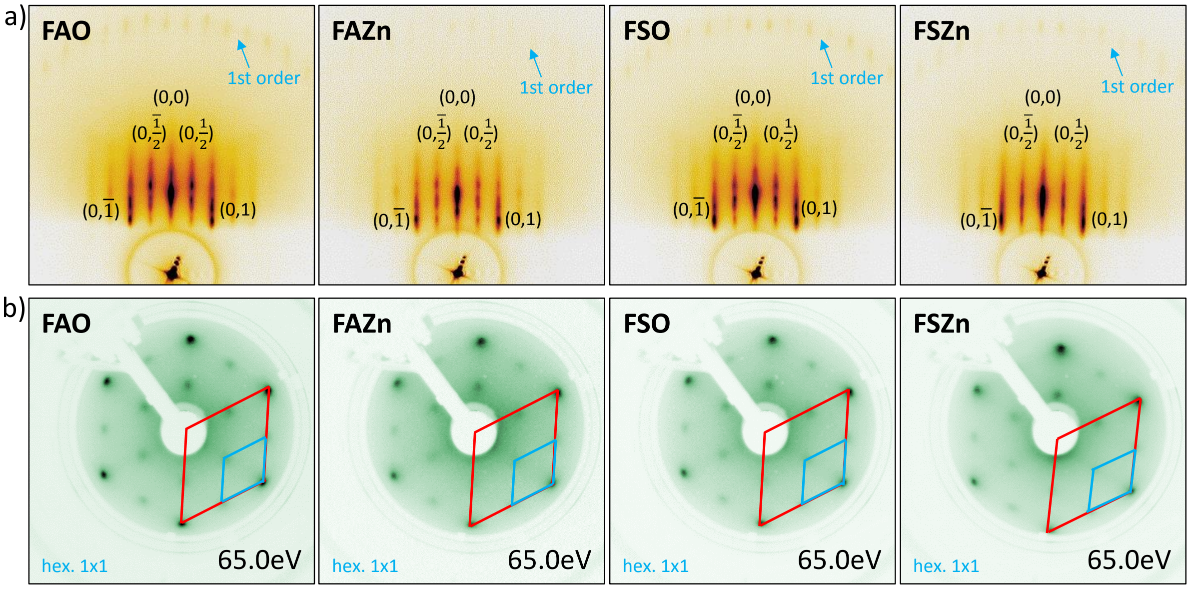

Figure 4.6: *(a) RHEED patterns in [$\bar{1}$10]-direction of 20 nm Fe_3O_4 films grown on ex situ annealed (FAO, FAZn) and in situ sputtered and annealed (FSO, FSZn) ZnO substrates with (b) the corresponding LEED patterns, displaying the respective surface structures.*

Figure 4.5 c). All grown films show grain sizes of about 50–100 μm, while the island heights seem to be minimal for FAO (~2 nm), medium for FAZn (~3 nm) and high for FSO and FSZn (~5–6 nm). Comparable island heights of Fe_3O_4 films with similarly prepared ZnO substrates are documented in other studies [6, 7]. Thus, it is possible that the substrate preparation method has a direct influence on the island shapes and sizes of the grown film. The corresponding film surface roughnesses determined by AFM are listed in Table 4.4.

Figure 4.6 a) presents the RHEED patterns of the 20 nm thick Fe_3O_4 films at room temperature. All RHEED pattern show similarly intense RHEED spots, while their background/Laue spot signal ratios are comparable to each other. Regarding their diffraction order, the spots are arranged in rows and slightly blurred, indicating the above-mentioned three-dimensional islands on the film surface. The additional Laue spots (0,$\bar{1}$/2) and (0,1/2) indicate the doubling of the surface lattice constant due to the bisection of the lattice constant in the reciprocal RHEED pattern. 1st order Laue spots are also visible for every grown film.

Beside the RHEED characterization, LEED measurements were performed to analyze the surface structure of the Fe_3O_4 films. Figure 4.5 b) shows the corresponding LEED patterns. No differences in the diffraction patterns are found between the four samples. All of them have a quasi-hexagonal 1x1 surface symmetry as expected for the (111) direction of the cubic Fe_3O_4. The red drawn rhombus represents the unit cell of the oxygen sublattice which is embedded into the iron sublattice of the spinel crystal structure by the double real space lattice constant. This is illustrated by the blue drawn rhombus.

The iron sublattice vector lengths of the four samples listed in Table 4.4 are in good agreement with the literature value of 5.94 Å.

4.3.2 Chemical depth profiling via X-ray photoelectron spectroscopy

Prior to the AFM measurement Fe_3O_4 samples were additionally analyzed *in situ* by XPS to prove the film stoichiometry regarding their iron/oxygen ratio. Figure 4.7 a) shows a typical XPS overview spectrum of one of the Fe_3O_4/ZnO heterostrutures, here FAO, measured at a photon energy of 1486.6 eV and rather bulk sensitive NE angle. All expected emission lines for Fe_3O_4 are present, while those for ZnO including the most intense Zn 2p core level peaks (at about 1045 eV and 1022 eV [201]) are not observable due to the 20 nm film thickness of Fe_3O_4 overlayer and escape depth of about 3.5 nm for the Zn 2p core level electrons. Surprisingly, in contrast, FAZn, FSO and FSZn have in their overview spectra very little spectral weight at the Zn 2p core level position (not shown) that could be a sign of Zn diffusion into the film. However, overview spectra of all samples measured at surface sensitive 50°off NE angles indicate no spectral weight at this peak position. Therefore, a potential increased diffusion of Zn near the interface region can not be excluded and needs to by studied by other characterization methods in more detail. Very clean film surfaces without contamination and the absence of carbon impurities in the film were confirmed by the missing C 1s core level peak in all overview spectra.

The film stoichiometry can be analyzed with the help of the Fe 2p core level. The different oxidation states of Fe can be determined by their charge transfer satellites in the Fe 2p spectrum. Figure 4.7 b) demonstrates the characteristic Fe 2p spectra of some relevant iron compounds. All of them have as final states the energetically shifted spin–orbit splitted core level peaks Fe $2p_{1/2}$ with $j = 1/2$ and Fe $2p_{3/2}$ with $j = 3/2$ (total angular momentum $j = |l \pm s|$), since the orbital angular momentum $l = 1$ and the spin of the unpaired electron in the 2p iron shell $s = 1/2$. The positions of these spin–orbit split core level peaks depend on the bonding type. A chemical bonding leads to an electron transfer which causes a change in the screening effect of the corresponding core potential. Therefore, the binding energy of all electrons of this atom shell shifts in comparison to the state without chemical bonding. This effect, also known as "chemical shift", is expressed by vertical lines at the Fe $2p_{3/2}$ peak positions.

Charge transfers (CTs) in the core levels of transition metal oxides often result in formation of additional satellite peaks, caused by another final state which can be induced by an electron transfer from the bonding O 2p orbitals of the O ligand shell (L) to the metal atom. Concerning not only the spin–orbit interaction but also the electron configuration, there are two possibilities for the final state $\Psi_f(N-1)$. On the one hand, if the ground state configuration $\Psi_f(N-1)$ is preserved after the creation of a 2p hole by photoemission, the final state is referred to as $3d^{n-1}L$ which results in the CT satellite

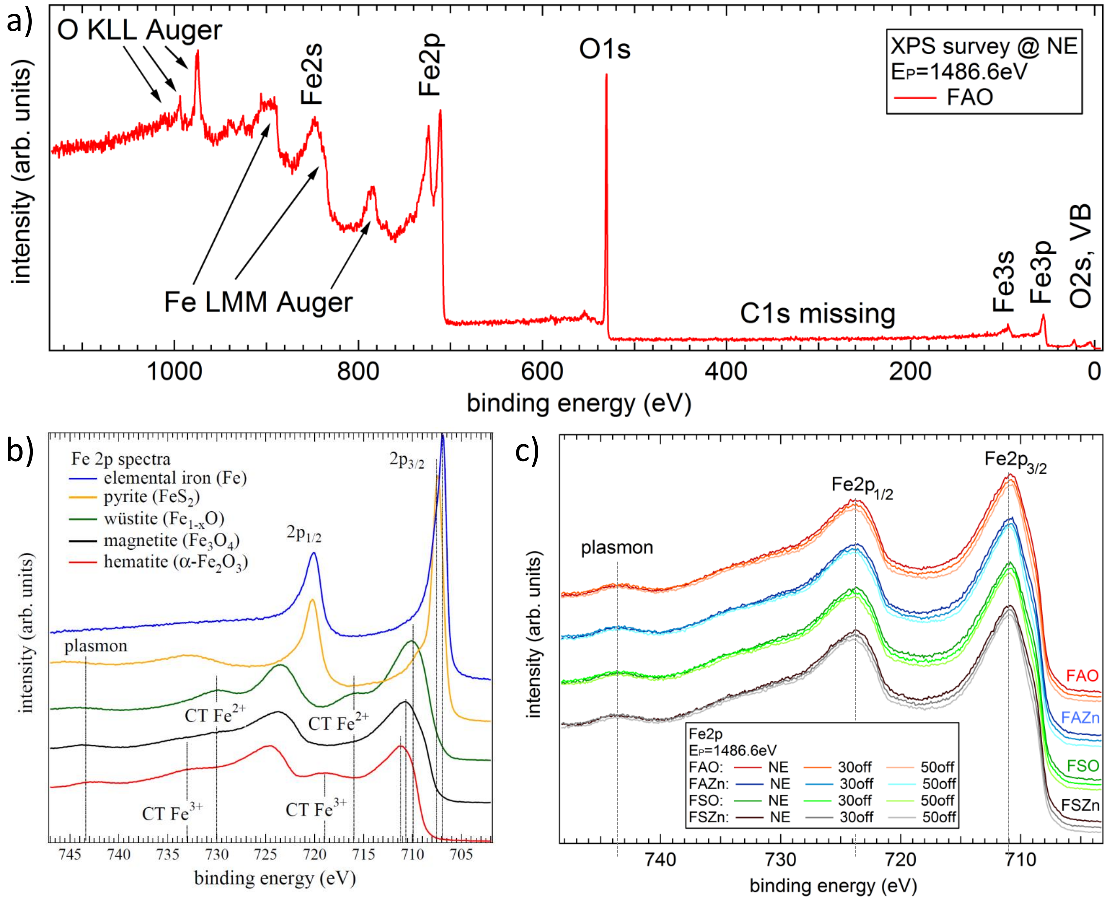

Figure 4.7: *(a) XPS overview spectrum of a 20 nm thick Fe_3O_4 film grown on an ex situ annealed O-terminated ZnO substrate (FAO) measured at NE. The characteristic photoemission peaks of Fe_3O_4 are labeled. (b) Reference Fe 2p spectra of different iron oxides including charge transfer satellite positions (labeled as CT Fe^{2+} and CT Fe^{3+}) of some relevant iron compounds. Adopted from [6]. (c) Chemical depth profiling of the various Fe_3O_4/ZnO heterostructures by analysis of their Fe 2p core level spectra measured at NE, 30° off and 50° off NE.*

peak. On the other hand, due to the photo-hole induced additional positive potential at the iron atom, a relaxation can be favorable too. This can happen by an electron transfer from the O ligand shell into the 3d shell of the Fe atom and is referred to as $3d^nL^{-1}$ which in turn describes the main peak. Here, the additional electron leads to screening of the photo-hole potential. This results in a different energy of the final state. In Figure 4.7 b) the CT satellite positions relating to the oxidation state of the iron atom are marked by vertical lines.

The energy shift of both final states is a specific feature of the different Fe valencies. Thus, the CT satellites enable an easy qualitative differentiation of the oxidation state of iron oxide samples. The satellites of the Fe $2p_{3/2}$ peak are fortunately located between the two spin–orbit split main peaks. For Fe_2O_3 and FeO with their main Fe $2p_{3/2}$ peaks at 711.0 eV and 709.5 eV, the additional local maxima (CT Fe^{3+} and CT Fe^{2+}) are loca-

Table 4.5: *Estimation of the film stoichiometries using a linear combination of reference Fe 2p core level spectra.*

heterostructure	FAO	FAZn	FSO	FSZn
NE	$Fe_{3.02\pm0.02}O_4$	$Fe_{3.05\pm0.02}O_4$	$Fe_{3.03\pm0.02}O_4$	$Fe_{3.05\pm0.02}O_4$
30°off NE	$Fe_{3.02\pm0.02}O_4$	$Fe_{3.04\pm0.02}O_4$	$Fe_{3.03\pm0.02}O_4$	$Fe_{3.03\pm0.02}O_4$
50°off NE	$Fe_{2.97\pm0.02}O_4$	$Fe_{2.96\pm0.02}O_4$	$Fe_{2.97\pm0.02}O_4$	$Fe_{2.95\pm0.02}O_4$

ted at about 718.8 eV and 715.5 eV, respectively [202]. In the case of Fe_3O_4 the spectral weights of both CT satellites combine to a smooth broad minimum between the two main peaks. This distribution of spectral weight is a characteristic feature of stoichiometrically grown Fe_3O_4 samples.

Figure 4.7 c) shows the performed XPS depth profiling of the four Fe_3O_4/ZnO heterostructures. For every sample, the Fe 2p core level spectra, measured at NE, 30°off and 50°off NE, indicate no additional local maxima between the two main peaks. Thus, the grown Fe_3O_4 films seem to be stoichiometric on their surface and in films depths of a few nm which is based on the maximum information depth of XPS. A quantitative estimation of the film stoichiometry can be done by a numeric fit of a linear combination of reference Fe 2p spectra of FeO, Fe_3O_4 and Fe_2O_3 from Figure 4.7 b) to a measured spectrum. Values for the film stoichiometries obtained by this procedure are tabulated in Table 4.5. The specified deviations from the ideal stoichiometry Fe_3O_4 are in good agreement with the values determined in former studies [6]. In particular, the marginally over-oxidized topmost film surface region can be found in these four samples too.

In addition, O 1s core level as well as valence band (VB) spectra were measured at NE for each sample. Figure 4.8 a) demostrates the O 1s peaks which are normalized to same spectral weight. The peak positions are all at 530.3 eV which is similar to the value of a Fe_3O_4 single crystal [202]. The peaks are almost symmetric and show no additional shoulder. Regarding the O 1s peak, all four films seem to be equivalent in bulk. The VB spectra which are normalized to the same spectral weight from 0 to 8 eV binding energy, are displayed in Figure 4.8 b). Interestingly, FAZn, FSO and FSZn films show the appearance of the Zn 3d peak at 10 eV [201]. As it was mentioned above, the same films also show a small spectral weight at the Zn 2p core level peak in the overview spectra. The reason why the Zn 2p core level peak in the overview spectra is suppressed can be explained with the very high background signal at higher binding energies due to secondary scattered photoelectrons. Only FAO has no additional spectral weight at 10.0 eV. The little increase of this peak for FAZn is probably caused by the very high substrate terrace steps which can be responsible for effectively thinner film regions too. In combination with the information depth of XPS, Zn core level photoelectrons might become detectable and lead to a small peak. In contrast, FSO and FSZn have significant Zn 3d core level peaks. Since these two exhibit no high substrate terrace steps, the Zn 3d signal must have a different reason. As mentioned for the overview spectra, Zn atoms

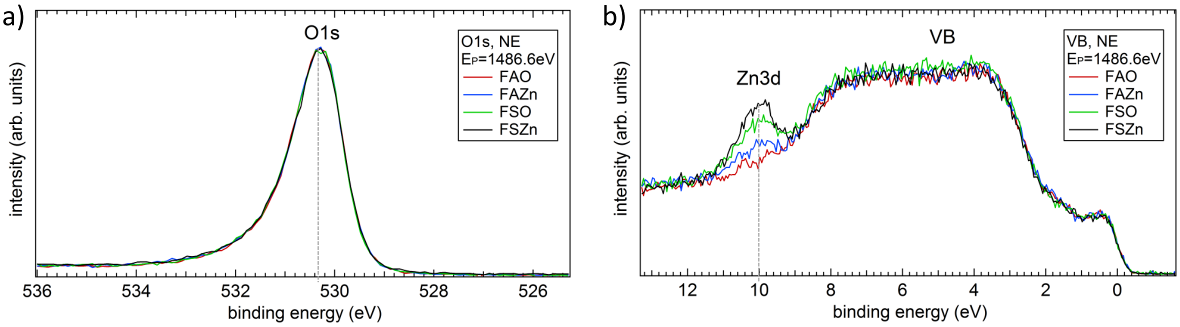

Figure 4.8: *(a) XPS O 1s core level and (b) valence band spectra of the various Fe_3O_4/ZnO heterostructures, both measured at normal emission. The valence band spectra indicate diffusion of Zn atoms into the Fe_3O_4 film for most of the Fe_3O_4/ZnO heterostructures.*

could diffuse into the film material. This hypothesis is confirmed by the observation of small particles on the *in situ* prepared substrates (see Figure 4.1 b)). These particles can be agglomerated Zn atoms which are diffused and built into the Fe_3O_4 lattice. However, this process seems not to reach the topmost film layers, because the Zn 3d peak is missing for all films measured at 50°off NE. Therefore, a potential intermixing of Zn atoms at the Fe_3O_4/ZnO interface needs to be considered when characterizing the samples by other volume sensitive analysis methods.

4.3.3 Characterization by X-ray diffraction and X-ray reflectivity

After the *in situ* analysis by XPS, the bulk properties of the Fe_3O_4/ZnO samples were characterized via XRD and XRR. The XRD scans were performed by a "Bruker D8 Discover" X-ray diffractometer in a 2θ angle range of 10° to 90° and are illustrated in Figure 4.9 a). All samples exhibit the two intense ZnO substrate Bragg peaks and the corresponding add-peak (β) which is generated by the Cu K_β irradiation. Since the 2θ scan probes along the c-axis of the sample, the expected Bragg peaks of the film are along the (111) direction of Fe_3O_4. Every sample shows the three relevant Fe_3O_4 Bragg peaks along (111). All peak intensities between the various samples are comparatively similar due to their same film and substrate thicknesses. The peak positions are in good agreement with other previous studies [6]. However, to determine the crystalline quality of the grown films, ω–scans were performed at the Fe_3O_4(222) Bragg peak. This type of scans are also known as "rocking curve" (RC) scans which is demonstrated in Figure 4.9 b). The RC scans are fitted by a Gaussian and afterwards the full width at half maximum (FWHM) value is identified. All samples have almost the same value of about FWHM=0.04°. Generally, FWHM values smaller than 0.05° are evidence of high crystalline quality of the grown thin films. Such sharp RC scans are mostly caused by low mosaicity, less dislocations and weak curvatures in the perfect parallelism of atomic planes in the film. Unfortunately, these values are still not good/small as those for some

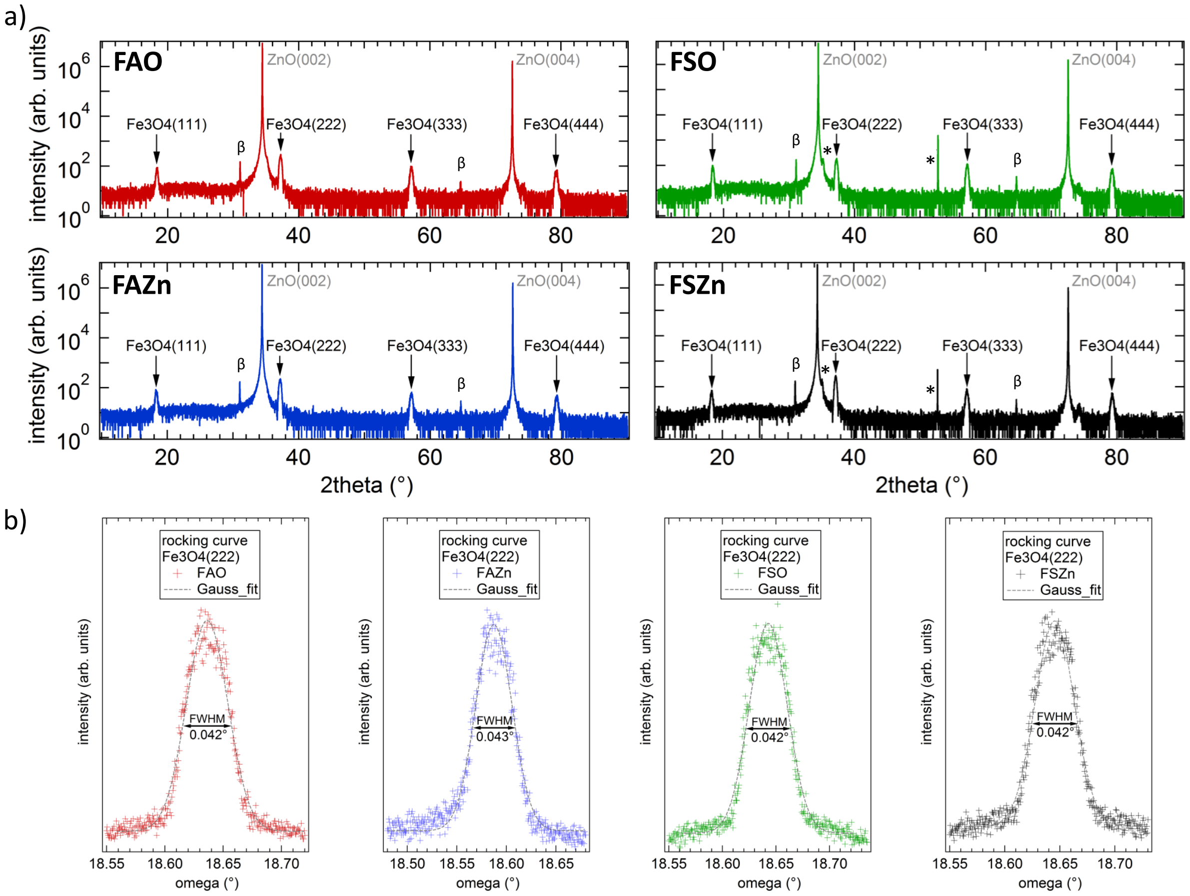

Figure 4.9: *(a) XRD 2θ scans of the various Fe_3O_4/ZnO heterostructures. FSO and FSZn additionally show an unknown sharp Bragg peak at about 53° which is probably caused by a Zn-doped ferrite phase. (b) Corresponding rocking curves performed at the Fe_3O_4(222) reflex and fitted by a Gaussian.*

single crystals. In Figure B.2 (see Appendix B.2) the RC scans for the ZnO(002) Bragg peak are shown. They yield FWHM values of about 0.01°–0.02° which represent ultimately high crystal quality caused by nearly complete absence of the defects. Of course, the film growth process itself creates a significant amount of defects within the grown film which results in comparatively broadened rocking curves.

Samples FSO and FSZn show two additional peaks at about 35° and 53° for 2θ which are marked with $*$ in Figure 4.9 a). The former peak is almost not visible due to the intense ZnO(002) Bragg peak, while the latter is extremely sharp and about 1/3 more intense than the Fe_3O_4(333) Bragg peak. As discussed for their XPS valence band spectra, it seems that diffused Zn atoms are built into the Fe_3O_4 film lattice and probably form a new phase by doping. Zn–doped ferrites ($Zn_xFe_{3-x}O_4$) can be responsible for the observed additonal Bragg peak. For $ZnFe_2O_4$ single crystals the (311) and (422) Bragg reflexes are exactly on the same positions [203–205]. One reason why XRD scans in former studies of Fe_3O_4 films with similarly prepared ZnO substrates do not show this

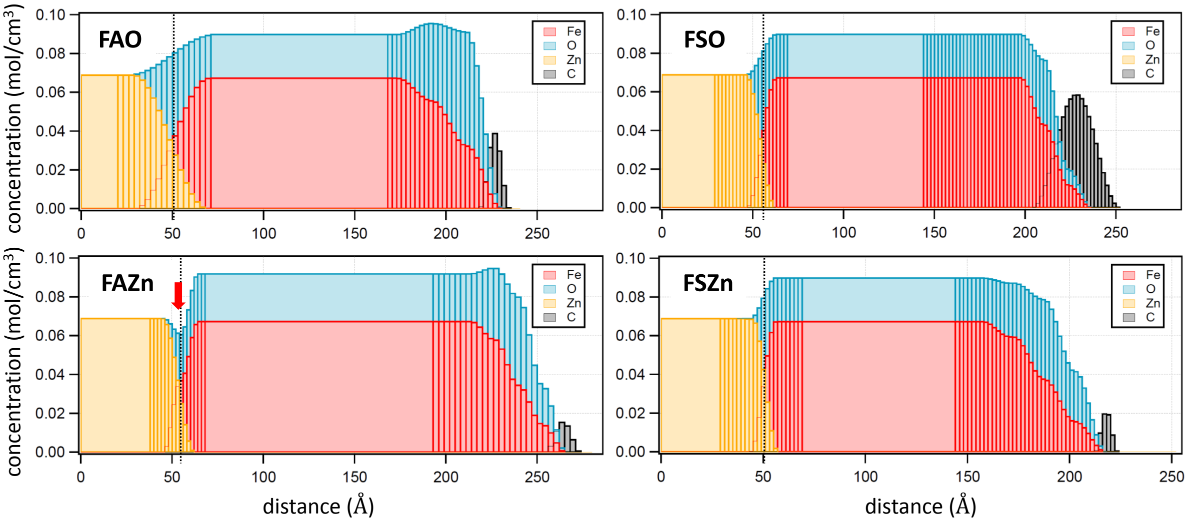

Figure 4.10: *Resulting chemical depth profiles of the various Fe_3O_4/ZnO heterostructures by means of fitting the measured XRR data. The dashed black line represents the interface. FAZn indicates a change in the film stoichiometry at the interface (see red arrow).*

additional peak is that about three times thicker samples were analysed by XRD [6]. If the formation of very low doped ferrites is constrictive to film regions nearby the interface, the additional (422) Bragg peak can be suppressed for very thick films. For the case when these doped ferrites play a role in Fe_3O_4 films grown on *in situ* prepared ZnO substrates, there will be distinct consequences in some of their physical properties, e.g. resistivity and magnetization.

Furthermore, a chemical depth profiling of the heterostructures was performed by XRR at the synchrotron BESSY II (Helmholtz Zentrum, Berlin) by Dr. V. Zabolotnyy, Dr. C. Schüßler-Langeheine and Dr. E. Schierle at the endstations UE56-2_PGM-2 and UE46_PGM-1. Measurements were done at RT in $\sigma-$ and $\pi-$polarized light. The applied photon energies which are constant off-resonance energies, ranged from about 200 to 1000 eV. Figures C.1 – C.4 (see Appendix C) show the measured XRR data of each sample at some selected photon energies. Since the data were measured at off-resonance energies, the off-resonance optical constants for materials from C. T. Chantler can be used [206]. A special software (ReMagX, by Dr. S. Macke) was used to fit the XRR data, which combines the implementation of the Parratt formalism [207] with a differential evolution for the optimization of fit parameters [208, 209]. Every sample is specified by a set of layers with a certain chemical compositions, which means certain roughness σ_i, thickness d_i and relevant atomic concentrations for each element c_i [210]. In general, c_i is kept fixed at its stoichiometric bulk value, while for the sample interface and surface finite roughnesses are implicated which are modeled as a smooth decay of c from its bulk value to zero. However, it is often necessary to to add surface contaminations as carbon, to develop a correctly matching fit to the data. The generated fits are plotted as black lines in the XRR curves.

Table 4.6: *By means of XRR determined film thicknesses d_{film} and sample specific interface $\sigma_{interface}$ and surface $\sigma_{surface}$ roughnesses of the various Fe_3O_4/ZnO heterostructures.*

heterostructure	FAO	FAZn	FSO	FSZn
d_{film}	(20.5±0.1) nm	(20.9±0.1) nm	(18.3±0.1) nm	(16.7±0.1) nm
$\sigma_{interface}$	(1.3±0.1) nm	(0.8±0.1) nm	(0.9±0.1) nm	(0.9±0.1) nm
$\sigma_{surface}$	(0.8±0.1) nm	(1.0±0.1) nm	(1.3±0.1) nm	(1.3±0.1) nm

The generated chemical depth profiles are presented in Figure 4.10. The plots show the corresponding concentrations of the contained elements in the sample depending on the relative depth distance. The determined film thicknesses d_{film}, sample specific interface roughnesses $\sigma_{interface}$ and surface roughnesses $\sigma_{surface}$ are listed in Table 4.6. In contrast to FAO and FAZn, the film thicknesses of FSO and FSZn are slightly smaller than the expected 20 nm. This can be caused by fluctuation of the Fe flux in the electron beam evaporator during growth. Moreover, sample FAO indicates the biggest interface roughness of all four heterostructures, while the other samples have comparatively small values. Due to the missing terrace steps on the substrate surfaces of the samples FSO and FSZn as well as the very wide and atomically flat terrace steps of sample FAZn, the determined values for these samples can be smaller, since this roughness is averaged to the whole substrate surface area during the fitting procedure. Therefore, these values has to be treated with tolerance if they are related to the sharpness of heterostructure interface regions on a small scale. Furthermore, the film surface roughnesses determined by XRR show the same trend as the obtained results via AFM (see Table 4.4), but almost halved values for FSO and FSZn seem slightly too small. Due to contaminations on the film surfaces (see gray colored concentration profile for carbon), caused by the *ex situ* transport from the home laboratory to the research facility, exact values of the surface roughnesses are not exactly accurate. Interestingly, the FAZn sample shows at the Fe_3O_4/ZnO interface a special feature: the O concentration decreases while the Fe concentration increases which is marked by a red arrow. For stoichiometric Fe_3O_4 both concentrations should behave similar as observed for the three other samples near the interface. There can be several reasons that can cause such a ”dip” in the profile of the O concentration. Most reasonable are film stoichiometry changes and density variations of the film nearby the interface. The *ex situ* prepared ZnO substrate of FAZn has chemisorbed OH^- groups on its surface as verified by XPS which can react with the deposited film material forming a compound with different density. By incorporating these adsorbates into the film lattice the film layers near the interface might acquire another phase which can differ in stoichiometry and density. This characteristic of sample FAZn should be visible in TEM micrographs. A more detailed information about the nature of the various interfaces in these samples can be revealed by TEM and will be discussed in the next subsections.

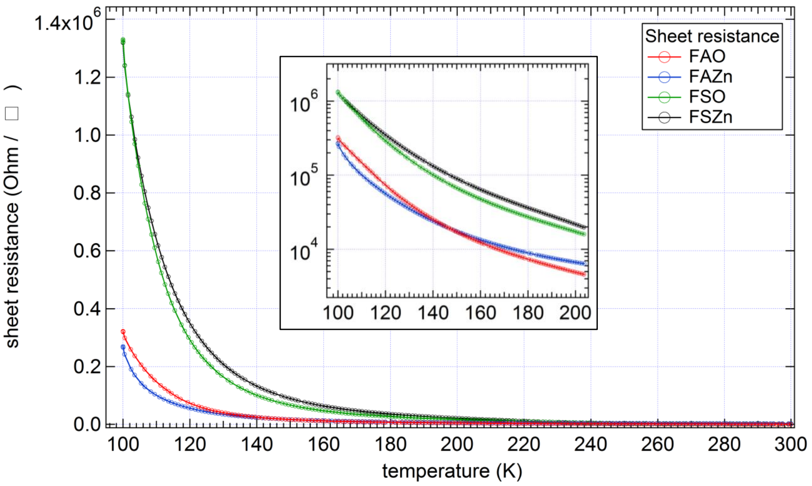

Figure 4.11: *Measured film sheet resistances of the various Fe_3O_4/ZnO heterostructures as a function of temperature. The inset shows a plot of the same data with logarithmic scaling of the sheet resistance values.*

4.3.4 Conductivity measurements and magnetometry

XRD measurements reveal an additional unknown Bragg peak in the 2θ scans for the Fe_3O_4/ZnO heterostructures with *in situ* sputtered and annealed ZnO substrates which is probably caused by the formation of Zn-doped ferrites ($Zn_xFe_{3-x}O_4$) nearby their interface regions. To analyze this in more detail, resistivity and magnetometry measurements were performed.

Figure 4.11 presents the film sheet resistances of the four samples as a function of temperature. The resistance was measured in the 4-point van–der–Pauw geometry and at temperatures ranging from 300 to 10 K. However, only data from 300 to 100 K are taken into account, since at lower temperatures the signal noise becomes very high and thus interpretation of data becomes hard. Reasons for the high signal noise at low temperatures are the limitation of the current which can be induced by the PPMS into the sample, the semiconducting nature of the films and, especially, contact loss of the Al bonds on the film surface.

All four films show the characteristic half–metallic nature of Fe_3O_4: an increase of the sheet resistance for lower temperatures. This increase is caused by the metal–insulator transition of the semiconducting Fe_3O_4 at the Ferwey transistion temperature at about 125 K. Samples FAO and FAZn show similar trends and values for the temperature dependent sheet resistance of Fe_3O_4 compared to the literature [211–213]. Indeed samples FSO and FSZn indicate the same semiconducting trend in their plotted curves, but for low temperatures sheet resistance values of about one order of magnitude higher than those for FAO and FAZn. The determined values at RT and 100 K are listed in Table 4.7. The reduced sheet resistance of FSO and FSZn can be attributed to a presence of

Table 4.7: *Sheet resistances of the various Fe_3O_4/ZnO heterostructures determined at RT and 100 K.*

heterostructure	FAO	FAZn	FSO	FSZn
sheet res. $(\Omega/\square)_{RT}$	700 ± 10	1500 ± 10	1300 ± 10	1100 ± 10
sheet res. $(\Omega/\square)_{100K}$	$(3.2\pm0.1)\cdot10^5$	$(2.7\pm0.1)\cdot10^5$	$(1.3\pm0.1)\cdot10^6$	$(1.3\pm0.1)\cdot10^6$

Zn-doped ferrites in films composition. $Zn_xFe_{3-x}O_4$ thin films grown on MgO(001) substrates show similar behaviors in conductivity measurements [214]. The Zn^{2+} ion preferably occupy the tetrahedrally coordinated A sites in the inverse-spinel structure of Fe_3O_4 [215]. Thus, some of the antiferromagnetically coupled moments on these sites are eliminated, resulting in an initial increase in the saturation magnetization at low Zn substitutions [216, 217]. Furthermore, substitution of Fe_A^{3+} by Zn^{2+} on the A sites reduces the amount of Fe_B^{2+} on the B sites by reasons of charge neutrality [214]. In other words, the itinerant charge carriers which induce the double-exchange on the B sublattice, are reduced. This effect was also verified by PES experiments [218]. Consequently, the electrical conductivity is reduced with increasing Zn substitution in $Zn_xFe_{3-x}O_4$ thin films.

Since the film magnetization is also affected by the Zn substitution, magnetometry measurements were performed to analyze the magnetic properties of the four samples.The following SQUID measurements were executed by Dr. E. Goering (MPI IS, Stuttgart). External magnetic fields from about +6 T to –6 T were applied parallel to the substrate and at the same time the sample magnetization was recorded for generating the magnetic field dependent hysteresis curve. Because SQUID magnetometry measures the integrated magnetization of the whole sample, an additional dia- and paramagnetic contributions by the substrate material occur in the data. However, they scale linearly with respect to the external applied magnetic field and can be fitted by a linear slope with an equal gradient as the measured data gradient at high field values. This is only feasible if a saturated ferromagnetism is assumed. As a rule, the absolute magnetization is measured in emu (electromagnetic units) and has to be normalized to the film volume $V_{Fe_3O_4}$. Thus, the sample magnetization can be determined by

$$M\ [\mu_B/f.u.] = M\ [emu]\frac{1}{1000}\frac{1}{\mu_B\rho_{Fe_3O_4}V_{Fe_3O_4}} \quad , \tag{4.2}$$

where $\rho_{Fe_3O_4}$ is the density of magnetite. Figure 4.12 a) presents the hysteresis curves of the various Fe_3O_4/ZnO heterostructures measured at RT (left) and 2 K (right). The plots show the enlarged areas from +1.0 T to –1.0 T. All samples display the typical hysteresis loop of a material with ferromagnetic behavior. The magnetization value for each sample at +1.0 T is listed in Table 4.8. As expected, the magnetization M for FSO and FSZn is much higher than for FAO and FAZn and corresponds to a relatively large increase of about 30%. This result is in good agreement with observations of D. Venkateshvaran *et al.* for $Zn_xFe_{3-x}O_4$ thin films [214]. Furthermore, the saturation

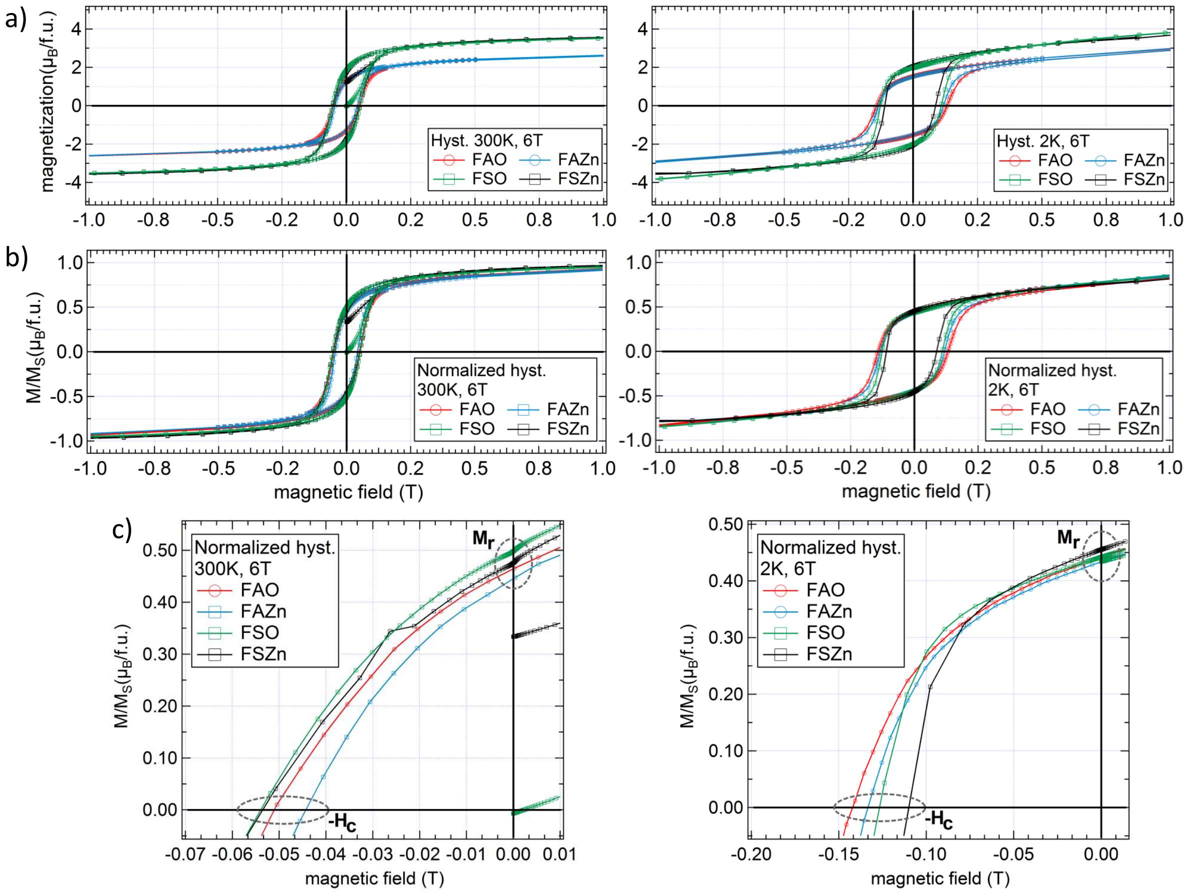

Figure 4.12: *Magnetic field dependent magnetization M of the various Fe_3O_4/ZnO heterostructures measured at RT (left) and 2 K (right). (a) Sample magnetizations M normalized to one formula unit Fe_3O_4. (b) Sample magnetization M normalized to the saturation magnetization M_S resulting in the relative sample magnetization M/M_S. (c) Enlarged areas of the M/M_S vs. magnetic field plots indicating variations in remanence magnetization M_r and coercive field strength H_c between the four samples.*

magnetization M_S of the samples, determined by a best straight line fit to the data from about +2 T to +6 T, indicates that the real M_S values are about 5–8% higher than the values at +1.0 T. Such high magnetic fields for the saturation can be attributed to the presence of APBs in the thin film [219]. The determined M_S values of FAO and FAZn are rather similar to those of M. C. Paul [6]. Note, that the theoretically expected value of M_S=4$\mu_B/f.u.$ for Fe_3O_4 is not obtained. However, the data of FSO and FSZ exhibit at 2 K M_S values among the highest reported in literature. To compare the samples in terms of their magnetization behavior, their magnetization M is normalized to the corresponding M_S. The relative sample magnetizations M/M_S for both temperatures are shown in Figure 4.12 b), while useful enlarged areas are presented in c). The identified remanence magnetization M_r and coercive field strength H_c values of each sample are tabulated in Table 4.8. For RT, FSO and FSZn have slightly higher M_r and H_c values

Table 4.8: *Sample magnetization M, saturation magnetization M_S, remanence magnetization M_r and coercive field strength H_c determined by SQUID at RT and 2 K by means of hysteresis loops. The Verwey transition temperature T_V of the various Fe_3O_4/ZnO heterostructures were identified by field cooling experiments.*

heterostructure	FAO	FAZn	FSO	FSZn
RT				
M at +1.0 T [$\mu_B/f.u.$]	2.60±0.05	2.55±0.05	3.45±0.05	3.35±0.05
M_S [$\mu_B/f.u.$]	2.85±0.05	2.85±0.05	3.70±0.05	3.65±0.05
M_r [$\mu_B/f.u.$]	0.465±0.015	0.445±0.015	0.500±0.015	0.480±0.015
H_c [mT]	51.5±1.5	44.0±1.5	55.0±1.5	54.0±1.5
2 K				
M at +1.0 T [$\mu_B/f.u.$]	2.8±0.1	2.8±0.1	3.8±0.1	3.7±0.1
M_S [$\mu_B/f.u.$]	3.1±0.1	3.0±0.1	3.9±0.1	3.8±0.1
M_r [$\mu_B/f.u.$]	0.445±0.015	0.430±0.015	0.440±0.015	0.455±0.015
H_c [mT]	140.0±1	132.0±1	125.0±1	112.0±1
Verwey transition				
T_V [K]	118.0±1.5	118.0±1.5	108.0±1.5	108.0±1.5

that can be again attributed to the above-mentioned Zn substitution and are consistent with the literature [203, 214, 220, 221]. In the case of low temperatures, the tendencies seems to be opposite. Here, samples FAO and FAZn have almost same M_r and higher H_c values compared to FSO and FSZn. Therefore, the Zn substitution affects mostly H_c, possibly occurring due to the different configuration and by regenerated double-exchange mechanisms within the sublattice.

Additionally, the temperature dependent magnetization of each sample is measured at 0.1 T. For this, the samples were first heated to about 330 K and saturated in a magnetic field of 6 T. Afterwards the magnetization was measured from RT to about 5 K in an external field of 0.1 T. Figure 4.13 demonstrates the field-cooling curves. The curves of FAO and FAZn reveal a similar dependance on temperature. Both samples exhibit between 150 K and 100 K a wide drop in magnetization which is a sign of a broadened Verwey transition, while Fe_3O_4 single crystals show a sharp drop in a range of a few K [222]. This change for grown films is due to the long ranged antiferromagnetic order of the magnetic moments of the Fe^{2+} cations compared to the remaining moments of the B-sublattice at temperatures below T_V [223]. At higher temperatures, this antiferromagnetic coupling is disturbed by thermal fluctuations resulting in an increase of M. As consequence a sharp Verwey transition is a measure of the distinct crystalline quality in Fe_3O_4.

In contrast, the Verwey transition in field-cooling curves of FSO and FSZn is not that

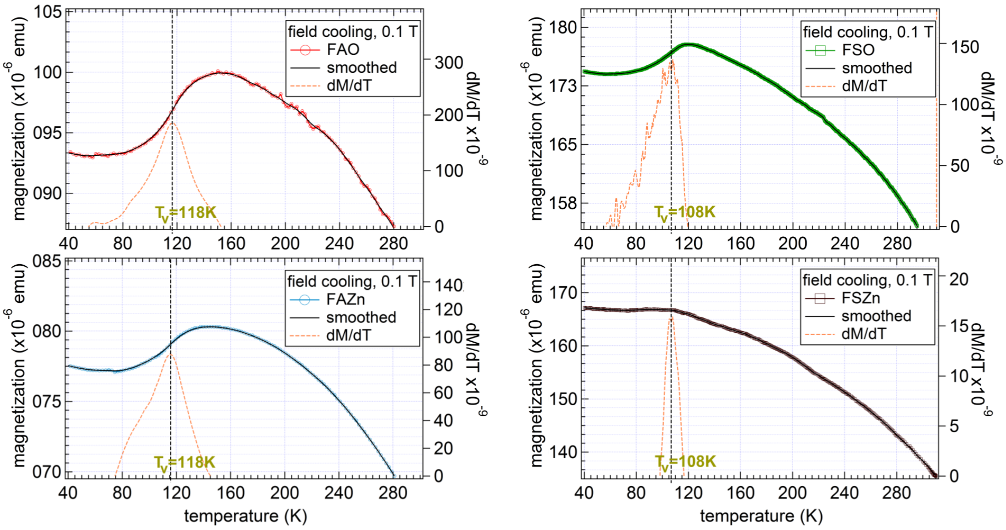

Figure 4.13: *Sample magnetizations (left scale) of the various Fe_3O_4/ZnO heterostructures as a function of temperature at 0.1 T in the temperature range of 40 K to 300 K. Derivatives of the sample magnetization with respect to temperature (right scale) marked as dashed orange lines are plotted to determine the corresponding Verwey transition temperatures.*

pronounced in the corresponding temperature range. While FSO shows a very small drop in M, FSZn indicates almost no signature of the Verwey transition which can be attributed to deviations from equal numbers of Fe_B^{2+} and Fe_B^{3+} on the B-sublattice. This can be considered as disorder on the B-sublattice, which smears out the Verwey transition. Thus, the observability of the Verwey transition is sensitively dependent on the perfect stoichiometry of the Fe_3O_4 crystal lattice as documentated in several studies [44, 224–227].

Because the Verwey transition point is defined as the inflection point of the magnetization curve, the derivatives of the sample magnetization with respect to the temperature are generated and additionally displayed in the plots. The peak positions of the derivatives represent the Verwey transition temperatures (T_V) of the various Fe_3O_4/ZnO heterostructures. The corresponding values of T_V are listed in Table 4.8. As expected, the T_V values for FAO and FAZn are slightly smaller (approx. 5%) than the T_V value for Fe_3O_4 single crystals of about 125 K [28] due to the broadened transition, relatively small film thickness and thus higher density of APBs in the film. However, the T_V values for FSO and FSZn are even smaller (approx. 15%) and have to be attributed again to Zn substitution and their differently acting sublattice magnetizations.

4.3.5 Magnetic depth profiling via polarized neutron reflectometry

Depth resolving measurements via XRMR (X-ray resonant magnetic reflectometry) and EELS reveal a change of the Fe valency at the interface of Fe_3O_4 films grown on an

O-terminated *in situ* prepared ZnO substrates [228]. Such modifications in the Fe_3O_4 sublattices are able to convert the magnetic properties of the film. To get an idea about the volume magnetization of the four Fe_3O_4/ZnO heterostructures, PNR experiments were performed at the beamline CRISP at the spallation source ISIS (Rutherford Appleton Laboratory, UK) by Dr. N.-J. Steinke, Dr. S. Brück and M.Sc. M. Zapf. Here, the time-of-flight mode is used for simultaneous measure of the momentum transfers. But during the measurement of the PNR intensity, the phase information of the neutrons gets lost. Thus, the analytical relationship between the measured PNR curve and the magnetic properties of the film is not given. Therefore, a layered system has to be modeled such that its theoretical PNR signal fits to the experimental data. Consequently, this can give much informations about the investigated films. The simulation of the PNR curves are realized by the special software SimulReflec [229] which is based on an analytic matrix formalism from reflection optics and is able to compute reflections at multilayer systems with smooth surfaces very precisely.

The following procedure is used to modulate the reflectivity curve to the measured PNR data. First, the layer structure of the system is defined by the layer thickness, roughness, magnetic moment and the material specific parameters of Table A.1 (see Appendix A). Then, an optimization of every each parameter is performed by means of algorithms based on the minimization of the root mean square deviation, while for the material specific parameters only a restricted variation is permitted. If no satisfying conformance of the simulation with the measured data is found, then additional layers can be included into the system to repeat the optimization process. Note that the simulation has to describe not only the reflectivity but also the corresponding spin asymmetry curve with the magnetic information as good as possible.

As a descriptive result one gets a profile of the scattering length density (SLD) ρb which represents a magnetic depth profiling, while the profile itself corresponds to the depth trend of the sample refraction indices as defined by Equation 3.65.

However, as the phase information gets lost during the measurement of the reflected intensities, there can be theoretically several possible SLD profiles that describe the same reflectivity and spin asymmetry. Therefore, it is advisable to cross-check the model by another characterization method that is sensitive to the sample magnetization.

For the PNR measurements, 10 nm Fe_3O_4 thin films were grown on the differently prepared ZnO substrates. Note, that the initial *in situ* sputtering and annealing treatment as described in subsection 4.1 was not possible to perform and it was replaced by an alternative preparation. Since epi-ready substrates are not that much different from the actual *in situ* prepared substrates regarding the surface morphology and structure, these substrates were only degased for 1 hour at 400°C in a O_2 atmosphere of $3.0{\cdot}10^{-6}$ mbar before the growth process. The Fe_3O_4 films on these substrates were grown without changing the partial pressure at $3.2{\cdot}10^{-6}$ mbar. XPS measurements indicate stoichiometric Fe_3O_4 films which are only at their surfaces slightly over-oxidized (not shown). This different surface stoichiometry has no radical effect on the following results, but still has to be considered. These samples with epi-ready substrates are labeled as FEO

Table 4.9: *Sample parameters of the PNR simulations for the various Fe_3O_4/ZnO heterostructures with estimated absolute errors of the PNR simulations ($\pm\Delta_{PNR}$). The Au cap thickness d_{Au} is the overall Au layer thickness including a surface Au layer with 5–7% reduced density. $d_{Fe_3O_4}$ is the Fe_3O_4 film thickness including the interface near layer with reduced magnetization. σ_{Au} is the surface roughness of the sample. $\sigma_{Fe_3O_4}$ and σ_{ZnO} are the interface roughnesses of Au/Fe_3O_4 and Fe_3O_4/ZnO, respectively. The magnetic moment μ represents the average magnetization in field direction of 1 formula unit (f.u.) Fe_3O_4 in the film bulk which means without the layer nearby the interface of reduced magnetization.*

heterostructure	FAO	FAZn	FEO	FEZn
$d_{Au} \pm \Delta_{PNR}$ [nm]	39.03±1.5	39.06±1.5	33.38±1.5	34.18±1.5
$\sigma_{Au} \pm \Delta_{PNR}$ [nm]	0.43±0.20	0.54±0.20	1.01±0.20	1.73±0.20
$d_{Fe_3O_4} \pm \Delta_{PNR}$ [nm]	8.07±0.60	7.84±0.60	11.97±0.60	12.05±0.60
$\sigma_{Fe_3O_4} \pm \Delta_{PNR}$ [nm]	1.65±0.20	1.48±0.20	0.60±0.20	0.85±0.20
$\sigma_{ZnO} \pm \Delta_{PNR}$ [nm]	0.14±0.50	0.13±0.50	0.05±0.50	0.05±0.50
$\mu \pm \Delta_{PNR}$ [$\mu_B/f.u.$]	1.89±0.30	1.71±0.30	2.02±0.30	2.10±0.30

and FEZn and investigated only in this subsection of the thesis.

After the XPS characterization of the grown films, all samples were *in situ* capped at RT with about 30 nm Au using a high temperature effusion cell. The deposition of such additional nonmagnetic layers represents a common procedure in thin magnetic film analysis by means of PNR and is originally traced back to studies of G. P. Felcher *et al.* [230] and J. A. C. Bland *et al.* [231, 232]. The Au cap serves as a passivation layer for the film material and protects it from further oxidization in air. Actually, the PNR curves of thin Fe_3O_4 films without Au cap exhibit large oscillation periods due to the reciprocal relation in Equation 3.58 and result in almost non-oscillating spin asymmetry curve. An Au overlayer thicker than the Fe_3O_4 film leads to the appearance of an additional shorter oscillation period in the PNR signal. New interference conditions arise from the additional interface between Fe_3O_4 film and Au layer. Thus, the maximum amplitude of the magnetic signal becomes higher and shifted to smaller momentum transfers Q_z. Since the SLD of the Au layer is much different to that of the Fe_3O_4 film, an easier analysis of the magnetic film is enabled, while magnetically inactive layers of a few Å (as it is expected from XRMR results [228]) can be resolved as accurate as possible.

Figure 4.14 presents the PNR data and Figure 4.15 the resulting spin asymmetry data of the four various Fe_3O_4/ZnO heterostructures. The error bars of the measured intensities are defined by the Poisson distribution of the neutrons and scale with $N^{-1/2}$, where N is the number of detected neutrons at the relevant Q_z value. Due to the increasing error bars at high Q_z values, the chosen model is ensured to have good agreement with the measured data at small Q_z values in the range of 0 to 0.07 Å^{-1}.

The only model, which described both PNR and spin asymmetry data of all four samples most accurately, has a reduced film magnetization near the Fe_3O_4/ZnO interface. The corresponding simulations are presented together with the PNR and spin asymmetry

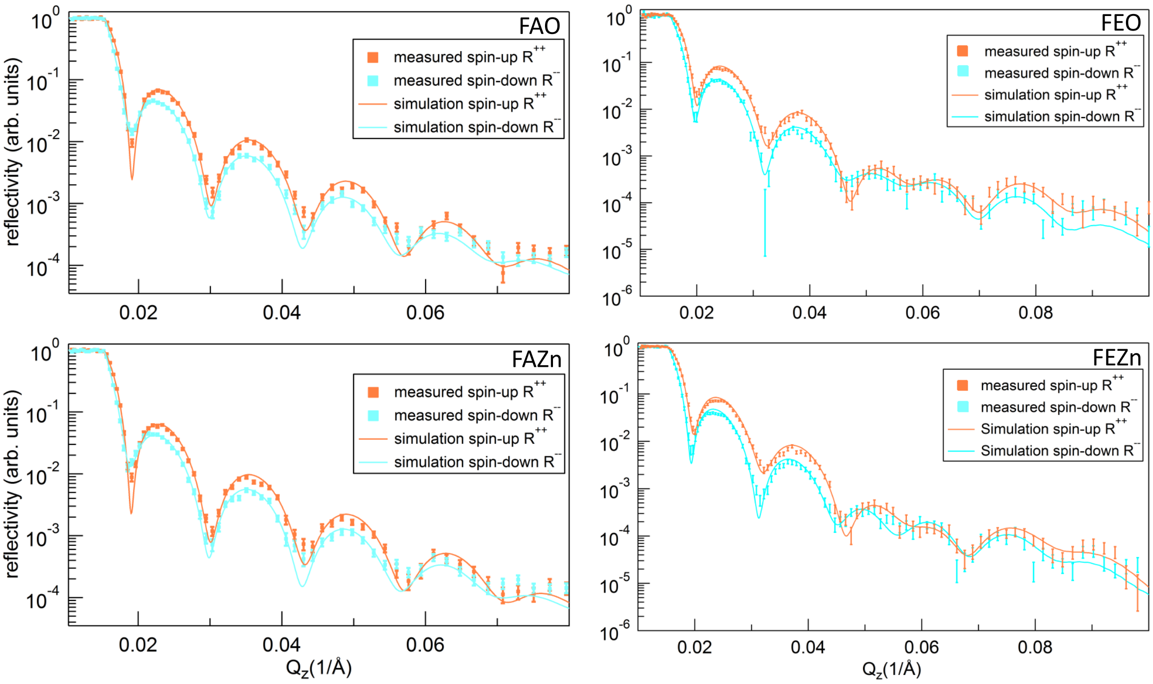

Figure 4.14: *Polarized neutron reflectometry data of the various Fe_3O_4/ZnO heterostructures and the corresponding adapted simulations with reduced film magnetization nearby their interfaces.*

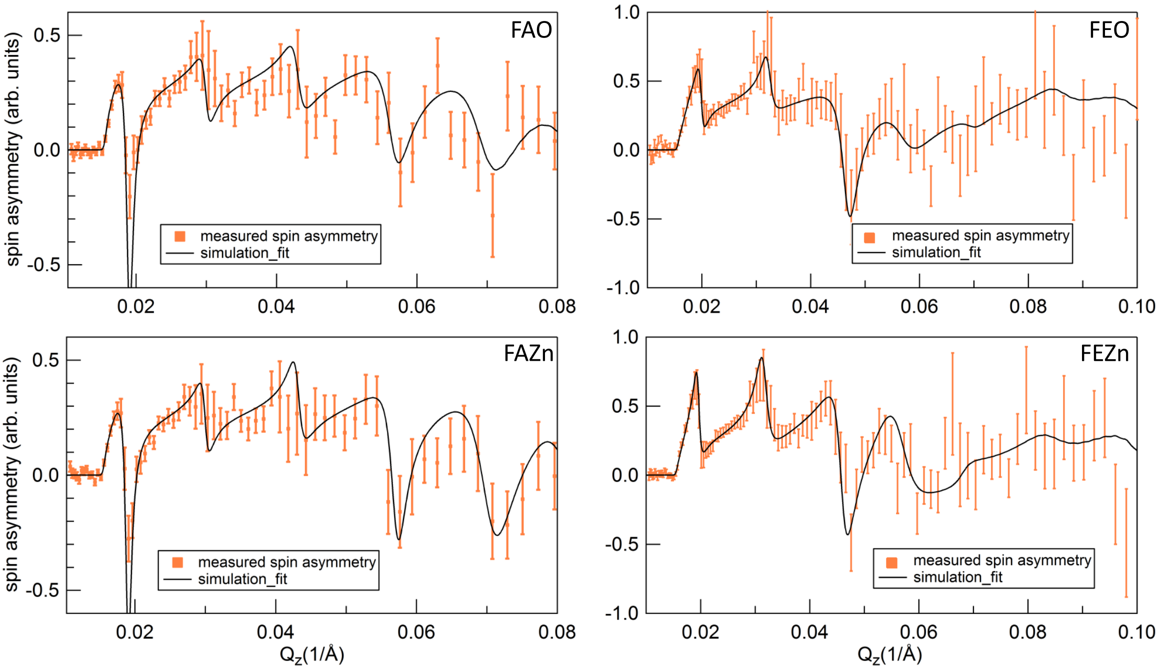

Figure 4.15: *Spin asymmetry data of the various Fe_3O_4/ZnO heterostructures and the corresponding adapted simulations with reduced film magnetization nearby their interfaces.*

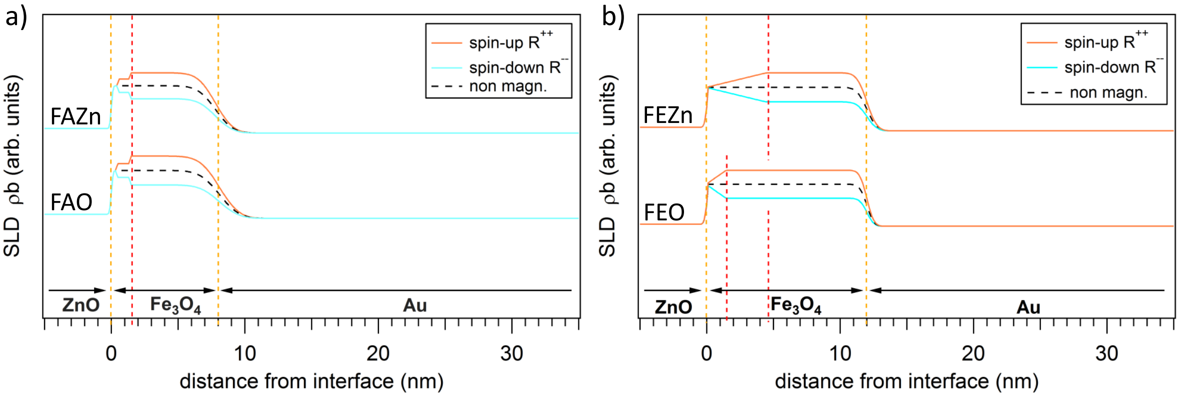

Figure 4.16: *Scattering length densities (SLDs) of the simulations (which are shown in Figures 4.14 and 4.15), shown for the Fe_3O_4 films grown on (a) ex situ and (b) in situ prepared ZnO substrates. All samples show a layer with reduced magnetization nearby the interface. The dashed orange lines represent the interfaces Fe_3O_4/ZnO and Au/Fe_3O_4, whereas the dashed red lines indicate the dimension of layer with reduced magnetization.*

plots and one can see the good agreement between them (see Figures 4.14 and 4.15). In each case, an optimized model with a linear increase of the film magnetization from the Fe_3O_4/ZnO interface into the film is assumed. The corresponding SLD profiles are demonstrated in Figure 4.16. The real trend and thickness of the layer with reduced magnetization can not be definitely determined by these identified data. A magnetization jump in the simulation gives no accurate consistence with the measurement. The rise of the film magnetization is modeled in the simulation by number of discrete Fe_3O_4 layers with a thickness of 0.1 nm and a magnetization which linearly increases with distance from the ZnO substrate. The sample parameters of the PNR simulations for the various Fe_3O_4/ZnO heterostructures are listed in Table 4.9. To simulate the measured data especially in the region of the critical angle correctly, the Au film is split into two separate layers, since its density at the sample surface is found to be up to -7% smaller. This density change can be attributed to Au clusters at the surface or holes in the Au layer. However, this Au surface density variation has no influence on the magnetization of the film.

Samples FEO and FEZn show the above-mentioned linear increase of the film magnetization as demonstrated in Figure 4.16 b). FEO reaches its average film magnetization of about 2.0 $\mu_B/f.u.$ in approx. 1.5 nm distance to the interface. In contrast, FEZn reaches its magnetization of almost equal value in about 4.5 nm distance. Since these both samples are differently prepared as the actual *in situ* prepared samples FSO and FSZn, it is hard to compare the results from the other characterization methods for FSO and FSZn with this PNR results for FEO and FEZn. Nevertheless, FEO and FEZn clearly indicate some differences in the film magnetization near the interface with respect to their substrate termination type. The Zn-terminated sample has a much larger Fe_3O_4 layer with reduced magnetization, that can be a result of a stronger perturbation of the magnetic behavior on the Zn-terminated substrate surface.

On the other hand, FAO and FAZn show only slightly different magnetization profiles. For both cases, the Fe_3O_4 layer near the interface is again reduced in magnetization, but its increase to the average film magnetization is not entirely linear. Here, the magnetization increases linearly for the first approx. 0.25 nm. Afterwards, the magnetization is for about 1.0 nm constant but still reduced. Finally, the magnetization increases to its average magnetization on the next about 0.25 nm. Both samples show this behavior and have therefore a Fe_3O_4 layer with reduced magnetization of about 1.5 nm. The average film magnetizations are about 1.9 $\mu_B/f.u.$ and 1.7 $\mu_B/f.u.$ for FAO and FAZn, respectively. Beside this, both samples are very similar regarding their other simulation parameters. Note that the in-field-direction-polarized magnetic moment μ per f.u. which is given in Table 4.9, can be derived from the spin asymmetry amplitude. The simulations of the spin asymmetry allow a fluctuation range of about 0.25 $\mu_B/f.u.$ till significant variations of the simulations are observable. Since the films grow as islands on ZnO, the density of the film near the interface can vary. Thus, the absolute error of the density dependent magnetic moment μ is about 5% higher ($\approx 0.30\ \mu_B/f.u.$).

In other studies, there are similar magnetically inactive layers found at the interfaces of Fe_3O_4 films which were grown on different substrates. However, in their publications only assumptions about this effect are given, while the direct experimental confirmation is missing [233, 234]. In principle, different reasons could be responsible for reduced magnetization in PNR measurements .

One reason can be that the orientation of the free magnetic moments of Fe_3O_4 along the the external applied field is impeded. This can happen by APBs which cause a strong additional antiferromagnetic coupling. Thus, a reduced film magnetization can be explained with a higher number of APBs due to initially small domain that form in the Fe_3O_4 layers close to the interface. With increasing film thickness these domains become larger and form less APBs. This theory is confirmed by TEM analysis of Fe_3O_4 films grown on Al_2O_3 and MgO substrates, demonstrating a reduction of the APB density by factor of $t^{-1/2}$ for increasing the film thickness t [219, 235]. But, the domain extension can also be attributed to a thermally activated recovery of APBs during the growth of thick films [235]. However, a successive vertical decrease of the APB density within the film is not explicitly proved.

The stoichiometry of the film can be another reason for the reduced magnetization at the interface. A variation in the stoichiometry can induce a lack of free moments which could be polarized. For instance, antiferromagnetic FeO has a similar SLD for neutrons as Fe_3O_4. Thus a nonmagnetic Fe_3O_4 layer is hard to distinguish from a FeO layer in PNR. But since the Fe_3O_4 films tend towards over-oxidization, a several nm thick antiferromagnetic FeO layer seems unlikely to appear.

Furthermore, the crystalline order of Fe_3O_4 can be disturbed at or by the interface which in turn affects the magnetic order. As an example, in PNR measurements of a 260 nm thick Fe_3O_4 films grown by cathodic sputtering on Si substrates, a magnetically inactive layer of 2.5 nm at the film surface was found [236]. This result was attributed to the large surface roughness of the film. Another PNR experiment, in which exchange-bias multilayer structures of Fe_3O_4/CoO were investigated, revealed that above the Néel temperature of CoO the magnetization of the Fe_3O_4 film at the interface is reduced [237]. It is assumed that a higher density of defects in the Fe_3O_4 lattice at the interface is responsible for the change in magnetization. For the Fe_3O_4/ZnO heterostructure, local strain effects and lattice imperfections at the interface are very likely to be present due to the large lattice misfit of Fe_3O_4 and ZnO.

In summary, there is the potential that the termination type of the ZnO substrate directly influences the film properties. Unfortunately, samples with *in situ* sputtered and annealed substrates as FSO and FSZn were not measured by PNR and it is questionable if the PNR results of the samples with epi-ready substrates can be translated to them. To identify this, more PNR measurements, especially on FSO- and FSZn-like samples, would be needed. However, in the case of samples with *ex situ* annealed substrates, the termination type seems to play a subordinate role. Here, both samples independently on their termination show a reduced magnetization at the interface and the same size of such region. Moreover, the possible Zn diffusion into the film and consequent increase of the film magnetization, as it was noticed for FSO and FSZn in XPS and SQUID measurements, can not be clarified by this PNR study.

4.3.6 Microstructure

In the following, a detailed STEM analysis is presented for identification of the crystalline order in the various Fe_3O_4/ZnO heterostructures as well as for the determination of their chemical composition including the Fe valencies at the interface. The measurements were performed by Dr. N. Gauquelin and Dr. H. Tian at the EMAT (Electron Microscopy for Materials Science) center of the University of Antwerp (Antwerp, BEL). Using a FEI dual beam FIB, the required lamellas were cut out perpendicular to the sample surface and afterwards milled from both sides by a focused ion beam to a thickness of about 50 nm. The lamella of each sample was then transferred to the TEM (FEI-Titan version) for the actual analysis.

Figure 4.17 shows the micrographs of the four Fe_3O_4/ZnO samples obtained by the HAADF-STEM mode. Furthermore, the termination type of the substrates are confirmed by red-green-blue colored images, where red is set for the HAADF, green for the inversed annular bright field (i-ABF) and blue for the actual annular bright field (ABF) signal. With this color imaging method it is possible to visualize the much lighter O atoms beside the Zn atoms in the ZnO lattice. Figure D.1 (see Appendix D) demonstrates this exemplarily for the substrates of FSO and FSZn.

Every Fe_3O_4 film reveals the expected AP/twin boundaries which are exemplified in Figure D.2 (see Appendix D) for the samples with *in situ* prepared substrates. The placement of the conjoined grain lattices can be explained by the coalescing of two Fe_3O_4 islands which differ in their stacking sequence by a shift of a half unit cell. Compared to each other, the overall density of grain boundaries in the films are very similar,

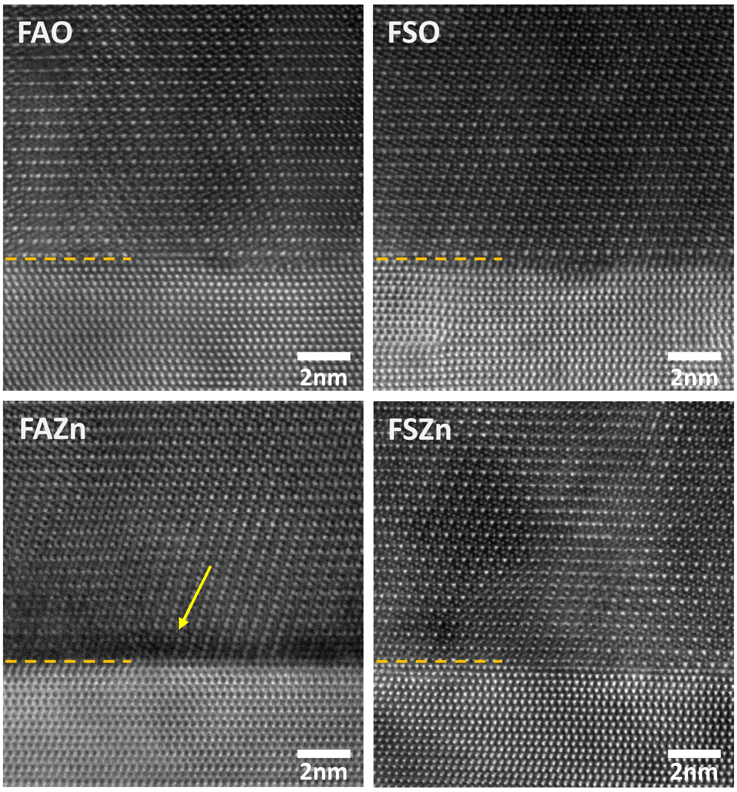

Figure 4.17: *HAADF-STEM micrographs of the various Fe_3O_4/ZnO heterostructures with the focused electron beam in [1$\bar{1}$0]-direction of the Fe_3O_4 film. The dashed orange lines indicate the interfaces.*

resulting possibly by the same thickness of about 20 nm. Furthermore, the size of the Fe_3O_4 crystallites range from approx. 1 nm to 40 nm.

In direct comparison of some more taken HAADF-STEM micrographs the four samples show some differences (see also Figure 4.17). Regarding the interface quality, FAO seems to have the sharpest interface with rather small number of steps at the interface, whereas FSO and FSZn exhibit, obviously more rough interfaces, while FSZn has a slightly sharper interface than FSO. However, FAZn shows the roughest interface of all four samples and a variation of contrast in the Fe_3O_4 film for the first 0.5–1.5 nm at the interface (marked by yellow arrow). The structure in this region is hard to resolve since in TEM it appears to be too dark over the complete lamella. On the contrary, the other samples show well ordered structures till the interface, although the atomic configuration at the transition region from the substrate to the film can not be accurately resolved as well. However, strong contrast variation within the film at the interface is not present for these three samples. The dark contrast in FAZn can originate from atomic rows in the lattice which are not exactly aligned in electron beam direction as for the rest of the film, being a potential sign of impurity phases, high density of defects or even lattice tilting in the film. Impurity phases by other iron oxides can be excluded by the previous XRD results and also by XPS measurements of very thin films of about 4 nm grown on

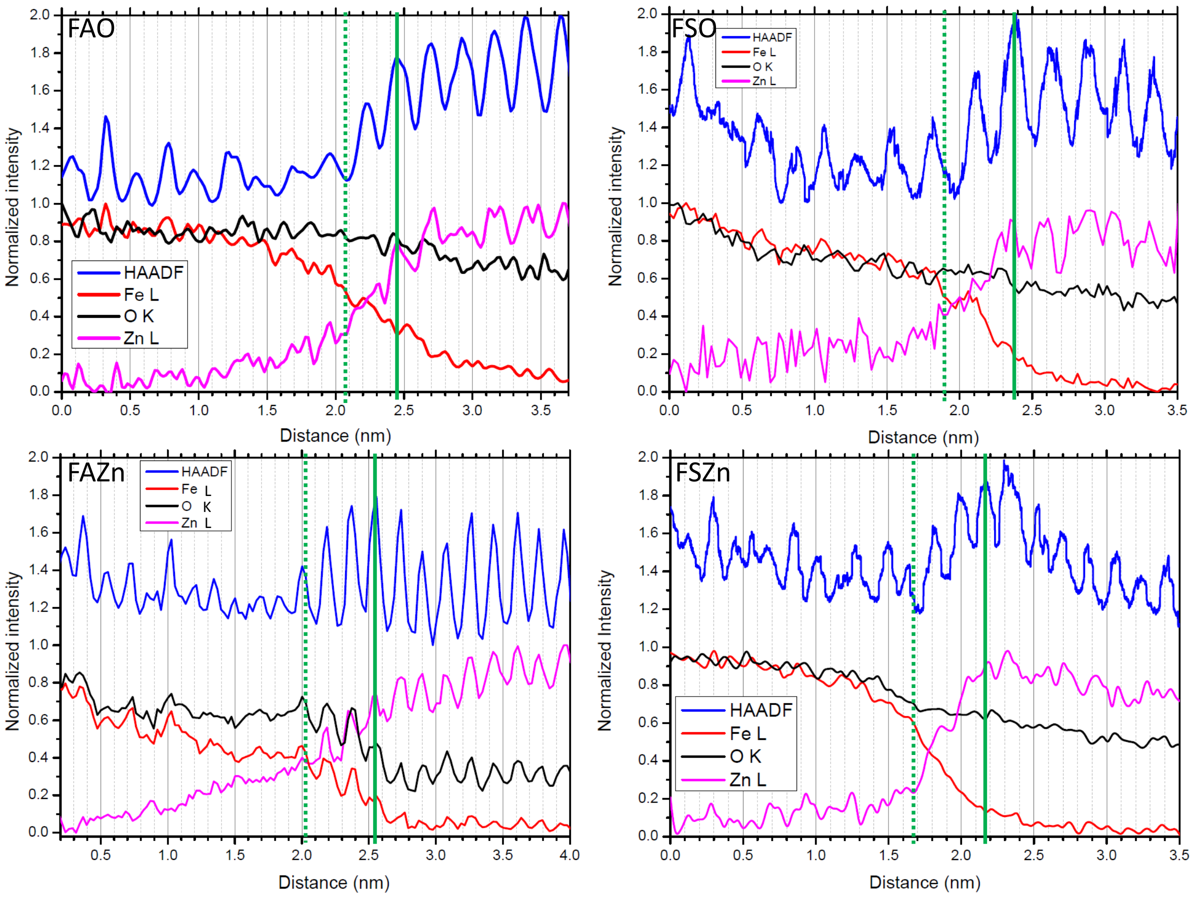

Figure 4.18: *Corresponding composition profiles of the various Fe_3O_4/ZnO heterostructures generated by scanning the focused electron beam in [$1\bar{1}0$]-direction of the Fe_3O_4 film across the sample interface. The element specific signal intensities which are determined by STEM-EELS as well as the overall HAADF signal intensity are plotted as a function of the distance covered by the electron beam.*

this substrate type (data not shown). Moreover, the growth condition are the same as for FAO which shows no dark region. K. Matsuzaki *et al.* presented TEM micrographs of not fully oxidized Fe_3O_4 films grown on YSZ substrates [238], which show at the interface a similarly dark HAADF-STEM contrast induced by FeO crystallites in the film. But in contrast to FAZn, its lattice structure which significantly differs from that of Fe_3O_4, is resolvable at the interface Fe_3O_4/YSZ.
The different substrate preparation (compared to that of FAO) can be another possibility of the dark region in FAZn. The Zn-terminated substrate was prepared in humid O_2 atmosphere, resulting in chemisorbed OH^- groups at its surface. At the initial growth process of the Fe_3O_4 film, these groups are potentially built into the film lattice and create defects and tiltings in the first layers which decrease with the film thickness. XPS measurements of thin FAZn samples show that the O 1s peak loses its adsorbate shoulder. Therefore, the OH^- groups on the substrate surface are not built in as they

are, but rather are first divided into O and H atoms which incorporate randomly into the film lattice. Interestingly, the big structural differences at the interfaces of FAO and FAZn do not seem to influence the magnetic properties which are investigated by SQUID and PNR. However, the dark region of FAZn could be just highly disordered Fe_3O_4 layer which is still phase pure and results in equivalent magnetic properties as FAO.

Unfortunately, the HAADF-STEM micrographs can not give accurate information on the intermixing effects of Zn atoms in FSO and FSZn films, since Fe and Zn atoms have almost identical atomic mass which results in same image contrast. But it is possible by means of STEM-EELS to make composition profiles across the interfaces of the various Fe_3O_4/ZnO samples. Figure 4.18 presents the corresponding composition profiles with the element specific signals for Fe, O and Zn determined by STEM-EELS by means of reference EELS spectra at the Fe L-edge, O K-edge and Zn L-edge, respectively. Additionally to these three signals, the overall HAADF signal is plotted as a function of the distance covered by the electron beam across the interface.

First, all samples show as expected upwards and downwards trends of the Fe and Zn signals at the interface as well as observable oscillations for the overall HAADF signal which result from the scanning across atomic rows with certain intensities and distances to each other. The interface region is determined as follows. It starts at the point of minimum Fe signal and at the same time maximum of Zn signal while being on a HAADF signal maximum. The interface region ends where the strongest increase of the Fe signal and strongest decrease of the Zn signal stops as well as at the transition point of uniform to much less defined oscillations in the HAADF signal. As expected, FAO has the smallest interface region dimension of about 0.4 nm. FAZn, FSO and FSZn have slightly larger regions of about 0.5 nm. However, FAZn shows no exponential decrease of the Zn signal within the interface region. Here, it is more a linear decrease which can be attributed to an intermixing effect of Zn and Fe atoms at the interface. Moreover, this linear decrease of the Zn signal extends into the film region of FAZn. This probably indicates a moderate Zn diffusion or, more likely, an effect of the large terraces with high steps on its substrate surface, because in the STEM micrographs these high steps are not observed anymore. The vanish of these large steps combined with the assumption of Zn-Fe intermixing could also explain the dark region at its interface.

Surprisingly, in case of FSO and FSZn, the Zn signal decreases exponentially at the interface region too, but in the film region there is still a significant Zn signal which is higher than that measured in FAO. Consequently, this slightly higher Zn intensity in the film region can be attributed to the Zn substitution in the Fe_3O_4 lattice near the interface. The resulting Zn-doped ferrites $Zn_xFe_{3-x}O_4$ near the interface seem to play the main role not only in the electronic but also in the magnetic and fine structure properties of FSO and FSZn.

Finally, FAO looks most defined regarding the interface and chemical composition of the sample layers compared to other three samples.

S. Brück *et al.* identify a change of the Fe valency in the first Fe layer of the grown

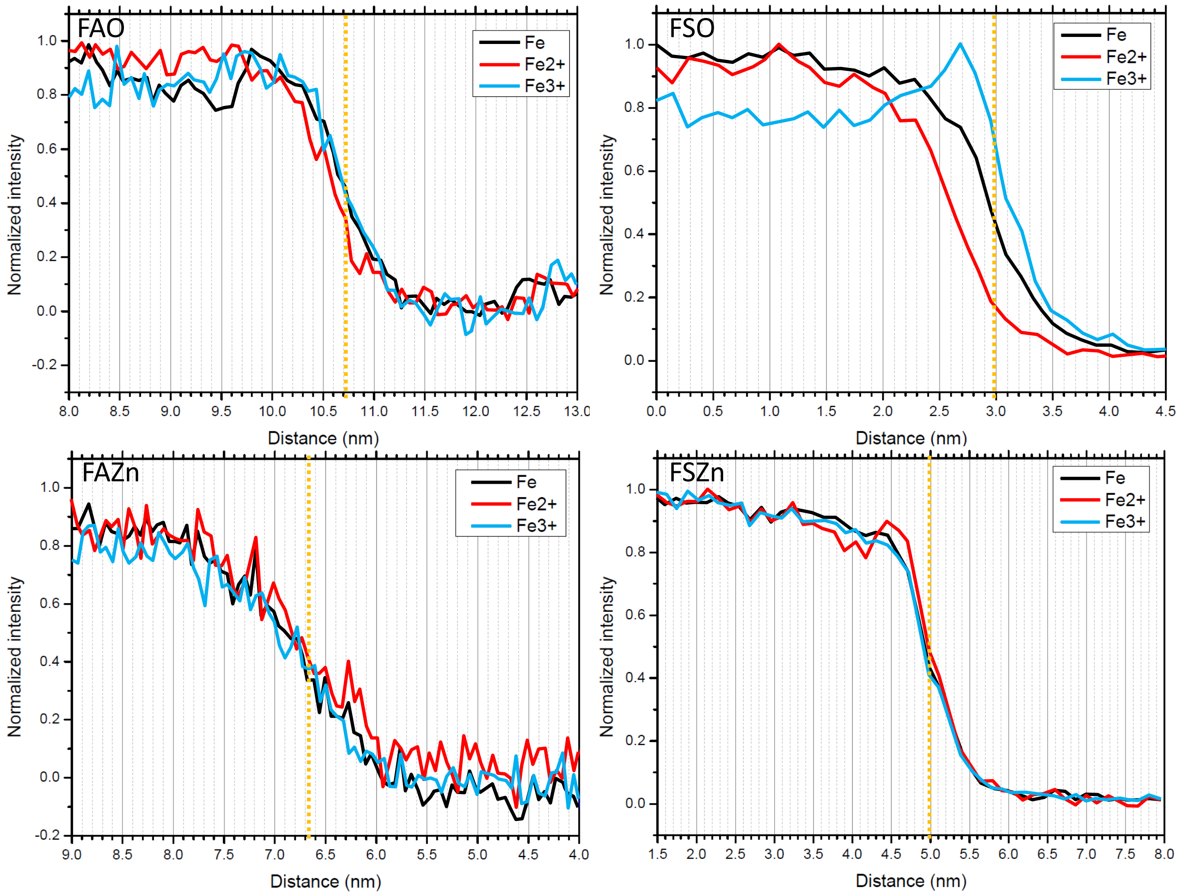

Figure 4.19: *Corresponding Fe valency resolved STEM-EELS line scans of the various Fe_3O_4/ZnO heterostructures generated by scanning the focused electron beam in $[1\bar{1}0]$-direction of the Fe_3O_4 film across the sample interface. The valency specific signal intensities are plotted as a function of the distance covered by the electron beam. Dashed orange lines mark the interface positions.*

Fe_3O_4 film on ZnO [228]. Here, the film is grown on an O-terminated and similarly *in situ* prepared ZnO substrate (as in the case of FSO and FSZn), while its first iron layer indicates only Fe^{3+} ions being determined by STEM-EELS. Additionally, the XRMR measurements suggest the formation of a magnetically dead layer at the interface which may affect the intention to inject a spin polarized current through the interface into the semiconductor.

Oxidation state sensitive STEM-EELS measurements were performed across the interfaces of various Fe_3O_4/ZnO heterostructures to determine the Fe valencies of the first Fe layer. Figure 4.19 demonstrates for each sample the Fe valency specific intensities plotted as a function of the distance covered by the electron beam across the interface. FSO confirms the result of S. Brück *et al.* [228] by showing a Fe^{3+}-peak, whereas FSZn indicates a Fe^{2+}-peak at the interface. Thus, these films which are grown on *in situ* prepared substrates seem to be affected by the termination type of their substrates, re-

sulting in a Fe valency change at the interface. Interestingly, FAO and FAZn do not show any increase in Fe^{3+} or Fe^{2+} intensity at the interface. This means that both films which are grown on *ex situ* prepared substrates are not influenced by the substrate termination type at the interface. These results can not be found in the literature and are possibly essential for the realization of a well working spin electrode that has no magnetically reduced layer at the interface. However, even if STEM-EELS results predict mixed valency for the films of FAO and FAZn at the interface, there are still the corresponding SQUID and PNR results for these samples which indicate clearly a film with reduced magnetization. For the samples with *ex situ* prepared substrates, it must be assumed that the reduced film magnetization is not the result of a possible Fe valency change at the interface, but rather a dislocation, strain or imperfection induced magnetic property of the film region near the interface.
The correct layer sequences, exactly at the interfaces of the the various Fe_3O_4/ZnO heterostructures still remain undetermined, which requires a theoretical approach by density functional theory (DFT) given below.

4.3.7 DFT-calculations for interface properties

A lot of information about the interface properties of the Fe_3O_4/ZnO heterostructures can be obtained by DFT calculations. The most interesting calculation results include the preferred layer sequence at the interface, relaxed structures and spin densities within the samples. This DFT study was performed by Dr. M. Karolak at the chair of theoretical physics I of the University of Würzburg (Würzburg, GER).
In principle, there are 4 different interface types which can be present between the film and the O-terminated ZnO substrate. Their corresponding sequences are as follows.
...-Zn-O-(interface)-[Fe(octa)-O-Fe(tetra)-Fe(octa)-Fe(tetra)-O]-[...]-... (= type A),
...-Zn-O-(interface)-[Fe(tetra)-Fe(octa)-Fe(tetra)-O-Fe(octa)-O]-[...]-... (= type B),
...-Zn-O-(interface)-[Fe(octa)-Fe(tetra)-O-Fe(octa)-O-Fe(tetra)]-[...]-... (= type C) and
...-Zn-O-(interface)-[Fe(tetra)-O-Fe(octa)-O-Fe(tetra)-Fe(octa)]-[...]-... (= type D). On the other hand, for the interface which is between the film and the Zn-terminated substrate, there can occur 2 different types with the following sequences.
...-O-Zn-(interface)-[O-Fe(tetra)-Fe(octa)-Fe(tetra)-O-Fe(octa)]-[...]-... (= type A) and
...-O-Zn-(interface)-[O-Fe(octa)-O-Fe(tetra)-Fe(octa)-Fe(tetra)]-[...]-... (= type B).
All these potential interface types for both O- and Zn-termination are schematically demonstrated in Figure 4.20. The previous TEM study assumes for the O-terminated case mostly the presence of the type A interface. However, the type C interface is also observed by TEM, but much less than the type A interface. For the Zn-terminated case, mainly the type B interface is observed by TEM. Since the energetic situation of the various interface types is not known and exclusion of certain interface types would be highly speculative, a DFT study is needed to get a confirmation about the observed structures and to reveal the energetically most favored interface type for each substrate termination.

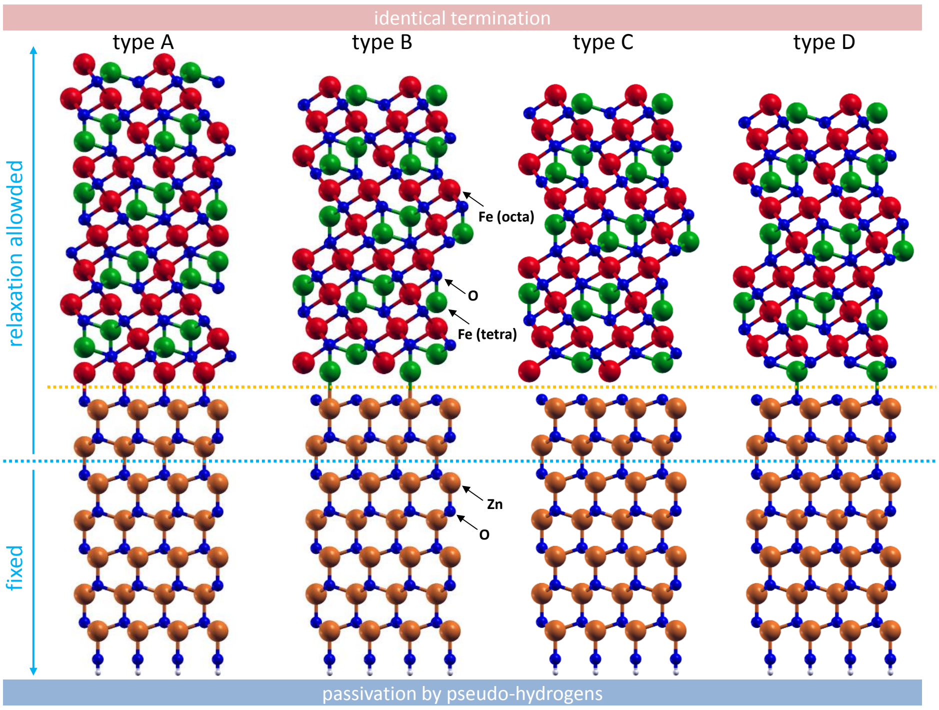

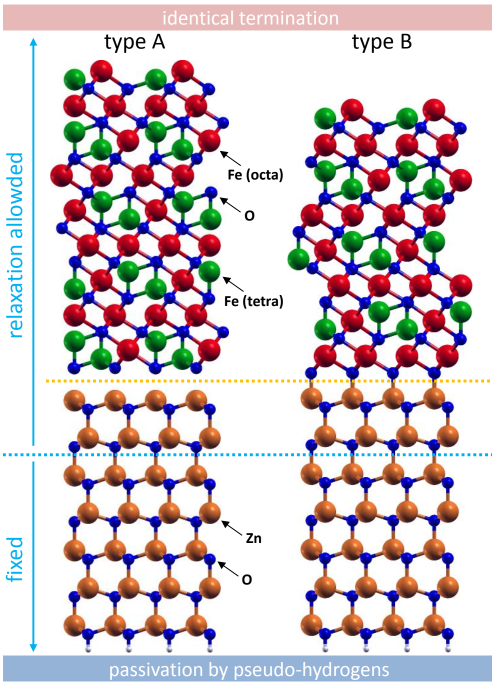

Figure 4.20: *Unrelaxed structures for the* Fe_3O_4/ZnO *heterostructure with O- (top) and Zn-terminated (bottom) substrate shown in the* Fe_3O_4 $[10\bar{1}]$ *and accordingly ZnO* $[\bar{2}110]$ *zone axis. The dashed orange line represents the interface, whereas the dashed blue line separates the fixed region from the region where relaxation is allowed.*

Before the actual relaxation is taken into account it is useful to define the starting geometries of the various structures. Due to the lattice mismatch the lateral lattices of film and substrate do not have certain docking points. However, preliminary analysis indicates that for a few structures the relaxation of the interface tries to move most interfacial ions to energetically more favorable positions which results in an obvious pull effect. As a consequence, all structures have starting geometries that show this effect very reduced in the relaxation. The starting geometries for the various interfaces are schematically presented in Figure 4.20.
The usual approach to compute the energy of a surface/interface is to use the Gibbs free energy or more precisely the surface free energy as

$$\gamma = \frac{1}{A}\left(E_{slab} - \sum_i N_i \mu_i\right) \quad , \tag{4.3}$$

where A is the surface area, E_{slab} the energy of the modeled material slab, N_i and μ_i the number and chemical potential of the atomic species i, respectively. Note that the effects of pressure, temperature ($T=0$ anyway) and vibrational contributions are disregarded which can be actually estimated as demonstrated by K. Reuter and M. Scheffler [239]. In case of Fe_3O_4/ZnO heterostructures, Equation 4.3 with the corresponding atomic species can be written as

$$\gamma = \frac{1}{A}\left(E_{slab}^{DFT} - N_{Fe}\mu_{Fe} - N_{Zn}\mu_{Zn} - N_O\mu_O\right) \quad , \tag{4.4}$$

where E_{slab}^{DFT} is the DFT total energy which contains the following terms as

$$E_{slab}^{DFT} = E_{atoms} + E_{top} + E_{bottom} + E_{interface} \quad , \tag{4.5}$$

while the bottom and top surfaces are the same in all cases, thus only the atomic and interface energies remain. The chemical potentials for the atomic species can be equated with the DFT bulk energies to

$$\gamma = \frac{1}{A}\left(E_{slab}^{DFT} - N_{Fe}E_{Fe}^{bulk} - N_{Zn}E_{Zn}^{bulk} - N_O E_O^{bulk}\right) \quad . \tag{4.6}$$

But, the fact that the bulk states have much different configurations and the interpretation of bulk oxygen is difficult, one has to consider that chemical potentials used in Eq. 4.6 are not independent, due to the following relation

$$\begin{aligned} \mu_{Fe_3O_4} &= 3\mu_{Fe} + 4\mu_O \quad \text{and} \\ \mu_{ZnO} &= \mu_{Zn} + \mu_O \quad . \end{aligned} \tag{4.7}$$

Therefore, any two potentials can be defined using the third independent potential. Typically oxygen is used for this, because an accurate upper limit on its chemical potential is well known [239]. Therefore, Equation 4.6 transforms to

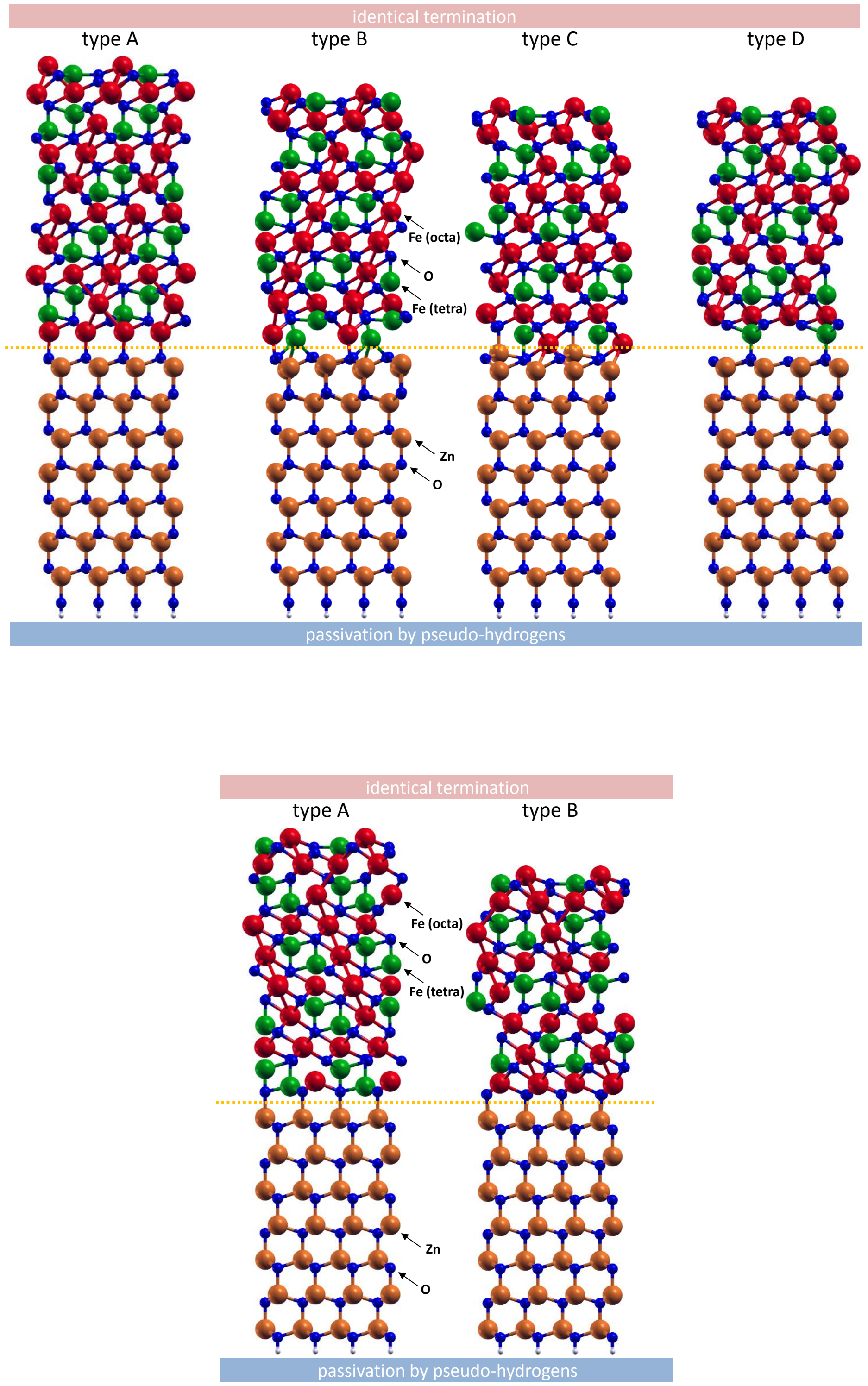

Figure 4.21: *Relaxed structures for the Fe_3O_4/ZnO heterostructure with O- (top) and Zn-terminated (bottom) substrate shown in the Fe_3O_4 $[10\bar{1}]$ and accordingly ZnO $[\bar{2}110]$ zone axis. The dashed orange line represents the interface.*

$$\gamma = \frac{1}{A}\left[E_{slab}^{DFT} - \frac{N_{Fe}}{3}E_{Fe_3O_4}^{bulk} - N_{Zn}E_{ZnO}^{bulk} - \left(N_O - N_{Zn} - \frac{4}{3}N_{Fe}\right)\mu_O\right] \quad . \tag{4.8}$$

Since Fe_3O_4 is slightly strained at the interface, the bulk energy of the strained Fe_3O_4 is used.

The chemical potential of oxygen can not vary without limits. An accepted upper limit is half of the oxygen molecule energy at *T=0* [239] which is given as

$$\max[\mu_O] = \frac{1}{2}E_{O_2} \quad , \tag{4.9}$$

whereas the lower limit for μ_O can be inferred from the formation heat of Fe_3O_4 which is then located about -3 eV lower than the upper limit.

One should also note that all structures with respect to their substrate type (O- or Zn-terminated) have identical film surface terminations as well as an identical passivation by pseudo hydrogens which is illustrated in Figure 4.20. Additionally, for structure relaxation procedure defined certain regions were allowed to relax, while others were fixed.

The resulting relaxed structures for the Fe_3O_4/ZnO heterostructures with O- and Zn-terminated substrate are illustrated in Figure 4.21. In case of O-terminated substrates, the four interface types show apparently different structures. Type A shows the most defined interface structure with a good match of film to substrate lattice. Note again that this type is observed in STEM micrographs most often as well. In contrast, interface types B, C and D have structures which differ much from that of the starting geometries. These three types should be conspicuous in STEM micrograph analysis due to the change in structure and density. Thus, interface types B, C and D seem to be less present at the real interface, since corresponding changes were not observed in STEM data. Moreover, type D changes its interface structure completely (not shown) during the relaxation. As a consequence Type D is actually not involved in the possible interface types which can be present within the heterostructure.

For the Zn-terminated case, interface type A as well as type B seem to be similarly well defined without too big changes from their starting geometries. Moreover, no obvious change in density near the interface can be observed for both types, thus both could be in principle present at the Zn-terminated surface. However, the previous STEM micrographs observed mostly type B. But this still needs to be confirmed.

As a next step, an energetic view is given to determine and confirm the correct interface type for both substrate terminations with respect to the surface energies. Note that the DFT calculations are done by the generalized gradient approximation including the Coulomb repulsion term U (GGA+U). In Table E.1 and E.2 (see Appendix E) all important data from the DFT calculations are listed. Figure 4.22 presents the Gibbs free surface energies for the corresponding interface types as a function of the chemical potential of oxygen. Since in several publications the U for Fe_3O_4 is estimated to be

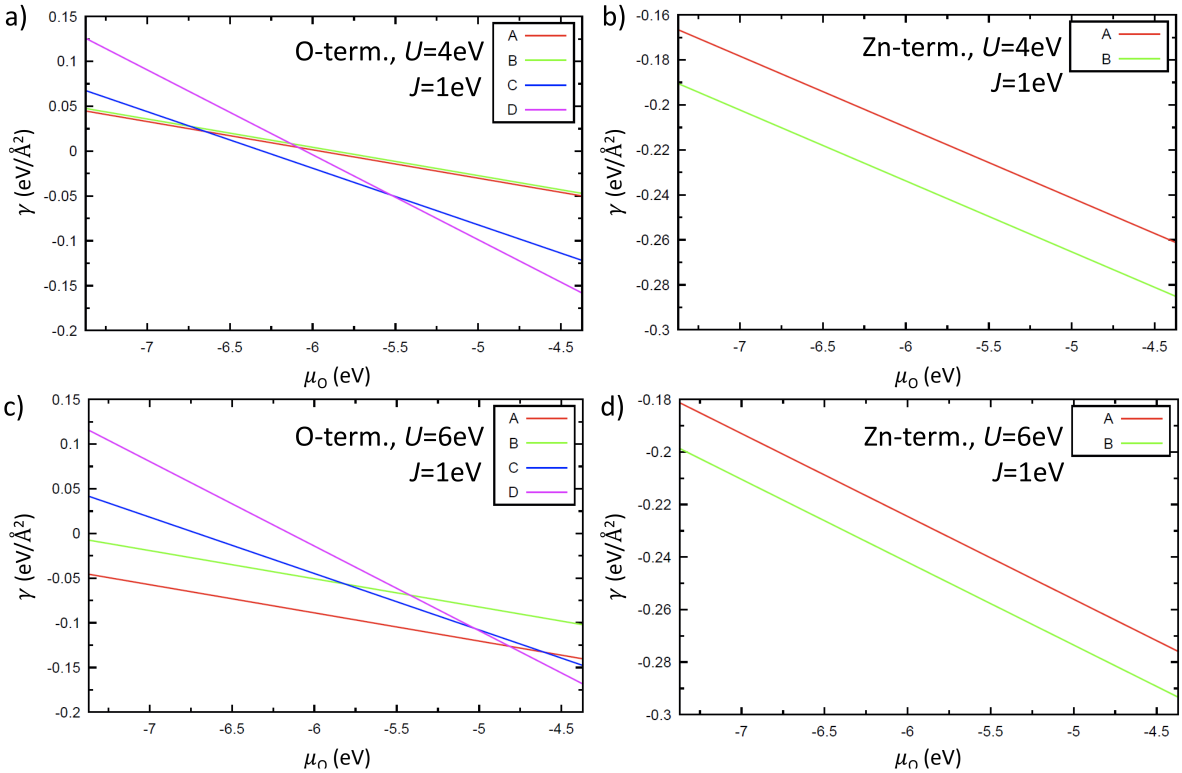

Figure 4.22: *Gibbs free surface energies γ of the determined interface types in the Fe$_3$O$_4$/ZnO heterostructures with (a and c) O-terminated and (b and d) Zn-terminated substrates plotted as a function of the chemical potential of oxygen μ_O. The calculations were performed for (a and b) U=4 eV, J=1 eV as well as for (c and d) U=6 eV, J=1 eV.*

about 3 eV to 6 eV, first the calculations were performed with U=4 eV, while the Hund's exchange coupling was J=1 eV. The resulting functions are plotted in panels a) and b). For the O-termination, interface types C and D seem to be energetically more favored than A and B for the half of the region of μ_O. As mentioned above, these both types C and D, are disclaimed by the results of the STEM study and especially type D due to the complete changing of its interface during the relaxation. For the Zn-termination, the situation seems to be more clear. Here, interface type B is energetically favorable for the full range of μ_O which is consistent with the observations by STEM. Furthermore, the similar calculations were also done for U=6 eV. The results for U=6 eV are demonstrated in panels c) and d). For the O-terminated case the results differ significantly from those with U=4 eV. Here, the functions of the four interface types show a more distinct trend. While now type C and D are energetically most unfavorable, type A indicates the lowest energy for almost the whole range of μ_O. Type B is between these three types. For the Zn-termination with U=6 eV, the situation is not much different than for U=4 eV. Even here, interface type B is obviously energetically more favorable than type A. The results with U=6 eV for the interface of Fe$_3$O$_4$/ZnO heterostructures with both O- and Zn-terminated substrates confirm the assumptions from the STEM

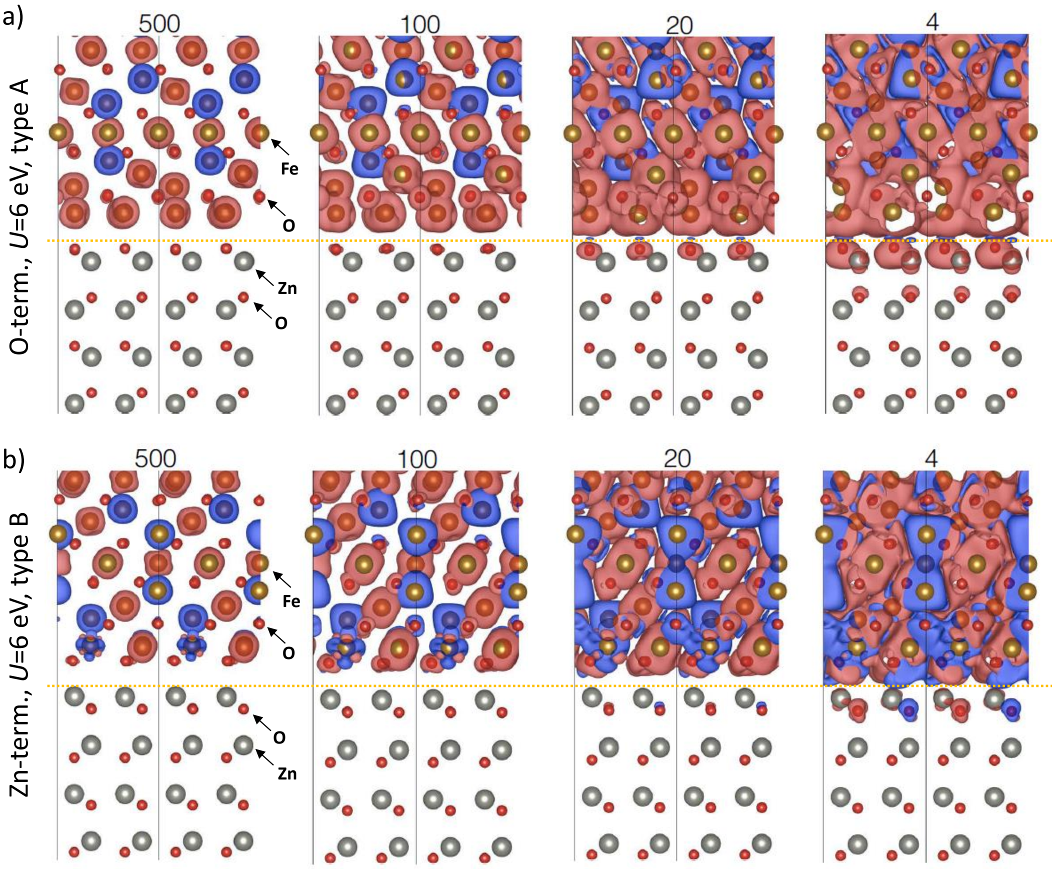

Figure 4.23: *Spin densities in Fe_3O_4/ZnO heterostructures with (a) O-terminated and (b) Zn-terminated substrates for U=6 eV. The dashed orange line indicates each interface. The calculations are done for the favored interface types, type A for the O-terminated and type B for the Zn-terminated case with different isosurface values, while spin-up and spin-down are marked red and blue, respectively.*

study. The interface with O-terminated substrate prefers the type A, whereas the interface with Zn-terminated substrate favors the type B.

One should keep in mind that the choice of the free parameter in Equations 4.7 and 4.8 is of secondary importance. The Gibbs free surface energy can be expressed also as a function of the iron chemical potential and can be written as

$$\gamma = \frac{1}{A}\left[E_{slab}^{DFT} - N_{Zn}E_{ZnO}^{bulk} + \left(\frac{N_{Zn}}{4} - \frac{N_O}{4}\right)E_{Fe_3O_4}^{bulk} \right.$$
$$\left. - \left(N_{Fe} + \frac{3}{4}N_{Zn} - \frac{3}{4}N_O\right)\mu_{Fe}\right]. \tag{4.10}$$

Here, the limits for the chemical potential of iron are not that defined as for oxygen, but using

$$\mu_{Fe_3O_4} = 3\mu_{Fe} + 4\mu_O \quad , \tag{4.11}$$

and by estimation of the chemical potential of oxygen to the value which is used in Equation 4.9, the exactly same results are retrieved. Therefore, both approaches are consistent.

Furthermore, spin density calculations were performed for the two favored interface types with the corresponding substrate termination. The spin densities which are illustrated in Figure 4.23 are determined for different isosurface values (surfaces of constant value of the magnetization density $= (\rho_{\uparrow}(\vec{r}) - \rho_{\downarrow}(\vec{r}))/V^3$, with its unit $[N_{electrons}/\text{Å}^3]$) and for a Coulomb repulsion term of U=6 eV. The spin up and down states are colored red and blue, respectively. The spin density for the O-terminated interface is shown in panel a) and indicates for the first two Fe layers a spin polarization compared to the rest of the film which is well observable for its isosurface "500". Interestingly, due to the spin polarized first film layers (here mostly spin-up, marked in red) the topmost substrate layers seems to imitate this behavior which is observable for its isosurface "4". Moreover, oxygen atoms of the O-terminated substrate surface are affected much stronger than the first Zn atoms, resulting by the orbital configuration in ZnO. A strong decrease of this effect to deeper substrate regions is given too, making the substrate surface sensitive for the polarization. Thus, in terms of spin injection from Fe_3O_4 into ZnO, these topmost O layer in ZnO could play an essential role. In contrast, panel b) shows the spin density for the Zn-terminated interface which acts totally different. Here, no spin polarized film layers near the interface exist, yielding to an alternating spin orientation within each plane in the topmost ZnO layer, again mostly at the O atoms. However, the polarized spin density in case of O-terminated interface is not present for all U values. In Figure E.1 (see Appendix E), the spin densities for both terminations are illustrated for U=4 eV. While the Zn-terminated interface shows the same character as for U=6 eV with a laterally alternating spin orientation in the topmost substrate region, the O-terminated interface exhibits no spin polarization in the first Fe layers anymore and even neither an alternating spin orientation in the substrate surface as given at the Zn-terminated interface. The results for the case of U=4 eV can be disregarded due to the previous calculations of the Gibbs surface energies and experimental results. Nevertheless, to determine the correct spin configuration at the interface of Fe_3O_4/ZnO heterostructures much more analysis is required, especially on the part of experiment which could give information about the interface type that is probably most promising for efficient spin injection into the substrate. For the sake of completeness, the corresponding layer resolved spin densities for U=6 eV which are generated by cuts in [110]-direction at different substrate depths, are displayed in Figure E.2 (see Appendix E).

Additionally, the density of states (DOS) was calculated for each Fe atom which differ in their localization in the Fe layers and coordination (not shown). The formal +2 and +3 valencies of the Fe atoms directly at the interface can not be distinguished by this method. However, there are differences between the O- and Zn-terminated interfaces

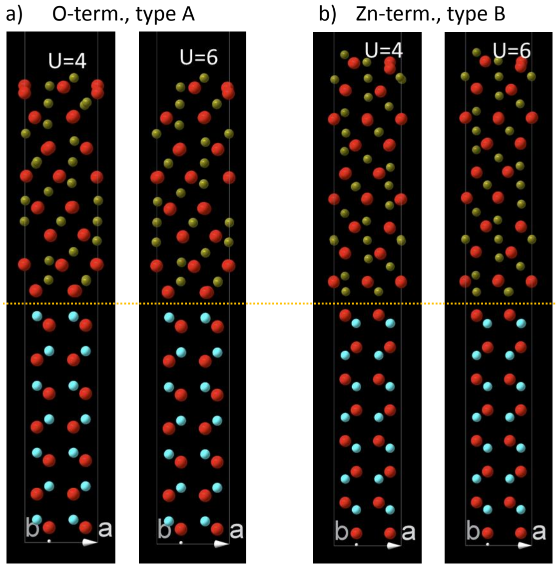

Figure 4.24: *Presentation of the energetically favored interface structure types in Fe_3O_4/ZnO heterostructures with (a) O-terminated and (b) Zn-terminated substrate for U=4 and 6 eV. The dashed orange line indicates the interface.*

when it comes to d orbital population. For bulk Fe_3O_4 all Fe atoms have d orbital fillings of 5.94 to 6.00 electrons (e^-). The calculations reveal an accumulation of charge (about 6.16 e^-) at the O-terminated interface, resulting in 18.48 e^- per u.c. at the interface. In contrast, a depletion of charge (about 5.88 e^-) is observed at the Zn-terminated interface, resulting in 17.76 e^- per u.c. at the interface. This means that for the O- and Zn-terminated cases the nominal Fe valencies at the interface are +2 and +3, respectively. This result is completely opposite to the observation from STEM-EELS measurements at the interfaces of samples with *in situ* prepared substrates (see Figure 4.19). However, one should note that the samples with *ex situ* prepared substrates do not show similar valency changes, which makes the comparison of the various results even more difficult. Moreover, the calculated d orbital fillings have been obtained from integrating the orbital projected DOS up to the Fermi level, while this DOS is not perfectly normalized to 1 (rather 0.95). Thus, these numbers have to be considered as preliminary. However, the trend given by those numbers should be real. Possible reasons for this discrepancy can be dislocations at the interface as well as the minimization of the lattice mismatch between film and substrate before the initial relaxation process from the calculations.

Finally, STEM simulations of the energetically favored interface structures for both interface termination types were performed to compare these with their real space STEM micrographs. Figure 4.24 shows the corresponding converged interface structure types for U=4 and 6 eV generated by the DFT calculations. The comparison of interface structures of one termination type at two different U values indicates no significant differences. The STEM simulations were performed for a 20 nm thick Fe_3O_4 film on

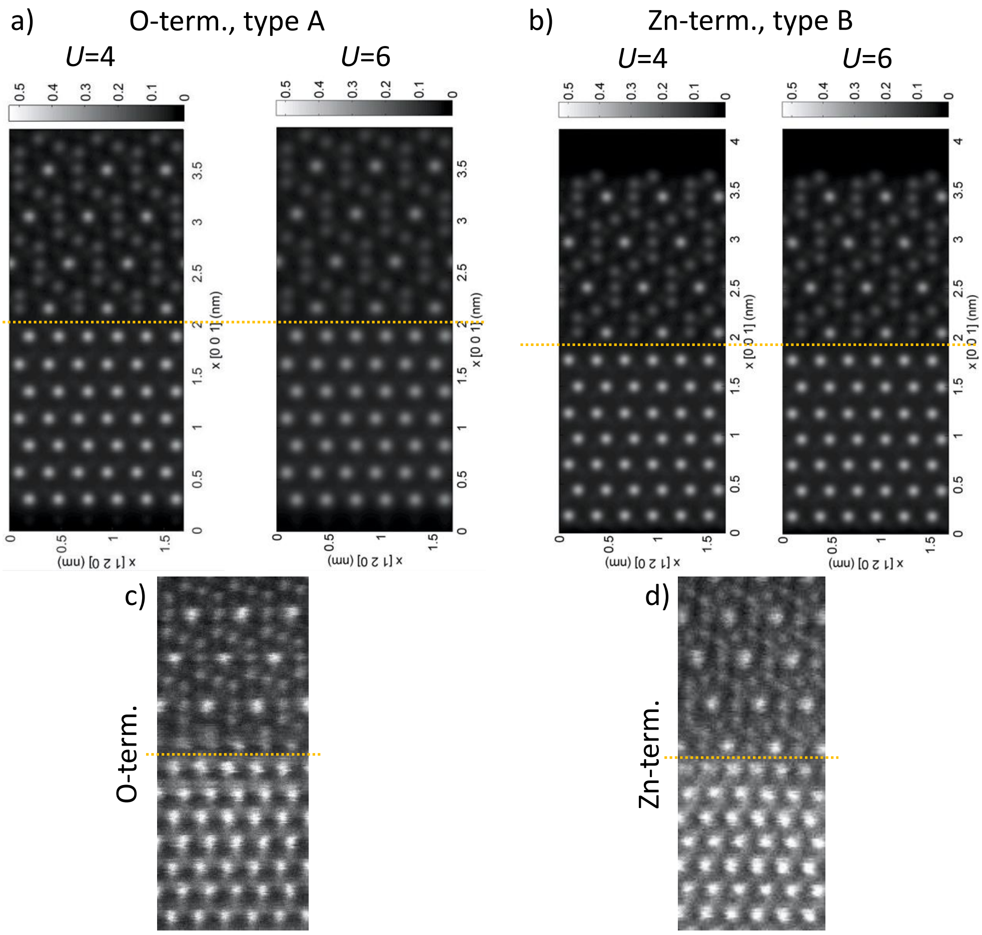

Figure 4.25: *STEM simulations of the interface structure types in Fe_3O_4/ZnO heterostructures with (a) O-terminated and (b) Zn-terminated substrate for U=4 eV and 6 eV. Real STEM micrographs of the interface regions in Fe_3O_4/ZnO heterostructures with (c) O-terminated and (d) Zn-terminated substrate. The dashed orange line indicates the interface.*

ZnO based on the respective interface structure types from the DFT calculations. For the simulation a special software named STEMSim is used [240]. Figures 4.25 a) and b) demonstrate the resulting STEM simulations of the interface structure types with O- and Zn-terminated substrate, respectively. Again, for each substrate termination type the results for U=4 and 6 eV are equivalent concerning the interface structure. Figures 4.25 c) and d) present the real STEM micrographs of the interface regions with the corresponding substrate termination. It is obvious that the simulations are in very good agreement with the real space STEM images of the samples, corroborating the correct interface structure types which are supposed from DFT for each termination type.

5 (RP–214) iridate thin films on terminated STO substrates

This chapter deals with the growth of (RP–214) iridate thin films on STO substrates by means of pulsed laser deposition (PLD) as well as with the characterization of their physical properties. A big challenge is to produce well defined stoichiometric (phase pure RP–214) BIO, SIO and La-doped SIO films with high quality comparable to some recent publications. Another crucial objective is to analyze these PLD grown iridate films by ARPES and to make a statement about their suitability for being studied by this characterization method. In the following chapter the crystalline and electronic structure of the PLD grown films will be investigated by several surface and volume sensitive characterization methods. Three different film types will be compared to each other at every characterization step.

5.1 Preparation of STO substrates

To achieve epitaxial growth of (RP–214) iridates on STO(001) substrates, the substrate surface has to be homogeneous, atomically flat and exhibit a defined termination. In the case of perovskite STO(001) single crystals, there are two chemical treatments established to obtain a TiO_2 terminated surface [241, 242]. In this thesis the preparation method of G. Koster *et al.* [242] is used which is carried out as follows. The commercially available single crystalline undoped, as well as Nb-doped, STO(001) substrates, which both have a mixed surface termination, are cleaned first with acetone and afterwards with ethanol for about 15 min. each in an ultrasonic bath. After being blow-dried with N_2 gas, the substrates are immersed into ultra pure demineralized water for about 30 min. in the ultrasonic bath. At this step, the SrO terminated surface areas react with water and produce SrOH complexes, whereas the TiO_2 surface areas remain unaffected due to their high chemical stability against water. Thus, the SrOH complexes can be further removed by immersing the substrates into an acidic solution of NH_4-HF for about 30 sec. After neutralization of the residual acid on the substrates by soaking into ultra pure demineralized water the substrates are blow-dried with N_2 gas before they are transferred into the crystal furnace. Finally, the substrate is annealed at 950°C for 90–120 min. under dry oxygen gas atmosphere (purity about 99.5%) that exhibits a flow of about 0.5 liters/min. Note that the length of the annealing step strongly depends on the crystal miscut angle, e.g. smaller miscut angles result in larger terraces on the substrate surface and consequently need more time to recover. With the help of AFM

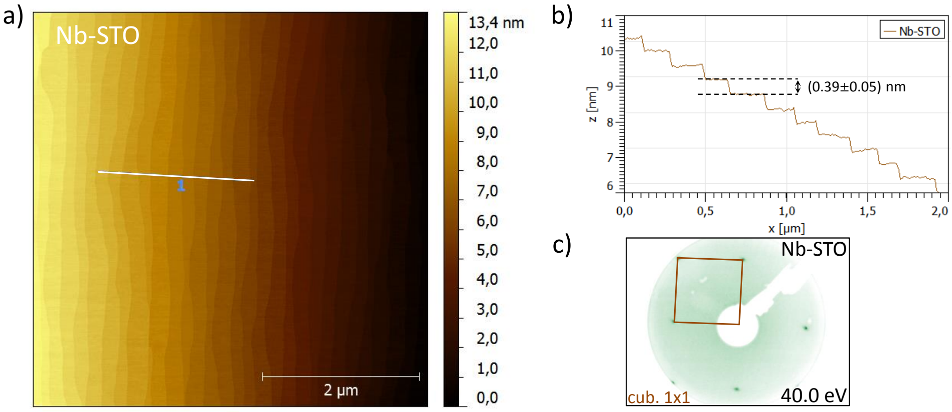

Figure 5.1: *(a) AFM surface morphology picture and (b) corresponding height profile and (c) LEED pattern of a terminated 0.1 wt% Nb-doped STO(001) substrate with* TiO_2 *surface.*

measurements it can be easily checked whether the substrate surface preparation is successfully completed or not.

5.1.1 Surface morphology and structure of terminated STO substrates

Figure 5.1 a) demonstrates a typical AFM morphology image of a terminated 0.1 wt% Nb-doped STO(001) substrate, displaying a homogeneous TiO_2 termination. The surface exhibits a characteristic terrace structure with step heights of (0.39±0.05) nm which is caused by the miscut of the substrate. The corresponding height profile is shown in Figure 5.1 b). The value of the step heights is in the same range as the lattice constant of a STO unit cell which in turn confirms a single-terminated surface. Additionally, Figure 5.1 c) presents the corresponding LEED pattern, displaying the unreconstructed 1x1 surface structure of the cubic perovskite STO(001).

Note that a SrO terminated surface of STO(001) single crystals can be obtained by growing a single layer of SrO on a TiO_2 terminated substrate. However, all (RP–214) iridate films in this thesis were grown on TiO_2 terminated substrates indicating well defined and atomically flat surfaces which provides best conditions for the epitaxial growth process.

5.2 Growth of (RP–214) iridate thin films

Within the past two decades a lot of studies on the topic of (RP) iridates were performed, mostly on bulk single crystals, whereas there are not so many publications on epitaxial growth of (RP) iridate thin films up to date. Moreover, for (RP–214) iridate film, there is only a very limited number of studies being done during the last few years. Studies on MBE grown (RP–214) iridate films are mainly done by the working group of K. M.

Table 5.1: *Parameters for the PLD growth of (RP–214) iridate films on STO(001) substrates.*

(RP–214) iridate film	BIO	SIO	LSIO
substrate temperature T_S [°C]	810	800	830
laser fluency F [J/cm^2]	2.0	2.0	2.0
repetition rate ν [Hz]	1.0–1.5	0.6	1.5
relaxation period R [sec.]	60	none	none
O_2 *partial pressure* p_{O_2} [mbar]	$8.0\text{–}5.1\cdot10^{-2}$	$4.6\cdot10^{-2}$	$7.0\cdot10^{-2}$

Shen [61, 63]. In case of PLD grown films, there are only a few more publications available [64, 65, 243–245]. Moreover, no ARPES study is published on PLD grown (RP–214) iridate films yet, raising some questions about the usability of such grown samples for this type of characterization method. Up to date, there are only ARPES measurements published for MBE grown (RP–214) iridate films [61, 63]. Note that for other (RP) phased materials, e.g. titanates and manganates, it seems that for their PLD grown (RP–113) phase a lot of ARPES data are available, while this is not the case for their other (RP) phases grown with the same technique. In this thesis a possible reason for this discrepancy will be presented beside the analysis of the physical properties of the PLD grown (RP–214) BIO, SIO and La-doped SIO films.

For the growth of (RP–214) iridate films via PLD, the polycrystalline targets of BIO, SIO and 20% La-doped SIO phase ($La_{0.2}Sr_{1.8}IrO_4$, from now on denoted as LSIO) were provided by Dr. M. Isobe from the Strongly Correlated Materials Group of NIMS (National Institute of Materials Science, Tsukuba, JPN). The doping level of 20% in LSIO is choosen with regard to the theoretical study by H. Watanabe *et al.* predicting a superconducting phase for this electron doping concentration [68]. In LSIO the doping level of 20% is defined as the number of electrons on the mixed-valence atom, resulting in 0.2 electrons on one Ir ion (Ir^{4+} + 0.2 e^-). All target materials were analyzed by powder XRD measurements, indicating pure (RP–214) phases without secondary or mixed phases (not shown). Before transferring into the UHV PLD system, the targets were carefully sandpapered to obtain planar target surfaces. A KrF excimer laser (COHERENT COMPexPro, λ=248 nm) was used for the material ablation and its beam was focused onto the target surface forming a spot size of about 1.2 mm^2. Furthermore, the ablation spot was centered to the middle of the sample holder. The substrate surface was placed at a distance of about 5.3 cm parallel to the target surface. The lattice mismatch ($(a_{substrate}-a_{film})/a_{substrate}$) of bulk BIO and bulk STO is –3.2%, resulting in an in-plane compressive strain on the BIO thin film. In contrast, the lattice mismatch of bulk SIO and bulk STO is only +0.46%, causing a weak in-plane tensile strain of the SIO thin film, as well as for LSIO.

In terms of the chosen growth parameters for each material system one should keep in mind that the parameter values from the few publications about (RP–214) iridate thin film growth vary significantly. Since RHEED oscillations are a good indication of epita-

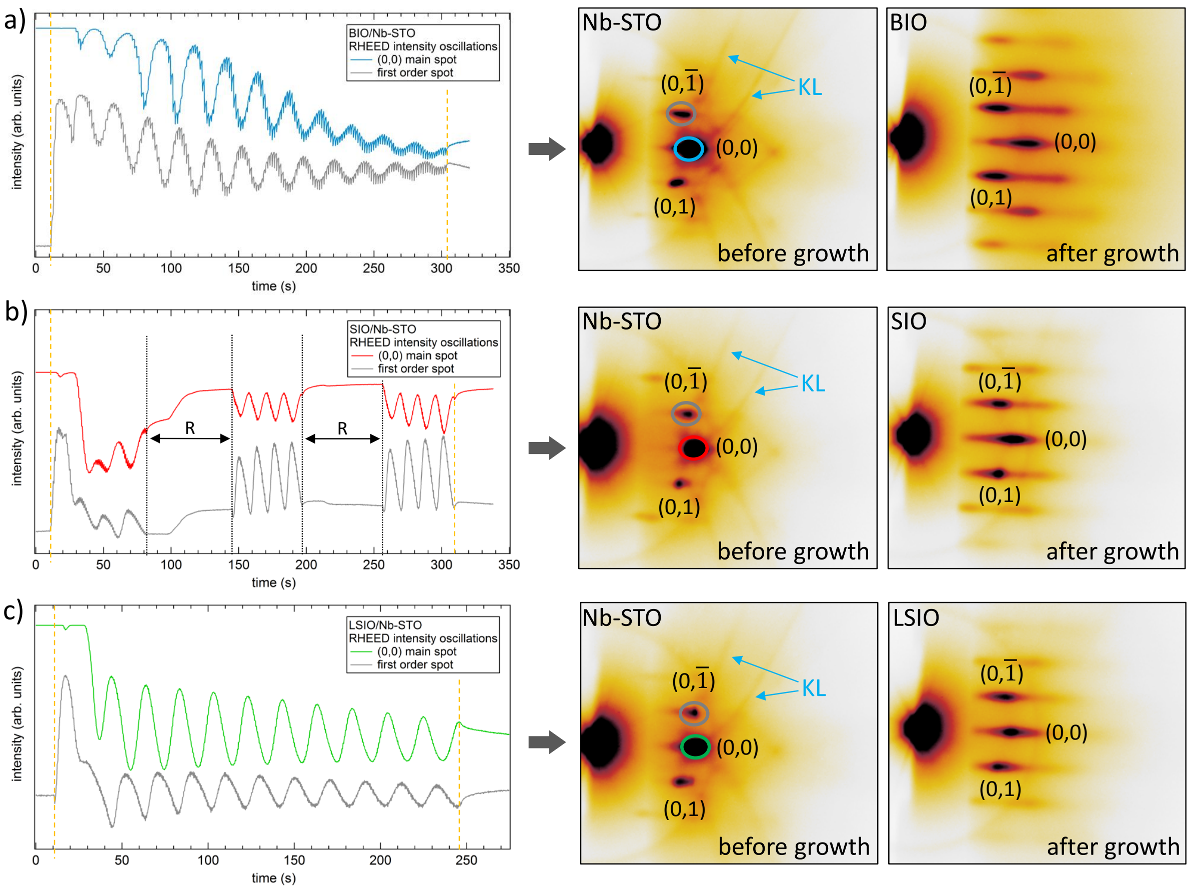

Figure 5.2: *RHEED oscillations and corresponding RHEED patterns before and after growth process for (a) 13 ML BIO, (b) 12 ML SIO and (c) 12 ML LSIO. The dashed orange lines in the oscillation plots represent start and end of the growth process. For SIO (see (b)), the intermittent relaxation periods are marked by "R". Clearly observable Kikuchi lines in the RHEED patterns of the Nb-doped STO substrates are indicated by "KL".*

xial layer-by-layer (Frank-van-der-Merwe) growth, the growth parameters are optimized in such a way that equidistant RHEED oscillations with highest amplitudes are observed and the resulting RHEED pattern with the corresponding Laue spots of the grown film indicates a two dimensional flat surface. Thus obtained growth parameters for BIO, SIO and LSIO films are given in Table 5.1.

Figure 5.2 presents the RHEED oscillations and RHEED paterns before and after the growth process of each grown (RP–214) iridate thin film with a thickness of about 12 monolayer (ML). In the case of BIO grown on Nb-doped STO (see Figure 5.2 a)), the oscillations are in fact equidistant but show after approximately the 5th oscillation a decrease of their amplitudes. A reason for this can be a transition from two dimensional layer-by-layer growth to island-like growth possibly caused by the relatively high lattice mismatch of the two materials. Moreover, the resulting RHEED pattern after growth shows streaky Laue spots and also additionally rudimentary spots which are a clear sign

of a not perfectly flat surface.
For the growth of SIO on Nb-doped STO (see Figure 5.2 b)) it turned out that additionally integrated relaxation periods promote the development of well defined RHEED oscillations. For that reason the SIO films were grown as follows. The first four ML were grown at 1.0 Hz and at a sightly higher O_2 partial pressure as afterwards. The next ML were grown at 1.5 Hz and at a bit reduced O_2 partial pressure (see Table 5.1). After every four ML a relaxation period of about 60 sec. was inserted. Thus, the oscillations increase their amplitudes, indicating an improvement of the layer-by-layer growth. Furthermore, the final RHEED pattern shows sharp Laue spots without the intense streaks as it is the case for BIO. Additional rudimentary Laue spots are missing too, revealing a smooth two dimensional film surface.
In the case of LSIO on Nb-doped STO (see Figure 5.2 c)), the oscillations are almost perfect in terms of equidistance and stability of the amplitude height. Its RHEED pattern after growth demonstrates an equal film surface quality as SIO.
The trick of inserting a relaxation periods into the growth process causing an improvement of the surface quality works only for SIO films. For BIO, such additional periods make the oscillations even worse, while for LSIO no changes in the trend of the oscillations are observed.
Note that for PLD grown (RP–214) iridate thin films there are no published RHEED oscillations yet mentioned.

5.3 Characterization of (RP–214) iridate thin films

In the following, the PLD grown (RP–214) iridate thin films on STO(001) substrates will be analyzed by a set of *in situ* and *ex situ* characterization methods. First of all, the films are analyzed by AFM and LEED. Additionally, their bulk film properties are explored by XRD and transport measurements are performed to determine their electrical behavior. Moreover, chemical depth profiles are made by XPS to determine their volume stoichiometry as well as ARPES experiments performed to characterize their electronic structures and to compare the data to already published studies of the same film materials. Finally, a TEM study is executed to determine the microstructure of the (RP–214) iridate films in detail, especially with regard to the stacking sequence.

5.3.1 Surface morphology and structure

Figure 5.3 presents the AFM images of 6 ML (≈4 nm) thick BIO, SIO and LSIO films. In row a) 5x5 μm^2 large images are shown. Here, all three films exhibit the terrace structure which is caused by the stepped substrate surface. Their film surfaces seem to be homogeneous and smooth. The enlarged 1x1 μm^2 images (row b)) display better resolved surface morphologies, while the corresponding height profiles of their terrace areas are demonstrated in row c). For BIO, the coverage of the last grown layer seems

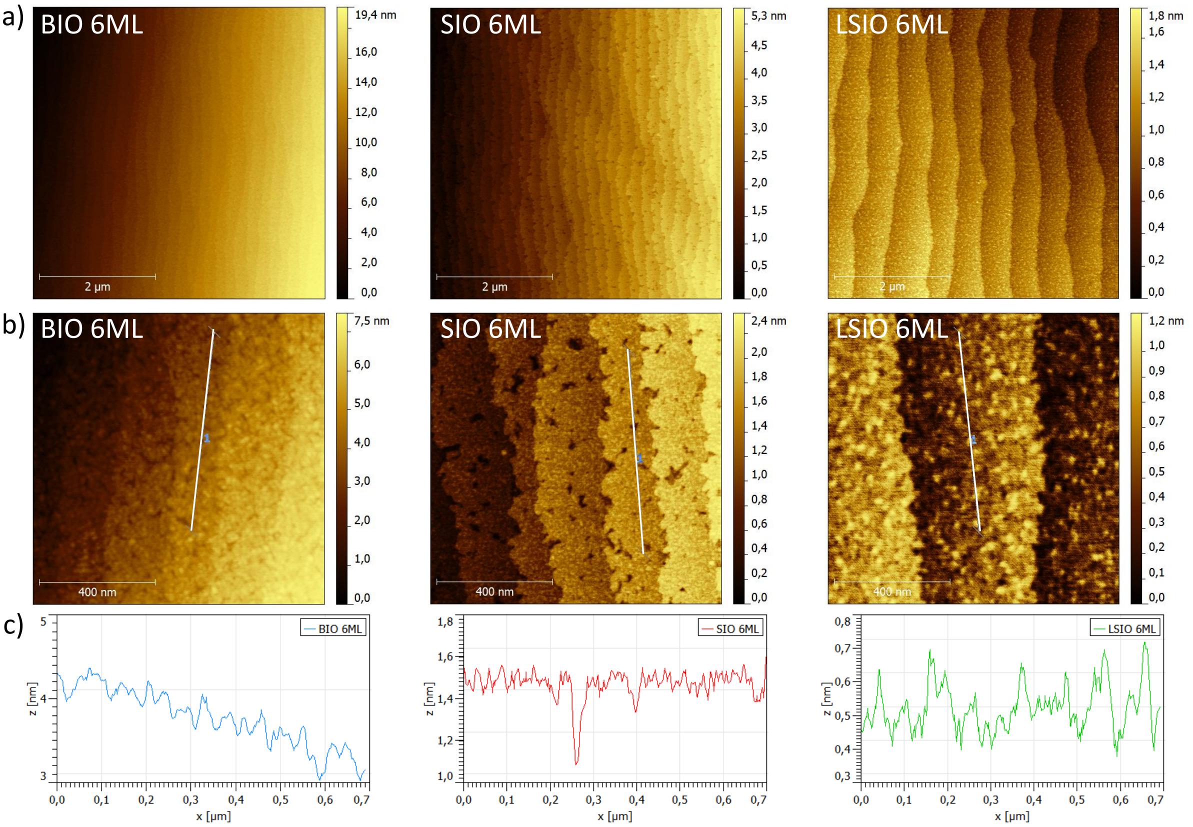

Figure 5.3: *(a) 5x5 μm^2 and (b) 1x1 μm^2 AFM pictures of the 6 ML thick (RP–214) iridate films grown on TiO_2 terminated 0.1 wt% Nb-doped STO(001) substrates and (c) the corresponding height profiles.*

to be completed. Its height profile indicates a homogeneous surface with a roughness of (0.2±0.05) nm.

In contrast, for SIO the enlarged AFM image displays approx. 0.4 nm deep holes on the terrace areas. The holes can be caused by an uncompleted last layer of the film due to lack of material to close the layer. This hypothesis can be real, because the depth of the holes are in the same range as the lattice constant of one unit cell of SIO. However, it is also possible that this is an initial state of a following island growth mode. Excluding these holes, the surface roughness of the thin SIO film is (0.1±0.05) nm.

For the LSIO film it is the other way around. Here, the last layer is indeed closed but there are a lot of particles on the terrace areas which could be caused by additional deposited material after completing the assumed last layer. The surface roughness for the thin LSIO film is (0.27±0.05) nm. But such a film surface morphology can be the beginning of island growth too.

To check if much thicker films show a transition to island growth, samples with 40 ML (≈26 nm) thick films were grown and analyzed by AFM and afterwards also by XRD (see subsection 5.3.2). Note that for these thick films RHEED oscillations are clearly

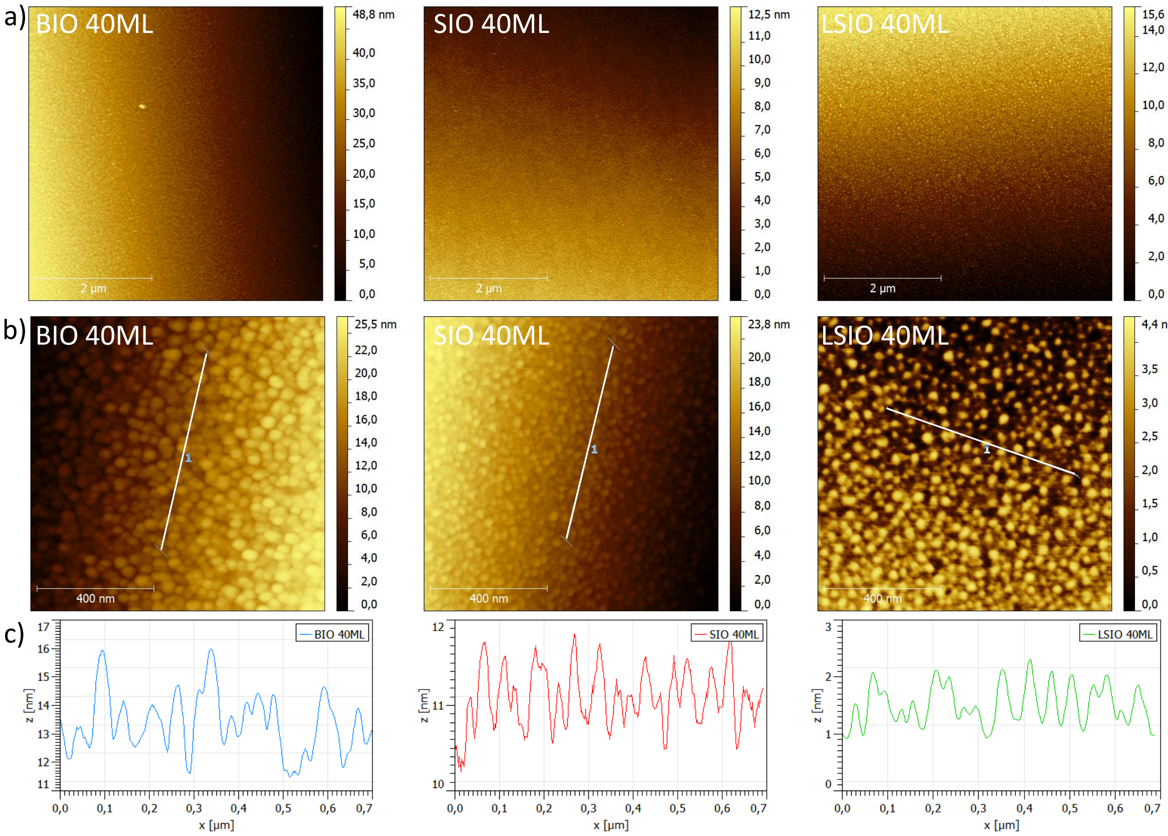

Figure 5.4: *(a) 5x5 μm^2 and (b) 1x1 μm^2 AFM pictures of the 40 ML thick (RP–214) iridate films grown on TiO_2 terminated 0.1 wt% Nb-doped STO(001) substrates and (c) the corresponding height profiles.*

visible till the end of their growth (not shown), although their oscillation amplitude is smaller. The final RHEED patterns show for all three thick films similar Laue peaks as for thin films. Figure 5.4 a) demonstrates the 5x5 μm^2 large AFM images of 40 ML thick BIO, SIO and LSIO films. Here, all three films exhibit no terrace structure on their surfaces anymore caused by the large film thickness. Their film surfaces seem to be homogeneous and smooth at first. However, again the enlarged 1x1 μm^2 images (see b)) resolve the surface morphologies in more detail, while the corresponding height profiles of their surfaces are demonstrated in c). All three samples have clearly visible islands on their surfaces which are in every case about (0.04 ± 0.02) μm wide. Even SIO (LSIO) with its negligible small lattice mismatch to STO has clearly observable islands. The film surface roughness is highest for BIO with (2.0 ± 0.4) nm and smallest for LSIO with (0.5 ± 0.1) nm, whereas for SIO it is (0.7 ± 0.1) nm. Interestingly, the roughness values seem to correlate with the uniformity of observed RHEED oscillations during the respective film growth process (see Figure 5.2).

The LEED patterns of 12 ML ($\approx$8 nm) thick RP–214) iridate films BIO, SIO and LSIO are presented in Figure 5.5. Note that the LEED patterns for much thicker films show

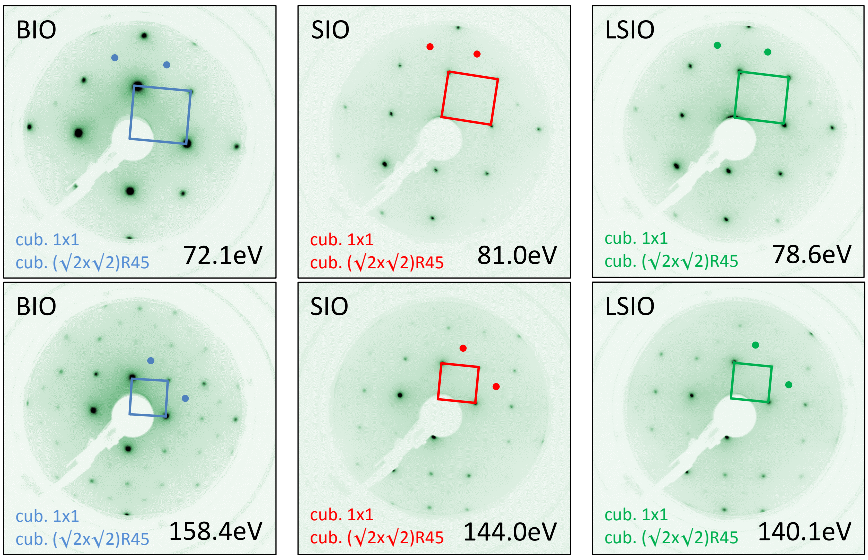

Figure 5.5: *LEED patterns of the 12 ML thick (RP–214) iridate films grown on TiO_2 terminated 0.1 wt% Nb-doped STO(001) substrates taken along the (001)-direction and recorded at lower (about 70 to 80 eV) and higher (about 140 to 160 eV) accelerating voltages, displaying the respective surface structures. Surface reconstruction spots are indicated by colored dots.*

the same results but with much weaker and diffuse diffraction spots due to the more pronounced surface roughness. The patterns were taken at normal incidence with beam energies of about 70–80 eV and 140–160 eV, while the intensely sharp diffraction spots indicate a short- and long-range ordered film surface structure. The assumed tetragonal diffraction pattern caused by the cubic 1x1 film surface structure are illustrated by colored squares. Moreover, at low as well as high beam energies weak Bragg peaks are visible at $(\sqrt{2}\,\mathrm{x}\,\sqrt{2})\ R45°$ relative to the 1x1 peaks, indicated by colored dots in the LEED patterns. These spots are probably a result of an in-plane film surface reconstruction, since such complementary peaks are missing in bulk sensitive XRD measurements (see next subsection). The sharpest LEED spots has the LSIO film, whereas the BIO film shows broader and the SIO film slightly weaker spots. Again, this could be associated with the uniformity of the observed RHEED oscillations which is also mentioned to be correlated to the surface roughness of the 40 ML thick films. The determined lattice constants of the 6 ML thick BIO, SIO and LSIO films are (4.05±0.15) Å, (3.90±0.15) Å and (3.85±0.15) Å, respectively, and are in good agreement with the literature values (see also subsection 2.6.3). Note that the surface quality of these 12 ML thick samples seems to be adequately high to provide valuable ARPES results.

5.3.2 Characterization by X-ray diffraction

After the film surfaces were characterized by AFM and LEED, the 40 ML thick films were analyzed by volume sensitive XRD measurements. The XRD scans which are illustrated

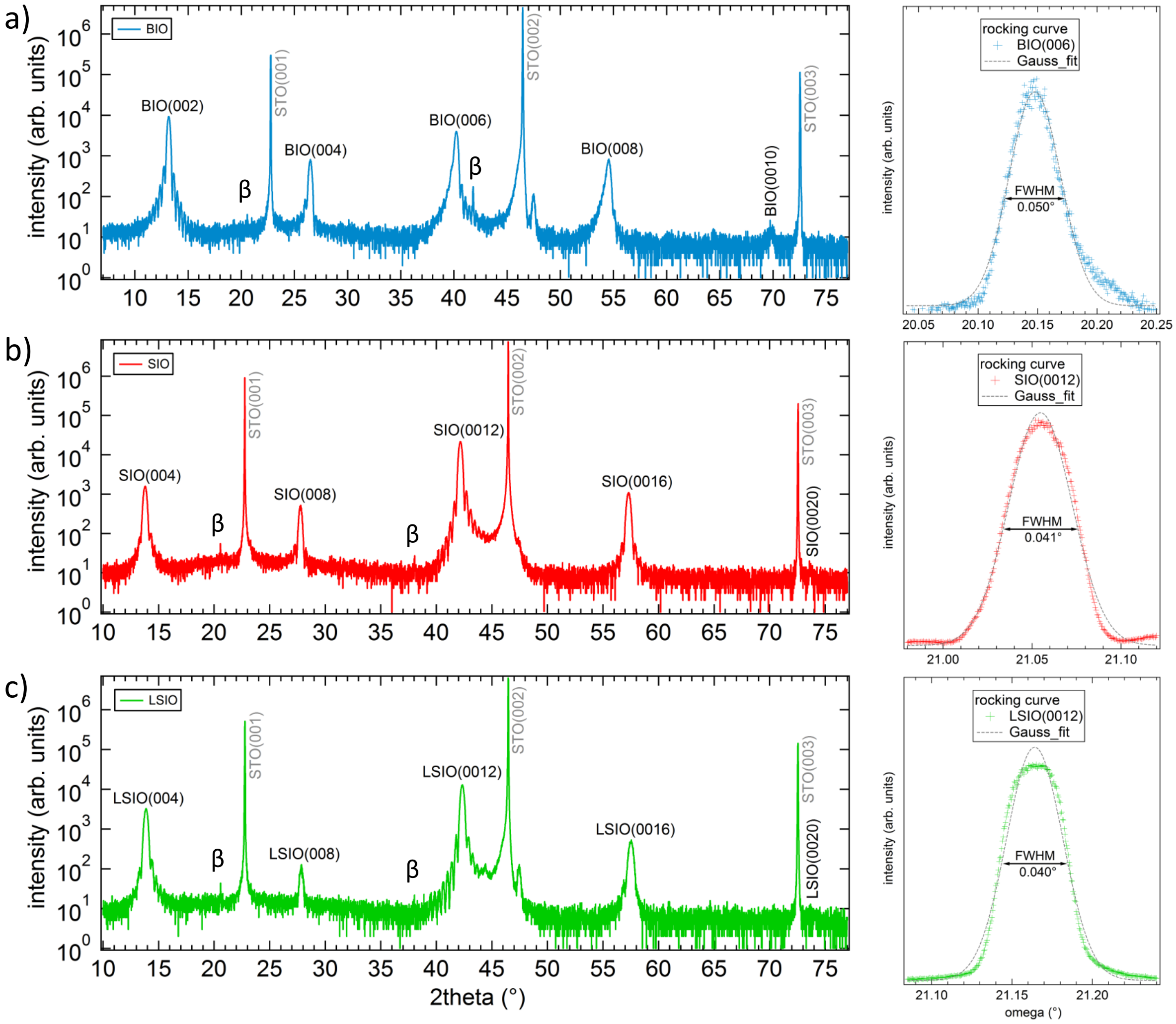

Figure 5.6: *XRD 2θ scans of the 40 ML thick (RP–214) iridate films (a) BIO, (b) SIO and (c) LSIO grown on TiO_2 terminated 0.1 wt% Nb-doped STO(001) substrates and the corresponding rocking curves performed at the (006), (0012) and (0012) film reflex, respectively. The rocking curves are fitted by a Gaussian.*

in Figure 5.6 were performed by a "Bruker D8 Discover" X-ray diffractometer in a 2θ angle range of 5° to 80° for BIO and 10° to 80° for SIO and LSIO. All samples exhibit the three intense STO substrate Bragg peaks and a corresponding add-peak (β) which is generated by the Cu K_β irradiation of the nonmonochromatic X-ray source. Since the 2θ scan probes along the c-axis of the sample, the expected Bragg peaks of the film are along the (001) direction of the samples. Every sample shows the five relevant (RP–214) iridate Bragg peaks along (001). Note that the Laue indices are doubled for SIO (LSIO) compared to those of BIO which is caused by the octahedral rotations in SIO (LSIO) generating an about two times larger unit cell in c-direction. Moreover, all three samples show for their film peaks clear Laue fringes, indicating good crystalline quality of the film volume. The determined film thicknesses by these fringes are (16.7±1.5) nm, (15.8±1.4) nm an (15.5±1.4) nm for the BIO, SIO and LSIO film, respectively, and are in good agreement with the assumed 40 ML of each film material. All peak intensities between the various samples are comparatively similar due to their similar film and substrate thicknesses. The peak positions are in good agreement with other studies [63, 244].

However, to determine the crystalline quality of the grown films, ω–scans were performed at the (006) and (0012) Bragg peak for BIO and SIO (LSIO), respectively. These so-called "rocking curve" (RC) scans are demonstrated on the right side of Figure 5.6. The RC scans are fitted by a Gaussian and afterwards the full width at half maximum (FWHM) value is identified. All samples have same values of FWHM=0.04°–0.05°. Generally, FWHM values smaller than 0.05° evidence highly crystalline quality of grown thin films. Such sharp RC scans correlate with low mosaicity, less dislocations and weak curvatures in the perfect paralellism of atomic planes in the film. But, these values are still not as good/small as those for some single crystals. In Figure F.1 (see Appendix F) the RC scans for the corresponding STO(002) Bragg peaks are shown. They yield FWHM values of about 0.02°–0.03° which represent very high crystal quality caused by nearly no present defects. To note, the film growth process itself creates a significant amount of defects within the grown film which results in comparatively broadened rocking curves.

Thus, regarding the 2θ and RC scans, all three 40 ML thick films show highly crystalline bulk quality.

5.3.3 Conductivity measurements

To check the electric properties of the 12 ML thick (RP–214) films, conductivity measurements were performed using a standard commercial PPMS (Quantum Design) and undoped STO(001) substrates to avoid an additional channel in conductivity. Note that these measurements were performed not in the van-der-Pauw geometry due to the very large sheet resistance values and the limitation of the applicable electrical voltage/current by the PPMS. As a consequence, the aluminum wires were bond linearly nearby each other in the center of the film surface, while the four points have distances of about 0.3–0.5 mm.

The transport measurements in Figure 5.7 confirm the insulating nature of the BIO and SIO films which exhibit a temperature dependent energy gap Δ_{res} which can be estimated from the activation energy (Δ_{res}=2E$_a$). Figure 5.7 a) demonstrates the temperature dependence of the measured resistance R of the three films BIO, SIO and LSIO. Here, an exponential upturn of R is observed for the BIO and SIO films at low temperatures which is a result of their insulating Mott ground state. The measurements could not be performed below 50 K for BIO and not below 80 K for SIO due to the limitations of the PPMS. Surprisingly, the n-doped LSIO film indicates from RT till approx. 100 K only a marginal increase of R. At 20 K, the LSIO film shows still a very low R, but also an additional upturn. Although, this is a sign of successful n-dopingof the Mott insula-

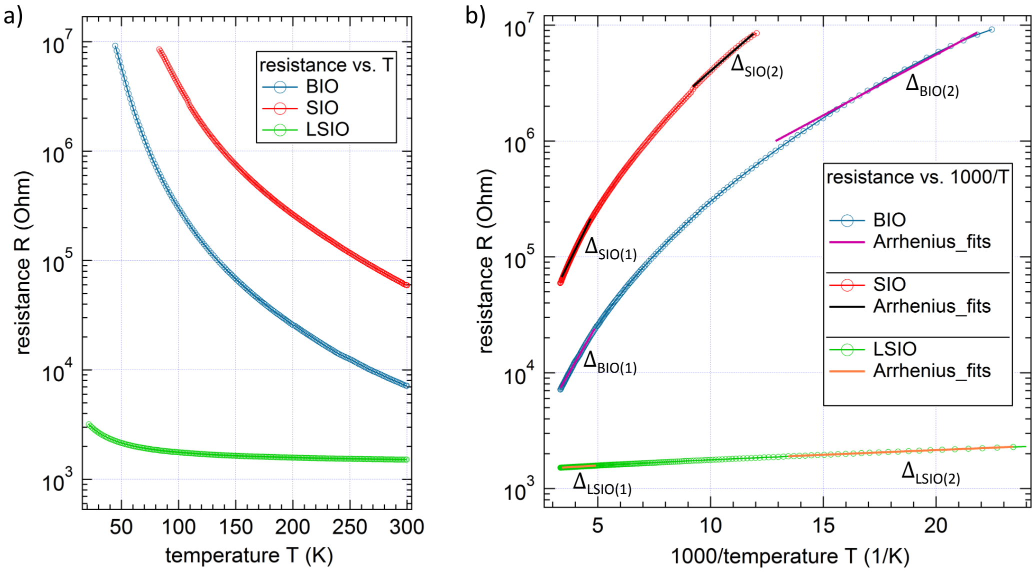

Figure 5.7: *(a) Temperature dependence of the measured resistance for the 12 ML thick BIO, SIO and LSIO films on undoped STO(001) substrates. (b) Same data with logarithmic resistance scale and reciprocal temperature scale. Arrhenius fits with gap energies (Δ_{res}=2E_a) estimated for two temperature regions (1) and (2) for each film.*

tor SIO by La atoms, a decrease of R for LSIO is not observed in this temperature range, making a potential transition into a superconducting state impossible.
Figure 5.7 b) demonstrates the same measured data for R but plotted at a logarithmic scale versus the reciprocal temperature (1/T)·1000. Arrhenius fits of

$$R = R_0 \cdot e^{\Delta_{res} T/(1000 \cdot 2k_B)} \quad , \tag{5.1}$$

where k_B is the Boltzmann constant, are included for each R curve. For all three films, the magnitudes of Δ_{res} is estimated at two temperature regions (high and low T marked by (1) and (2), respectively) and presented in Table 5.2. At every temperature, the values for Δ_{res} are smallest for LSIO and highest for SIO, while those for BIO are slightly smaller than for SIO. Furthermore, the values for BIO and SIO significantly increase as the temperature increases, whereas the value for LSIO persists almost constant. For BIO and SIO, such a temperature dependence of the gap energy is abnormal compared to other materials, e.g. semiconductors, where no change in Δ_{res} arises. This behavior suggests that BIO and SIO become less insulating at low temperatures and indicates that the nature of their insulating Mott states are quite different from common band insulators. This phenomenon has also been oberserved in iridate bulk single crystals as well as in thin films [124, 246]. However, LSIO does not show such trend for its gap energy which can be attributed to additional charge carriers in the La-doped Mott system of SIO trying to close the gap.

Table 5.2: *Energy gap values estimated from the activation energies (Δ_{res}=$2E_a$) of the 12 ML thick BIO, SIO and LSIO films grown on STO(001) substrates for two different temperature regions (see also Figure 5.7).*

(RP–214) iridate film	BIO	SIO	LSIO
for high T	$\Delta_{BIO(1)}$=133.3 meV	$\Delta_{SIO(1)}$=155.9 meV	$\Delta_{LSIO(1)}$=4.4 meV
for low T	$\Delta_{BIO(2)}$=41.6 meV	$\Delta_{SIO(2)}$=67.5 meV	$\Delta_{LSIO(2)}$=3.2 meV

5.3.4 Chemical depth profiling via X-ray photoelectron spectroscopy

As a next step, the 12 ML thick BIO, SIO and LSIO films which are grown on 0.1 wt% Nb-doped STO(001) substrates were analyzed by means of XPS in order to characterize their electronic structure and film stoichiometry. Note that the films are directly transferred after the LEED measurements into the PES chamber to retain the conditions of clean sample surfaces. In addition, the Fermi energy is determined from the photoemission spectrum of an Ar-ion sputtered clean gold foil sample. Figure 5.8 presents the XPS overview spectra of all three (RP–214) iridate films, measured at a rather bulk sensitive normal emission (NE) angle using a monochromated Al K_α irradiation (hν=1486.6 eV). The films show their respective characteristic photoemission peaks, whereas the carbon C 1s peak is missing in all spectra (see also Figure 5.9 b)), indicating no carbon contaminations for the film volume (surface sensitive measurements with 50°off normal emission angle also reveal clean film surfaces, not shown). One should notice that for BIO (see a)) the Ba 3d core level peak is much more intense compared to the other peaks due to its relatively high ionization cross section value at Al K_α photon energy. In contrast, SIO and LSIO show O 1s core level as most intense peak in their spectra. For LSIO, the La doping effect is clearly visible, especially in its La 3d core level peak. With comparison to the Sr core level peaks, one can determine a doping level of (21.5±0.55)% which is in good agreement with the desired value of 20% in the LSIO film. Moreover, for SIO and LSIO (see b) and c)) there is a noticeable spectral weight at the peak position of the Ba 3d core level, although these film should not exhibit Ba atoms. This spectral weight is not increased for the surface sensitive measurement, indicating not a diffusion of Ba impurities to the film surface but rather a constant contamination of Ba within the film. For SIO and LSIO a substitution of Sr by Ba of less than 1% is determined to be (0.20±0.05)% and (0.23±0.05)%, respectively. A reason for this undesired Ba impurities can be the purity of the Sr source which is used for the fabrication of the SIO and LSIO target. However, a small amount of impurities as here can be neglected and should essentially not affect the upcoming experimental results.

To check the film stoichiometries of the three (RP–214) iridate films, chemical depth profiles were executed with respect to their most relevant XPS core level spectra using emission angles of NE, 30° off and 50° off NE.

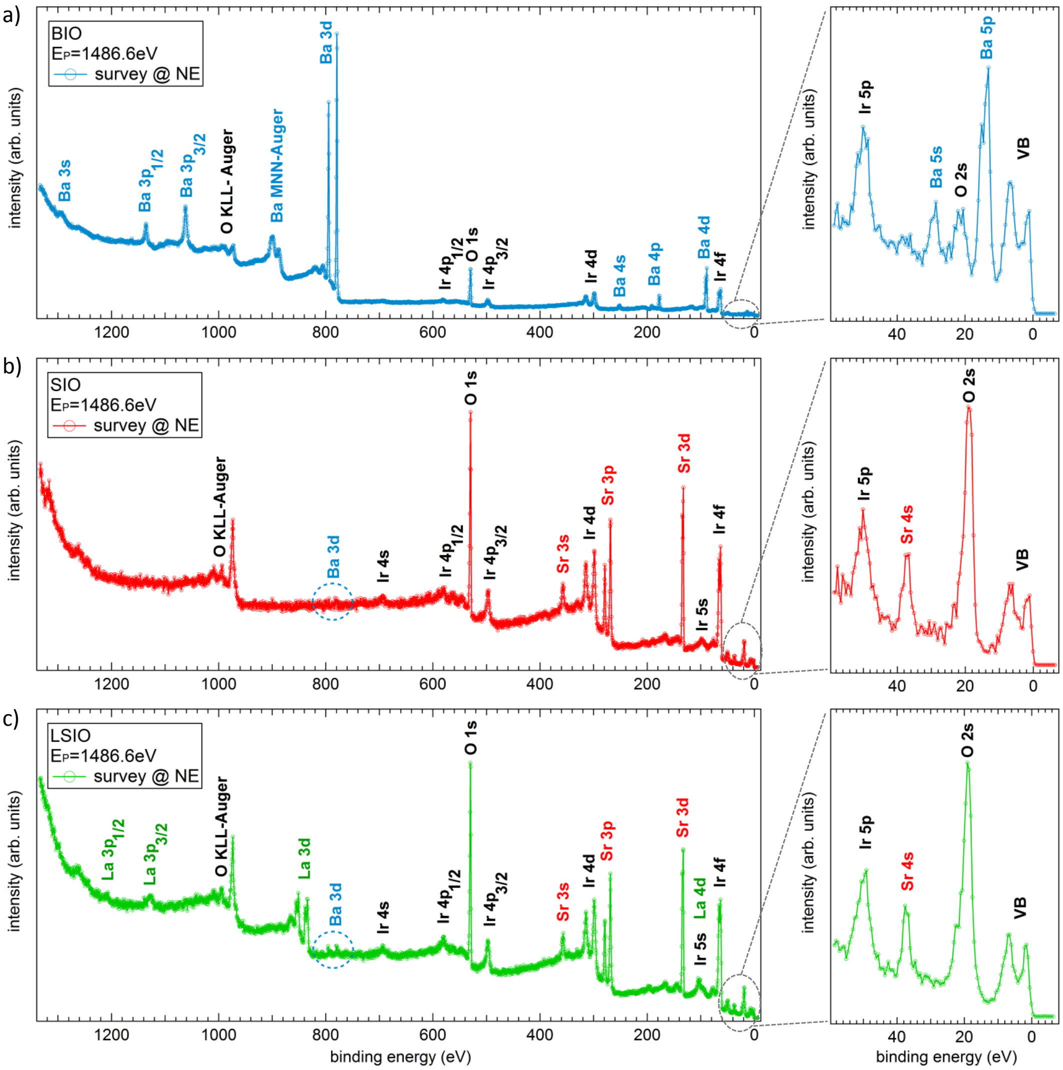

Figure 5.8: *XPS overview spectrum of the 12 ML thick (RP–214) iridate films (a) BIO, (b) SIO and (c) LSIO grown on TiO_2 terminated 0.1 wt% Nb-doped STO(001) substrates measured at NE. The characteristic photoemission peaks of the film materials are labeled. The SIO and LSIO films show a small amount of Ba impurity atoms.*

Those spectra are presented in Figure 5.9, 5.10 and 5.11. Figure 5.9 a) shows their depth profiled O 1s core level spectra which are corrected by scaling to the same secondary electron background and Shirley background subtraction. It is obvious that the O 1s core level spectra of these (RP–214) iridates involve a triplet peak structure. In fact, all O 1s spectral shapes can be perfectly fitted by a combination of three Gaussian-profiles, the latter are not added to this Figure but rather their positions by dashed black lines. As supplement, some of the generated fits for area normalized O 1s spectra measured at 30° off are demonstrated in Figure G.1 (see Appendix G). Peak ”1” at about 529.7 eV binding energy represents the main characteristic O 1s core level peak, since it shows no

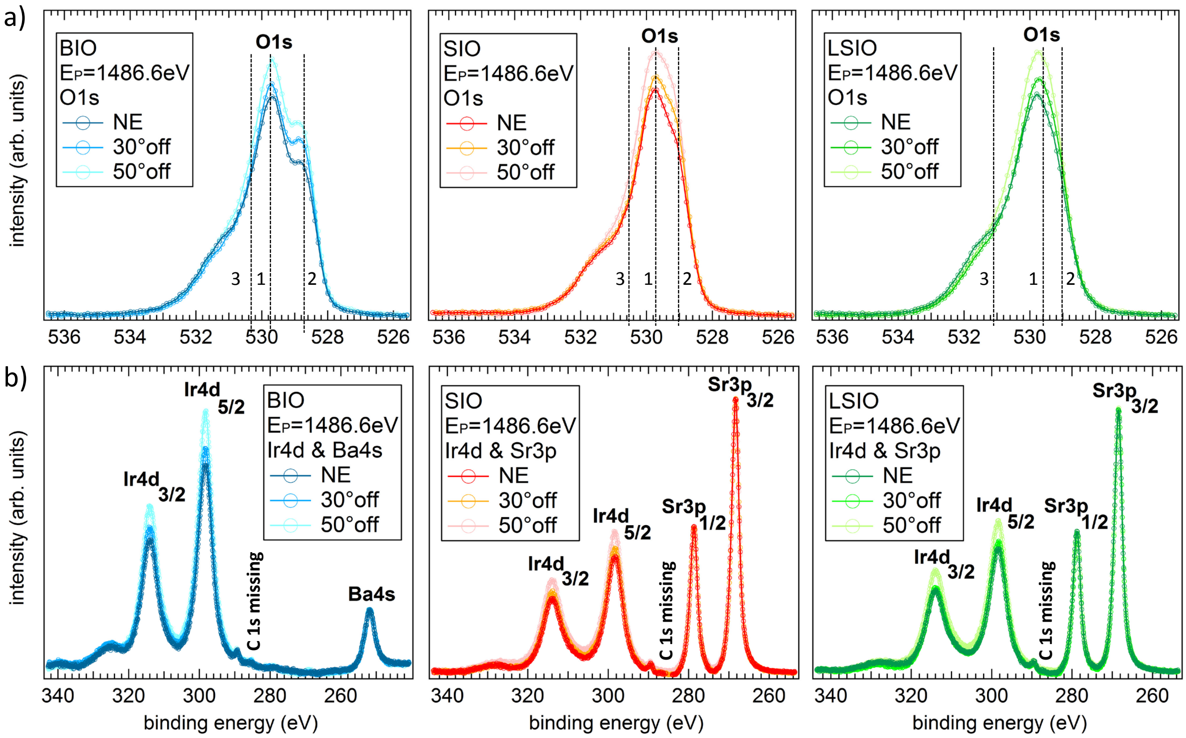

Figure 5.9: *Chemical depth profiling: (a) XPS O 1s core level spectra of the 12 ML thick (RP–214) iridate films BIO, SIO and LSIO grown on TiO_2 terminated 0.1 wt% Nb-doped STO(001) substrates measured at NE, 30° off and 50° off NE. (b) Corresponding XPS Ir 4d, Ba 4s and Sr 3p core level spectra measured at the same emission angles.*

variation in binding energy in all three films. The spectral weight of this O 1s peak ”1” (see also Figure G.1) increases from BIO over SIO to LSIO which is mostly affected by the variation of the two other peaks.

In contrast, peaks ”2” and ”3” located at lower and higher binding energies, respectively, show an energy shift to higher binding energies and a decreasing spectral weight from BIO over SIO to LSIO. The energy shift is more distinct for peak ”3”, whereas the decrease of spectral weight is stronger for peak ”2”. In the BIO O 1s spectrum, peak ”2” is split from peak ”1” relatively wide with a binding energy difference of ∼1.0 eV, while for SIO and LSIO binding energy split values are ∼0.8 eV and ∼0.6 eV, respectively. In addition, the energy shifts of peak ”3” from peak ”1” are calculated to be ∼0.6 eV, ∼0.8 eV and ∼1.5 eV for BIO, SIO and LSIO, respectively.

All three iridate films show just marginal changes in the shape of O 1s core level spectra for the different emission angles. Such XPS O 1s core level peak characteristics of (RP–214) iridate thin films are not reported in the literature. A possible reason for their unique peak shapes could be the typical crystal structure of BIO and SIO, where octahedral rotations play a major role. These rotations cause different chemical environments of the O atoms within their in-plane lattices structures, resulting in chemical shifts in

Table 5.3: *Film stoichiometries of the three 12 ML thick (RP–214) iridate films determined by means of XPS depth profiling using emission angles of NE, 30° off NE and 50° off NE.*

iridate film	BIO	SIO	LSIO
50° off NE	$B_2\, I_{1.30\pm0.16}\, O_{4.41\pm0.26}$	$S_2\, I_{1.23\pm0.16}\, O_{4.38\pm0.22}$	$L_{0.2}\, S_{1.8}\, I_{1.25\pm0.14}\, O_{4.35\pm0.21}$
30° off NE	$B_2\, I_{1.12\pm0.12}\, O_{4.18\pm0.19}$	$S_2\, I_{1.11\pm0.13}\, O_{4.16\pm0.18}$	$L_{0.2}\, S_{1.8}\, I_{1.13\pm0.12}\, O_{4.13\pm0.17}$
NE	$B_2\, I_{1.02\pm0.09}\, O_{4.05\pm0.16}$	$S_2\, I_{1.01\pm0.10}\, O_{4.03\pm0.16}$	$L_{0.2}\, S_{1.8}\, I_{1.02\pm0.09}\, O_{4.04\pm0.16}$

XPS spectra. Moreover, the stacking sequence of BaO (or SrO) and IrO_2 layers in (RP–214) iridates causes two different O atom environments. The O atoms of the IrO_2 layer are affected by the chemical configuration of an upper and lower BaO (or SrO) layer, whereas O-atoms of a BaO (or SrO) layer are influenced by a configuration of an IrO_2 and BaO (or SrO) layer. Note that the last BaO (or SrO) layer is an exception, since here the O atoms of this layer see a different chemical environment. Other reasons for the special O 1s peak shapes could be crystal defects and charge transfers from the O ligands to the Ir atoms which should affect the Ir core level peak shapes as well. However, the unambiguous assignment of the peaks in the triplet peak structure in the O 1s spectrum is not possible at this point and needs further studies.

Figure 5.9 b) presents the corresponding XPS Ir 4d, Ba 4s and Sr 3p core level spectra of the three films measured at the same emission angles. All spectra are corrected by scaling to the same secondary electron background and Shirley background subtraction. While the Ba 4s and Sr 3p core level peaks for BIO and SIO (and LSIO) indicate no change for the three emission angles, the spectral weight of the corresponding Ir 4d core level increases for all samples at larger (more surface sensitive) emission angles. This is a clear sign for missing Sr atoms or an excess of Ir atoms nearby the film surface, which will be verified in the last subsection of this chapter by a TEM analysis. Note that for LSIO the La 3d core level peak shows also no change in spectral weight for its chemical depth profile (not shown) which indicates a homogeneous doping level within the LSIO sample.

The film stoichiometries, more precisely the Ba/Ir, Sr/Ir, Ba/O and Sr/O ratios, depending on the information depth can be determined by Equation 3.38 using the acquired depth profiles. The calculated values of ratios are given in Table 5.3. The values indicate a clear increase of Ir and O amount within the film material from bulk to surface region, while the trend seems to go to a (RP–113) phase. Therefore, BaO (or SrO) units seem to be missing in the topmost layers of these PLD grown (RP–214) iridate films, although all other previously performed characterization methods confirm phase pure films. However, one should keep in mind that IrO_3 is volatile at specific conditions, especially at high temperatures (starting from about 850°C) and high O concentrations [247–249]. Since the PLD growth parameters for these films (see Table 5.1) are quite similar to those specific conditions, re-evaporation of Ir atoms from the film surface during and at the end of the growth process has to be taken into account. However, a decrease of the

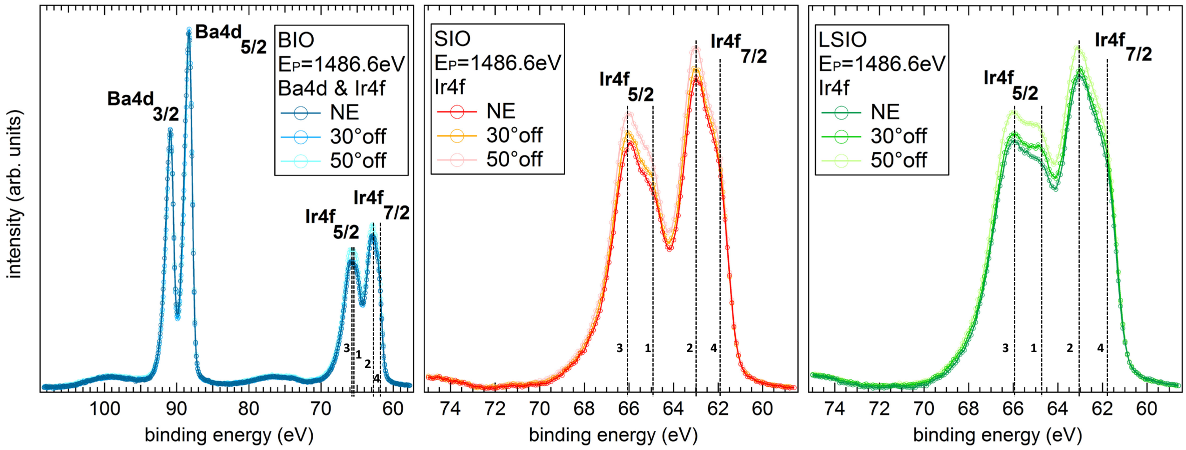

Figure 5.10: *Chemical depth profiling: Corresponding XPS Ba 4d and Ir 4f core level spectra of the 12 ML thick (RP–214) iridate films BIO, SIO and LSIO grown on TiO_2 terminated 0.1 wt% Nb-doped STO(001) substrates measured at NE, 30° off and 50° off NE.*

Ir signal is not observed for the surface sensitive XPS measurements for all grown films, making this effect of re-evaporated Ir negligible.

Figure 5.10 demonstrates the depth profils of Ba 4d and Ir 4f core level spectra which are corrected by Shirley background subtraction and normalized to the Ba 4s and Sr 3p core level peaks (for BIO and SIO (LSIO), respectively). For BIO, the Ba 4d core level spectra indicates no change in spectral weight for the various emission angles. Moreover, all three (RP–214) iridates films exhibit Ir 4f core level spectra which increases in spectral weight with increasing emission angle. This confirms again the observation of the increasing Ir amount in the topmost film layers. Beside this, the spectral line shape of the Ir 4f core level of each film is almost fully preserved for all three emission angles (only marginal differences). Furthermore, the Ir 4f core level spectra of the SIO and BIO films are in good agreement with the results of A. Yamasaki *et al.* [250]. Interestingly, for all three films, the spin-orbit split Ir 4f core level does not have a simple symmetric double peak structure of Ir $4f_{5/2}$ and Ir $4f_{7/2}$ but rather more complicated shape. It is a reasonable assumption that such peak shape results from a multiplet splitting which is quite common for metal oxides. Such a split arises when an atom contains partially filled shells. By creation of a core electron vacancy by photo-ionization, this photohole in the core can couple with the partially filled outer shell. This generates a number of final states which result in a multi-peak structure in the spectrum. In fact, all Ir 4f spectral shapes of the analyzed films can be perfectly fitted by a combination of two Gaussian- and two Voigt-profiles: their center positions are marked by dashed black lines in Figure 5.11. Here, peaks "1" and "2" are Gaussian-profiles, whereas peaks "3" and "4" are Voigt-profiles. Some of the generated fits for area normalized Ir 4f spectra measured at NE are demonstrated in Figure G.2 (see Appendix G). Note that the main peaks ($|4f^{13}5d^5\rangle$ final states) of the spin-orbit split Ir 4f core level (Ir $4f_{5/2}$ and Ir $4f_{7/2}$)

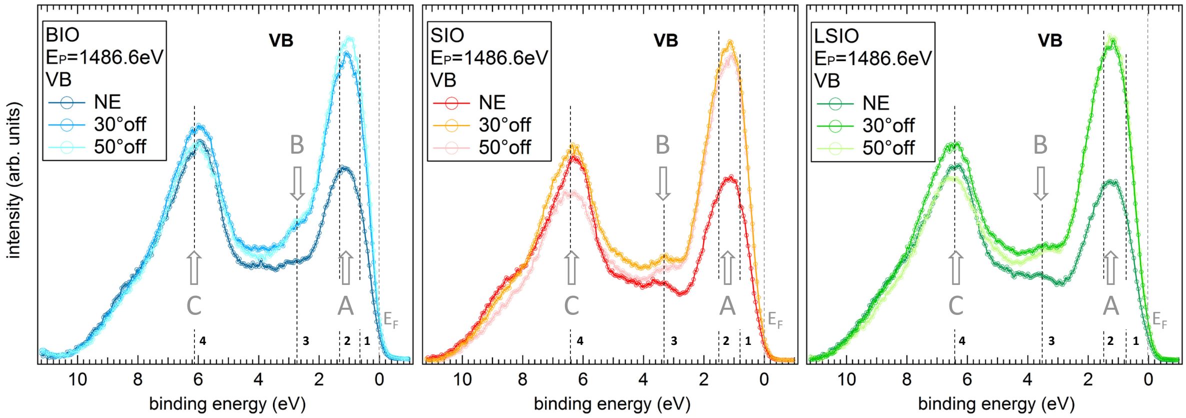

Figure 5.11: *Depth profiling: Corresponding VB spectra of the 12 ML thick (RP–214) iridate films BIO, SIO and LSIO grown on TiO_2 terminated 0.1 wt% Nb-doped STO(001) substrates measured at NE, 30° off and 50° off NE.*

are located at the positions of peaks "2" and "3", whereas the peaks "1" and "4" create the corresponding peak shoulders at lower binding energies which are derived from the well-screened ($|4f^{13}5d^{6}\,\underline{L}\rangle$) final state due to the charge transfer from the O 2p states, where $\underline{L}$ denotes an additional hole in the ligand states [251].

For all three films, the main peak "2" is fixed at binding energy of ∼63 eV. Surprisingly, in the case of SIO and LSIO, the main peak "3" slightly shifts to higher binding energies. The binding energy differences between the spin-orbit split peaks "2" and "3" is ∼2.75 eV for BIO and ∼3 eV for SIO and LSIO. Interestingly, the peak shoulders "1" and "4" shift to lower energies from BIO over SIO to LSIO. Here, the shift of peak shoulder "1" (∼0.9 eV) is much stronger than that of shoulder "4" (∼0.2 eV). No definite trend within the three (RP–214) iridate films can be observed in the spectral weights of the main Ir 4f peaks and their shoulders (see also Figure G.2).

Furthermore, the characteristic line shapes of their valence bands are analyzed to get some information about the electronic band structure. The depth profiled VB spectra which are corrected by Shirley background subtraction and normalized to the Ba 4s and Sr 3p core level peaks (for BIO and SIO (LSIO), respectively) are shown in Figure 5.11. Every film indicates more or less a three-peak structure in its spectrum which is formed mainly from the large spectral weights of both Ir 5d and O 2p states. But in fact, it has a multiple peak structure which can be fitted by a set of Gaussian-profiles. Some of the generated fits for area normalized VB spectra measured at 50° off are demonstrated in Figure G.3 (see Appendix G). However, the most relevant here are the peaks "1", "2", "3" and "4", while "1" and "2" together with a part of peak "3" induce the peak (labeled as "A") near the Fermi level.

For all three films, this peak "A" is located at ∼1 eV binding energy and originates from the Ir $5d_{t_{2g}}$–O 2p (≡ Ir $5d_{J_{eff}}$–O 2p) anti-bonding states, whereas peak "C" at ∼6 eV binding energy is represented by peak "4" and attributed to the corresponding bonding states (π-type). In contrast, peak "B" which is represented by peak "3", is found between these two peaks and originates mostly from the O 2p non-bonding states [252]. Interestingly, the position of peak "B" shifts to higher binding energies from BIO over SIO to LSIO which are ~2.7 eV, ~3.1 eV and ~3.6 eV, respectively. Moreover, its spectral weight decreases in the same direction. Peak "C" seems to have a similar behavior as peak "B", but is much weaker distinctive in energy shift and spectral weight loss. Additionally, peaks "A" and "B" become slightly more broadened from BIO over SIO to LSIO. The trend of this three-peak structure in the VB spectra can be possibly explained by the different strength of spin-orbit interaction of the three films. Assuming that peak "B" contains the J_{eff}=3/2 states and peak "A" is the LHB with the J_{eff}=1/2 states (note that this is only an idealized picture), the trend would act like the evolution shown in Figure 2.15. However, compared to each other, every film has the same minor spectral weight and also identical VB edges near the Fermi level. The VB maximum offsets of the three films are almost equal at ~0.01 eV binding energy. Moreover, no quasiparticle peak is observed at the Fermi level in the XPS VB spectrum for the LSIO film, resulting rather in a persisting Mott insulator with strong electron interactions than in a correlated metal.

In principle, there are also the Ir 5d$_{e_g}$–O 2p bonding states (σ-type), containing strong O 2p components which create two peaks at ~10 and ~13 eV binding energy [252]. However, for the XPS VB spectra in this thesis, these two additional peaks are not observed, since at this photon energy the photo-ionization cross section of the Ir 5d states is much larger than that of O 2p states.

Regarding the depth profiles of the VB of each film, it is obvious that peaks "A" and "B" are more intense for the surface sensitive 30° and 50° off NE measurements. Surprisingly, both have almost the same spectral weight at this emission angles, whereas the intensity of peak "C" does not show a systematic change for the three films. But the reason for this spectral change is still not fully understood and can not be answered accurately enough. One reason could be that the J_{eff} states in the LHB are more surface than bulk sensitive. Some further studies must be performed to clarify this behavior of the VB spectra of (RP–214) iridate thin film.

5.3.5 Soft X-ray photoelectron spectroscopy

Even though the previously carried out characterizations mostly suggest single crystalline and pure phase (RP–214) iridate films, it is still questionable if these PLD grown films exhibit the same crystal quality, in particular the region close to the surface, as their equivalents which are grown by MBE or consist of cleaved single crystals. The quality of the surface and topmost layers of a film directly depends on the roughness, homogeneity in stoichiometry (phase purity) and defect density. In case PLD grown films own equal surface quality as, e.g., MBE grown films, they should also provide similar results from experiments using soft X-ray PES which is a very surface sensitive characterization method with a relatively short information depth. Therefore, as a next step, the electronic structures of the PLD grown (RP–214) iridate films were analyzed by soft X-ray ARPES (SX-ARPES) and compared to similarly performed studies in the literature.

The SX-ARPES experiments using unpolarized light from a twin helical undulator were performed at the actinide science beamline BL23SU of the synchrotron facility SPring-8 (Japan Atomic Energy Agency (JAEA), Hyōgo, JP) in cooperation with Prof. Dr. A. Yamasaki (Kobe University) and Prof. Dr. H. Fujiwara (Osaka University). The 12 ML thick (RP–214) iridate films were stored under high-purity N_2 gas atmosphere during the travel from the PLD growth chamber to the load lock chamber in the beamline (using glove bags), and then transferred into the SX-ARPES chamber under UHV. The photon energy was set to 760 eV for all measurements and the temperature was fixed at 100 K for the BIO and SIO film (to avoid charging) and 20 K for the LSIO film. The energy resolution of the measurements of the energy band dispersion along high-symmetry lines (for k-space mapping) was set to about 200 meV, while the angular resolution was 0.5° and 0.3° perpendicular to the slit for the rough and high resolution mapping, respectively. The samples are oriented with the light coming along the [110] direction of the Nb-STO substrate. O 1s and C 1s spectra were checked before all k-space mappings to confirm clean film surfaces. In addition, the Fermi energy was determined from the photoemission spectrum of an *in situ* evaporated gold film.

Figures 5.12 a), b) and c) demonstrate the evolution of the constant energy (k_x-k_y) surface maps in the k-space with increasing binding energy for BIO, SIO and LSIO, respectively. Note that the maps are made symmetric by utilizing the symmetry operation of a N-rotation group (360°/N, here N=2 is used). The high symmetry points Γ, M and X are relatively similarly located in the k-space maps of all three samples due to their quite similar crystal structure and lattice parameters. Compared to BIO, the Brillouin zone of SIO and LSIO is reduced by half in momentum space due to the $\sqrt{2} \times \sqrt{2}$ in-plane distortion (see dashed green lines). But, beside these geometrical disparity, there are some basic differences between the measured maps of the three films. The overall sharpness of the k-resolved electronic structure in k-space maps of SIO and LSIO is better than in BIO. Nevertheless, all k-space maps presented in this thesis show much weaker energy band dispersions compared to other studies demonstrated for MBE grown films or cleaved single crystals [57–60, 63, 70–73]. However, the intensity evolution at the highsymmetry points are satisfactory for comparison with the literature.

In addition, highsymmetry cuts (binding energy versus k-spectra) along ΓMXΓ are presented together with the corresponding energy distribution curves (EDCs) in Figure 5.13. These cuts show equal resolution of the energy band dispersions as the corresponding k-space maps. Surprisingly, their second derivative images do not show an improvement in details (not shown). Note that the intensity scaling is rescaled for every each k-space map (see color scaling of measured maps with lowest and highest reached intensity). Due to the high and low intensities at higher and lower binding energies, respectively, the energy band dispersions within the first 0.5 eV are hard to resolve in the highsymmetry cuts. Thus, a possible quasiparticle band indicating a Fermi-arc structure in LSIO is

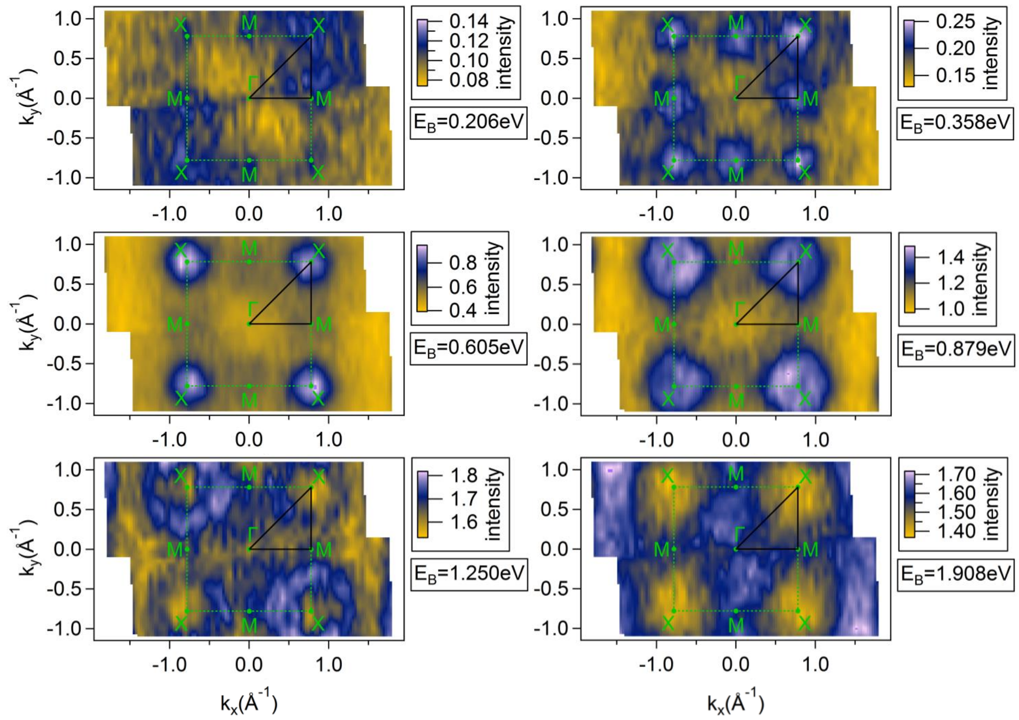
a) BIO, E_P=760eV, 100K

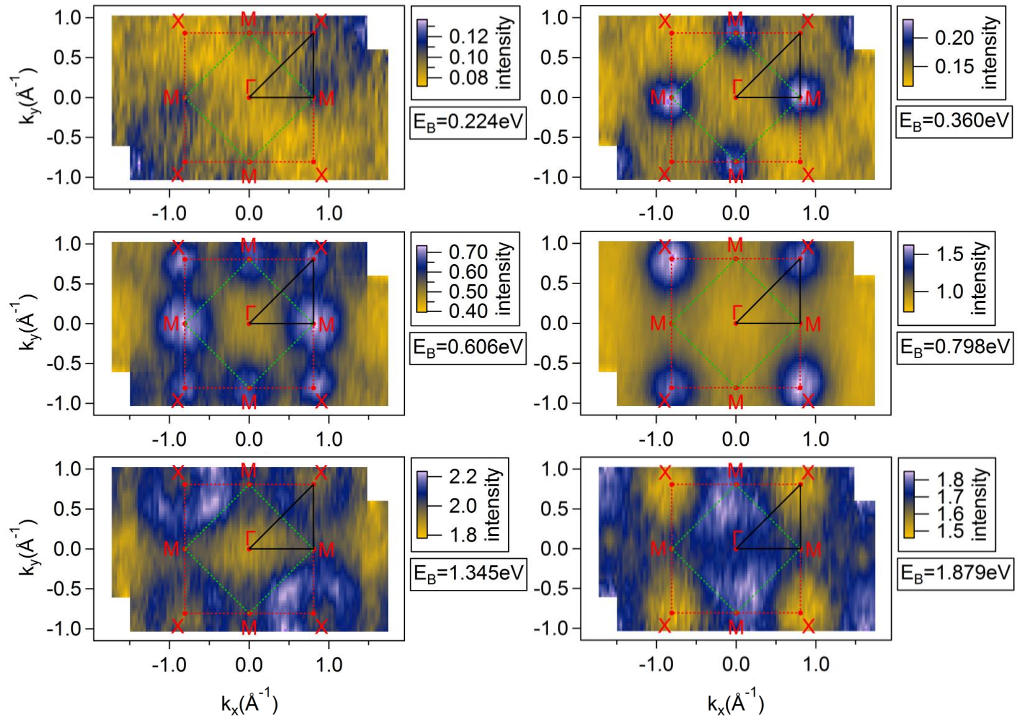
b) SIO, E_P=760eV, 100K

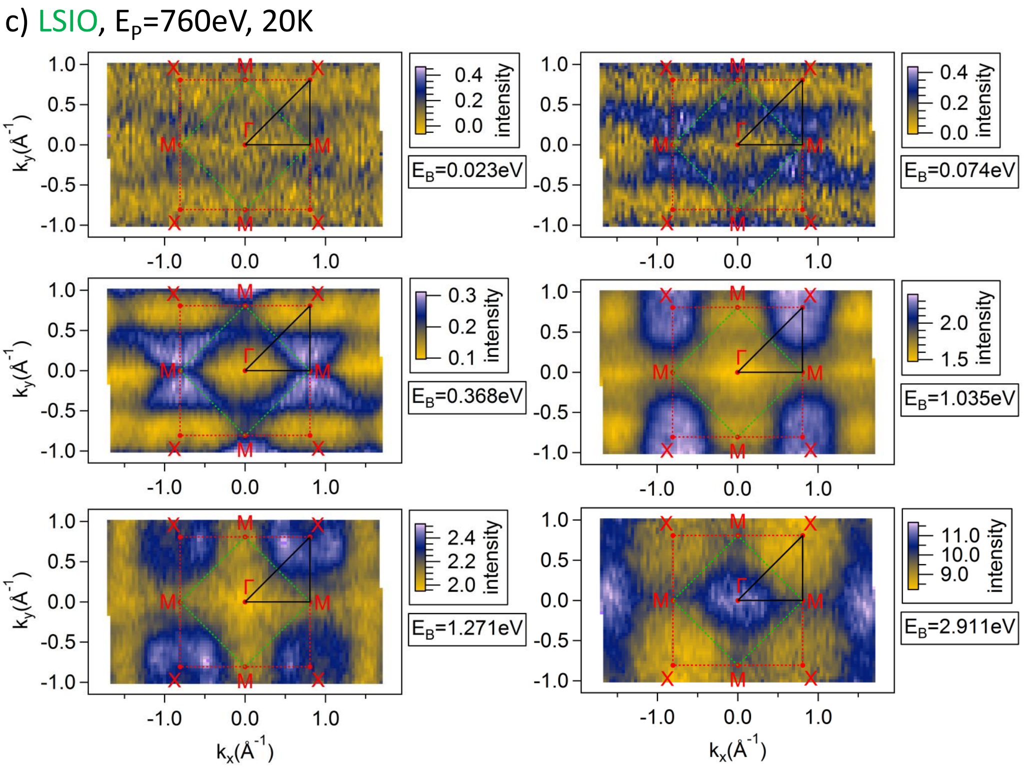

Figure 5.12: *Constant binding energy (k_x-k_y) maps of the 12 ML thick (RP214) iridate films measured by SX-ARPES at a photon energy of 760 eV. Measuring temperature is set to 100 K for a) BIO and b) SIO, and 20 K for c) LSIO. The dashed green lines indicate the corresponding real in-plane Brillouin zones of the three films, whereas the dashed red lines represent the relative pseudo in-plane Brillouin zones of SIO and LSIO relating to the undistorted in-plane structure of BIO. The black lines represent the paths of the highsymmetry cuts along* ΓMXΓ.

not visible in such a cut but rather in the k-space map due to the mentioned rescaling. For this reason, plots of the corresponding EDCs (see Figure 5.13 b)) indicate just very weak band dispersions from 0 to 2.5 eV binding energy with just marginal features around the X points for all three samples. This situation is in clear disagreement with the literature of MBE grown films and single crystals for which strong band dispersion are demonstrated [61, 63, 71]. Furthermore, the spectral weight at the Fermi level for the LSIO film can not be observed in EDCs.

Only the k-space map for LSIO shows some spectral weight (from band with J_{eff}=1/2 character) close to the Fermi level, which could originate from a quasiparticle (see Figure 5.12 c)). The first indication of this appears at ~0.01 eV binding energy between M points and could originate from the formation of a Fermi-arc. In contrast, BIO and SIO have no spectral weight at these points till ~0.2 eV and ~0.25 eV binding energy, respectively (see Figures 5.12 a) and b)). These band maximum positions at the M points are in good agreement with observations of other working groups [59, 63, 72]. Moreover, spectral weight around the X points (from band with J_{eff}=3/2 character)

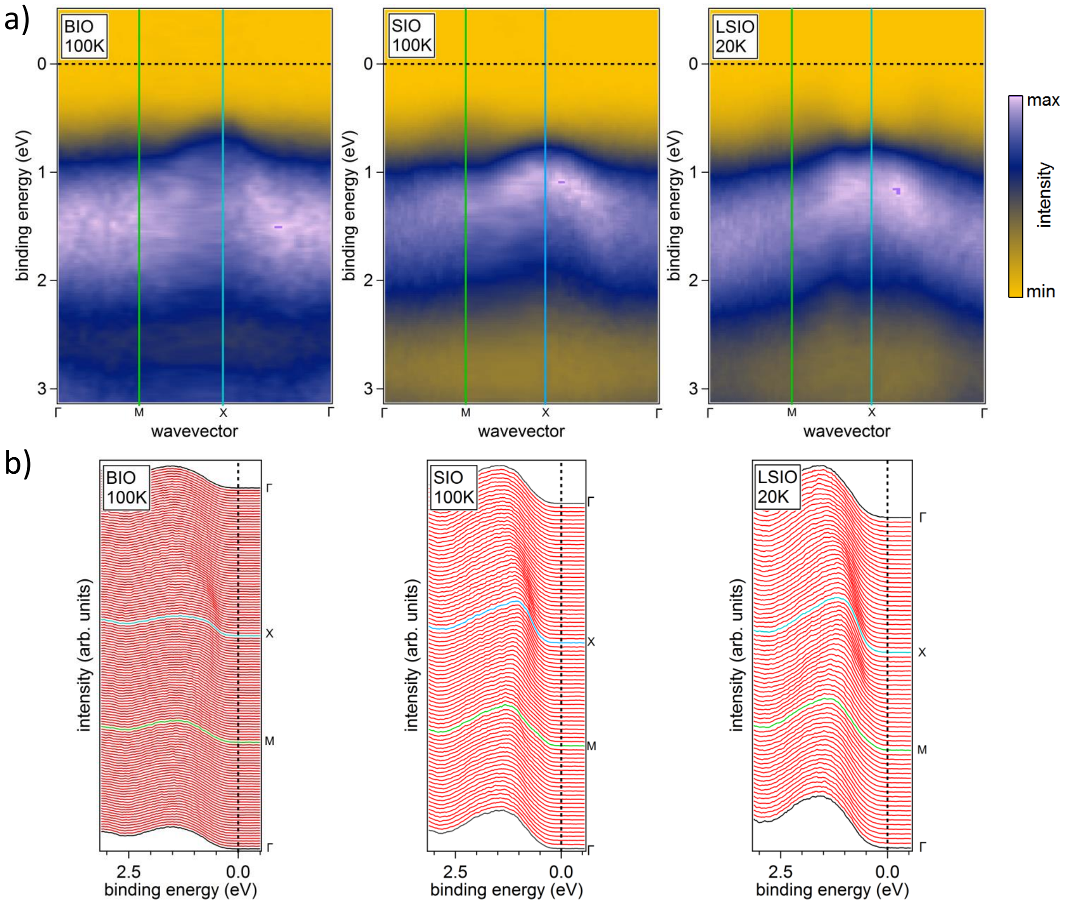

Figure 5.13: *(a) Highsymmetry cuts of the ARPES data of the 12 ML thick BIO, SIO and LSIO films along* ΓMXΓ *and (b) the corresponding EDCs.*

arise at ~0.25 eV,~0.55 eV and ~0.45 eV for BIO, SIO and LSIO, respectively (see Figures 5.12 a), b) and c)).
To resolve the spectral weight between the M points for the LSIO film in more detail, the sample was rotated by 45° around the normal vector which is perpendicular to the sample surface. With this geometry, it is possible to make a highsymmetry cut along XΓX and to resolve the spectral weight exactly in the middle of two M points. Figure 5.14 a) shows such highsymmetry cut. The additional spectral weight between M points is clearly visible at ~0.1 eV as well as the weight at X points at higher binding energy. A. de la Torre *et al.* observed for lightly La-doped SIO ($La_{0.01}Sr_{1.99}IrO_4$) single crystals similar results between M points. In case of La-doped SIO single crystals doped high enough, one of these "spots" should be split into pairs of Fermi-arcs at the Fermi level as demonstrated in publication [71]. Figure 5.14 b) presents the corresponding plot of EDCs. Again, this plot indicates very weak dispersion with almost no additional spectral weight close to the Fermi level in contrast to the results of A. de la Torre. There can be different reasons why the energy band dipsersions of the PLD grown (RP–214) iridate

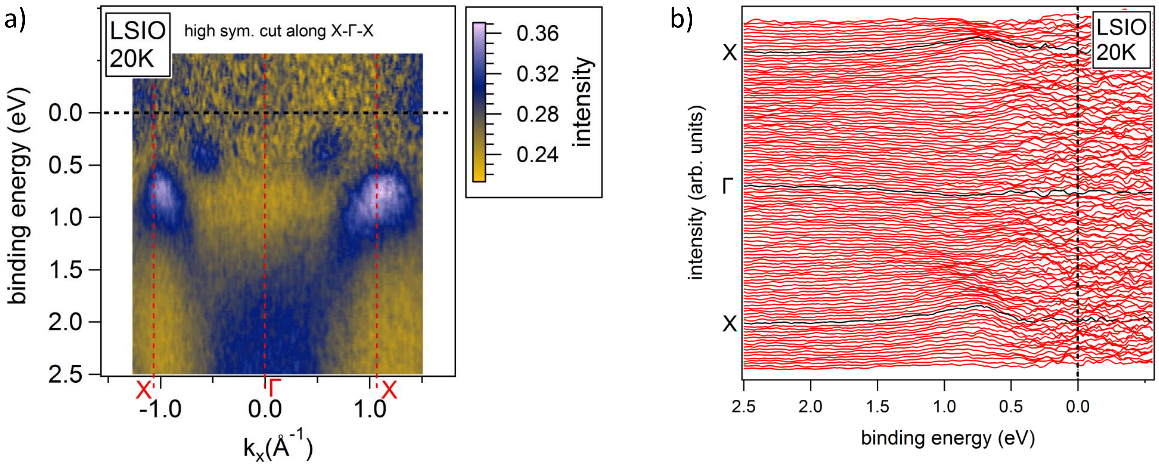

Figure 5.14: *(a) Highsymmetry cut of the ARPES data of the 12 ML thick LSIO film along* XΓX *and (b) corresponding EDCs.*

films are that weak. Since the surface roughness of the films is quite small and in the range of those from other studies, the most obvious explanation are defects or anomalies in the topmost layers of the films. To check this last possible cause, one of the PLD grown films was analyzed by TEM which will be discussed next.

5.3.6 Microstructure

In the following, a STEM analysis is presented for the identification of the crystalline order in a exemplary 16 ML thick PLD grown SIO film on STO(001). The measurements were performed by Dr. M. Kamp at the RCCM (Röntgen Center for Complex Materials Systems) of the University of Würzburg (Würzburg, GER). Using a FEI dual beam FIB, the required lamella is cut out perpendicular to the sample surface and afterwards milled from both sides by a focused ion beam to a thickness of about 50-100 nm. The lamella of the SIO film is then transferred to the TEM (FEI-Titan version) for the actual analysis. Figure 5.15 a) shows the transmission electron diffraction pattern of 16 ML thick PLD grown SIO sample, whereas Figure 5.15 b) demonstrates a reference pattern measured by C. Lu *et al.* who also analyzed PLD grown SIO films [64]. Obviously there are no differences between the two shown diffraction patterns in number and sharpness of spots. This reveals that the crystalline order in the volume of the sample is well defined too, which provides a constructive and destructive interference (at least in the same quality as the reference pattern). Furthermore, Figures 5.15 c) and d) present the cross sectional STEM overview image of the 16 ML thick SIO film and a corresponding enlarged section of the film. The sample consists of Pt protection layer, film, sharp film to substrate interface and substrate. The film itself shows some lighter and darker regions which originate probably from the creation of crystallites without changing in orientation or forming antiphase and/or twin boundaries. However, C. Lu *et al.* show a

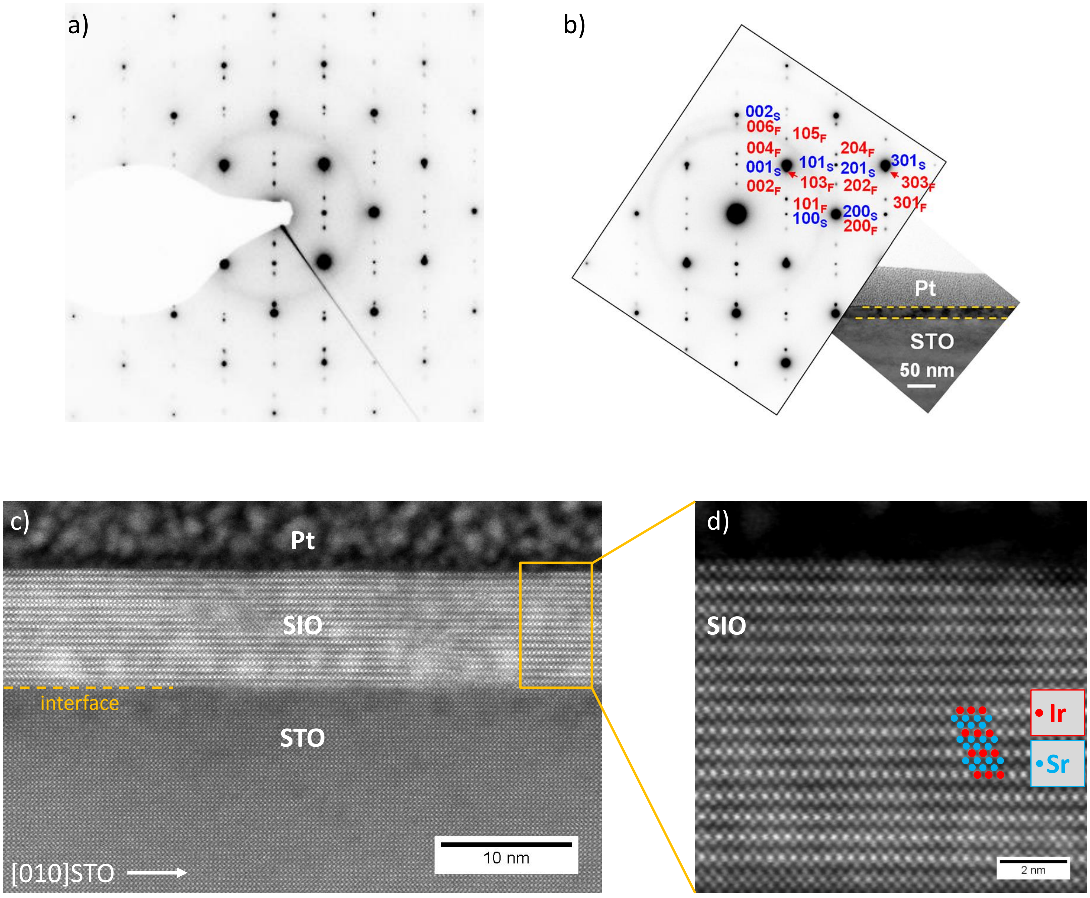

Figure 5.15: *Transmission electron diffraction pattern of SIO films: a) Diffraction pattern of the 16 ML thick PLD grown SIO film. b) Equal diffraction pattern of a similarly grown thick SIO sample [64] where the spots are indexed for the substrate and film with "S" and "F", respectively. A cross sectional image of the lamella is shown on the right side. c) Cross sectional STEM overview image of the 16 ML thick PLD grown SIO film on STO(001) substrate with Pt protection capping. d) Corresponding enlarged section of the STEM image with Ir and Sr atoms marked red and blue, respectively.*

very similar STEM image of the film which may reveal a minor role of such crystallites for the sample quality. The detailed STEM image of the 16 ML thick SIO film (see Figure d)) indicates a very low defect density and a phase pure sample with correct stacking sequence of continuous IrO$_2$ and SrO layers. Note that basically the very light O atoms are not visible, whereas the heavier atoms Sr and Ir arise with high contrast. Since Ir atoms are much heavier than Sr atoms, they appear brighter than Sr atoms in STEM images. However, this is just one of many film areas which can be analyzed on the serveral μm wide lamella.

Thus, a few more film regions were analyzed by STEM and the results are demonstrated in Figures 5.16 a) to d). Here, some local defects within the film seem to arise due to various reasons. In Figure a) and b) the film exhibits some holes at the surface (yellow arrows). Interestingly, right next to them, there is a missing SrO layer causing a stacking

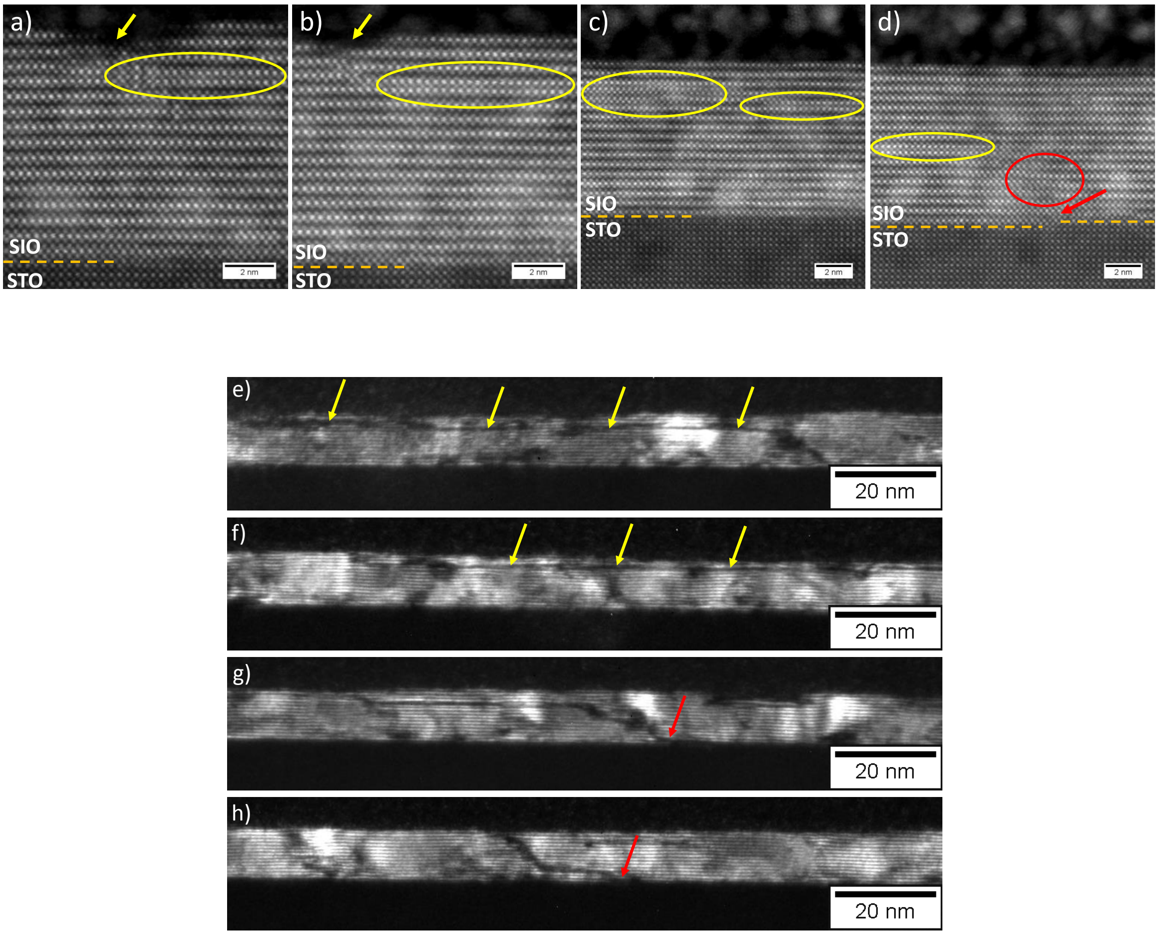

Figure 5.16: *STEM and TEM dark field images of the 16 ML thick SIO film: a) and b) STEM images with surface defect (hole) on the film surface with close missing SrO layer. c) Presence of missing SrO layers without film surface defects or substrate step edges. d) Presence of missing SrO layer with close substrate step edge. e) and f) TEM dark field images of the sample with prolonged missing SrO layer close to the film surface without certain starting point. g) and h) TEM dark field images of the sample with prolonged missing SrO layer close to the film surface with starting point at a substrate step edge.*

fault close to the film surface (yellow ellipse). Note that this defect changes the stoichiometry and phase of the film. However, missing SrO layers are also observable in film regions which do not show any holes or other defects at the film surface. Figure c) presents this situation. Here, even more than one SrO layers are missing which induce a dramatically change of the crystal structure of a (RP–214) film. In addition, Figure d) shows a film region where a SrO layer is relatively deep in the film volume missing (red ellipse). Not far away from this point, a step edge of the STO substrate is located (red arrow). Surprisingly, there are many other regions found with substrate step edges which feature a missing SrO layer close to them.

Figures 5.16 e) to h) show TEM dark field images of a wide range of the 16 ML thick SIO film. The four dark field images confirm the absence of SrO layers in the film close to the surface and reveal their dimensions. Figure e) and f) indicate missing SrO layers (yellow arrows) which are located very close to the film surface. But more interesting, these missing layers are of the dimension of about 100 nm. These wide faults of the stacking sequence of the SIO film can cause a different phase at the surface which consists of large areas. Moreover, these missing SrO layers seem to have no certain starting point, e.g. at surface defects. Figures 5.16 g) and h) demonstrate similar images with missing SrO layers which have starting points, possibly at step edges of the STO substrate (red arrows). The missing SrO layers cross the film volume and some even reach till the sample surface (see figure h)).

To conclude, it must be considered that the PLD grown SIO films contain many missing SrO layers in average, but especially in the surface near regions. Thus, the inadequate SX-ARPES study of the (RP–214) iridate films with the presence of very weak energy band dispersion may has its origin from these layer defects.

It must be considered too that not only the SIO films show such missing SrO layers but also the other two film types BIO and LSIO. In general, this effect may be also a crucial factor for other RP phase compounds and could explain why there are mainly studies published of PLD grown (RP–113) compounds.

6 Summary and outlook

The present thesis describes the thin film growth of the transition metal oxides Fe_3O_4 and (RP–214) iridates using MBE and PLD, respectively. Moreover, this thesis comprises a detailed characterization of their structural, chemical, magnetic, and electronic properties.

The heterostructure Fe_3O_4/ZnO is a promising candidate as an insertable resource of spin polarized electric currents for spintronic applications. Theoretical calculations predict 100% spin polarization of the electrons at the Fermi level for the ferrimagnetic electrode material Fe_3O_4. The main objective is to transmit these characteristic bulk properties of Fe_3O_4 to thin films and to make use of those for effective injection of spin polarized charge carriers into the semiconducting ZnO. Here, a critical aspect for the film growth as well as for the injection efficiency of charge carriers into the semiconductor is the quality of the substrate surface. ZnO has two different surfaces in [0001]-direction due to the polar character of its wurtzite structure without inversion center, the Zn-terminated (0001) and O-terminated $(000\bar{1})$ surfaces. In this thesis certain different preparation methods of these two surface types were investigated in details. It is shown that *in situ* preparation (as performed in previous studies) results in macroscopically roughened surfaces. However, an *ex situ* annealing treatment using dry and humid O_2 gas for the O- and Zn-terminated substrates, respectively, produces stepped surfaces with atomically flat terraces which are confirmed by AFM measurements. Regarding their surface structure, LEED patterns reveal the same unreconstructed surface for the *ex situ* prepared O-terminated substrate as for the *in situ* prepared substrates. In contrast, the *ex situ* Zn-terminated substrate indicates a reconstructed surface originating from its stabilization mechanism. XPS measurements of the O 1s core level peak show that the adsorption of adatoms may play an essential role in surface stabilization. While for the O-terminated surface it is assumed that a protonation of the O atoms stabilizes the surface, the Zn-terminated surface seems to get stabilized by the adsorption of OH^- groups and/or H_2O molecules. Even after being annealed at 800°C in O_2 partial pressure of $3\cdot10^{-6}$ mbar, XPS measurements indicate remaining adsorbates on the ZnO surfaces which could influence the first material layers of the initial growth of Fe_3O_4.

Well defined Fe_3O_4 films were successfully grown by MBE on the four different ZnO substrates. The surface morphology and structure as well as the film stoichiometry which are determined by AFM, LEED and chemical depth profiling via XPS, are in good agreement with the results of previous studies [6, 7]. However, the films grown on *in situ* prepared substrates show a much higher surface roughness plus a significant

amount of Zn within the film volume. It was established that samples with *in situ* prepared substrates exhibit an intermixing effect at their interfaces, while diffused Zn atoms into the film create Zn-doped ferrite layers of $Zn_xFe_{3-x}O_4$.
Moreover, volume sensitive XRD analysis confirm this observation, since only the films with *ex situ* prepared substrates show 2θ scans of phase pure $Fe_3O_4(111)$, whereas those with *in situ* prepared substrates have additional Bragg peaks which can be definitely attributed to the presence of Zn-doped ferrites.
Further XRR measurements reveal for the film with the *ex situ* prepared Zn-terminated substrate a change in stoichiometry and density of a few Fe_3O_4 layers close to the interface which can be ascribed to reactions of OH^- groups on the substrate surface with the deposited material.
It is demonstrated that films with *ex situ* prepared substrates have temperature dependent sheet resistance which which agree well with the data from the literature, whereas films with *in situ* prepared substrates possses sheet resistance values one order of magnitude higher, most likely, due to the presence of Zn-doped ferrites in these samples.
The presence of Zn-doped ferrites in Fe_3O_4 films with *in situ* prepared substrates is also verified by magnetometry measurements. While the films with *ex situ* prepared substrates exhibit hysteresis loops and saturation magnetization values which are comparable to other studies for thin films, the samples with *in situ* prepared substrates, although show typical hysteresis loops of a ferromagnetic material, reveal much higher saturation magnetization. Moreover, the former samples indicate the Verwey transition temperature almost equal to that of bulk Fe_3O_4, whereas the latter samples have clearly lower values, possibly originating from the Zn substitution in the film.
Magnetic depth profiling via PNR shows that the termination type plays a subordinate role for the film magnetization in samples with *ex situ* prepared substrates, since both films show the same gradient of reduced magnetization close to the interface. This reduced magnetization can be attributed to some anomalies of the crystalline order in the first layers of the films, e.g. APBs or interfacial strain effects. Such deviations of the magnetic order from the bulk Fe_3O_4 are also connected to variations of the charge carriers on the cation lattice which, in turn, may affect the electronic structure and the degree of spin polarization. Furthermore, they can also be responsible for increasing Schottky-barriers between the two materials, causing a potential decline of the spin injection efficiency.
A detailed TEM study of various Fe_3O_4/ZnO samples reveals the microstructural arrangement of the film layers and their interface properties. STEM micrographs show that all samples own the same density of APBs, while the interface in the film with *ex situ* prepared O-terminated substrate is the sharpest. In contrast, the interface in the sample with *ex situ* prepared Zn-terminated substrate indicates a dark region of the film layers close to the interface, which is the result of a highly disordered film lattice and/or high density of crystal defects generating the roughest interface among all samples. Moreover, composition profiles by means of STEM-EELS corroborate the smallest interface region dimension of this sample with the *ex situ* prepared O-terminated sub-

strate, whereas those for samples with *in situ* prepared substrates are much larger and comparable to that of the sample with the *ex situ* prepared Zn-terminated substrate. But most exciting is the significant amount of Zn atoms determined in the films with *in situ* prepared substrates, again confirming the presence of Zn-doped ferrites. Therefore, the sample with *ex situ* prepared O-terminated substrate seems to be the most defined regarding the interface and chemical composition of the films layers. Furthermore, Fe oxidation state analysis was performed across the interfaces and revealed for the samples with *in situ* prepared substrates in the case of Zn- and O-termination an increase of the Fe^{2+} and Fe^{3+} valency for the first Fe layer, respectively. The result for the O-terminated case is in good agreement with the literature [228], while that for the Zn-terminated case is new and not found in literature. For these samples, the termination type affects the Fe valency at the interface and can explain the presence of a magnetically dead layer. In contrast, samples with *ex situ* prepared substrates indicate no change in the oxidation state of the first Fe layer thus questioning the origin of their magnetically dead layer at the interface (revealed by SQUID and PNR). Consequently, their magnetically dead layer may originate from other effects, e.g., dislocations strain induced magnetic variations.

The film layer sequences are determined by DFT calculations (GGA+U) as ...-Zn-O-(interface)-[Fe(octa)-O-Fe(tetra)-Fe(octa)-Fe(tetra)-O]-[...]-... and ...-O-Zn-(interface)-[O-Fe(octa)-O-Fe(tetra)-Fe(octa)-Fe(tetra)]-[...]-... for the samples with O- and Zn-terminated substrates, respectively. These results are in good agreement with the findings from the structural analysis in the TEM study. However, the calculations do not show the expected valence change of the first Fe layer as revealed for samples with *in situ* prepared substrates by TEM, but rather opposite situation: Fe^{2+} and Fe^{3+} layer on the O- and Zn-terminated surface, respectively. It is possible that idealized starting configurations, e.g. minimized lattice mismatch and disregard of dislocations at the interface, have a crucial effect on the results of the calculations. In addition, spin density calculations show that in case of O-termination the topmost substrate layers imitate the spin polarization of the contiguous film layers. Here, the first O layer of the substrate is affected much stronger than the first Zn layer. Due to the strong decrease of this effect, only the substrate surface becomes sensitive to the electron spin polarization. In case of Zn-termination, spin polarization of Fe_3O_4 layers close to the interface is not observed, while the first Zn and O atoms of the substrate also do not show spin polarization. Thus, in terms of spin injection, the topmost O layer of the O-terminated substrate could play the most essential role.

In summary the *ex situ* prepared O-terminated ZnO substrate seems to be the most convenient choice to realize the spin transistor made of Fe_3O_4 as spin electrodes and ZnO as semiconducting gateway of the spin polarized charge carriers. However, direct experimental measurements of the polarization degree of the injected charge carriers into the semiconductor are necessary to evaluate the usability of Fe_3O_4/ZnO heterostructure as a resource of a spin polarized current. As an example for this, a magnetic field dependent transport measurements as described in experiments by P. Li *et al.* can be performed as first approach [253]. Here, the electronic properties of the two polar crystal directions are factors which are same important as the magnetic properties of the Fe_3O_4 film. In addition, formation of Schottky-barriers between substrate and film must be considered which could be the most critical in terms of interface resistance and impedance match.

The 5d transition metal oxides (RP–214) iridates BIO and SIO (LSIO) are of great interest in current research, since they both have many similarities to the isostructural cuprates. Beside this, they exhibit strong spin–orbit interaction due to heavy iridium atoms which makes them a spin–orbit coupling driven Mott insulators with a half filled narrow J_{eff}=1/2 LHB. On the one hand, it is interesting that BIO and SIO show almost the same crystal structure and magnetic properties which corroborate the possibility of activation of superconductivity in these materials. On the other hand, only a few publications report on the PLD grown BIO and SIO films, while there are no published data on the PLD grown LSIO films. Moreover, publications with SX-ARPES data are only available for MBE grown BIO and SIO films or their single crystals. Ultimately, one can find publications on SX-ARPES on PLD grown (RP–113) iridates.
Well defined SIO, BIO and LSIO films were successfully grown by PLD on undoped and Nb-doped STO(001) substrates. Every film shows nice RHEED oscillations till the end of its growth and an unreconstructed RHEED pattern, but without remaining Kikuchi lines which may indicate a not perfectly structured film surface.
The surface morphology and structure determined by AFM and LEED are in good agreement with the results of other studies [63, 65]. However, 40 ML thick films show much higher surface roughness than corresponding thin films of a 6 ML thickness. It must be assumed that PLD growth changes from a 2D layer-by-layer into a 3D island growth mode, resulting in an increase of the surface roughness with increasing film thickness.
Additionally, volume sensitive XRD analysis of 40 ML thick films showed Bragg peaks of phase pure (RP–214) iridates with Laue fringes. The latter is a sign of well ordered crystalline films. The corresponding rocking curves revealed very low mosaicity in the films.
Conductivity measurements confirm the insulating nature of the 12 ML BIO and SIO films. Exponential upturns of their resistances are observed at low temperatures. In contrast, the LSIO film shows only a marginal increase of its resistance at low temperatures, revealing a successful n-doping of the Mott insulator SIO by La atoms. However, a decrease of its resistance is not observed, which makes a potential transition into a superconducting state unlikely. The trends of the temperature dependent resistances of the films and their energy gap values are in good agreement with the literature [124, 246].
Analysis by XPS reveals clean film surfaces without C contamination. For the SIO and LSIO films, only a small amout of Ba impurity atoms was found, whereas for the BIO film no impurities were observed. In addition, XPS chemical depth profiling of the O 1s, Ir 4d and 4f, Ba 4s and 4d (BIO), Sr 3p (SIO and LSIO) core level spectra reveals an increase of the Ir and O spectral weight at higher emission angles which indicates an increase of their amount in the film layers close to the surface. While the bulk-sensitive

measurements reveal almost stoichiometric composition of films, such increase of Ir and O in the surface region is a sign of (RP–113) phase formation. Moreover, the slightly different three-peak structure of the VB spectra can be explained by different strength of spin-orbit interaction in the films, while their shapes are in good agreement with other studies [252]. It seems that for LSIO, the broadening of the VB peaks could create a spectral weight at the Fermi level, which could be attributed to the formation of the quasiparticles. However, the LSIO film shows a similar spectral weight and equal VB maximum offset as BIO and SIO, resulting rather in a persisting Mott insulator with strong electron correlations than in a correlated metal. Furthermore, depth profiling of the VB spectra points out that J_{eff} states are more surface than bulk sensitive.

SX-ARPES measurements were performed to compare the data with the results from previous studies which were done on single crystals. In principle, all three films show indication of the spectral weight at the correct highsymmetry points in the measured constant binding energy k-space maps. However, the k-space maps of all three 12 ML thick films indicate very weak energy band dispersions which is also demonstrated by highsymmetry cuts and their corresponding EDC plots. It should be considered that these films are imperfect at and close to the surface. In case of LSIO, the measurements could resolve small spectral weight between the highsymmetry M points just below the Fermi level. This observation can be attributed to the quasiparticle states which may indicate the evolution of a Fermi-arc. This result is in good agreement with the literature data for not optimally La-doped SIO single crystals [71].

An exemplary 16 ML thick SIO film was analyzed by TEM. STEM micrographs and dark field images reveal missing SrO layers within the film, resulting in stacking sequence faults and locally in a (RP–113) phase. Some of these missing SrO layers are close to the film surface and about 100 nm in dimension. This fact can explain a lot of the effects observed in the previous characterization steps of the films. The missing SrO layers may affect not only the growth mode for thicker films and the increasing amount of Ir and O in the film layers close to the surface, but also the weak dispersion strength of the energy bands in k-space maps in surface sensitive SX-ARPES measurements. The incoherently scattered photoelectrons are a plausible reason for the blurred k-space maps.

Consequently, it is essential to analyze PLD grown (RP–214) iridates by TEM and to ensure the correct stacking sequence of the film. In combination with XPS depth profiling and XRD, one should be able to optimize the film volume stoichiometry. However, since growth recipes of these (RP–214) iridates from the literature are mostly the same, it must be considered that these materials need different growth procedures than presented in this thesis. This could also play a major role in the fact that there is only a small number of publication on PLD grown iridates with $n \neq \infty$, especially in case of SX-ARPES studies. It is possible that MBE samples are easier to get grown for these kind of iridates, since here each layer is grown separately (SrO, IrO_2, ...). To grow in a similar way with PLD, one has to use two targets with the corresponding layer materials SrO and IrO_2.

Therefore, the main objectives for further investigations of PLD grown (RP–214) iridates are the improvement of the film quality developing more effective recipes. The main goal is a homogeneous growth of stacking sequences without missing layers as well as further ultimate validation of films by SX-ARPES. Concerning the PLD grown LSIO film in this thesis, it should be proved if the film is optimally doped by La atoms, since the SX-ARPES measurements already revealed the formation of additional states close to the Fermi level. Moreover, different dopants and also different substrates should be tried out to activate a superconducting phase after all.

Appendix

A Material specific parameters for reflectometry analysis

Table A.1: *Overview of the particle number densities ρ, real part b and imaginary part b_i of the nuclear scattering lengths [160] for thermal neutrons, and real part δ and imaginary part β of the optical refractive index [254] at 1.54 Å for the relevant materials. For the calculations of the neutron scattering lengths, a natural isotope distribution in the materials is assumed.*

material	$\rho\,(10^{22}\,\mathrm{f.u./cm})$	$b\,(\mathrm{fm/f.u.})$	$b_i\,(10^{-2}\mathrm{fm/f.u.})$	$\delta(10^{-5})$	$\beta(10^{-6})$
Fe_3O_4	1.34 [38]	51.57	0.21	1.53	1.40
Fe_2O_3	1.83 [38]	36.32	0.14	1.44	1.26
FeO	4.94 [38]	15.26	0.07	1.34	1.69
ZnO	4.15 [255]	11.49	0.03	1.61	0.33
Au	5.90 [158]	7.90	2.74	4.71	4.85

B.1 RHEED patterns of the prepared polar ZnO substrates before growth

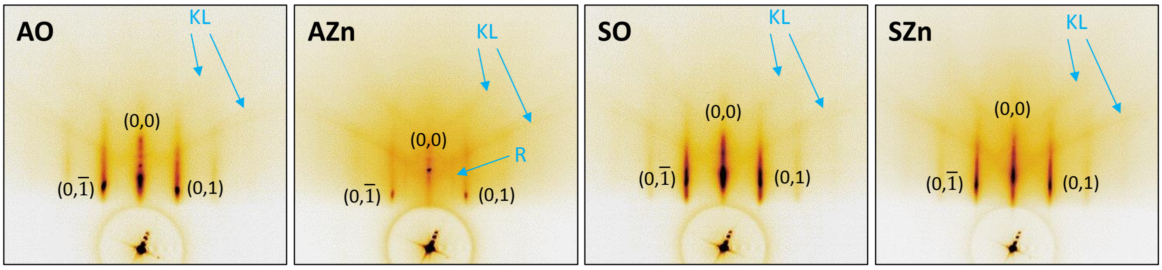

Figure B.1: *Analogical RHEED patterns of* ex situ *annealed (AO, AZn) and* in situ *sputtered and annealed (SO, SZn) ZnO substrates in $[\bar{1}10]$-direction at 400° C just before the initial growth process of Fe_3O_4. Kikuchi lines and surface reconstructions are indicated by "KL" and "R", respectively.*

B.2 Characterization of prepared ZnO substrates by XRD

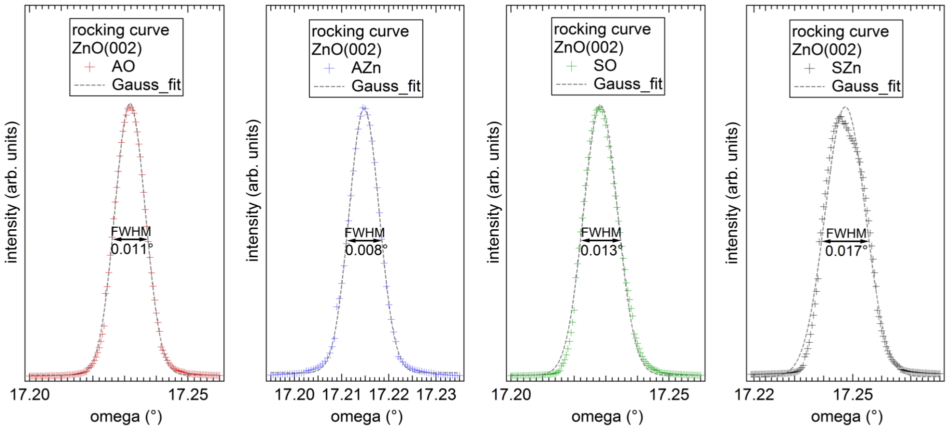

Figure B.2: *Rocking curves of the ZnO(002) Bragg peaks of the* ex situ *annealed (AO, AZn) and* in situ *sputtered and annealed (SO, SZn) ZnO substrates. All curves are fitted by Gaussians.*

C Characterization of the Fe_3O_4/ZnO heterostructures by XRR

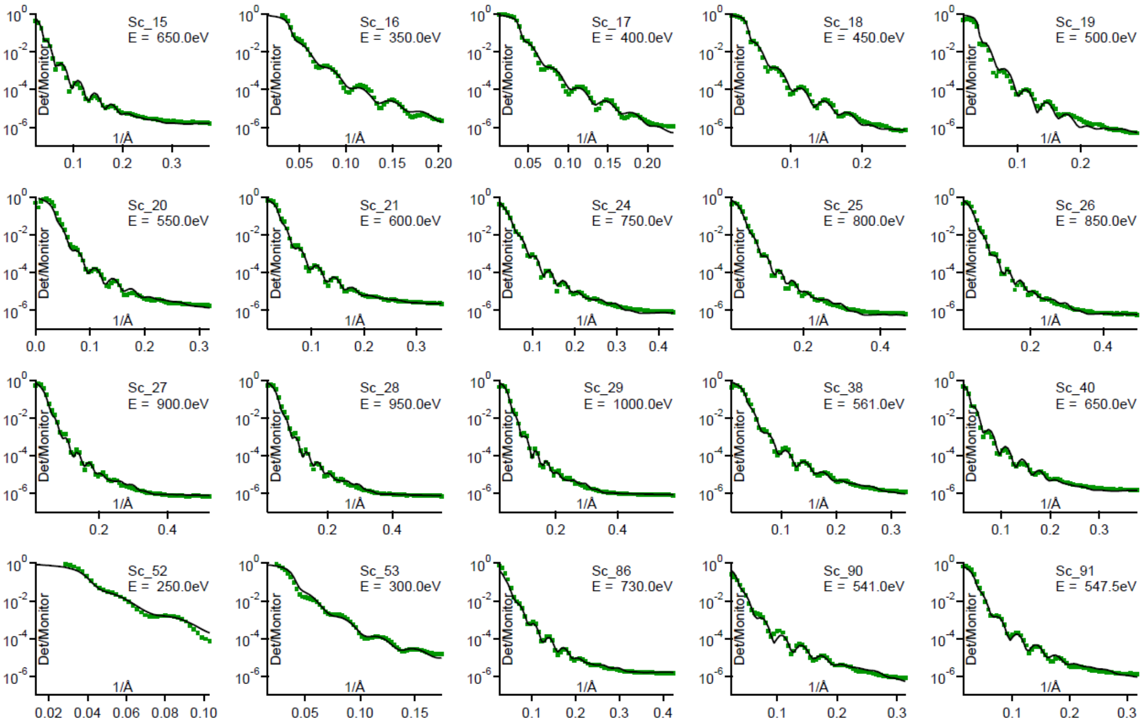

Figure C.1: *XRR data measured at various off-resonance energies and corresponding fits for sample FAO.*

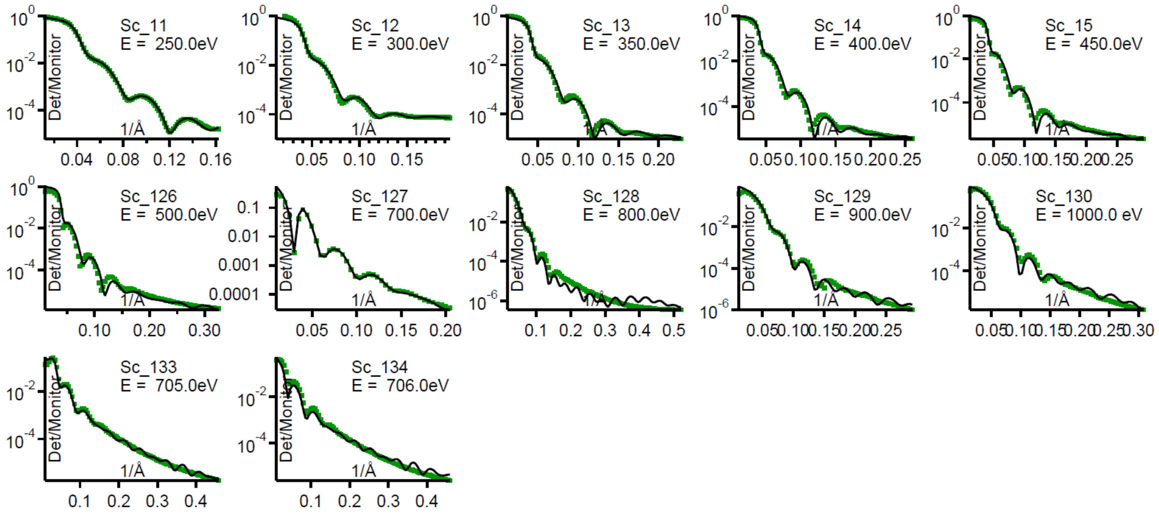

Figure C.2: *XRR data measured at various off-resonance energies and corresponding fits for sample FSZn.*

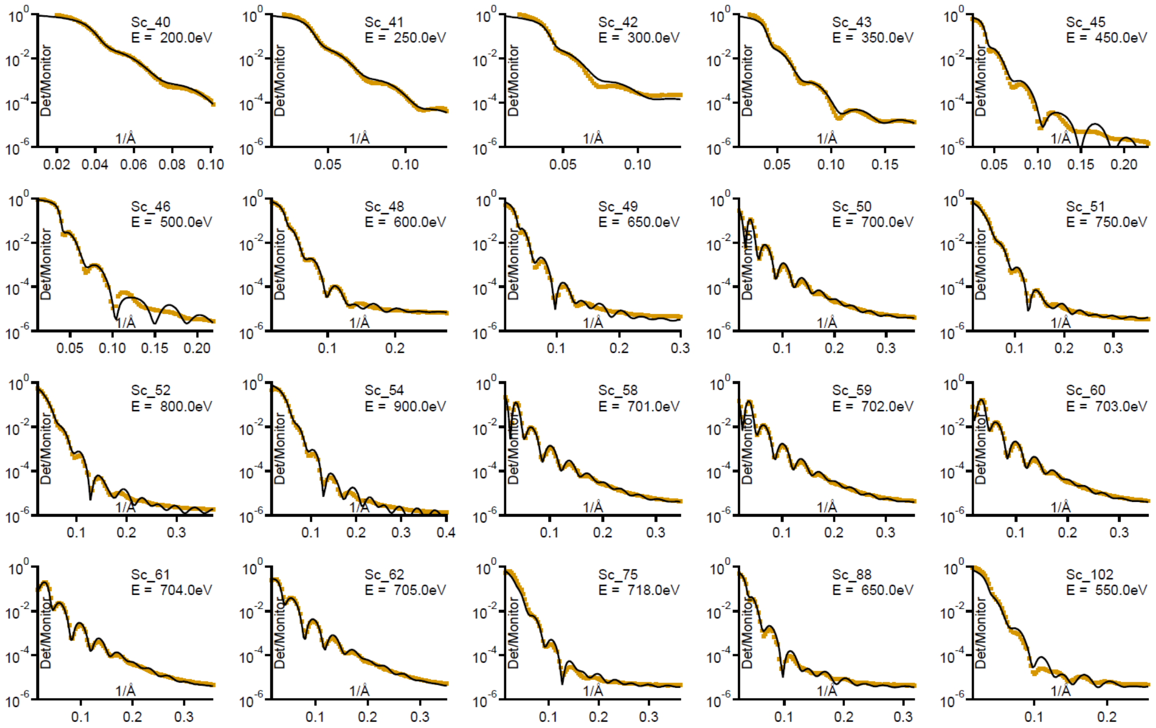

Figure C.3: *XRR data measured at various off-resonance energies and corresponding fits for sample FSO.*

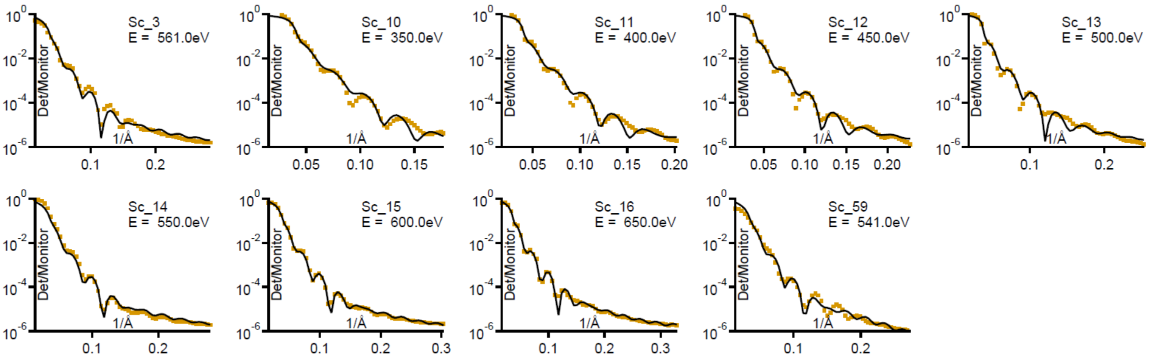

Figure C.4: *XRR data measured at various off-resonance energies and corresponding fits for sample FAZn.*

D Identification of the ZnO substrate termination in Fe_3O_4/ZnO heterostructures by STEM

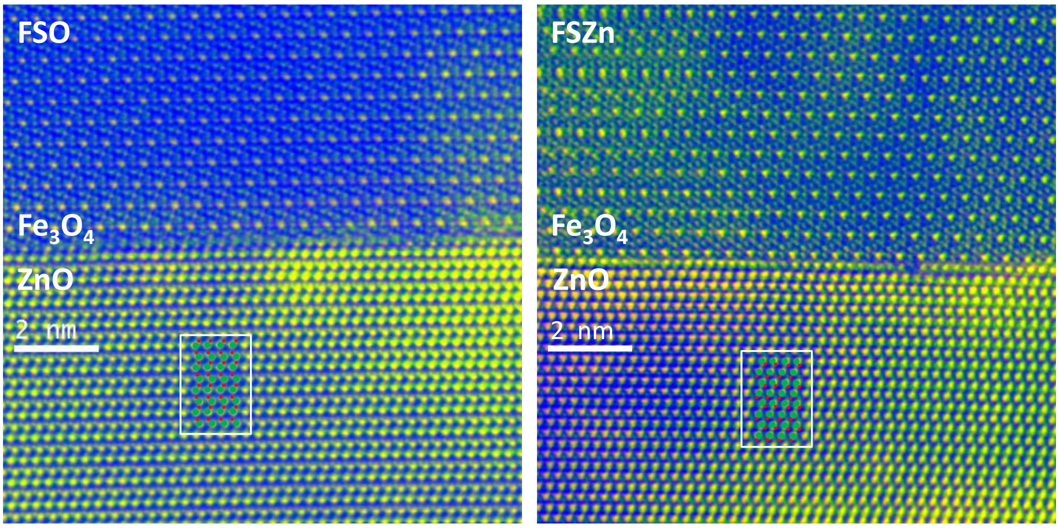

Figure D.1: *RGB colored images (red(R)=HAADF, green(G)=i-ABF, blue(B)=ABF)) of* Fe_3O_4*/ZnO heterostructures with in situ sputtered and annealed ZnO substrates. Positions of O atoms (marked red within the white frame) beside the Zn atoms (marked green within the white frame) can be visualized. Thus, the identification of the ZnO polarity is enabled.*

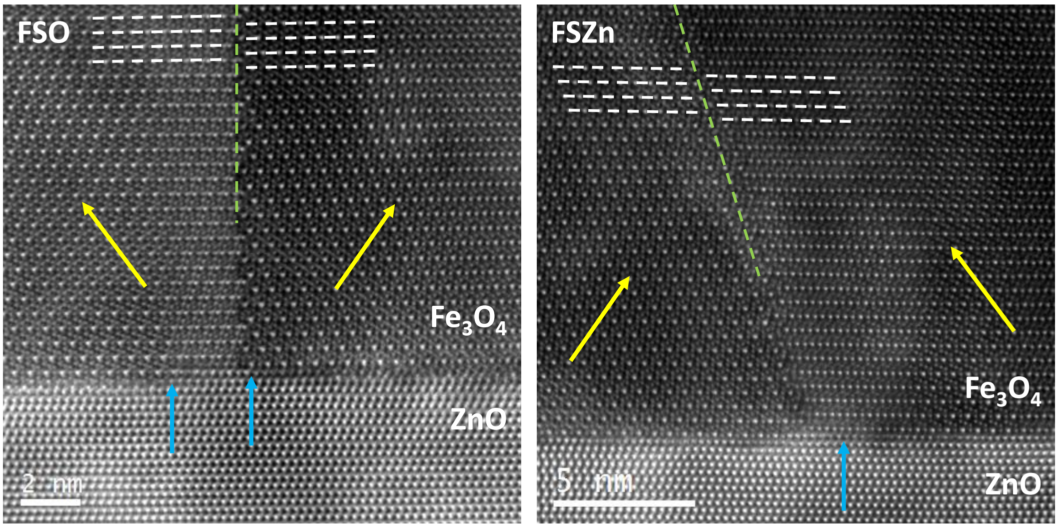

Figure D.2: *APBs in FSO and FSZn. Regions with a APB/twin boundary (marked by dashed green lines) changing the orientation of the [110] film direction (marked by yellow arrows) by a rotation of* $\pi/3$ *and* $-\pi/3$ *for FSO and FSZn, respectively, while one step is present at their interfaces (marked by blue arrows).*

E Results from DFT calculations for the interface types of Fe_3O_4/ZnO heterostructures

Table E.1: *Results: total energy* E*, Gibbs free surface energy* γ *and number of atoms* N *for the interface types A, B, C and D in the case of O-terminated substrates for* Fe_3O_4*/ZnO heterostructures.*

interface type	A	B	C	D
total energy E [eV]	-722.706	-674.503	-667.458	-658.796
γ [meV/Å^2]	-51	-47	-122	-160
N_{atoms}	129	122	121	120
N_{Fe}	29	26	25	24
N_{Zn}	28	28	28	28
N_O	68	64	64	64

Table E.2: *Results: total energy E, Gibbs free surface energy γ and number of atoms N for the interface types A and B in the case of Zn-terminated substrates for Fe_3O_4/ZnO heterostructures.*

interface type	A	B
total energy E [eV]	-683.545	-636.471
γ [meV/Å^2]	-261	-280
N_{atoms}	118	111
N_{Fe}	26	23
N_{Zn}	28	28
N_O	64	60

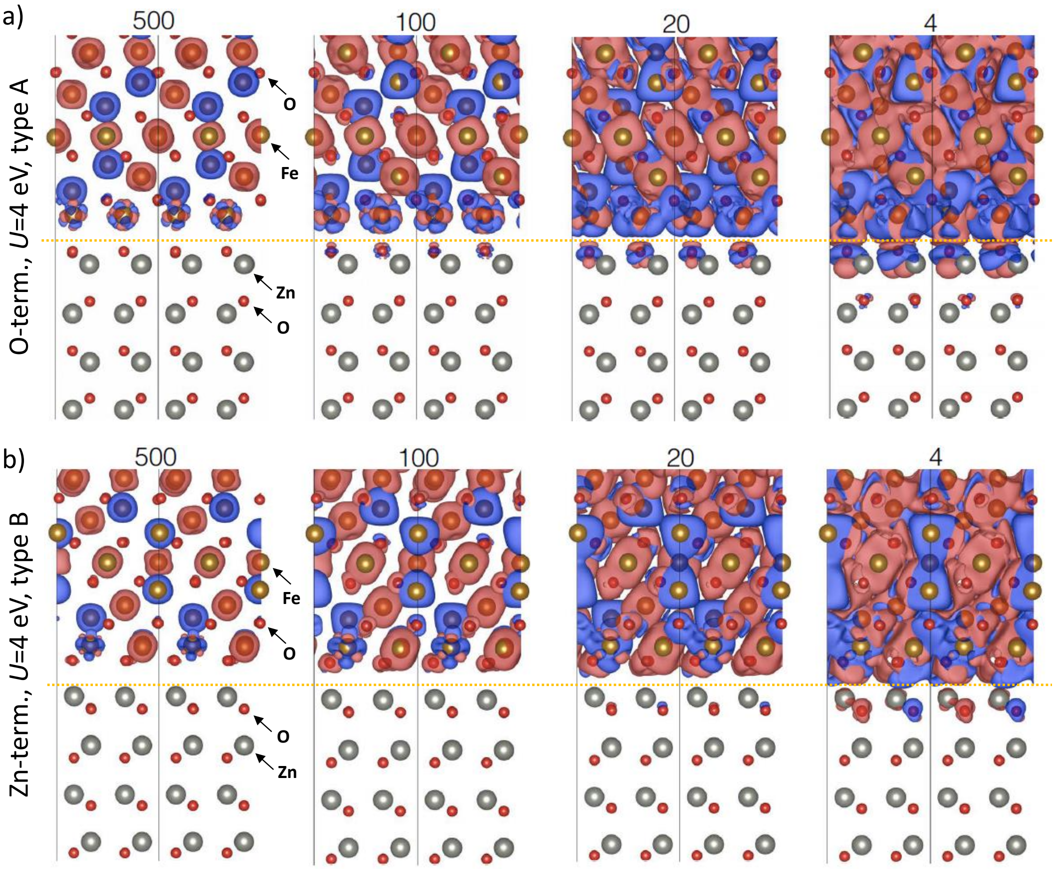

Figure E.1: *Spin densities in the Fe_3O_4/ZnO heterostructure with (a) O-terminated and (b) Zn-terminated substrate for U=4 eV. The dashed orange line indicates each interface. The calculations are done for the favored interface types, type A for the O-terminated and type B for the Zn-terminated case with different isosurface values, while spin-up and spin-down are marked red and blue, respectively.*

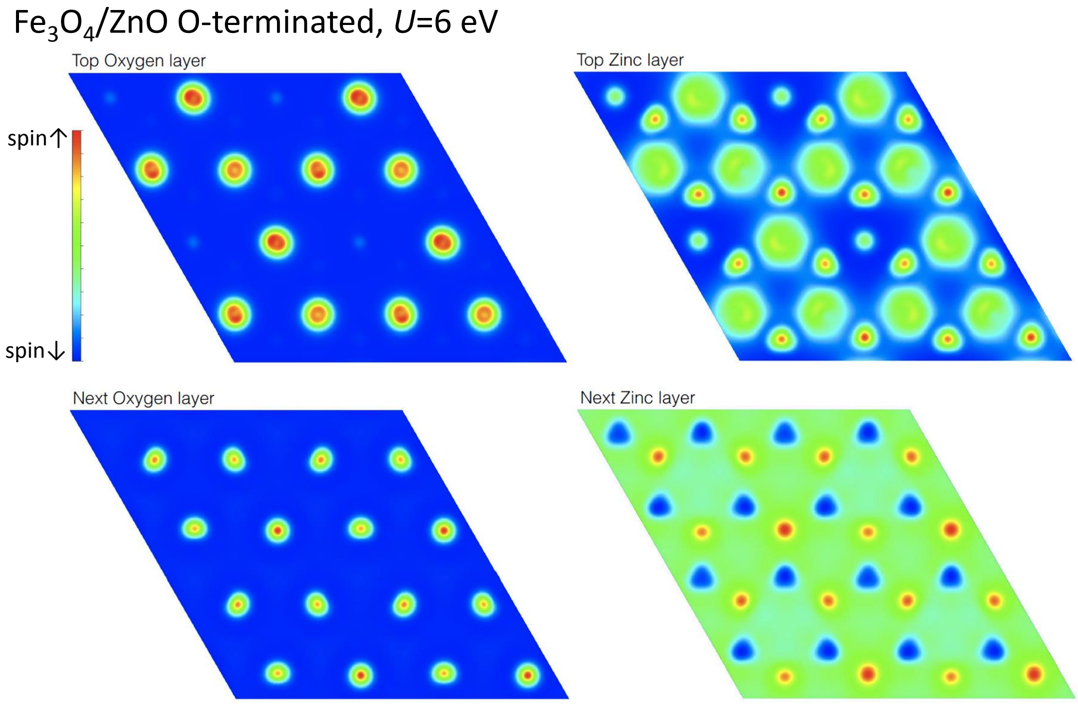

Fe_3O_4/ZnO O-terminated, *U*=6 eV

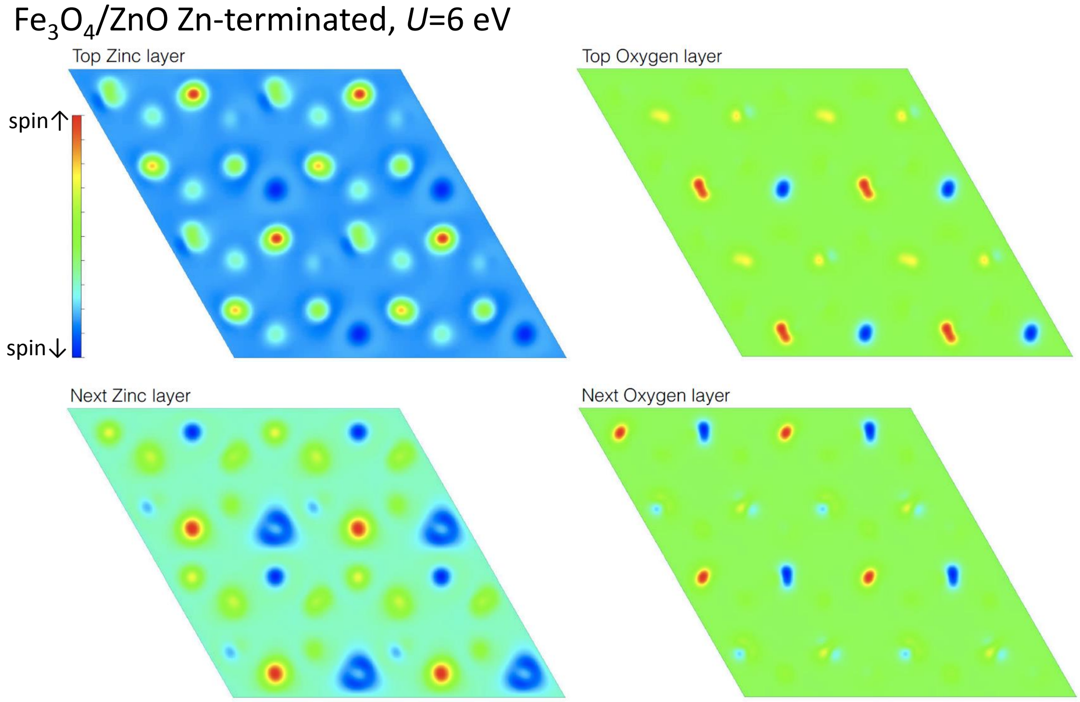

Fe_3O_4/ZnO Zn-terminated, *U*=6 eV

Figure E.2: *Layer resolved spin densities in the Fe_3O_4/ZnO heterostructure for cuts in [110]-direction, obtained at different depths (first 4 layers) of the relevant ZnO substrate with certain termination.*

F Characterization of STO substrates by XRD rocking curves

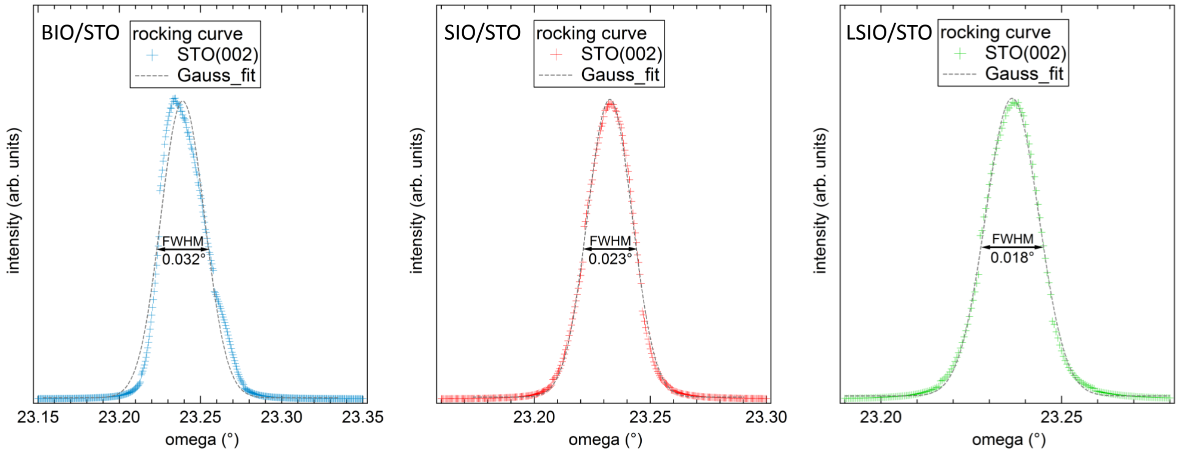

Figure F.1: *Rocking curves of the STO(002) Bragg peaks of the 40 ML thick (RP–214) iridate films grown on STO(001) substrates. All curves are fitted by Gaussians.*

G Fitting procedure of the O 1s and Ir 4f core level and VB spectra

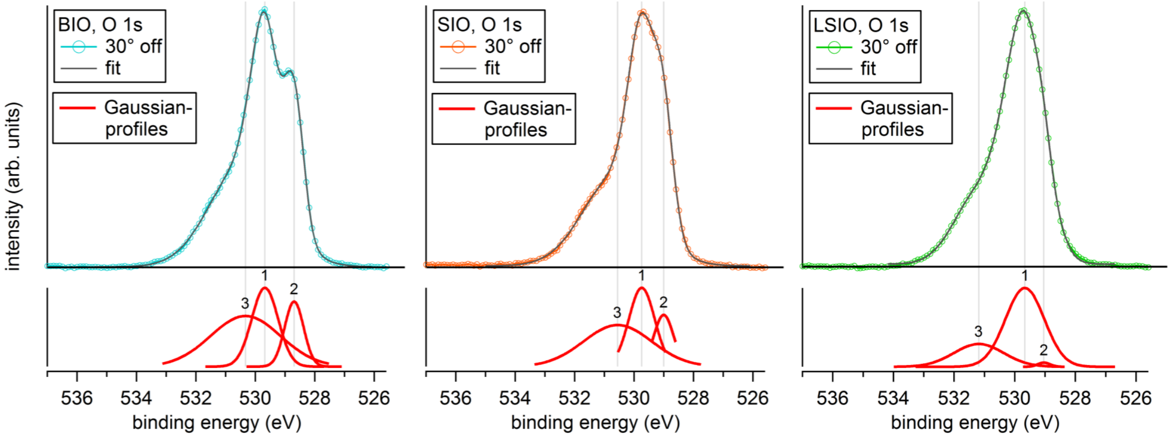

Figure G.1: *Area normalized and fitted O 1s core level spectra of the 12 ML thick (RP–214) iridate films measured at 30° off NE.*

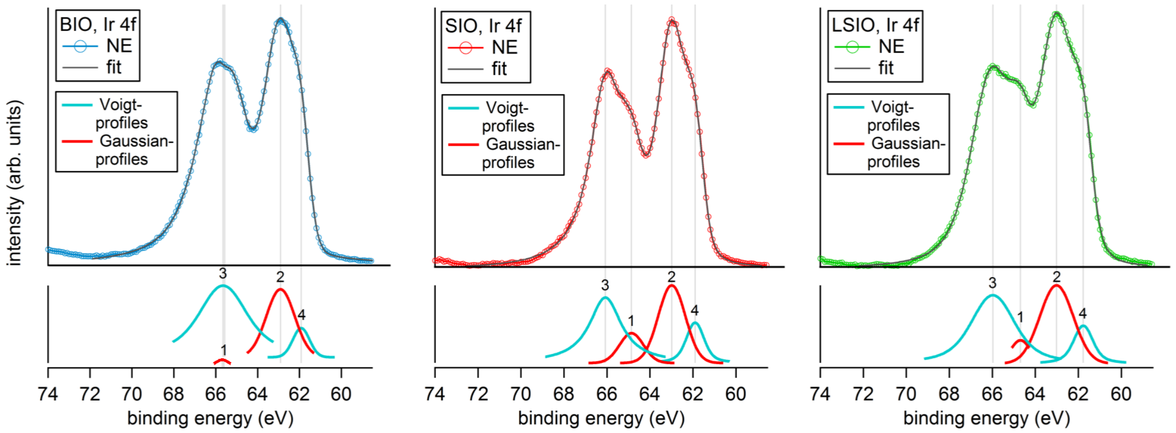

Figure G.2: *Area normalized and fitted Ir 4f core level spectra of the 12 ML thick (RP–214) iridate films measured at NE.*

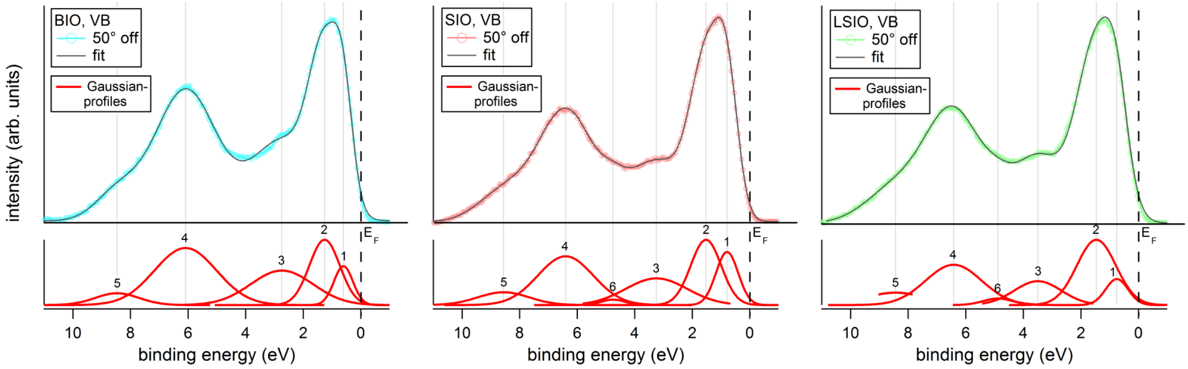

Figure G.3: *Area normalized and fitted VB spectra of the 12 ML thick (RP–214) iridate films measured at 50° off NE.*

Bibliography

[1] G. E. Uhlenbeck and S. Goudsmit. Ersetzung der Hypothese vom unmechanischen Zwang durch eine Forderung bezüglich des inneren Verhaltens jedes einzelnen Elektrons. *Die Naturwissenschaften*, **13**:953–954, 1925.

[2] G. E. Uhlenbeck and S. Goudsmit. Spinning Electrons and the Structure of Spectra. *Nature*, **117**:264–265, 1926.

[3] R. A. de Groot, F. M. Mueller, P. G. van Engen, and K. H. J. Buschow. New Class of Materials: Half-Metallic Ferromagnets. *Phys. Rev. Lett.*, **50**:2024–2027.

[4] M. Ziese. Extrinsic magnetotransport phenomena in ferromagnetic oxides. *Reports on Progress in Physics*, **65**:143, 2002.

[5] G. Schmidt. Concepts for spin injection into semiconductors–a review. *Journal of Physics D: Applied Physics*, **38**:R107, 2005.

[6] M. C. Paul. *Molecular beam epitaxy and properties of magnetite thin films on semiconducting substrates.* Dissertation, Würzburg, 2010.

[7] A. Müller. *Towards functional oxide heterostructures.* Dissertation, Würzburg, 2012.

[8] R. Winkler and M. Oestreich. Überblick-Spinelektronik. *Physik Journal*, **3**:39–44, 2004.

[9] G. S. Parkinson, U. Diebold, L. Malkinski, and J. Tang. *Tailoring the interface properties of magnetite for spintronics.* INTECH Open Access Publisher (Advanced Magnetic Materials), Rijeka, 2012.

[10] S. A. Wolf, D. D. Awschalom, R. A. Buhrman, J. M. Daughton, S. von Molnár, M. L. Roukes, A. Y. Chtchelkanova, and D. M. Treger. Spintronics: A Spin-Based Electronics Vision for the Future. *Science*, **294**:1488–1495, 2001.

[11] S. Datta and B. Das. Electronic analog of the electro–optic modulator. *Applied Physics Letters*, **56**:665–667, 1990.

[12] H. Kronmüller and S. S. P. Parkin. *Handbook of magnetism and advanced magnetic materials, Volume 4.* John Wiley and Sons, New Jersey, 2007.

[13] X. Zhang, S. Mizukami, Q. Ma, T. Kubota, M. Oogane, H. Naganuma, Y. Ando, and T. Miyazaki. Spin-dependent transport behavior in C60 and Alq3 based spin valves with a magnetite electrode (invited). *Journal of Applied Physics*, **115**:172608, 2014.

[14] X. Zhang, Q. Ma, K. Suzuki, A. Sugihara, G. Qin, T. Miyazaki, and S. Mizukami. Magnetoresistance Effect in Rubrene-Based Spin Valves at Room Temperature. *ACS Applied Materials & Interfaces*, **7**:4685–4692, 2015.

[15] H. T. Wang, B. S. Kang, F. Ren, L. C. Tien, P. W. Sadik, D. P. Norton, S. J. Pearton, and Jenshan Lin. Hydrogen-selective sensing at room temperature with ZnO nanorods. *Applied Physics Letters*, **86**:243503, 2005.

[16] P.-S. Cho, K.-W. Kim, and J.-H. Lee. NO2 sensing characteristics of ZnO nanorods prepared by hydrothermal method. *Journal of Electroceramics*, **17**:975–978, 2006.

[17] N. Volbers. *Sekundärionenmassenspektrometrie an Zinkoxid.* Dissertation, Giessen, 2007.

[18] Ü. Özgür, Ya. I. Alivov, C. Liu, A. Teke, M. A. Reshchikov, S. Doğan, V. Avrutin, S.-J. Cho, and H. Morkoç. A comprehensive review of ZnO materials and devices. *Journal of Applied Physics*, **98**:041301, 2005.

[19] H. Morkoç and Ü. Özgür. *Zinc oxide.* Wiley-VCH, Weinheim, 2009.

[20] M. Althammer, E.-M. Karrer-Müller, S. T. B. Goennenwein, M. Opel, and R. Gross. Spin transport and spin dephasing in zinc oxide. *Applied Physics Letters*, **101**:082404, 2012.

[21] M. W. Allen, D. Y. Zemlyanov, G. I. N. Waterhouse, J. B. Metson, T. D. Veal, C. F. McConville, and S. M. Durbin. Polarity effects in the x-ray photoemission of ZnO and other wurtzite semiconductors. *Applied Physics Letters*, **98**:101906, 2011.

[22] A. N. Mariano and R. E. Hanneman. Crystallographic Polarity of ZnO Crystals. *Journal of Applied Physics*, **34**:384–388, 1963.

[23] V. Melfos, B. Helly, and P. Voudouris. The ancient Greek names “Magnesia” and “Magnetes” and their origin from the magnetite occurrences at the Mavrovouni mountain of Thessaly, central Greece. A mineralogical–geochemical approach. *Archaeological and Anthropological Sciences*, **3**:165–172, 2011.

[24] C. Jimenez-Lopez, C. S. Romanek, and D. A. Bazylinski. Magnetite as a prokaryotic biomarker: A review. *Journal of Geophysical Research: Biogeosciences*, **115**:G00G03, 2156–2202, 2010.

[25] M. E. Fleet. The structure of magnetite. *Acta Crystallographica Section B*, **37**:917–920, 1981.

[26] E. P. Wohlfarth and K. H. J. Buschow. *Ferromagnetic materials: a handbook on the properties of magnetically ordered substances, Volume 3.* Amsterdam [u.a.] North-Holland Publ. Co, 1987.

[27] R. C. O'Handley. *Modern Magnetic Materials: Principles and Applications.* John Wiley and Sons, New York, 2000.

[28] E. J. W. Verwey. Electronic Conduction of Magnetite Fe_3O_4 and its Transition Point at Low Temperatures. *Nature*, **144**:327–328, 1939.

[29] F. Walz. The Verwey transition - a topical review. *Journal of Physics: Condensed Matter*, **14**:R285, 2002.

[30] J. García and G. Subías. The Verwey transition - a new perspective. *Journal of Physics: Condensed Matter*, **16**:R145, 2004.

[31] Z. Kąkol, J. Sabol, J. Stickler, and J. M. Honig. Effect of low-level titanium(IV) doping on the resistivity of magnetite near the Verwey transition. *Phys. Rev. B*, **46**:1975–1978, 1992.

[32] M. G. Chapline and S. X. Wang. Observation of the Verwey transition in thin magnetite films. *Journal of Applied Physics*, **97**:123901, 2005.

[33] K. H. J. Buschow. *Handbook of Magnetic Materials, Volume 8.* Amsterdam [u.a.] North-Holland Publ. Co, 1995.

[34] C. Zener. Interaction between the *d*-Shells in the Transition Metals. II. Ferromagnetic Compounds of Manganese with Perovskite Structure. *Phys. Rev.*, **82**:403–405, 1951.

[35] A. Yanase and N. Hamada. Electronic Structure in High Temperature Phase of Fe3O4. *Journal of the Physical Society of Japan*, **68**:1607–1613, 1999.

[36] L. Néel. Magnetic properties of ferrites: ferrimagnetism and antiferromagnetism. *Ann. Phys*, **3**:137–198, 1948.

[37] E. Goering, S. Gold, M. Lafkioti, and G. Schütz. Vanishing Fe 3d orbital moments in single-crystalline magnetite. *EPL (Europhysics Letters)*, **73**:97, 2006.

[38] R. M. Cornell and U. Schwertmann. *The iron oxides : structure, properties, reactions, occurrences, and uses.* Wiley-VCH, 2nd, completely rev. and extended edition, Weinheim, 2003.

[39] H.-T. Jeng and G. Y. Guo. First-principles investigations of the electronic structure and magnetocrystalline anisotropy in strained magnetite Fe_3O_4. *Phys. Rev. B*, **65**:094429, 2002.

[40] Z. Zhang and S. Satpathy. Electron states, magnetism, and the Verwey transition in magnetite. *Phys. Rev. B*, **44**:13319–13331, 1991.

[41] A. R. Lennie, N. G. Condon, F. M. Leibsle, P. W. Murray, G. Thornton, and D. J. Vaughan. Structures of Fe_3O_4 (111) surfaces observed by scanning tunneling microscopy. *Phys. Rev. B*, **53**:10244–10253, 1996.

[42] Yu. S. Dedkov, U. Rüdiger, and G. Güntherodt. Evidence for the half-metallic ferromagnetic state of Fe_3O_4 by spin-resolved photoelectron spectroscopy. *Phys. Rev. B*, **65**:064417, 2002.

[43] M. Friák, A. Schindlmayr, and M. Scheffler. Ab initio study of the half-metal to metal transition in strained magnetite. *New Journal of Physics*, **9**:5, 2007.

[44] D. T. Margulies, F. T. Parker, M. L. Rudee, F. E. Spada, J. N. Chapman, P. R. Aitchison, and A. E. Berkowitz. Origin of the Anomalous Magnetic Behavior in Single Crystal Fe_3O_4 Films. *Phys. Rev. Lett.*, **79**:5162–5165, 1997.

[45] S. Celotto, W. Eerenstein, and T. Hibma. Characterization of anti-phase boundaries in epitaxial magnetite films. *The European Physical Journal B - Condensed Matter and Complex Systems*, **36**:271–279, 2003.

[46] A. M. Bataille, L. Ponson, S. Gota, L. Barbier, D. Bonamy, M. Gautier-Soyer, C. Gatel, and E. Snoeck. Characterization of antiphase boundary network in Fe_3O_4(111) epitaxial thin films: Effect on anomalous magnetic behavior. *Phys. Rev. B*, **74**:155438, 2006.

[47] W. Eerenstein, T. T. M. Palstra, S. S. Saxena, and T. Hibma. Spin-Polarized Transport across Sharp Antiferromagnetic Boundaries. *Phys. Rev. Lett.*, **88**:247204, 2002.

[48] I. Knittel, J. Wei, Y. Zhou, S. K. Arora, I. V. Shvets, M. Luysberg, and U. Hartmann. Observation of antiferromagnetic coupling in epitaxial ferrite films. *Phys. Rev. B*, **74**:132406, 2006.

[49] W. Eerenstein, T. T. M. Palstra, T. Hibma, and S. Celotto. Origin of the increased resistivity in epitaxial Fe_3O_4 films. *Phys. Rev. B*, **66**:201101, 2002.

[50] W. Eerenstein, L. Kalev, L. Niesen, T.T.M. Palstra, and T. Hibma. Magnetoresistance and superparamagnetism in magnetite films on MgO and $MgAl_2O_4$. *Journal of Magnetism and Magnetic Materials*, **258 - 259**:73–76, 2003.

[51] U. Schwertmann and R. M. Cornell. *Iron Oxides in the Laboratory: Preparation and Characterization.* Wiley-VCH, Weinheim, 2007.

[52] J. G. Bednorz and K. A. Müller. Possible high Tc superconductivity in the Ba-La-Cu-O system. *Zeitschrift für Physik B Condensed Matter*, **64**:189–193, 1986.

[53] M. Imada, A. Fujimori, and Y. Tokura. Metal-insulator transitions. *Rev. Mod. Phys.*, **70**:1039–1263, 1998.

[54] Y. Tokura and N. Nagaosa. Orbital Physics in Transition-Metal Oxides. *Science*, **288**:462–468, 2000.

[55] H. Watanabe, T. Shirakawa, and S. Yunoki. Microscopic Study of a Spin-Orbit-Induced Mott Insulator in Ir Oxides. *Phys. Rev. Lett.*, **105**:216410, 2010.

[56] J. Nichols, J. Terzic, E. G. Bittle, Korneta O. B., L. E. De Long, J. W. Brill, G. Cao, and S. S. A. Seo. Tuning electronic structure via epitaxial strain in Sr2IrO4 thin films. *Applied Physics Letters*, **102**:141908, 2013.

[57] B. J. Kim, Hosub Jin, S. J. Moon, J.-Y. Kim, B.-G. Park, C. S. Leem, Jaejun Yu, T. W. Noh, C. Kim, S.-J. Oh, J.-H. Park, V. Durairaj, G. Cao, and E. Rotenberg. Novel $J_{\text{eff}} = 1/2$ Mott State Induced by Relativistic Spin-Orbit Coupling in Sr_2IrO_4. *Phys. Rev. Lett.*, **101**:076402, 2008.

[58] Q. Wang, Y. Cao, J. A. Waugh, S. R. Park, T. F. Qi, O. B. Korneta, G. Cao, and D. S. Dessau. Dimensionality-controlled Mott transition and correlation effects in single-layer and bilayer perovskite iridates. *Phys. Rev. B*, **87**:245109, 2013.

[59] A. Yamasaki, H. Fujiwara, S. Tachibana, D. Iwasaki, Y. Higashino, C. Yoshimi, K. Nakagawa, Y. Nakatani, K. Yamagami, H. Aratani, O. Kirilmaz, M. Sing, R. Claessen, H. Watanabe, T. Shirakawa, S. Yunoki, A. Naitoh, K. Takase, J. Matsuno, H. Takagi, A. Sekiyama, and Y. Saitoh. Three-dimensional electronic structures and the metal-insulator transition in Ruddlesden-Popper iridates. *Phys. Rev. B*, **94**:115103, 2016.

[60] S. Moser, L. Moreschini, A. Ebrahimi, B. Dalla Piazza, M. Isobe, H. Okabe, J. Akimitsu, V. V. Mazurenko, K. S. Kim, A. Bostwick, E. Rotenberg, J. Chang, H. M. Rønnow, and M. Grioni. The electronic structure of the high-symmetry perovskite iridate Ba_2IrO_4. *New Journal of Physics*, **16**:013008, 2014.

[61] Y. F. Nie, P. D. C. King, C. H. Kim, M. Uchida, H. I. Wei, B. D. Faeth, J. P. Ruf, J. P. C. Ruff, L. Xie, X. Pan, C. J. Fennie, D. G. Schlom, and K. M. Shen. Interplay of Spin-Orbit Interactions, Dimensionality, and Octahedral Rotations in Semimetallic $SrIrO_3$. *Phys. Rev. Lett.*, **114**:016401, 2015.

[62] J. K. Kawasaki, Masaki Uchida, Hanjong Paik, Darrell G. Schlom, and Kyle M. Shen. Evolution of electronic correlations across the rutile, perovskite, and Ruddelsden-Popper iridates with octahedral connectivity. *Phys. Rev. B*, **94**:121104, 2016.

[63] M. Uchida, Y. F. Nie, P. D. C. King, C. H. Kim, C. J. Fennie, D. G. Schlom, and K. M. Shen. Correlated vs. conventional insulating behavior in the $\mathrm{J_{eff}} = \frac{1}{2}$ vs. $\frac{3}{2}$ bands in the layered iridate $\mathrm{Ba_2IrO_4}$. *Phys. Rev. B*, **90**:075142, 2014.

[64] C. Lu, A. Quindeau, H. Deniz, D. Preziosi, D. Hesse, and M. Alexe. Crossover of conduction mechanism in Sr2IrO4 epitaxial thin films. *Applied Physics Letters*, **105**:082407, 2014.

[65] C. R. Serrao, L. Jian, J. T. Heron, G. Singh-Bhalla, A. Yadav, S. J. Suresha, R. J. Paull, D. Yi, J.-H. Chu, M. Trassin, A. Vishwanath, E. Arenholz, C. Frontera, J. Železný, T. Jungwirth, X. Marti, and R. Ramesh. Epitaxy-distorted spin-orbit Mott insulator in $\mathrm{Sr_2IrO_4}$ thin films. *Phys. Rev. B*, **87**:085121, 2013.

[66] S. S. A. Seo, J. Nichols, J. Hwang, J. Terzic, J. H. Gruenewald, M. Souri, J. Thompson, J. G. Connell, and G. Cao. Selective growth of epitaxial $\mathrm{Sr_2IrO_4}$ by controlling plume dimensions in pulsed laser deposition. *Applied Physics Letters*, **109**:201901, 2016.

[67] F. Wang and T. Senthil. Twisted Hubbard Model for $\mathrm{Sr_2IrO_4}$: Magnetism and Possible High Temperature Superconductivity. *Phys. Rev. Lett.*, **106**:136402, 2011.

[68] H. Watanabe, T. Shirakawa, and S. Yunoki. Monte Carlo Study of an Unconventional Superconducting Phase in Iridium Oxide J_{eff}=1/2 Mott Insulators Induced by Carrier Doping. *Phys. Rev. Lett.*, **110**:027002, 2013.

[69] Z. Y. Meng, Y. B. Kim, and H.-Y. Kee. Odd-Parity Triplet Superconducting Phase in Multiorbital Materials with a Strong Spin-Orbit Coupling: Application to Doped $\mathrm{Sr_2IrO_4}$. *Phys. Rev. Lett.*, **113**:177003, 2014.

[70] Y. K. Kim, O. Krupin, J. D. Denlinger, A. Bostwick, E. Rotenberg, Q. Zhao, J. F. Mitchell, J. W. Allen, and B. J. Kim. Fermi arcs in a doped pseudospin-1/2 Heisenberg antiferromagnet. *Science*, **345**:187–190, 2014.

[71] A. de la Torre, S. McKeown Walker, F. Y. Bruno, S. Riccó, Z. Wang, I. Gutierrez Lezama, G. Scheerer, G. Giriat, D. Jaccard, C. Berthod, T. K. Kim, M. Hoesch, E. C. Hunter, R. S. Perry, A. Tamai, and F. Baumberger. Collapse of the Mott Gap and Emergence of a Nodal Liquid in Lightly Doped $\mathrm{Sr_2IrO_4}$. *Phys. Rev. Lett.*, **115**:176402, 2015.

[72] V. Brouet, J. Mansart, L. Perfetti, C. Piovera, I. Vobornik, P. Le Fèvre, F. Bertran, S. C. Riggs, M. C. Shapiro, P. Giraldo-Gallo, and I. R. Fisher. Transfer of spectral weight across the gap of Sr_2IrO_4 induced by La doping. *Phys. Rev. B*, **92**:081117, 2015.

[73] Y. Cao, Q. Wang, J. A. Waugh, T. J. Reber, H. Li, X. Zhou, S. Parham, S.-R. Park, N. C. Plumb, E. Rotenberg, A. Bostwick, J. D. Denlinger, T. Qi, M. A. Hermele, G. Cao, and D. S. Dessau. Hallmarks of the Mott-metal crossover in the hole-doped pseudospin-1/2 Mott insulator Sr_2IrO_4. *Nature Communications*, **7**:11367, 2016.

[74] G. Koster and G. Rijnders. *In Situ Characterization of Thin Film Growth.* Woodhead Publishing, 1st edition, Cambridge, 2011.

[75] K. van Benthem, C. Elsässer, and R. H. French. Bulk electronic structure of $SrTiO_3$: Experiment and theory. *Journal of Applied Physics*, **90**:6156–6164, 2001.

[76] R. W. Hesse. *Jewelrymaking Through History: An Encyclopedia.* Handicrafts through world history. Greenwood Press, 2007.

[77] Power Sources for Remote Arctic Applications. *Washington, DC: U.S. Congress, Office of Technology Assessment*, **OTA-BP-ETI-129**, 1994.

[78] W. J. F. Standring, Ø. G. Selnæs, M. Sneve, I. E. Finne, A. Hosseini, I. Amundsen, and P. Strand. Assessment of environmental, health and safety consequences of decommissioning radioisotopic thermal generators (RTGs) in Northwest Russia. *(StrålevernRapport 2005:4), Østerås: Norwegian Radiation Protection Authority*, 2005.

[79] ESPI metals. *Strontium Titanate – data sheet*, Oregon, 2013 (accessed December 14, 2016). `http://archive.is/3qAYr`.

[80] A. Ohtomo and H. Y. Hwang. A high-mobility electron gas at the $LaAlO_3/SrTiO_3$ heterointerface. *Nature*, **427**:423–426, 2004.

[81] V. M. Goldschmidt. Die Gesetze der Krystallochemie. *Naturwissenschaften*, **14**:477–485, 1926.

[82] K. A. Müller, W. Berlinger, and F. Waldner. Characteristic Structural Phase Transition in Perovskite-Type Compounds. *Phys. Rev. Lett.*, **21**:814–817, 1968.

[83] J. A. Blackman and J. Tagüeña. *Disorder in condensed matter physics: a volume in honour of Roger Elliott.* Oxford University Press, USA, 1991.

[84] H. P. R. Frederikse, W. R. Thurber, and W. R. Hosler. Electronic Transport in Strontium Titanate. *Phys. Rev.*, **134**:A442–A445, 1964.

[85] W. Luo, W. Duan, S. G. Louie, and M. L. Cohen. Structural and electronic properties of n-doped and p-doped $SrTiO_3$. *Phys. Rev. B*, **70**:214109, 2004.

[86] J. F. Schooley, W. R. Hosler, and M. L. Cohen. Superconductivity in Semiconducting $SrTiO_3$. *Phys. Rev. Lett.*, **12**:474–475, 1964.

[87] J. F. Schooley, W. R. Hosler, E. Ambler, J. H. Becker, M. L. Cohen, and C. S. Koonce. Dependence of the Superconducting Transition Temperature on Carrier Concentration in Semiconducting $SrTiO_3$. *Phys. Rev. Lett.*, **14**:305–307, 1965.

[88] C. S. Koonce, M. L. Cohen, J. F. Schooley, W. R. Hosler, and E. R. Pfeiffer. Superconducting Transition Temperatures of Semiconducting $SrTiO_3$. *Phys. Rev.*, **163**:380–390, 1967.

[89] G. Binnig, A. Baratoff, H. E. Hoenig, and J. G. Bednorz. Two-Band Superconductivity in Nb-Doped $SrTiO_3$. *Phys. Rev. Lett.*, **45**:1352–1355, 1980.

[90] E. Dagotto. Complexity in Strongly Correlated Electronic Systems. *Science*, **309**:257–262, 2005.

[91] A. Biswas, K.-S. Kim, and Y. H. Jeong. Metal-Insulator Transitions and non-Fermi Liquid Behaviors in 5d Perovskite Iridates. *arXiv preprint arXiv:1508.04929*, 2015.

[92] N. F. Mott and R. Peierls. Discussion of the paper by de Boer and Verwey. *Proceedings of the Physical Society*, **49**:72, 1937.

[93] J. Hubbard. Electron Correlations in Narrow Energy Bands. *Proceedings of the Royal Society of London A: Mathematical, Physical and Engineering Sciences*, **276**:238–257, 1963.

[94] M. C. Gutzwiller. Effect of Correlation on the Ferromagnetism of Transition Metals. *Phys. Rev. Lett.*, **10**:159–162, 1963.

[95] J. Kanamori. Electron Correlation and Ferromagnetism of Transition Metals. *Progress of Theoretical Physics*, **30**:275, 1963.

[96] J. Hubbard. Electron Correlations in Narrow Energy Bands. II. The Degenerate Band Case. *Proceedings of the Royal Society of London A: Mathematical, Physical and Engineering Sciences*, **277**:237–259, 1964.

[97] J. Hubbard. Electron Correlations in Narrow Energy Bands. III. An Improved Solution. *Proceedings of the Royal Society of London A: Mathematical, Physical and Engineering Sciences*, **281**:401–419, 1964.

[98] J. Hubbard. Electron Correlations in Narrow Energy Bands. IV. The Atomic Representation. *Proceedings of the Royal Society of London A: Mathematical, Physical and Engineering Sciences*, **285**:542–560, 1965.

[99] P. Fazekas. *Series in Modern Condensed Matter Physics: Volume 5, Lecture notes on electron correlation and magnetism.* World Scientific, Singapore, 1999.

[100] S. J. Moon, H. Jin, K. W. Kim, W. S. Choi, Y. S. Lee, J. Yu, G. Cao, A. Sumi, H. Funakubo, C. Bernhard, and T. W. Noh. Dimensionality-Controlled Insulator-Metal Transition and Correlated Metallic State in $5d$ Transition Metal Oxides $Sr_{n+1}Ir_nO_{3n+1}$ ($n = 1$, 2, and ∞). *Phys. Rev. Lett.*, **101**:226402, 2008.

[101] S. N. Ruddlesden and P. Popper. New compounds of the K_2NIF_4 type. *Acta Crystallographica*, **10**:538–539, 1957.

[102] S. N. Ruddlesden and P. Popper. The compound $Sr_3Ti_2O_7$ and its structure. *Acta Crystallographica*, **11**:54–55, 1958.

[103] H. Okabe, M. Isobe, E. Takayama-Muromachi, A. Koda, S. Takeshita, M. Hiraishi, M. Miyazaki, R. Kadono, Y. Miyake, and J. Akimitsu. Ba_2IrO_4: A spin-orbit Mott insulating quasi-two-dimensional antiferromagnet. *Phys. Rev. B*, **83**:155118, 2011.

[104] M. K. Crawford, M. A. Subramanian, R. L. Harlow, J. A. Fernandez-Baca, Z. R. Wang, and D. C. Johnston. Structural and magnetic studies of Sr_2IrO_4. *Phys. Rev. B*, **49**:9198–9201, 1994.

[105] T. Vogt and D. J. Buttrey. Temperature Dependent Structural Behavior of Sr_2RhO_4. *Journal of Solid State Chemistry*, **123**:186–189, 1996.

[106] J. G. Rau, E. K.-H. Lee, and H.-Y. Kee. Spin-orbit physics giving rise to novel phases in correlated systems: Iridates and related materials. *Annual Review of Condensed Matter Physics*, **7**:195–221, 2016.

[107] G. Jackeli and G. Khaliullin. Mott Insulators in the Strong Spin-Orbit Coupling Limit: From Heisenberg to a Quantum Compass and Kitaev Models. *Phys. Rev. Lett.*, **102**:017205, 2009.

[108] B. J. Kim, H. Ohsumi, T. Komesu, S. Sakai, T. Morita, H. Takagi, and T. Arima. Phase-Sensitive Observation of a Spin-Orbital Mott State in Sr_2IrO_4. *Science*, **323**:1329–1332, 2009.

[109] J. W. Kim, Y. Choi, Jungho Kim, J. F. Mitchell, G. Jackeli, M. Daghofer, J. van den Brink, G. Khaliullin, and B. J. Kim. Dimensionality Driven Spin-Flop Transition in Layered Iridates. *Phys. Rev. Lett.*, **109**:037204, 2012.

[110] P. A. Lee, N. Nagaosa, and X.-G. Wen. Doping a Mott insulator: Physics of high-temperature superconductivity. *Rev. Mod. Phys.*, **78**:17–85, 2006.

[111] F. Ye, S. Chi, B. C. Chakoumakos, J. A. Fernandez-Baca, T. Qi, and G. Cao. Magnetic and crystal structures of Sr_2IrO_4: A neutron diffraction study. *Phys. Rev. B*, **87**:140406, 2013.

[112] J. Kim, D. Casa, M. H. Upton, T. Gog, Y.-J. Kim, J. F. Mitchell, M. van Veenendaal, M. Daghofer, J. van den Brink, G. Khaliullin, and B. J. Kim. Magnetic Excitation Spectra of Sr_2IrO_4 Probed by Resonant Inelastic X-Ray Scattering: Establishing Links to Cuprate Superconductors. *Phys. Rev. Lett.*, **108**:177003, 2012.

[113] R. Coldea, S. M. Hayden, G. Aeppli, T. G. Perring, C. D. Frost, T. E. Mason, S.-W. Cheong, and Z. Fisk. Spin Waves and Electronic Interactions in La_2CuO_4. *Phys. Rev. Lett.*, **86**:5377–5380, 2001.

[114] N. S. Headings, S. M. Hayden, R. Coldea, and T. G. Perring. Anomalous High-Energy Spin Excitations in the High-T_c Superconductor-Parent Antiferromagnet La_2CuO_4. *Phys. Rev. Lett.*, **105**:247001, 2010.

[115] M Souri, JH Gruenewald, J Terzic, JW Brill, G Cao, and SSA Seo. Investigations of metastable Ca2IrO4 epitaxial thin-films: systematic comparison with Sr_2IrO_4 and Ba_2IrO_4. *Scientific reports*, **6**, 2016.

[116] S. Fujiyama, H. Ohsumi, T. Komesu, J. Matsuno, B. J. Kim, M. Takata, T. Arima, and H. Takagi. Two-Dimensional Heisenberg Behavior of J_{eff}=1/2 Isospins in the Paramagnetic State of the Spin-Orbital Mott Insulator Sr_2IrO_4. *Phys. Rev. Lett.*, **108**:247212, 2012.

[117] S. Boseggia, R. Springell, H. C. Walker, H. M. Rønnow, Ch. Rüegg, H. Okabe, M. Isobe, R. S. Perry, S. P. Collins, and D. F. McMorrow. Robustness of Basal-Plane Antiferromagnetic Order and the J_{eff}=1/2 State in Single-Layer Iridate Spin-Orbit Mott Insulators. *Phys. Rev. Lett.*, **110**:117207, 2013.

[118] H. Okabe, M. Isobe, E. Takayama-Muromachi, N. Takeshita, and J. Akimitsu. Carrier doping effect for transport properties of a spin-orbit Mott insulator Ba_2IrO_4. *Phys. Rev. B*, **88**:075137, 2013.

[119] X. Liu, M. P. M. Dean, Z. Y. Meng, M. H. Upton, T. Qi, T. Gog, Y. Cao, J. Q. Lin, D. Meyers, H. Ding, G. Cao, and J. P. Hill. Anisotropic softening of magnetic excitations in lightly electron-doped Sr_2IrO_4. *Phys. Rev. B*, **93**:241102, 2016.

[120] I. Battisti, K. M. Bastiaans, V. Fedoseev, A. de la Torre, N. Iliopoulos, A. Tamai, E. C. Hunter, R. S. Perry, J. Zaanen, F. Baumberger, and M. P. Allan. Universality of pseudogap and emergent order in lightly doped Mott insulators. *Nat Phys*, **13**:21–25, 2017.

[121] S. Calder, J. W. Kim, A. E. Taylor, M. H. Upton, D. Casa, Guixin Cao, D. Mandrus, M. D. Lumsden, and A. D. Christianson. Strong anisotropy within a Heisenberg model in the $J_{\mathrm{eff}} = \frac{1}{2}$ insulating state of $\mathrm{Sr_2Ir_{0.8}Ru_{0.2}O_4}$. *Phys. Rev. B*, **94**:220407, 2016.

[122] J. Cheng, X. Sun, S. Liu, B. Li, H. Wang, P. Dong, Y. Wang, and W. Xu. La-doping effect on spin–orbit coupled $\mathrm{Sr_2IrO_4}$ probed by x-ray absorption spectroscopy. *New Journal of Physics*, **18**:093019, 2016.

[123] O. B. Korneta, T. Qi, S. Chikara, S. Parkin, L. E. De Long, P. Schlottmann, and G. Cao. Electron-doped $\mathrm{Sr_2IrO_{4-\delta}}$ $(0 \leq \delta \leq 0.04)$: Evolution of a disordered $J_{\mathrm{eff}} = \frac{1}{2}$ Mott insulator into an exotic metallic state. *Phys. Rev. B*, **82**:115117, 2010.

[124] M. Ge, T. F. Qi, O. B. Korneta, D. E. De Long, P. Schlottmann, W. P. Crummett, and G. Cao. Lattice-driven magnetoresistivity and metal-insulator transition in single-layered iridates. *Phys. Rev. B*, **84**:100402, 2011.

[125] J. S. Lee, Y. Krockenberger, K. S. Takahashi, M. Kawasaki, and Y. Tokura. Insulator-metal transition driven by change of doping and spin-orbit interaction in $\mathrm{Sr_2IrO_4}$. *Phys. Rev. B*, **85**:035101, 2012.

[126] S. Chikara, G. Fabbris, J. Terzic, G. Cao, D. Khomskii, and D. Haskel. Charge partitioning and anomalous hole doping in Rh-doped $\mathrm{Sr_2IrO_4}$. *Phys. Rev. B*, **95**:060407, 2017.

[127] J. F. Mitchell. Sr2IrO4: Gateway to cuprate superconductivity? *APL Materials*, **3**:062404, 2015.

[128] M. Uchida, K. Ishizaka, P. Hansmann, Y. Kaneko, Y. Ishida, X. Yang, R. Kumai, A. Toschi, Y. Onose, R. Arita, K. Held, O. K. Andersen, S. Shin, and Y. Tokura. Pseudogap of Metallic Layered Nickelate $R_{2-x}\mathrm{Sr}_x\mathrm{NiO_4}$ $(R = \mathrm{Nd, Eu})$ Crystals Measured Using Angle-Resolved Photoemission Spectroscopy. *Phys. Rev. Lett.*, **106**:027001, 2011.

[129] A. Y. Cho. How molecular beam epitaxy (MBE) began and its projection into thefuture . *Journal of Crystal Growth*, **201-202**:1–7, 1999.

[130] R. Eason. *Pulsed Laser Deposition of Thin Films: Applications-Led Growth of Functional Materials.* John Wiley and Sons, New Jersey, 2006.

[131] P. R. Willmott and J. R. Huber. Pulsed laser vaporization and deposition. *Rev. Mod. Phys.*, **72**:315–328, 2000.

[132] D. B. Chrisey and G. K. Hubler. *Pulsed Laser Deposition of Thin Films.* John Wiley and Sons, 1st edition, New York, 1994.

[133] G. Rijnders. *Growth of complex oxides: study and manipulation.* Dissertation, Twente, 2001.

[134] A. Ichimiya and P. I. Cohen. *Reflection High-Energy Electron Diffraction.* Cambridge University Press, 2004.

[135] J. O'Connor, B. Sexton, and R. S. C. Smart. *Surface Analysis Methods in Materials Science.* Springer-Verlag Berlin Heidelberg, 2nd edition, 2003.

[136] J. C. Vickerman and I. S. Gilmore. *Surface Analysis: The Principal Techniques.* John Wiley and Sons, 2nd edition, Chichester, 2009.

[137] K. Oura, V.G. Lifshits, A. Saranin, A.V. Zotov, and M. Katayama. *Surface Science: An Introduction.* Springer-Verlag Berlin Heidelberg, 2003.

[138] C. Nordling, E. Sokolowski, and K. Siegbahn. Precision Method for Obtaining Absolute Values of Atomic Binding Energies. *Phys. Rev.*, **105**:1676–1677, 1957.

[139] E. Sokolowski, C. Nordling, and K. Siegbahn. Arkiv för Fysik. **12**:310, 1957.

[140] S. Hüfner. *Photoelectron Spectroscopy: Principles and Applications.* Springer-Verlag, 3rd edition, Berlin Heidelberg, 2003.

[141] F. Reinert and S. Hüfner. Photoemission spectroscopy–from early days to recent applications. *New Journal of Physics*, **7**:97, 2005.

[142] S. Suga and A. Sekiyama. *Photoelectron Spectroscopy: Bulk and Surface Electronic Structures.* Springer-Verlag Berlin Heidelberg, 2014.

[143] K. Siegbahn. Electron Spectroscopy for Atoms, Molecules, and Condensed Matter. *Science*, **217**:111–121, 1982.

[144] H. Hertz. Ueber einen Einfluss des ultravioletten Lichtes auf die electrische Entladung. *Annalen der Physik und Chemie*, **267**:983–1000, 1887.

[145] A. Damascelli. Probing the Electronic Structure of Complex Systems by ARPES, journal = Physica Scripta. **T109**:61–74, 2004.

[146] A. Einstein. Über einen die Erzeugung und Verwandlung des Lichtes betreffenden heuristischen Gesichtspunkt. *Annalen der Physik*, **322**:132–148, 1905.

[147] S. Doniach and M. Sunjic. Many-electron singularity in X-ray photoemission and X-ray line spectra from metals. *Journal of Physics C: Solid State Physics*, **3**:285–291, 1970.

[148] S. Tanuma, T. Shiratori, T. Kimura, K. Goto, S. Ichimura, and C. J. Powell. Experimental determination of electron inelastic mean free paths in 13 elemental solids in the 50 to 5000 eV energy range by elastic-peak electron spectroscopy. *Surface and Interface Analysis*, **37**:833–845, 2005.

[149] M. P. Seah and W. A. Dench. *Quantitative electron spectroscopy of surfaces: A standard data base for electron inelastic mean free paths in solids*, volume **1**, issue 1, pages 2-11. John Wiley and Sons, Teddington Middlesex, 1979.

[150] D. A. Shirley. High-Resolution X-Ray Photoemission Spectrum of the Valence Bands of Gold. *Phys. Rev. B*, **5**:4709–4714, 1972.

[151] D. Briggs and M.P. Seah. *Volume 1, Practical Surface Analysis, Auger and X-ray Photoelectron Spectroscopy.* Practical Surface Analysis. John Wiley and Sons, 2nd edition, Chichester, 1990.

[152] J. J. Yeh and I. Lindau. Atomic subshell photoionization cross sections and asymmetry parameters: $1 \leq Z \leq 103$. *Atomic Data and Nuclear Data Tables*, **32**:1–155, 1985.

[153] M. B. Trzhaskovskaya, V. I. Nefedov, and V. G. Yarzhemsky. Photoelectron Angular Distribution Parameters For Elements Z=1 To Z=54 In The Photoelectron Energy Range 100–5000 eV. *Atomic Data and Nuclear Data Tables*, **77**:97–159, 2001.

[154] P. Ruffieux, P. Schwaller, O. Gröning, L. Schlapbach, P. Gröning, Q. C. Herd, D. Funnemann, and J. Westermann. Experimental determination of the transmission factor for the Omicron EA125 electron analyzer. *Review of Scientific Instruments*, **71**:3634–3639, 2000.

[155] M. Baclayon, G. J. L. Wuite, and W. H. Roos. Imaging and manipulation of single viruses by atomic force microscopy. *Soft Matter*, **6**:5273–5285, 2010.

[156] R. Wiesendanger. *Scanning Probe Microscopy and Spectroscopy: Methods and Applications.* Cambridge University Press, 1994.

[157] U. Pietsch, V. Holy, and T. Baumbach. *High-Resolution X-Ray Scattering: From Thin Films to Lateral Nanostructures.* Springer, 2nd edition, New York, 2004.

[158] A. C. Thompson et al. *Center for X-ray optics and advanced light source: X-ray data booklet.* Lawrence Berkeley National Laboratory (LBNL), University of California, 3rd edition, Berkeley, 2009.

[159] H. Kronmüller and S. S. P. Parkin. *Handbook of magnetism and advanced magnetic materials, Volume 3.* John Wiley and Sons, New Jersey, 2007.

[160] A.-J. Dianoux and G. Lander. *Neutron Data Booklet.* OCP Science, 2nd edition, Grenoble, 2003.

[161] V. F. Sears. Electromagnetic neutron-atom interactions. *Physics Reports*, **141**:281 – 317, 1986.

[162] H. Zabel. Neutron reflectivity of spintronic materials. *Materials Today*, **9**:42–49, 2006.

[163] J. Daillant and A. Gibaud. *X-ray and Neutron Reflectivity: Principles and Applications (Lecture Notes in Physics).* Springer-Verlag, Berlin Heidelberg, 2009.

[164] S. Blügel, T. Brückel, and C. M. Schneider. *Lecture Manuscripts of the 36th Spring School of the Institute of Solid State Research: Magnetism goes Nano, Volume 26.* Forschungszentrum Jülich, Jülich, 2005.

[165] A. Müller, A. Ruff, M. Paul, A. Wetscherek, G. Berner, U. Bauer, C. Praetorius, K. Fauth, M. Przybylski, M. Gorgoi, M. Sing, and R. Claessen. Fe_3O_4 on ZnO: A spectroscopic study of film and interface properties. *Thin Solid Films*, **520**:368–373, 2011.

[166] T. Chatterji (Editor). *Neutron Scattering from Magnetic Materials.* Elsevier Science, Amsterdam, 2006.

[167] B. D. Josephson. Possible new effects in superconductive tunnelling. *Physics Letters*, **1**:251 – 253, 1962.

[168] P. K. Muduli. *Ex situ SQUID magnetometry*, 2005 (accessed July 27, 2016). `http://www.geocities.ws/pranab_muduli/squid.html`.

[169] Walther-Meiner-Institute for Low Temperature Research. *SQUID Magnetometry*, (accessed July 27, 2016). `http://www.wmi.badw.de/methods/squid.htm`.

[170] J. Clarke. SQUIDs (for superconducting quantum interference devices) are the most sensitive detectors of magnetic fields. Their applications range from diagnosis of brain tumors to tests of relativity. *Scientific American*, **271**:46–53, 1994.

[171] J. Clarke and A. I. Braginski. *The SQUID Handbook: Vol.1 Fundamentals and Technology of SQUIDs and SQUID Systems.* Wiley-VCH, 1st edition, Weinheim, 2004.

[172] J. Clarke and A. I. Braginski. *The SQUID Handbook: Vol.2 Applications of SQUIDs and SQUID Systems.* Wiley-VCH, 1st edition, Weinheim, 2006.

[173] R. Kleiner and W. Buckel. *Superconductivity: An Introduction.* Wiley-VCH, 3rd edition, Berlin, 2015.

[174] B. D. Cullity and C. D. Graham. *Introduction to Magnetic Materials.* John Wiley and Sons, 2nd edition, New Jersey, 2008.

[175] Quantum Design (Inc.). *MPMS from Quantum Design*, (accessed July 27, 2016). `http://www.qdusa.com/products/mpms3.html`.

[176] L. J. van der Pauw. A method of measuring the resistivity and Hall coefficient on lamellae of arbitrary shape. *Philips Technical Review*, **20**:220–224, 1958.

[177] L. J. van der Pauw. A method of measuring specific resistivity and Hall effect of discs of arbitrary shape. *Philips Research Reports*, **13**:1–9, 1958.

[178] G. Cox. *Optical Imaging Techniques in Cell Biology.* CRC Press, Taylor and Francis Group, 2nd edition, Boca Raton, 2012.

[179] Toshi. *STEM*, 2009 (accessed August 14, 2016). `http://toshiboston.web.fc2.com/STEMbasics.htm`.

[180] R. Erni. *Scanning Transmission Electron Microscopy (STEM)*, 2013 (accessed August 14, 2016). `https://microscopy.empa.ch/bin/view/Main/STEM`.

[181] N. Wilkinson. *Brunel TEM presentation: Some applications of TEM for Biological Applications*, 2013 (accessed August 14, 2016). `http://de.slideshare.net/ETCbrunel/brunel-bio-tem-presentation-june-2013`.

[182] D. B. Williams and C. B. Carter. *Transmission Electron Microscopy, Part 1: Basis.* Springer Science and Business Media, LLC, 2nd edition, New York, 2009.

[183] D. B. Williams and C. B. Carter. *Transmission Electron Microscopy, Part 2: Diffraction.* Springer Science and Business Media, LLC, 2nd edition, New York, 2009.

[184] D. B. Williams and C. B. Carter. *Transmission Electron Microscopy, Part 3: Imaging.* Springer Science and Business Media, LLC, 2nd edition, New York, 2009.

[185] D. B. Williams and C. B. Carter. *Transmission Electron Microscopy, Part 4: Spectrometry.* Springer Science and Business Media, LLC, 2nd edition, New York, 2009.

[186] C. Noguera. Polar oxide surfaces. *Journal of Physics: Condensed Matter*, **12**:R367, 2000.

[187] A. Wander, F. Schedin, P. Steadman, A. Norris, R. McGrath, T. S. Turner, G. Thornton, and N. M. Harrison. Stability of Polar Oxide Surfaces. *Phys. Rev. Lett.*, **86**:3811–3814, 2001.

[188] J. M. Carlsson. Electronic structure of the polar ZnO{0001}-surfaces. *Computational Materials Science*, **22**:24–31, 2001.

[189] O. Dulub, L. A. Boatner, and U. Diebold. STM study of the geometric and electronic structure of ZnO(0001)-Zn, $(000\bar{1})$-O, $(10\bar{1}0)$, and $(11\bar{2}0)$ surfaces. *Surface Science*, **519**:201–217, 2002.

[190] G. Kresse, O. Dulub, and U. Diebold. Competing stabilization mechanism for the polar ZnO(0001)-Zn surface. *Phys. Rev. B*, **68**:245409, 2003.

[191] C. Wöll. The chemistry and physics of zinc oxide surfaces. *Progress in Surface Science*, **82**:55–120, 2007.

[192] S. Akasaka, K. Nakahara, H. Yuji, A. Tsukazaki, A. Ohtomo, and M. Kawasaki. Preparation of an Epitaxy-Ready Surface of a ZnO(0001) Substrate. *Applied Physics Express*, **4**:035701, 2011.

[193] M. Valtiner, S. Borodin, and G. Grundmeier. Preparation and characterisation of hydroxide stabilised ZnO (0001)–Zn–OH surfaces. *Physical Chemistry Chemical Physics*, **9**:2406–2412, 2007.

[194] S. Graubner, C. Neumann, N. Volbers, B. K. Meyer, J. Bläsing, and A. Krost. Preparation of ZnO substrates for epitaxy: Structural, surface, and electrical properties. *Applied Physics Letters*, **90**:042103, 2007.

[195] H.-J. Ko, M.-S. Han, Y.-S. Park, Y.-S. Yu, B.-I. Kim, S. S. Kim, and J.-H. Kim. Improvement of the quality of ZnO substrates by annealing. *Journal of Crystal Growth*, **269**:493 – 498, 2004.

[196] M. Kunat, St. Gil Girol, Th. Becker, U. Burghaus, and Ch. Wöll. Stability of the polar surfaces of ZnO: A reinvestigation using He-atom scattering. *Phys. Rev. B*, **66**:081402, 2002.

[197] L. Zhang, D. Wett, R. Szargan, and T. Chassé. Determination of ZnO(0001) surface termination by x-ray photoelectron spectroscopy at photoemission angles of 0 and 70. *Surface and Interface Analysis*, **36**:1479–1483, 2004.

[198] R. T. Girard, O. Tjernberg, G. Chiaia, S. Söderholm, U. O. Karlsson, C. Wigren, H. Nylén, and I. Lindau. Electronic structure of ZnO(0001) studied by angle-resolved photoelectron spectroscopy. *Surface Science*, **373**:409–417, 1997.

[199] P. D. C. King, T. D. Veal, A. Schleife, J. Zúñiga Pérez, B. Martel, P. H. Jefferson, F. Fuchs, V. Muñoz Sanjosé, F. Bechstedt, and C. F. McConville. Valence-band electronic structure of CdO, ZnO, and MgO from x-ray photoemission spectroscopy and quasi-particle-corrected density-functional theory calculations. *Phys. Rev. B*, **79**:205205, 2009.

[200] J. Williams, H. Yoshikawa, S. Ueda, Y. Yamashita, K. Kobayashi, Y. Adachi, H. Haneda, T. Ohgaki, H. Miyazaki, T. Ishigaki, and N. Ohashi. Polarity-dependent photoemission spectra of wurtzite-type zinc oxide. *Applied Physics Letters*, **100**:051902, 2012.

[201] J. F. Moulder, W. F. Stickle, P. E. Sobol, K. D. Bomben, and J. Chastain (Editor). *Handbook of X-ray Photoelectron Spectroscopy: A Reference Book of Standard Spectra for Identification and Interpretation of XPS Data.* Physical Electronics Division, Perkin-Elmer Corporation, 1992.

[202] T. Yamashita and P. Hayes. Analysis of XPS spectra of Fe^{2+} and Fe^{3+} ions in oxide materials. *Applied Surface Science*, **254**:2441–2449, 2008.

[203] S. Nakashima, K. Fujita, K. Tanaka, and K. Hirao. High magnetization and the high-temperature superparamagnetic transition with intercluster interaction in disordered zinc ferrite thin film. *Journal of Physics: Condensed Matter*, **17**:137, 2005.

[204] C. T. Lie, P. C. Kuo, W.-C. Hsu, I. J. Chang, and J. W. Chen. Effect of Zn doping on the magnetoresistance of sintered Fe3O4 ferrites. *Journal of Magnetism and Magnetic Materials*, **239**:160–163, 2002.

[205] G .S. Y. Kumar, H. S. B. Naik, A. S. Roy, K. N. Harish, and R. Viswanath. Synthesis, Optical and Electrical Properties of $ZnFe_2O_4$ Nanocomposites. *Nanomaterials and Nanotechnology*, **2**:19, 2012.

[206] C. T. Chantler. Theoretical Form Factor, Attenuation, and Scattering Tabulation for Z=1–92 from E=1–10 eV to E=0.4–1.0 MeV. *Journal of Physical and Chemical Reference Data*, **24**:71–643, 1995.

[207] L. G. Parratt. Surface Studies of Solids by Total Reflection of X-Rays. *Phys. Rev.*, **95**:359–369, 1954.

[208] M. Björck and G. Andersson. GenX: an extensible X-ray reflectivity refinement program utilizing differential evolution. *Journal of Applied Crystallography*, **40**:1174–1178, 2007.

[209] R. Storn and K. Price. Differential Evolution – A Simple and Efficient Heuristic for global Optimization over Continuous Spaces. *Journal of Global Optimization*, **11**:341–359, 1997.

[210] S. Macke, A. Radi, J. E. Hamann-Borrero, A. Verna, M. Bluschke, S. Brck, E. Goering, R. Sutarto, F. He, G. Cristiani, M. Wu, E. Benckiser, H.-U. Habermeier, G. Logvenov, N. Gauquelin, G. A. Botton, A. P. Kajdos, S. Stemmer, G. A. Sawatzky, M. W. Haverkort, B. Keimer, and V. Hinkov. Element Specific Monolayer Depth Profiling. *Advanced Materials*, **26**:6554–6559, 2014.

[211] F.-P. Amalio. *Studies of Nanoconstrictions, Nanowires and Fe_3O_4 Thin Films: Electrical Conduction and Magnetic Properties. Fabrication by Focused Electron/Ion Beam.* Springer-Verlag Berlin Heidelberg, 2011.

[212] R. Prakash, R. J. Choudhary, L. S. Sharath Chandra, N. Lakshmi, and D. M. Phase. Electrical and magnetic transport properties of Fe_3O_4 thin films on a GaAs(100) substrate. *Journal of Physics: Condensed Matter*, **19**:486212, 2007.

[213] K. B. Paul. Magnetic and transport properties of monocrystalline Fe_3O_4. *Central European Journal of Physics*, **3**:115–126, 2005.

[214] D. Venkateshvaran, M. Althammer, A. Nielsen, S. Geprägs, M. S. Ramachandra Rao, S. T. B. Goennenwein, M. Opel, and R. Gross. Epitaxial $Zn_xFe_{3-x}O_4$ thin films: A spintronic material with tunable electrical and magnetic properties. *Phys. Rev. B*, **79**:134405, 2009.

[215] V. G. Harris, N. C. Koon, C. M. Williams, Q. Zhang, M. Abe, and J. P. Kirkland. Cation distribution in NiZn–ferrite films via extended x–ray absorption fine structure. *Applied Physics Letters*, **68**:2082–2084, 1996.

[216] J. Takaobushi, H. Tanaka, T. Kawai, S. Ueda, J.-J. Kim, M. Kobata, E. Ikenaga, M. Yabashi, K. Kobayashi, Y. Nishino, D. Miwa, K. Tamasaku, and T. Ishikawa. $Fe_{3-x}Zn_xO_4$ thin film as tunable high Curie temperature ferromagnetic semiconductor. *Applied Physics Letters*, **89**:242507, 2006.

[217] Y. Li, Q. Li, M. Wen, Y. Zhang, Y. Zhai, Z. Xie, F. Xu, and S. Wei. Magnetic properties and local structure studies of Zn doped ferrites. *Journal of Electron Spectroscopy and Related Phenomena*, **160**:1–6, 2007.

[218] J. Takaobushi, M. Ishikawa, S. Ueda, E. Ikenaga, J.-J. Kim, M. Kobata, Y. Takeda, Y. Saitoh, M. Yabashi, Y. Nishino, D. Miwa, K. Tamasaku, T. Ishikawa, I. Satoh, H. Tanaka, K. Kobayashi, and T. Kawai. Electronic structures of $Fe_{3-x}M_xO_4$ ($M = \mathrm{Mn, Zn}$) spinel oxide thin films investigated by x-ray photoemission spectroscopy and x-ray magnetic circular dichroism. *Phys. Rev. B*, **76**:205108, 2007.

[219] J.-B. Moussy, S. Gota, A. Bataille, M.-J. Guittet, M. Gautier-Soyer, F. Delille, B. Dieny, F. Ott, T. D. Doan, P. Warin, P. Bayle-Guillemaud, C. Gatel, and E. Snoeck. Thickness dependence of anomalous magnetic behavior in epitaxial Fe_3O_4(111) thin films: Effect of density of antiphase boundaries. *Phys. Rev. B*, **70**:174448, 2004.

[220] Y. F. Chen, D. Spoddig, and M. Ziese. Epitaxial thin film $ZnFe_2O_4$: a semi-transparent magnetic semiconductor with high Curie temperature. *Journal of Physics D: Applied Physics*, **41**:205004, 2008.

[221] M. Lorenz, M. Brandt, K. Mexner, K. Brachwitz, M. Ziese, P. Esquinazi, H. Hochmuth, and M. Grundmann. Ferrimagnetic $ZnFe_2O_4$ thin films on $SrTiO_3$ single crystals with highly tunable electrical conductivity. *Phys. Status Solidi RRL*, **5**:438–440, 2011.

[222] F. Delille, B. Dieny, J.-B. Moussy, M.-J. Guittet, S. Gota, M. Gautier-Soyer, and C. Marin. Study of the electronic paraprocess and antiphase boundaries as sources of the demagnetisation phenomenon in magnetite. *Journal of Magnetism and Magnetic Materials*, **294**:27–39, 2005.

[223] K. P. Belov. Electronic processes in magnetite (or, "Enigmas of magnetite"). *Physics-Uspekhi*, **36**:380, 1993.

[224] J. P. Shepherd, R. Aragón, J. W. Koenitzer, and J. M. Honig. Changes in the nature of the Verwey transition in nonstoichiometric magnetite (Fe_3O_4). *Phys. Rev. B*, **32**:1818–1819, 1985.

[225] K. A. Shaw, E. Lochner, and D. M. Lind. Interdiffusion study of magnesium in magnetite thin films grown on magnesium oxide (001) substrates. *Journal of Applied Physics*, **87**:1727–1733, 2000.

[226] P. Wang, Z. Kąkol, M. Wittenauer, and J. M. Honig. Electrical properties of zinc ferrites $Fe_{3-x}Zn_xO_4$ with $0 \leq x < 0.3$. *Phys. Rev. B*, **42**:4553–4558, 1990.

[227] D. T. Margulies, F. T. Parker, F. E. Spada, R. S. Goldman, J. Li, R. Sinclair, and A. E. Berkowitz. Anomalous moment and anisotropy behavior in Fe_3O_4 films. *Phys. Rev. B*, **53**:9175–9187, 1996.

[228] S. Brück, M. Paul, H. Tian, A. Müller, D. Kufer, C. Praetorius, K. Fauth, P. Audehm, E. Goering, J. Verbeeck, G. Van Tendeloo, M. Sing, and R. Claessen. Magnetic and electronic properties of the interface between half metallic Fe_3O_4 and semiconducting ZnO. *Applied Physics Letters*, **100**:081603, 2012.

[229] F. Ott. SimulReflec. Version 1.72, 2007.

[230] G. P. Felcher, K. E. Gray, R. T. Kampwlrth, and M. B. Brodsky. Magnetic depth profiles by neutron reflection. *Physica B+C*, **136**:59–63, 1986.

[231] D. Pescia, R. F. Willis, and J. A. C. Bland. Magnetic moments of ultrathin films by spin polarized neutron reflection. *Surface Science*, **189**:724–728, 1987.

[232] S. J. Blundell and J. A. C. Bland. Polarized neutron reflection as a probe of magnetic films and multilayers. *Phys. Rev. B*, **46**:3391–3400, 1992.

[233] P. A. A. van der Heijden, P. J. H. Bloemen, J. M. Gaines, J. T. W. M. van Eemeren, R. M. Wolf, P. J. van der Zaag, and W. J. M. de Jonge. Magnetic interface anisotropy of MBE-grown ultra-thin (001) Fe_3O_4 layers. *Journal of Magnetism and Magnetic Materials*, **159**:L293–L298, 1996.

[234] Y. Zhou, C. McEvoy, R. Ramos, and I. V. Shvets. The magnetic and magnetoresistance properties of ultrathin magnetite films grown on MgO substrate. *Journal of Applied Physics*, **99**:08J111, 2006.

[235] W. Eerenstein, T. T. M. Palstra, T. Hibma, and S. Celotto. Diffusive motion of antiphase domain boundaries in Fe_3O_4 films. *Phys. Rev. B*, **68**:014428, 2003.

[236] S. S. P. Parkin, R. Sigsbee, R. Felici, and G. P. Felcher. Observation of magnetic dead layers at the surface of iron oxide films. *Applied Physics Letters*, **48**:604–606, 1986.

[237] A. R. Ball, H. Fredrikze, D. M. Lind, R. M. Wolf, P. J. H. Bloemen, M. Th. Rekveldt, and P. J. van der Zaag. Polarized neutron reflectometry studies of magnetic oxidic Fe_3O_4/NiO and Fe_3O_4/CoO multilayers. *Physica B: Condensed Matter*, **221**:388–392, 1996.

[238] K. Matsuzaki, V. K. Lazarov, L. Lari, H. Hosono, and T. Susaki. Fe_3O_4(111) thin films with bulk-like properties: growth and atomic characterization. *Journal of Physics D: Applied Physics*, **46**:022001, 2013.

[239] K. Reuter and M. Scheffler. Composition, structure, and stability of RuO_2(110) as a function of oxygen pressure. *Phys. Rev. B*, **65**:035406, 2001.

[240] A. Rosenauer, M. Schowalter, A. G. Cullis (Editor), and P. A. Midgley (Editor). *Microscopy of Semiconducting Materials: STEMSIM—a New Software Tool for Simulation of STEM HAADF Z-Contrast Imaging*, pages 170–172. Springer Netherlands, 2008.

[241] M. Kawasaki, K. Takahashi, T. Maeda, R. Tsuchiya, M. Shinohara, O. Ishiyama, T. Yonezawa, M. Yoshimoto, and H. Koinuma. Atomic Control of the $SrTiO_3$ Crystal Surface. *Science*, **266**:1540–1542, 1994.

[242] G. Koster, G. Rijnders, D. H. A. Blank, and H. Rogalla. Surface morphology determined by (001) single-crystal $SrTiO_3$ termination. *Physica C: Superconductivity*, **339**:215–230, 2000.

[243] J. Nichols, O. B. Korneta, J. Terzic, G. Cao, J. W. Brill, and S. S. A. Seo. Epitaxial Ba_2IrO_4 thin-films grown on $SrTiO_3$ substrates by pulsed laser deposition. *Applied Physics Letters*, **104**:121913, 2014.

[244] J. Nichols, J. Terzic, E. G. Bittle, O. B. Korneta, L. E. De Long, J. W. Brill, G. Cao, and S. S. A. Seo. Tuning electronic structure via epitaxial strain in Sr_2IrO_4 thin films. *Applied Physics Letters*, **102**:141908, 2013.

[245] L. Miao, Hong Xu, and Z. Q. Mao. Epitaxial strain effect on the $J_{eff} = 1/2$ moment orientation in Sr_2IrO_4 thin films. *Phys. Rev. B*, **89**:035109, 2014.

[246] J. Nichols, O. B. Korneta, J. Terzic, L. E. De Long, G. Cao, J. W. Brill, and S. S. A. Seo. Anisotropic electronic properties of a-axis-oriented Sr_2IrO_4 epitaxial thin-films. *Applied Physics Letters*, **103**:131910, 2013.

[247] E. H. P. Cordfunke and G. Meyer. The system iridium - oxygen I. Measurements on the volatile oxide of iridium. *Recueil des Travaux Chimiques des Pays-Bas*, **81**:495–504, 1962.

[248] Y. Tian, Y. Gong, Z. Li, F. Jiang, and H. Jin. Synthetic process and spark plasma sintering of $SrIrO_3$ composite oxide. *Journal of Advanced Ceramics*, **2**:347–352, 2013.

[249] X. Hou, R. Takahashi, T. Yamamoto, and M. Lippmaa. Microstructure analysis of IrO_2 thin films. *Journal of Crystal Growth*, **462**:2 –28, 2017.

[250] A. Yamasaki, O. Kirilmaz, A. Irizawa, A. Higashiya, T. Muro, H. Fujiwara, F. Pfaff, P. Scheiderer, J. Gabel, M. Sing, M. Yabashi, K. Tamasaku, A. Hloskovskyy, H. Okabe, H. Yoshida, M. Isobe, J. Akimitsu, W. Drube, T. Ishikawa, S. Imada, A. Sekiyama, R. Claessen, and S. Suga. Spin-Orbit-Coupling-Induced j_{eff} States in Perovskite Iridates Studied by Photoemission Spectroscopy. *Proceedings of the International Conference on Strongly Correlated Electron Systems (SCES2013)*, JPS Conf. Proc. 3, 013001, 2014.

[251] A. Yamasaki, O. Kirilmaz, A. Irizawa, A. Higashiya, T. Muro, H. Fujiwara, F. Pfaff, P. Scheiderer, J. Gabel, M. Sing, M. Yabashi, K. Tamasaku, A. Hloskovskyy, H. Okabe, H. Yoshida, M. Isobe, J. Akimitsu, W. Drube, T. Ishikawa, S. Imada, A. Sekiyama, R. Claessen, and S. Suga. Spin-Orbit-Coupling-Induced j_{eff} States in Perovskite Iridates Studied by Photoemission Spectroscopy. Proceedings of the International Conference on Strongly Correlated Electron Systems (SCES2013).

[252] A. Yamasaki, S. Tachibana, H. Fujiwara, A. Higashiya, A. Irizawa, O. Kirilmaz, F. Pfaff, P. Scheiderer, J. Gabel, M. Sing, T. Muro, M. Yabashi, K. Tamasaku, H. Sato, H. Namatame, M. Taniguchi, A. Hloskovskyy, H. Yoshida, H. Okabe, M. Isobe, J. Akimitsu, W. Drube, R. Claessen, T. Ishikawa, S. Imada, A. Sekiyama, and S. Suga. Bulk nature of layered perovskite iridates beyond the Mott scenario: An approach from a bulk-sensitive photoemission study. *Phys. Rev. B*, **89**:121111, 2014.

[253] P. Li, B. L. Guo, and H. L. Bai. Spin injection from epitaxial Fe_3O_4 films to ZnO films. *Journal of Applied Physics*, **109**:013908, 2011.

[254] S. Brück. *dbEditor, Version 2.0.2b3.* 2011.

[255] IFA. *GESTIS-Stoffdatenbank*, (accessed December 09, 2016). `http://www.dguv.de/ifa/gestis/gestis-stoffdatenbank/index.jsp`.

List of own publications

- **O. Kirilmaz**, M. Karolak, N. Gauquelin, M. Zapf, J. Verbeeck, G. Sangiovanni, M. Sing, and R. Claessen, *Substrate termination and preparation dependent interface properties in the all-oxide heterostructure* Fe_3O_4/ZnO, in preparation.
- K. Fürsich, V. B. Zabolotnyy, E. Schierle, L. Dudy, **O. Kirilmaz**, M. Sing, R. Claessen, R. J. Green, M. W. Haverkort, and V. Hinkov, *Theory-restricted resonant x-ray reflectometry of quantum materials*, Phys. Rev. B **97**, 165126 (2018).
- F. Pfaff, H. Fujiwara, G. Berner, A. Yamasaki, H. Niwa, H. Kiuchi, A. Gloskovskii, W. Drube, **O. Kirilmaz**, A. Sekiyama, J. Miyawaki, Y. Harada, S. Suga, M. Sing, and R. Claessen, *Raman and fluorescence contributions to the resonant inelastic soft x-ray scattering on* $LaAlO_3/SrTiO_3$ *heterostructures*, Phys. Rev. B **97**, 035110 (2018).
- A. Yamasaki, H. Fujiwara, S. Tachibana, D. Iwasaki, Y. Higashino, C. Yoshimi, K. Nakagawa, Y. Nakatani, K. Yamagami, H. Aratani, **O. Kirilmaz**, M. Sing, R. Claessen, H. Watanabe, T. Shirakawa, S. Yunoki, A. Naitoh, K. Takase, J. Matsuno, H. Takagi, A. Sekiyama, and Y. Saitoh, *Three-dimensional electronic structures and the metal-insulator transition in Ruddlesden-Popper iridates*, Phys. Rev. B **94**, 115103 (2016).
- A. Yamasaki, S. Tachibana, H. Fujiwara, A. Higashiya, A. Irizawa, **O. Kirilmaz**, F. Pfaff, P. Scheiderer, J. Gabel, M. Sing, T. Muro, M. Yabashi, K. Tamasaku, H. Sato, H. Namatame, M. Taniguchi, A. Hloskovskyy, H. Yoshida, H. Okabe, M. Isobe, J. Akimitsu, W. Drube, R. Claessen, T. Ishikawa, S. Imada, A. Sekiyama, and S. Suga, *Bulk nature of layered perovskite iridates beyond the Mott scenario: An approach from a bulk-sensitive photoemission study*, Phys. Rev. B **89**, 121111 (2014).

Danksagung

Abschließend möchte ich an dieser Stelle noch die Gelegenheit nutzen mich bei all denjenigen zu bedanken, die zum Gelingen dieser Doktorarbeit beigetragen und mich während der Bearbeitungszeit unterstützt haben.

- Mein allererster Dank geht an Prof. Dr. Ralph Claessen, der es mir ermöglicht hat, meine Doktorarbeit an seinem Lehrstuhl anzufertigen. Besonders bedanken möchte ich mich bei ihm außerdem dafür, dass mir die Gelegenheit gegeben wurde meine Experimente an zahlreichen Synchrotrons durchzuführen und an vielen Konferenzen, Tagungen und Schulen teilzunehmen, womit ich sehr viele wertvolle Erfahrungen für die Zukunft sammeln konnte.

- Genauso wichtig ist es mir, mich bei Prof. Dr. Michael Sing für die vielen Ratschläge in den letzten Jahren und für das Korrekturlesen meiner Doktorarbeit zu bedanken. Auch danke ich ihm für die vielen amüsanten und interessanten Gespräche, die den ein oder anderen anstrengenden Arbeitstag durchaus aufzulockern wussten.

- I want to thank Prof. Dr. Atsushi Yamasaki for his agreement to become one of the assessors of my PhD thesis and one of the examinants during my PhD defense. In addition, I want to thank him for the nice visit I had at his chair at Konan-University in Kobe and for the chance to give a guest talk there. Last but not least, I highly appreciate his helpful advice on the iridate topics. Domo arigato gozaimasu!

- Many thanks to all members of Prof. Dr. Atsushi Yamasaki's group from the Konan-University and Prof. Dr. Hidenori Fujiwara's group from the Osaka-University. Thank you so much for your help during the SPring-8 beamtimes and an unforgettable time in Japan, including the melon-pan and hormone-yaki-udon experiences! Also many thanks to Prof. Dr. Shigemasa Suga, Prof. Dr. Akira Sekiyama and Dr. Yuji Saitoh for their big support at SPring-8.

- Auch ein großes Dankeschön an Prof. Dr. Giorgio Sangiovanni, der sich bereit erklärt hat einer der Prüfer in meinem Promotionskolloquium zu sein. Grazie mille!

- Großer Dank geht auch an Dr. Michael Karolak für seine umfangreichen DFT Rechnungen und die daraus entstandenen Ergebnisse zum Thema Magnetit auf Zinkoxid.

- Bei meinem Bürokollegen Dr. Lenart Dudy will ich mich für die Hilfe bei der ARPES-Datenauswertung und das Korrekturlesen meiner Doktorarbeit bedanken. Aber besonders möchte ich ihm für den ganzen Bürospaß in den letzten Jahren danken, an den ich mich sicherlich noch Jahrzehnte später erinnern werde. Special thanks also to my other office colleague Dr. Victor Rogalev for proof reading my PhD thesis and the occasional "V"-sessions (you know what i mean).

- Außerdem möchte ich mich noch bei folgenden Personen besonders bedanken: Judith Gabel für ihre Hilfe bei den Transportmessungen am PPMS, Michael Zapf für die tatkräftige Unterstützung rund um das Thema Magnetit, Dr. Florian Pfaff für die vielen gemeinsamen lustigen Pausen und seine große Hilfe im Labor, Martin Zinner für die vielen Tipps bei der Verwendung der Glovebox, Dr. Eberhard Goering für die SQUID-Messungen an Magnetit, Dr. Nicolas Gauquelin, Dr. He Tian und Prof. Dr. Johan Verbeeck für die detaillierte TEM-Studie an den Magnetit-Proben, Dr. Volodymyr Zabolotnyy, Dr. Christian Schüßler-Langeheine, Dr. Enrico Schierle und Prof. Dr. Vladimir Hinkov für die XRR-Messungen an den Magnetitfilmen, Dr. Martin Kamp für die TEM-Charakterisierung der Iridat-Probe, Dr. Masaaki Isobe für die Bereitstellung der Iridat-Targets, Dr. Nina-Juliane Steinke und Dr. Sebastian Brück für ihre Unterstützung bei den PNR-Messungen, Knut Peters für die vielen Informationen bezüglich der verwendeten Substrate, Franz Schwabenländer und Thomas Demarczyk für ihre technisch sehr hilfreichen Dienste im Labor und zu guter Letzt noch bei unserer lieben Sekretärin Monika Seifer für all die große Hilfe in so vielen Angelegenheiten.

- Liebe "Godfathers of Flyfishing", vielen Dank, dass ihr (Markus Theophel, Markus Knell abi und vor allem mein Bro Marcus Orth) immer Verständnis dafür hattet, wenn ich mal wieder keine Zeit zum Fischen mit euch hatte. Aber ab jetzt geht es immer zusammen ans Wasser!

- Bei meiner lieben Verlobten Kamonrat Kuhlmann möchte ich mich ganz herzlich dafür bedanken, dass sie stets Geduld mit mir hatte und immer für mich da war, auch in besonders schwierigen Zeiten. Khop khun khap thilak!

- Mein größter Dank gebührt jedoch meinen Eltern, Kamile und Selman Kırılmaz: Canım annem ve aslan babam, size hersey için teşekkür ederim. Size ne kadar teşekkür etsemde, yeterli olamaz. Hep arkamdaydınız, bana hep güvendiniz, bana hep inandınız, bana hep sonsuz sevgi verdiniz ve saygı gösterdiniz. İyiki vardınız yanımda, iyiki varsınız hayatımda.